Simulation and Control of Stationary Crossflow Vortices

Vinan Mistry

Department of Aeronautical and Automotive Engineering

Loughborough University

A thesis submitted for the degree of

Doctor of Engineering

May 2014

To my father, mother, sister
and
loving wife ...

Acknowledgements

I would like to express my sincere gratitude to Dr Gary Page not only for his invaluable supervision for this research project but also for his general guidance and support during my time at Loughborough University. I would also like to express my gratitude to Prof J. J. McGuirk for his useful, thorough and challenging advice throughout the research.

A special thanks goes out to Dr Chris Ford, Dr Max Rife, Tim Coates, Dr Lara Schembri-Puglisevich, Dr Andrew McMullan, Dr Chris Pokora and Vipram Kannan who were apart of the 'SM1.20' research office. Your useful discussions and suggestions were helpful and more than made up for the lack of footballing talent.

I would also like to thank Murray Cross, Stefano Tursi and Jeremy Benton at Airbus, Filton for funding the project and additional supervision. The Airbus workshops were a great way to connect to other researchers and to get involved in exciting research, I feel privileged to have been apart of it.

Furthermore, I would like to acknowledge my family for their love and support during this project and throughout my entire education from a young age.

Finally, I would like to dedicate this thesis to my partner Devisha. We met when I began this research project and your patience and continuous encouragement has made it possible for me to get to the finish line. I am honoured and privileged to complete this thesis with you as my wife.

Abstract

Turbulent flow and transition are some of the most important phenomena of fluid mechanics and aerodynamics and represent a challenging engineering problem for aircraft manufacturers looking to improve aerodynamic efficiency. Laminar flow technology has the potential to provide a significant reduction to aircraft drag by manipulating the instabilities within the laminar boundary layer to achieve a delay in transition to turbulence.

Currently prediction and simulation of laminar-turbulent transition is conducted using either a low-fidelity approach involving the stability equations or via a full Direct Numerical Simulation (DNS). The work in this thesis uses an alternative high-fidelity simulation method that aims to bridge the gap between the two simulation streams. The methodology uses an LES approach with a low-computational cost sub-grid scale model (WALE) that has inherent ability to reduce its turbulent viscosity contribution to zero in laminar regions. With careful grid spacing the laminar regions can be explicitly modelled as an unsteady Navier-Stokes simulation while the turbulent and transitional regions are simulated using LES. The methodology has been labelled as an unsteady Navier-Stokes/Large Eddy Simulation (UNS/LES) approach.

Two test cases were developed to test the applicability of the method to simulate and control the crossflow instability. The first test case replicated the setup from an experiment that ran at a chord-based Reynolds number of $390,000$. Two methods were used to generate the initial disturbance for the crossflow vortices, firstly using a continuous suction hole and secondly an isolated roughness element. The results for this test case showed that the approach was capable of modelling the full transition process, from explicitly modelling the growth of the initial amplitude of the disturbances to final breakdown to turbulence. Results matched well with the available experimental data.

The second test case replicated an experimental setup using a custom-designed aerofoil run at a chord-based Reynolds number of 2.4 million. The test case used Distributed Roughness Elements (DRE) to induce crossflow vortices at both a critical and a control wavelength. By forcing the crossflow vortices at a stable (control) wavelength a delay in laminar-turbulent transition can be achieved. The results showed that the UNS/LES approach was capable of capturing the initial disturbance amplitudes due to the roughness elements and their growth rates matched well with experimental data. Finally, downstream a transitional region was assessed with low-freestream turbulence provided using a modified Synthetic Eddy Method (SEM). The full laminar-turbulent transition process was simulated and results showed significant promise.

In conclusion, the method employed in this thesis showed promising results and demonstrated a possible route to high-fidelity transition simulation run at more realistic flow conditions and geometries than DNS. Further work and validation is required to test the secondary instability region and the final breakdown to turbulence.

Contents

List of Figures

Nomenclature

Acronyms

TS	Tollmien-Schlichting
CFL	Courant Friedrichs Lewy Number
CFD	Computational Fluid Dynamics
DRE	Distributed Roughness Elements
GDP	Gross Domestic Product
DOC	Direct Operating Cost
CF	Crossflow
NLF	Natural Laminar Flow
HLFC	Hybrid Laminar Flow Control
LFC	Laminar Flow Control
RANS	Reynolds Averaged Navier Stokes
LES	Large Eddy Simulation
DNS	Direct Numerical Simulation
UNS	Unsteady Navier Stokes
NPSE	Non-Linear Parabolized Stability Equations
LSE	Linear Stability Equations
SGS	Subgrid Scale
SEM	Synthetic Eddy Method
CPU	Central Processing Unit
WALE	Wall Adapting Local Eddy Viscosity
PIV	Particle Image Velocimetry

Latin Symbols

Tu	Turbulent Intensity

k	Roughness Element Height
Re_c	Chord-based Reynolds Number
Re_k	Roughness Height based Reynolds Number
Re_θ	Momentum Thickness based Reynolds Number
Re_v	Vorticity based Reynolds Number
C_w	WALE Constant
C_s	Smagorinsky Constant
C_K	Kolmogorov Constant
Q_0	Freestream Velocity
C_q	Suction Rate
c	Chord
W_{MF}	Mission Fuel Weight
W_P	Payload Weight
W_E	Aircraft Empty Weight
R	Aircraft Range
H	Calorific Value of Fuel
L	Lift
D	Drag
M	Mach Number
x, y, z	Cartesian Coordinate Components
u, v, w	x, y, z Velocity Components
p	Pressure
$\widetilde{u_i}$	Resolved Velocity Component Vector
$\mathrm{u'}_i$	Subgrid Scale Velocity Component Vector
$\overline{R}$	Attachment Line Reynolds Number
S_{ij}	Strain-Rate Tensor
$\widetilde{g_{ij}}$	Resolved Velocity Gradient Tensor
R_{ij}	Reynold Stress Tensor
a_{ij}	Cholesky Decomposition of Reynold Stress Tensor

Greek Symbols

π	Pi
λ	Spanwise Wavelength
τ_{ij}	Viscous Stress Tensor

ρ	Density
η	Overall Propulsion Efficiency
ν	Kinematic Viscosity
ν_t	Subgrid Scale Viscosity
Δ	Filter Width
δ_{ij}	Kronecker Delta
σ	Characteristic Length Scale
θ	Momentum Thickness

Operators

$\bar{.}$	LES Reynolds averaged quanities
$\widetilde{.}$	LES Favre filtered quantities
G()	Convolution Function for Filtering

Chapter 1

Introduction

1.1 Systems Viewpoint

The aircraft industry is an invaluable asset to the global economy; aviation's economic and societal contribution generates around £200 billion for the global economy and provides 4.5 million jobs worldwide. For evidence of the global value of the aircraft industry, the economic impact of the disruption to the European air transport system of 2010's volcanic eruption in Iceland has estimated to amount to approximately £2.2 billion in the first week.

The demand for air transportation can historically be considered proportional to GDP and population density. With world population increasing substantially year on year and developing economies maturing, the demand for air travel is expected to continue to rise. According to the Airbus Global Market Forecast [5], overall world passenger traffic is expected to increase 4.7% per annum in the next decade and the frequency of flights offered on passenger routes will double, despite the current economic crisis.

This substantial increase in air traffic is causing the civil aviation sector to consider its cost to the global environment and to its customers. This has led to leading European industry partners to agree an ambitious target in reducing 75% of carbon emissions from commercial aircraft by 2050, relative to 2000 levels [3; 37]. For kerosene fuelled aircraft, reducing carbon emissions equates to reducing *fuel burn*. Reduction of aircraft fuel burn has always been a high priority for the aircraft manufacturing industries, especially since the rising cost of fuel has a compounding impact on Airbus's customers.

Figure 1.1 shows the monthly crude oil prices over the last 5 decades adjusted

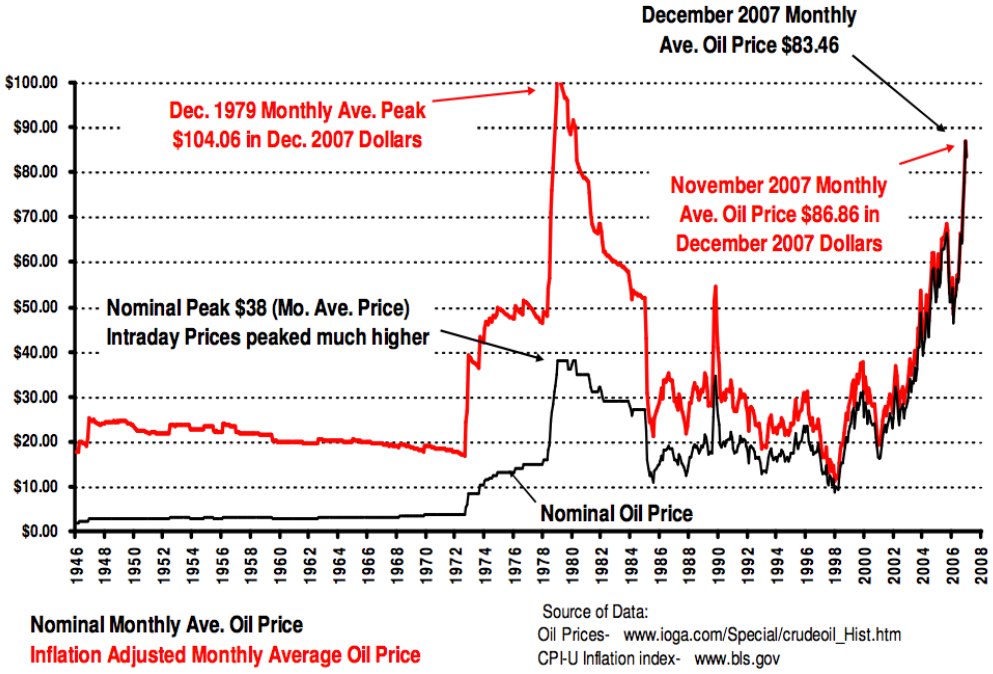

Figure 1.1: Inflation adjusted monthly crude oil prices [32]

for inflation. The average price for one US gallon of kerosene over the period from mid 1986 to the end of 2001 was 59 US-cents. However, between 2002 and 2005, the price of kerosene rose to a level above 180 US cents. At 60 US cents/US gallon the fuel for a typical 6,000nm mission of a long range aircraft costs about 17% of the DOC. Keeping other parameters constant, the fuel share rises to 38% of DOC at 180 US cents per gallon [32; 106]. This substantial increase in costs of fuel further demonstrates the civil aircraft industries need for a reduction in aircraft fuel burn.

Looking to the past can give an indicator as to the current efficiency trend for civil aircraft and the potential for improvement in aircraft fuel burn using current aircraft design methods. Commercial aircraft over the last 60 years have been mainly based on what is called the conventional layout. This is characterised by a slender fuselage mated to a high aspect ratio wing with aft mounted empennage and pod mounted engines under the wing, first designed for commercial use by Boeing with the 707. Since the manufacture of their first aircraft, the A300, Airbus have made significant progress in optimising the fuel burn of its conventional layout aircraft range.

The term fuel burn is defined as the mass of fuel burned divided by a product of the payload and flight range, which can be determined from the Breguet range equation. The Breguet range equation is a robust statement and defines the bounds of what is achievable in aircraft performance. A form of the Breguet Range Equation

was derived by Green [32] which can be cast as an expression for fuel burn per unit payload-range, described in Equation 1.1.

$$\frac{W_{MF}}{RW_P} = \frac{1}{X}(1 + \frac{W_E}{W_P})(\frac{e^{\frac{R}{X}} - 1}{\frac{R}{X}}), \qquad X = H\eta\frac{L}{D} \tag{1.1}$$

By calculating this ratio for a flight range from 10kft to flight altitude the average aerodynamic efficiency can be calculated for an aircraft. To assess the increase in efficiency in the past Figure 1.2 shows the average aerodynamic efficiency for the families of Airbus aircraft over the last 50 years (data acquired from Becker and Abbas-Beyoumi [11]).

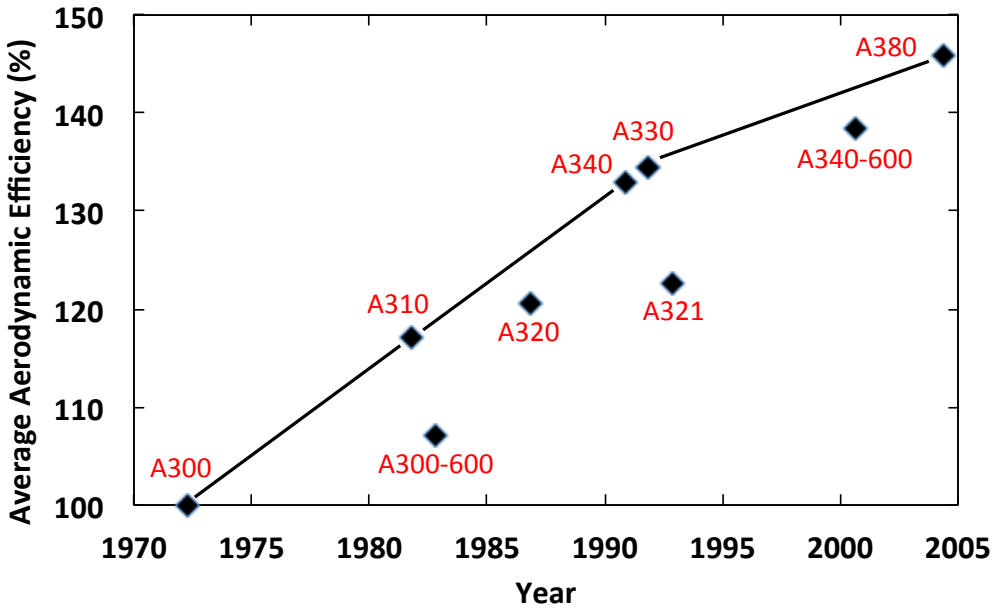

Figure 1.2: Average aerodynamic efficiency of Airbus aircraft

It is evident when assessing the improvement in aerodynamic efficiency throughout the Airbus aircraft family that classical aircraft design is still open to optimisation. With each generation of aircraft a steady amount of improvement in efficiency has been made. However it is also evident when considering the shallower gradient of improvement with the A380 aircraft that classical aircraft design may be reaching an asymptote in its performance improvement. For this reason, only using conventional aircraft design any further improvement is estimated to be about only half of what is finally required to reach the 2050 efficiency targets. Consequently the aviation sector is heading into an era of efficiency improvement by adopting a 'holistic' viewpoint. By viewing the industry from a higher level of abstraction it may be possible to achieve

the additional improvements in efficiency using more multidisciplinary optimisation and system integration.

By taking a holistic viewpoint, all aviation industry partners and systems are involved in achieving the ambitious fuel burn reduction target. This not only involves aircraft and engine manufacturers but also airport turnaround time, congestion and landing/take-off waiting times. Optimising flight paths and improving regulation with combined European airspace control will have a substantial impact on reducing fuel burn per flight. Also, reducing airport congestion and adopting advanced communication, navigation, and surveillance and air traffic management systems can reduce the time aircraft spend idling on runways or circling airports waiting to land, thus reducing fuel use and associated emissions. According to the Pew Center on Global Climate Change [65], the benefit from new regulations and optimisation of airport systems is estimated to provide a 5% reduction in carbon emission per passenger mile by 2050.

Additionally the aircraft powerplant is also undergoing a period of innovation and new concepts. Larger bypass ratio engines, the geared turbofan (GTF) or even open rotor engines (CROR) are near to becoming a viable option. It is expected that the introduction of new engine innovations will provide a 30% reduction in carbon emissions per passenger mile by 2050 [65].

Alternative fuel sources have lower new emissions than traditional petroleum-based aircraft fuel. Bio-fuels could present a feasible alternative in the future. While these fuels do not present an immediate alternative, their adoption presents a long-term path toward lower carbon flight. To be seriously considered, alternative fuels must be both cost-competitive and offer significant reductions in green house gas emissions. It is expected that a 24% reduction in emissions can be achieved, however unlikely by the 2050 target [65].

Therefore, the remaining 40% reduction in emissions is required to come from innovation in aircraft design and advanced aerodynamics technologies. For this reason aircraft manufacturers are looking to plan future design projects with a blank canvas. Alternative aircraft configurations that were popular in the 1950's are making a return to research efforts. These include the Blended Wing Body (BWB) which combines the fuselage and wing of the aircraft, and other configurations including forward swept wings. A deeper understanding and research of their aerodynamic advantages and optimisation is required before a proper judgement on their value can be determined.

From an aerodynamics perspective, reducing aircraft fuel burn equates to im-

proving the airframe aerodynamic efficiency: the Lift/Drag ratio. To improve the aerodynamic efficiency, aircraft manufacturers are looking to reduce the drag of the airframe.

Figure 1.3 shows a breakdown of drag on a modern civil airliner.

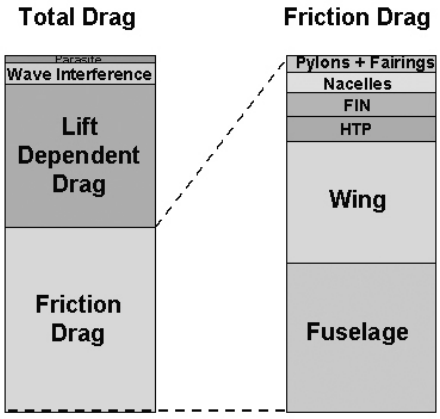

Figure 1.3: Drag breakdown of civil airliner in cruise [106]

The figure shows that skin-friction drag constitutes more than half of the total aircraft drag, with a total of 18% attributed to friction drag from the wing.

Skin friction drag occurs in the fluid region in the immediate neighbourhood of the aircraft walls, the boundary layer, in which the influence of viscosity is confined. [85; 105]. One of the most relevant characteristics of the boundary layer is the flow state in which it is moving: laminar, turbulent or transitional. A laminar boundary layer is well structured, layered and deterministic (Latin *Lamina*: a layer or coat lying over another). A turbulent boundary layer however is characterised by near random, always unsteady and highly non-linear behaviour with the presence of multiple, different sizes of eddies (turbulent vortices) that create an additional shear stress which enhances momentum transfer from the relatively fast moving outer parts of the boundary layer to the portions closer to the surface. Consequently the distribution of time-averaged velocity is characterised by higher velocities near the surface and a greater total boundary layer thickness in a turbulent boundary layer than an equivalent laminar boundary layer [1]. The evolution and breakdown from a steady laminar flow to a turbulent flow is called *laminar-turbulent transition*. The origins of turbulent flow and transition are the most important unsolved problems of fluid mechanics and aerodynamics and research has been ongoing for more than century.

According to Schrauf [106], if the flow were laminar on 20%, 30% or 40% of the surfaces, the total drag of the aircraft would be reduced by 8%, 12% or 16%. It is

for this reason that civil aircraft manufacturers such as Airbus have invested heavily into methods of controlling laminar-turbulent transition on wing boundary layers and delaying as far aft as possible. Any potential reduction in drag would help Airbus and the civil aviation industry to meet ambitious targets in reduction of carbon emissions and fuel burn for passenger jets.

1.2 Swept-Wing Laminar-Turbulent Transition

A deep understanding of the mechanisms that cause transition to turbulence within a laminar boundary layer must be obtained before control can be achieved. The Reynolds number is the ratio of inertial forces to viscous forces and is consequently a crucial parameter in determining whether a fluid flow is likely to be laminar or turbulent since viscous forces act to damp out any flow disturbances present. The definition of the Reynolds number is described in Equation 1.2, where U is the freestream velocity, L is a reference length (for airfoils: chord, pipe flows: diameter) and ν is the kinematic viscosity.

$$Re = \frac{UL}{\nu} \tag{1.2}$$

The range of Reynolds number for which laminar flow is observed is limited and as a result turbulent flow is usually observed for practical applications. Reynolds (1883) [91] was the first to propose a criterion for differentiation between laminar and turbulent flows in his classic dye visualisation; he suggested that for pipe flows (closed systems) the critical Re is estimated at $Re = 2100$. A flow of Re below this value is expected to be laminar, while flows at slightly above this value are transitional and flows $Re > 10,000$ are turbulent. Further research showed that the critical Reynolds number could be increased by minimising external disturbances and careful design of pipe entrances, Pfenniger [77] was able to maintain laminar flow at a Reynolds number of 100,000.

For airfoils and flat plates however (open systems) no such simple criterion exists that can predict the laminar, turbulent and transitional Reynolds numbers [102]. One reason for this is that open systems, such as an aircraft wing in flight, have many environmental and design variables (freestream conditions, sound, pressures, geometry, surface quality, etc.) that all play a role in determining the mechanisms for transition, and at the time of writing they are still not fully understood.

The process in which laminar-turbulent transition occurs is complex, consisting of

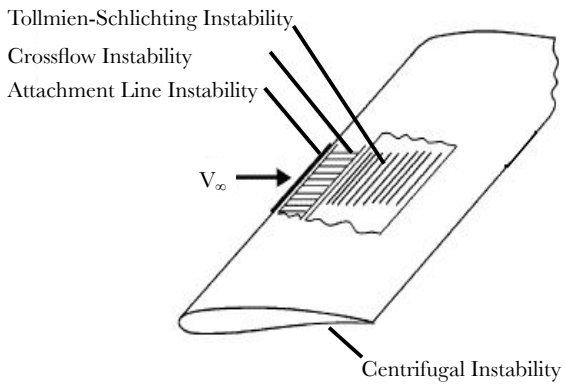

Figure 1.4: Transition instabilities on aircraft wings [106]

a large number of competing events and stages of disturbance growth. The transition process begins with external disturbances such as freestream unsteadiness, freestream acoustic waves, or boundary effects such as surface roughness and vibrations. The internal boundary layer respond to these external disturbances in a process called receptivity [69]. The disturbances enter the boundary layer as steady and/or unsteady fluctuations about the mean flow. The process of receptivity establishes the initial conditions of disturbance, amplitude, frequency, and phase for the eventual breakdown of laminar flow [102]. The next stage of transition depends on the initial amplitude of the disturbance, for higher freestream turbulence conditions, such as occur in compressor blades within gas turbine engines, transition occurs through transient growth and so-called bypass transition mechanisms. For low freestream turbulence environments, such in civil aircraft flight, the laminar boundary layer first undergoes a primary instability due to a variety of transition mechanisms, explained in the next paragraph, before undergoing a secondary instability and final breakdown to turbulence.

To achieve a delay in laminar-turbulent transition design engineers must tailor their wing geometry to manipulate the instabilities that cause a laminar flow to breakdown to turbulence. Four basic instability mechanisms can contribute to transition on a swept wing: attachment line, streamwise, centrifugal and the crossflow instability, the latter is the main interest of this thesis and is explained in detail in the next section. The wing area in which different instabilities exert an influence are illustrated in Figure 1.4.

Attachment line instabilities can be a mechanism for transition via two sources: contamination and instability. Turbulent contamination of the attachment line of the

wing can arise when a swept body is attached to a solid wall (fuselage, wind tunnel wall). The attachment line can also undergo an instability which can be controlled by keeping the leading-edge radius below a critical value. This was first observed by Pfenninger during X-21 laminar flow flight tests [78]. Pfenninger formulated a criterion based on an attachment line Reynolds number ($\overline{R} < 250$) which was later confirmed by Poll in wind tunnel experiments with swept cylinders [83]. Several investigations have validated this criterion over many years. These studies include wind tunnel experiments, flight experiments and Direct Numerical Simulations [7]. These studies have concluded that if $\overline{R} < 250$, the bursts of turbulence convected along the wall are damped and vanish as they travel along the attachment line. For $\overline{R} > 250$ these bursts are self-sustaining. They grow, overlap and the leading edge region becomes fully turbulent.

Streamwise instabilities occur in the form of *Tollmien-Schlichting (TS) waves* (natural transition) that typically occur in the mid-chord region. When a laminar boundary layer becomes linearly unstable beyond a critical Reynolds number, TS waves start to grow. The instability is via a subtle mechanism whereby viscosity destabilises the waves and they begin to grow exponentially, and lead to transition when critical flow parameters are reached. It is now well known that shaping the airfoil for a favourable gradient and minimising the extent of the pressure- recovery region both contribute to the control of this instability.

Centrifugal instabilities appear in concave regions on a surface, resulting in the development of *Görtler vortices*. They are reminiscent of counter-rotating vortices and are usually found on the lower surface of wings [97].

1.3 The Crossflow Instability

The final mechanism, the *crossflow instability*, is commonly the dominant source of laminar-turbulent transition on modern swept wings. The primary stage of this instability originates due to the combined influences of sweep and pressure gradient on an aircraft wing, generating curved streamlines at the boundary-layer edge. Curved streamlines cause centrifugal forces that are balanced by radial pressure gradients. Since static pressure can reasonably assumed to be constant in the wall-normal direction within a boundary layer, the excess pressure due to its radial gradient at the boundary layer edge generates a mean cross-flow velocity. Because the crossflow velocity must vanish at the wall and at the edge of the boundary layer, an inflection

point exists and provides the source of an inviscid instability [101; 123]. Figure 1.5(a) shows the inflectional velocity profiles within the boundary layer [123] and Figure 1.5(b) shows the formation of a crossflow vortex on a swept wing [47].

The crossflow instability exhibits amplified disturbances that can be stationary or travelling. Linear stability theory indicates that both stationary and travelling modes are unstable but that travelling waves are more amplified. However, at low free stream turbulence conditions such as in aircraft flight, stationary modes, excited from minute surface non-uniformity or roughness, have been found to be dominant with a stronger integrated disturbance [13; 101]. The receptivity to the disturbance dictates whether travelling or stationary modes grow; Deyhle and Bippes [23] estimated background turbulence levels between 0.15% and 0.3% were necessary before travelling modes became the leading mechanism for laminar-turbulent transition.

The stationary modes result in co-rotating crossflow vortices that are typically aligned with the potential flow producing a large disturbance in the streamwise boundary layer profile. They grow linearly for a small distance in the streamwise direction; however, growth quickly becomes non-linear and results in amplitude saturation of the modes at disturbance amplitudes between $10\% - 30\%$ [123]. As the crossflow vortices begin to grow the disturbance velocities begin to distort the base laminar flow. High momentum fluid is convected down toward the wing surface and low momentum fluid away from the wall resulting in a double inflection point in the wall-normal velocity profile. The inflection points are high in the boundary layer causing the saturated vortices to become susceptible to a high frequency secondary instability that quickly leads to transition to turbulence. This secondary instability is highly amplified and leads to rapid local breakdown, characterised by a turbulent wedge and a 'saw-tooth' pattern [122]. Figure 1.5(c) shows crossflow transition and the formation of turbulent wedges across the transition line using Temperature Sensitive Paint (TSP) [21]. The secondary instability region is not nearly as well understood as its primary instability with a considerable research effort in the last decade [123].

A detailed literature review into the crossflow instability is provided in the Literature Review Chapter of this thesis (Chapter 2). This chapter provides an overview of the fundamentals of crossflow transition as well as key literature in the understanding of the stages of laminar-turbulent transition.

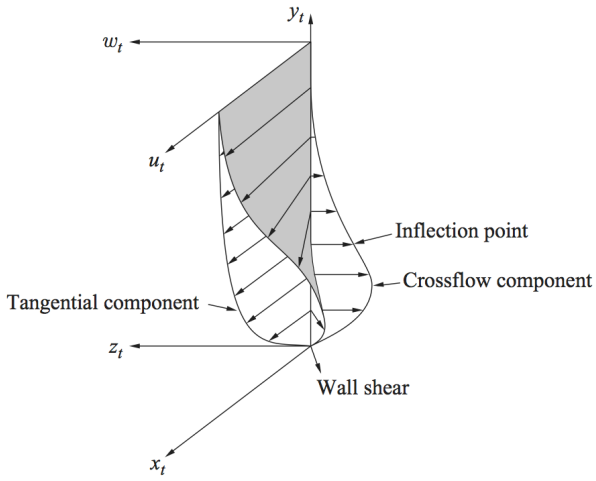

(a) Crossflow boundary layer profiles, Adapted from White et al. [123]

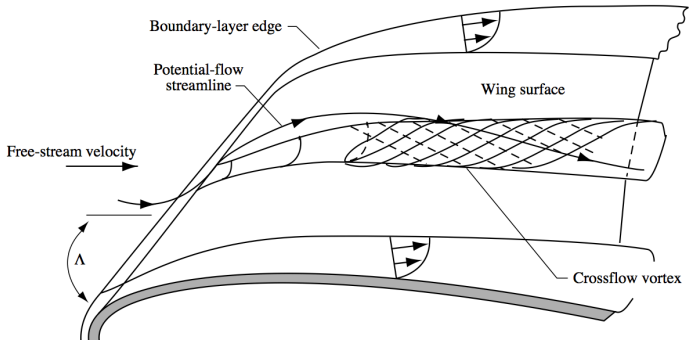

(b) Formation of Stationary Crossflow Vortex, Adapted from Joslin [47]

(c) Transition line for crossflow dominated laminar-turbulent transition [21]

Figure 1.5: The crossflow instability

1.4 Distributed Roughness Elements (DRE)

Control of laminar-turbulent transition is the ultimate goal for design engineers looking to improve efficiency of their wing. A robust and reliable prediction and control strategy for 2D instabilities (streamwise) exists, which involves shaping the aerofoil such that the pressure minimum moves as far aft as possible and employing a favourable pressure gradient to this location. However for aircraft with sweep, crossflow instabilities become problematic and the dominant mechanism for laminar-turbulent transition. Controlling CF disturbances is a difficult task, because the crossflow mean velocity profiles always exhibits at least one inflection point, which cannot be removed. Also, while a favourable pressure gradient stabilises streamwise instabilities it acts to destabilise crossflow.

Previous industrial attempts at control have used a strategy to eliminate streamwise instabilities using the strategy described above and to remove the crossflow instabilities by either greatly reducing the sweep angle or by active methods. The most common active flow control method (*Hybrid Laminar Flow Control (HLFC)*) involves using suction to remove the crossflow velocity component from the leading edge to the front spar location of the wing (around 20% chord) and to apply a favourable pressure gradient up to the mid chord region.

The main problem with this control method is the additional system complexity of suction systems and surfaces. In addition, the manufacture of suction surfaces with micron sized holes requires the use of heavier, more durable materials. This increase in weight in turn reduces the overall impact of the drag reduction method.

Subsequently, Saric et al. [100] proposed a control strategy that aimed at controlling the crossflow vortices instead of removing their development. Here the crossflow vortices are manipulated to promote the growth of stable crossflow wavelengths and delay the growth of unstable wavelengths that lead to early transition. Saric et al. [100] demonstrated a delay in transition to turbulence using an array of distributed roughness elements (DRE) of micron size and a wavelength spacing less than the most unstable wavelength (critical wavelength). The smaller wavelength (control wavelength) modifies the basic flow such that the most unstable wavelength can no longer grow. The control wavelength decays before its amplitude is large enough to cause transition. This control method requires substantial further research, however a recent flight test by Carpenter et al. [18] showed a successful delay in transition using the method.

1.5 Large Eddy Simulation of Crossflow Vortices

The ability to simulate and predict accurately the non-linear flow phenomena downstream of distributed roughness elements (DRE's) and the associated transition location is a significant research goal. Typically, a high-fidelity approach must be adopted. The governing equations for laminar, transitional and turbulent flows are the Navier-Stokes equations (described in detail in Chapter 3). No closed form analytical solutions to these non-linear partial differential equations are known and numerical methods are used to provide an approximate solution. Direct Numerical Simulation (DNS) aims to resolve the full energy cascade of a turbulent flow from the largest turbulent eddies right down to the smallest turbulent eddies, known as the Kolmogorov scales. With careful spatial and temporal resolution highly accurate results can be obtained. DNS is becoming an important tool in understanding the physics of the transition process associated with the crossflow instability with recent literature aiding the understanding of the breakdown region. However, DNS is in general an extremely expensive simulation method even for moderate Re_c, since the required CPU time roughly scales as Re_c^3 and practical simulation of high Re_c cases may be decades away.

Practical simulation of high Re_c flows require simplification of the equations for example conventionally achieved by Reynolds decomposition into time averaged and fluctuating quantities, known as the Reynolds-Averaged Navier Stokes (RANS) method. RANS approaches do not lend themselves easily to transitional flows, where both linear and non-linear effects are relevant, RANS models cannot capture the effect of disturbance growth.

A simulation method that bridges the space between DNS and RANS is Large Eddy Simulation (LES). In an LES, the turbulent eddies larger than a certain size are resolved on the numerical grid, whereas the effect of the smaller scales is modelled via a sub-grid scale (SGS) model. The idea behind such scale-separation is that smaller eddies approach homogeneous and isotropic characteristics while the large energy carrying eddies are strongly anisotropic and affected by geometry and flow conditions. Also, the self-similarity of the small scales makes these easier to model. As not all the scales of turbulence need to be resolved on the computational grid, LES accounts for only a small fraction of the cost of a fully resolved DNS at high Re_c. Transitional flows however, are substantially different from an equilibrium turbulent flow since there is no fully developed energy cascade in transitional flows. A transitional flow contains complex interactions between the base flow and various instability modes

which must all be resolved or modelled reliably.

LES of crossflow vortices has previously been attempted only by Huai et al. [41] using a 45° swept wedge geometry. Stationary and travelling crossflow vortices were generated using steady and random amplitude suction/blowing in the simulation. The LES captured the essential features of the spatial evolution of the crossflow vortex packet and was in good agreement with DNS data. The study showed the capability of LES for a low Re_c case and a simplified geometry.

More recent studies of LES on transitional flows have showed promise including an extensive study by Schlatter [104] on natural laminar-turbulent transition. However most of these studies were conducted on simplified geometries at unrealistic flow conditions ($Re_c < 500,000$). Further research is required to test the LES approach on more relevant test cases and move towards using an LES approach in an industrial context.

1.6 Thesis Goal & Structure

The research described in this thesis aims to develop a high fidelity simulation capability for simulation of stationary crossflow vortices on swept wing flows. A Large Eddy Simulation (LES) methodology will be applied that will use recent key developments within academia to accurately model the transition location on swept wings and simulate the appropriate physics of the breakdown process. For a complex flow phenomena such as crossflow transition, an LES approach may bridge the gap between high fidelity research typically conducted in academia and complex geometries and conditions required within industry.

The LES methodology will require careful implementation for accurate resolution of the transitional flow behaviour. Since the smaller scales are spatially filtered in LES a sub-grid scale (SGS) model is required for modelling of dissipation. The SGS model must be able to handle the different regions associated with laminar, transitional and turbulent flow. There have been a number of recent advancements in SGS modelling of transitional flows and the optimum choice of model will depend on its applicability to industrial CFD codes and its computational expense. An SGS model will be chosen that will allow the turbulent viscosity contribution to be reduced to zero in a laminar region. Thus by carefully resolving the unsteady aspects of the laminar boundary layer and initial disturbance induced unsteadiness the approach can be considered an unsteady Navier-Stokes approach. Coupled with a full LES in the turbulent region

the methodology employed in this thesis is termed an unsteady Navier-Stokes/Large Eddy Simulation (UNS/LES).

Key considerations for successful UNS/LES are the generation of the primary instability for crossflow vortices and the impact of the external environment on the flow receptivity. Surface roughness and free stream turbulence play a key role in determining the mechanisms of transition and the breakdown location. Therefore an investigation into the impact of roughness elements and free stream conditions will be conducted to further understand the modelling and simulation of this area. The research will be conducted using an independent experimental test case to measure the results against and for validation of the UNS/LES method.

Distributed Roughness Elements (DRE) may be a possible route for laminar flow control for aircraft. As the DRE concept involves the non-linear interaction between crossflow vortices it requires a higher fidelity method for simulation and prediction. For accurate prediction in a design context the simulation requires a 'holistic' approach to be taken to laminar-turbulent transition modelling: by involving modelling of all parts of the transition process including receptivity to the roughness elements and modelling the breakdown region. The UNS/LES approach may be a possible route to prediction of DRE's and hence have the ability to predict the relevant stages of transition. This thesis will aim to show the capability of modelling laminar-turbulent transition from DRE's with validation against existing experimental data.

A more detailed overview of the aims and objectives for the research conducted in this thesis is explained in the literature review chapter (Chapter 2).

The remainder of this thesis is structured as follows:

Chapter 2 - 'Literature Review' - The literature review will give a critical analysis of the key and relevant literature and explain in detail the difficulties that arise for crossflow transition prediction and simulation. This chapter will explain in further detail the crossflow instability mechanism with reference to the literature and explain the current industrial methods for control and simulation. Finally the thesis aims and objectives will be explained in detail and the key benefits this work will aim to provide.

Chapter 3 - 'Methodology' - This chapter will detail the UNS/LES numerical methodology used to achieve the aims and objectives set out in the literature re-

view chapter. The chapter will explain the governing equations, CFD code used, UNS/LES solving strategy, sub-grid modelling and boundary conditions used. A detailed description of the models that were implemented into the CFD code will be given. A Wall Adapting Local Eddy Viscosity (WALE) SGS model and a Synthetic Eddy Method (SEM) for synthetic turbulence generation were implemented into the CFD code.

Chapter 4 - 'Simulation of Crossflow Vortices on a C16 Swept Wing' - Details the results of an initial experimental validation test case to demonstrate the capability of the method. The experimental results were taken from an independent study conducted by Chernoray et al. [20]. Two methods for primary instability generation are considered: a continuous suction hole and an isolated roughness element. The results will be compared on various grids and different resolutions and show the impact of the sub-grid model for the various stages of the laminar-turbulent transition.

Chapter 5 - 'Simulation and Control of Crossflow Vortices by DRE' - This chapter will investigate the capability of UNS/LES to model the flow disturbed by distributed roughness elements (DRE) and potential for delay in laminar-turbulent transition. An experimental validation test case was chosen from Texas A&M and conducted by Hunt [42]. The predicted receptivity of the roughness elements will be validated against the experiment. Further tests will be made including the use of SEM for providing a free stream turbulence environment to model the breakdown to turbulence.

Chapter 6 - 'Conclusions' - Finally the conclusions made from the results in this thesis will be outlined along with suggestions for further work.

Chapter 2

Literature Review

2.1 Introduction

Understanding and accurate simulation of crossflow transition has been one of the key objectives for the fluid dynamics research community in recent years. A substantial amount of research effort has resulted in a wealth of literature investigating crossflow instability from a number of research groups. This Chapter will give a critical analysis of this literature and explain in detail the difficulties that arise for transition prediction and simulation. An introduction to laminar-turbulent transition for swept wing aircraft has been given in Chapter 1 and the crossflow instability was also explained. This chapter will explain in further detail the crossflow instability mechanism with reference to research literature and explain the current industrial methods for control and simulation. Finally, the thesis aims and objectives will be explained in detail and the key benefits this work aims to provide.

The literature review in this Chapter is organised into the following 3 areas:

1. **Understanding** - The first part of this chapter will explain in more detail the cause and effects the crossflow instability has on swept wings. Also as explained in Chapter 1, transition occurs through a number of complex stages and each stage of the transition process will be explained and analysed.

2. **Control** - The ultimate aim for design engineers working at aircraft manufacturers is to achieve control of the crossflow instability for delay in laminar-turbulent transition. Control strategy for laminar flow can be grouped into three areas: natural laminar flow (NLF), active flow control (AFC) and distributed roughness elements (DRE). The DRE control strategy is explained in detail as it is

the main control method investigated in this thesis.

3. **Simulation and Prediction** - A number of methods for predicting crossflow transition exist, ranging from low fidelity experimentally correlated methods to high fidelity Direct Numerical Simulations. These methods are explained with reference to the recent literature to establish their current state of art. A Large Eddy Simulation (LES) method is used for the work in this thesis and a justification into why this method was chosen will also be detailed.

2.2 Understanding of the Crossflow Instability

2.2.1 Origins & Fundamentals

The initial discovery of the crossflow instability can be attributed to experiments on transition on swept wing flow by the (British) Royal Aircraft Establishment. Gray [31] showed that laminar-turbulent transition occurred much closer to the leading edge for a swept wing than on a corresponding unswept wing. Using a china clay flow visualisation technique, regular spaced streamwise streaks could be seen. These were initially interpreted as stationary streamwise vortices.

These initial observations led to the work of Stuart in Gregory et al. [33] who gave a theoretical basis for the instability, that remains today. In an experimental and theoretical study on stability and transition of rotating disk flow, it was identified that sweep and a favourable pressure gradient (accelerating flow) create curved streamlines in the inviscid region. The curved streamlines over a swept wing are shown in Figure 2.1. Inside the boundary layer streamwise velocity is reduced, but the pressure gradient is unchanged, thus the balance between centripetal acceleration and pressure gradient does not exist. This leads to a secondary flow in the boundary layer, perpendicular to the direction of the inviscid streamline, called crossflow.

As this crossflow velocity component must be zero at the wall and approach zero at the boundary layer edge, an inflection point exists that is subject to an inviscid instability. This discovery led to a wealth of validation from crossflow instability experiments. The disturbance within the laminar boundary layer can be stationary (steady) or travelling (unsteady) depending on the external environment. The process in which laminar-turbulent transition occurs is complex, consisting of a large number of 'competing' events and stages of disturbance growth. A general, simplified roadmap of laminar-turbulent transition for wall bounded flows was developed by Morkovin et

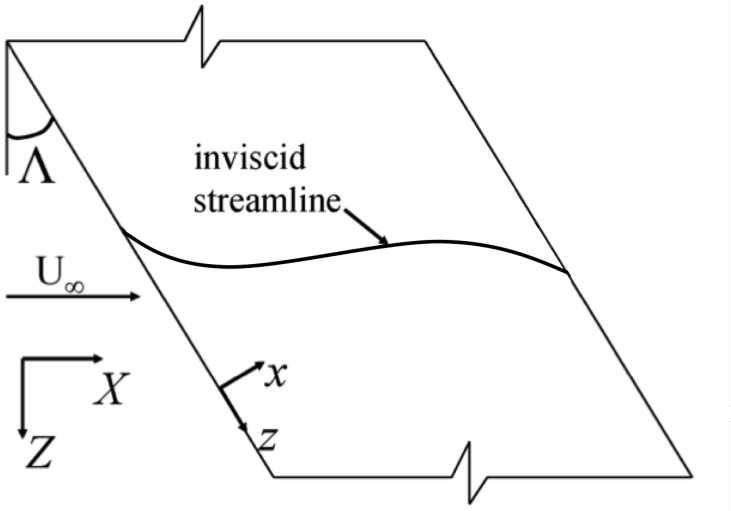

Figure 2.1: Curved streamlines over a swept wing

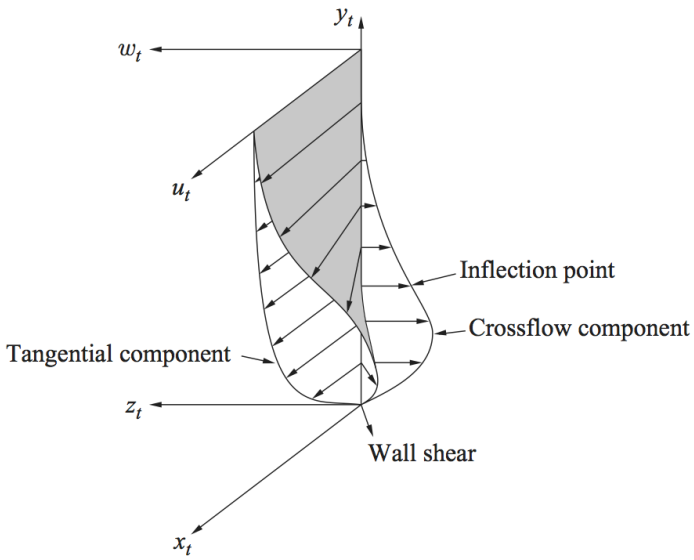

Figure 2.2: Crossflow boundary layer inflection point, Adapted from White et al. [123]

al. [70] (Figure 2.3).

The transition process begins with external disturbances such as freestream fluctuations and freestream acoustic fluctuations or boundary effects such as surface roughness and vibrations. The external disturbances are convert to internal disturbances by a process called receptivity [69]. The process of receptivity establishes the initial conditions of boundary layer disturbance amplitude, frequency, and phase for

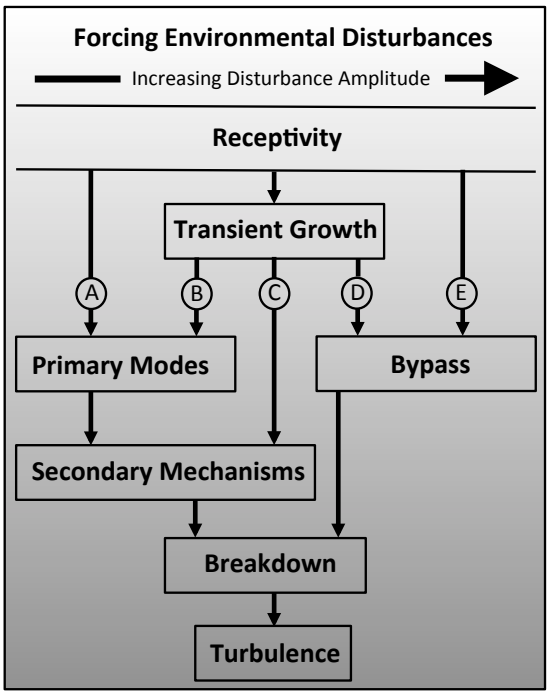

Figure 2.3: Path to turbulence in wall layers (Reconstructed from [70])

the breakdown of laminar flow [102]. The next stage of transition depends on the initial amplitude of the disturbance. For higher free stream turbulence conditions such as compressor blades within gas turbine engines, transition occurs through Paths B-E with transient growth and bypass transition mechanisms. A low free stream turbulence environment such as civil aircraft flight, transition typically goes through Path A in Figure 2.3. Each stage of the process plays a role in determining the location of laminar-turbulence transition.

The remaining sub-sections will explain in detail each stage of the transition process and detail the relevant literature associated with each area. The first stage of laminar-turbulent transition is the receptivity stage, explained in the next sub-section.

2.2.2 Receptivity & Initial Amplitude

The phrase receptivity wascoined by Morkovin [68], and was also understood independently by Ruban [94] and Goldstein[30]. It is the process which determines the initial form and size of primary instability waves that are generated by disturbances associated with the external environment. Receptivity theory was initiated from experimental observations of laminar-turbulent transition on various aerodynamic bodies. It was found that when the same body (like an aircraft wing) was tested in

different wind tunnels, laminar-turbulent transition did not take place at the same position on the wing surface even though Reynolds number and Mach number were reproduced in each of the tunnels. It was realised that the difference in the position of the transition point could be explained by the difference in the quality of the flow in the test section: level of free-stream turbulence and acoustic noise, model surface finish, etc.

Understanding of the receptivity stage is one of the crucial remaining challenges to transition control. Disturbance growth models require inputs resulting from the receptivity process. Laminar flow control requires a better understanding of the factors that result in disturbance amplitude generation. Despite on-going experimental and computational efforts this process is still not well understood. Receptivity is especially difficult in experimental studies due to the small size of the scales involved. In crossflow transition, the disturbance levels are too small to measure at the location where the disturbances are first generated. Measurements can only be taken when the disturbances have had some spatial distance to grow. Another difficulty lies in the multiple factors that may influence the receptivity process. More than one disturbance source can influence the generation of the initial amplitude. Additionally multiple instability modes may be generated from the disturbance sources, adding to the overall complexity of experimental studies and computational models. The first step in understanding receptivity is to understand each disturbance source.

2.2.2.1 Impact of Freestream Turbulence

The effect of freestream turbulence on crossflow transition was investigated by Deyhle & Bippes [23]. They performed transition measurements on a crossflow-dominated swept-plate model in a number of different wind-tunnel facilities with varying freestream turbulence levels. They concluded that in free stream turbulence in which the turbulent intensity (Tu) is less than 0.15%, stationary crossflow modes were found to dominate transition. At slightly increased turbulence levels between 0.15% and 0.3% travelling modes dominate. Interestingly in these experiments, transition was delayed for the increased Tu case relative to low-Tu cases at the same Reynolds number. The explanation given for this was that the travelling modes excited were sufficiently strong to prevent the stationary modes from causing transition but were not strong enough to cause transition as quickly as the stationary waves they replaced. Another conclusion made was that as flight Tu are generally less than 0.1% many wind tunnel experiments may have no relevance to inflight transition results where different

mechanisms may be dominant.

In another experiment, Radeztsky et al. [86] found that transition behavior on a swept wing is insensitive to freestream acoustic waves, even at amplitudes greater than $125dB$. The conclusion is that the variations observed by Deyhle & Bippes [23] at varying levels of Tu are due primarily to variations in the vortical component of the freestream fluctuations and not to the acoustic component.

2.2.2.2 Impact of Surface Roughness

Surface roughness has a significant impact on crossflow transition. This was established by Müller & Bippes [71], who conducted experiments in a number of wind tunnels and found that the recurring stationary transition pattern was fixed to the model. The instability features they observed had to be related to model roughness rather than to features of the freestream flow. Surface roughness has an impact on transition in different ways depending on the type of roughness. Roughness can be summarised in two forms: isolated roughness or distributed roughness.

Isolated roughness elements involved with three-dimensional irregularities (rivets, insects, dirt, etc.) that have a common feature to enhance the receptivity to external disturbances. For isolated three-dimensional roughness elements of height k, a relevant parameter to characterise the roughness element is a Reynolds number R_k defined as:

$$Re_k = \frac{U_k k}{\nu_k} \tag{2.1}$$

where U_k and ν_k denote the mean velocity and the kinematic viscosity at the boundary layer height $y = k$. It is important to note that these values are computed for the baseline undisturbed laminar flow. The pioneering flow visualizations by Gregory and Walker [34] established that the flow about an isolated 3D element consists of a steady horseshoe vortex wrapped around the upstream side of the obstacle, with two steady counter-rotating legs trailing downstream.

Early work on isolated roughness elements and transition were concerned with defining a critical roughness height at which the transition mechanism moves from a subtle impact on the laminar base flow to bypass transition and an early breakdown to turbulence. Extensive roughness studies with isolated 3D roughness features were completed experimentally by Juillen et al. [48]. They found that as the roughness is applied to the laminar boundary layer with increasing height, at first the roughness height did not impact the transition location greatly, however as Re_k exceeds a critical

value the transition location moves greatly forward.

When the roughness element reaches sufficiently high values of Re_k, unsteady disturbances (hairpin vortices) originate from the separated region just aft of the roughness element. Their growth rate increases with increasing values of Re_k. When Re_k is less than the critical value disturbances stabilise before transition can occur. When Re_k is greater than the critical value the growth rate becomes large enough that the non-linear behaviour moves the transition location close to the roughness element. This phenomena has been investigated extensively by Ergin and White [28].

Further work showed that the critical Re_k is dependant on the a ratio d/k, where d is a measure of the spanwise extent (diameter) of the roughness element. A well known criterion was discovered by von Doenhoff and Braslow [117]. They found that the critical value of R_k scales roughly as $d/k^{-2/5}$, meaning that transition occurs for progressively lower values of $Re_{k,crit}$ when the roughness diameter is increased for a given height. $Re_{k,crit}$ is of the order of $500 - 600$ for $d/k = 1$ and $200 - 250$ for $d/k = 10$.

Radeztsky et al. [86] showed that roughness elements below the critical Re_k impact the transition behaviour. They found that roughness is most effective at generating crossflow disturbances at or just upstream of the first boundary layer neutral point, that the transition location is quite sensitive to roughness height even for roughness Reynolds numbers as low as $Re_k = 0.1$, and that the roughness diameter must be greater than 10% of the most amplified stationary wavelength to be effective.

In addition to isolated 3-D roughness, natural surface roughness can also play a significant role in transition location. A striking example of the effect of roughness-induced receptivity on transition has been documented in Carpenter et al. [17], where transition was noted to move from between $25 - 30$ percent chord to 80 percent chord when the painted leading edge was polished so as to reduce the roughness amplitude from $1.0\mu m$ rms ($3.8\mu m$ average peak-to-peak) to $0.3\mu m$ rms ($2.2\mu m$ average peak-to-peak).

Radeztsky et al. [86] found that a decrease in surface-roughness amplitude from $9.0\mu m$ rms to $0.25\mu m$ rms increases the transition Reynolds number by 70%, another example of how surface roughness can adversely impact transition location. Reibert et al. [88] conducted an experiment in which carefully placed distributed roughness elements near to the leading edge were used to promote a narrow band of crossflow wavelengths. Reibert et al. [88] were able to show that an artificial distributed roughness array with an amplitude of $6.0\mu m$ rms or greater applied near the leading edge

produced transition behaviour almost completely insensitive to roughness amplitude in the range of $6 - 50\mu m$ rms. The cause was that as a narrow band of crossflow wavelengths was promoted it led to non-linear amplitude saturation (non-linear saturation is explained in section 3.2.3) of the most unstable crossflow wavelength very quickly. This is opposed to the Radeztsky et al. [86] experiment that saw a strong roughness-amplitude effect. This demonstrates the sensitivity of the experimental setup to the results shown literature. The differences in results can be attributed to different test conditions such as freestream turbulence levels and whether the test model is swept or unswept. The model in Jullien et al. [48] was run with an unswept body and shows very different sensitivity to roughness height to the experiment of Radeztsky et al. [86] for a swept body.

The discovery of promoting a narrow band of wavelengths to control the crossflow growth became an important potential laminar flow control technique, as explained in further detail in the next section.

2.2.3 Linear & Non-Linear Growth

The receptivity process sets the initial amplitude and phase of the disturbance from a variety of external disturbance sources. From this initial amplitude the development of stationary crossflow vortices occurs in two stages. The first stage is linear and is characterised by small vertical (v') and spanwise (w') disturbance velocities that convect low-momentum fluid away from the wall and high-momentum fluid toward the wall [98]. This momentum exchange occurs in a region very close to the wall where there are large gradients in the initial laminar boundary streamwise velocity. Because of this large gradient, the small displacements caused by the (v') and (w') disturbance components quickly lead to large disturbances in the streamwise velocity (u') downstream. The growth of a stationary crossflow vortex is shown in Figure 2.4. The figure is taken from Chapter 6 of this thesis and shows contours of streamwise velocity at various chord wise locations on a swept wing. The first two contour plots show the effect of the momentum exchange in the linear growth phase.

After a further streamwise distance the disturbance soon becomes too large ($> 10\%U_0$), and non-linear interactions begin to occur. This is the second stage, evidenced by the rollover effect seen in the streamwise-velocity contours. Here the low momentum fluid begins to overlap the high momentum fluid. If the most unstable spanwise wavelength is forced, non-linear saturation occurs, much earlier than the eventual transition to turbulence. Although the initial growth rate increases with increasing roughness height, the saturation amplitude remains largely unaffected by changes in the roughness height [101]. The presence of a large laminar extent with non-linear effects and non-linear saturation makes it difficult to predict crossflow transition using linear stability methods, as discussed in more detail in the Section 3.4.

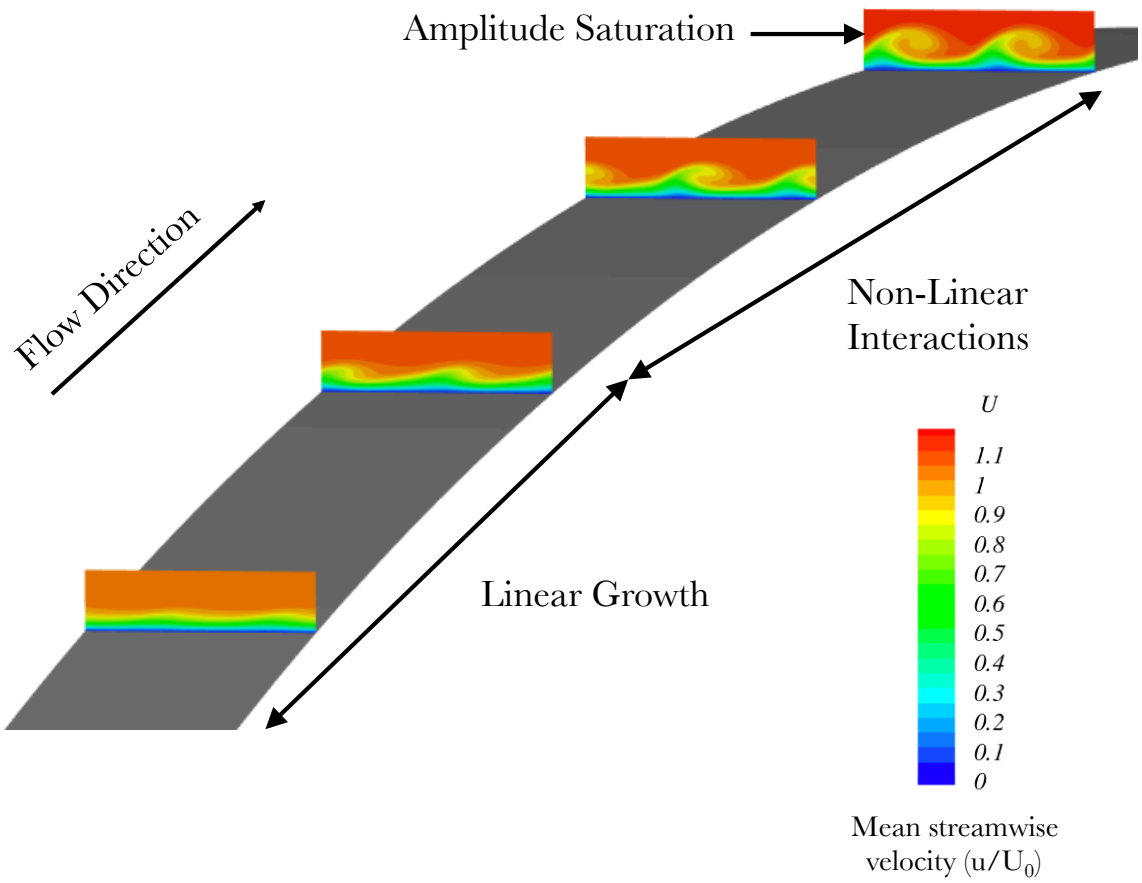

Figure 2.4: Development of crossflow vortices - contours of streamwise velocity u/U_0

2.2.4 Secondary Instability & Breakdown

The process in which the saturated crossflow vortices break down to turbulence has been a recent topic of a great interest and was previously not nearly as well understood as its primary instability. The saturated crossflow vortex can persist for a considerable streamwise distance before becoming unstable. A contour of a typical saturated crossflow vortex taken from an experiment by Reibert et al. [88] is shown in Figure 2.5.

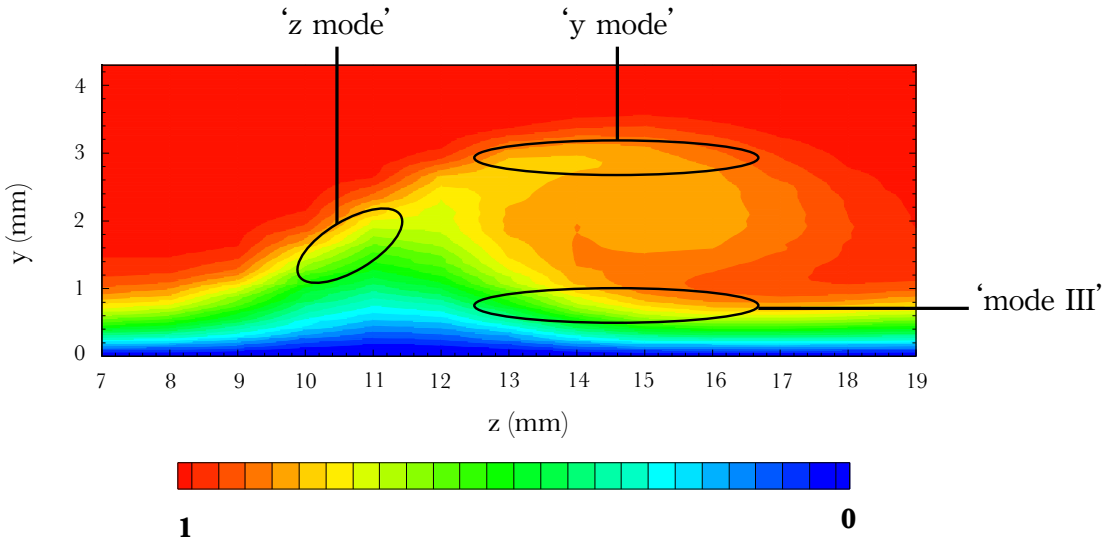

Figure 2.5: Streamwise velocity (u/U_0) contour of a saturated crossflow vortex - adapted from Reibert et al. [88]

The velocity contour shows low momentum fluid above high momentum fluid, resulting in a double inflection point in the wall-normal velocity profile. The inflection points are high in the boundary layer causing the saturated vortices to become susceptible to a high frequency secondary instability that leads to transition to turbulence. This secondary instability is highly amplified and leads to rapid local breakdown, characterised by a turbulent wedge and a 'saw-tooth' pattern [122]. Figure 1.5(c) in Chapter 1 shows crossflow transition and the formation of turbulent wedges across the transition line using Temperature Sensitive Paint (TSP) [21].

Malik et al. [63] introduced a naming convention for three different classes of secondary instability modes identified resulting from the literature: (1) high-frequency or 'z mode' induced by the minimum of the spanwise gradient of the streamwise velocity component, located on the updraft vortex side, (2) high frequency or 'y mode', induced by the local maximum of the wall normal gradient, located on top

of the vortex, and (3) 'mode III' linked to the maximum of the spanwise gradient, located close to the wall. The locations of the high frequency modes are annotated in Figure 2.5.

A number of key experimental, theoretical and numerical studies have contributed to an increasing amount of knowledge on the high frequency secondary instability. An overview of the literature in each area is described in the following sub-sections.

2.2.4.1 Experimental Work

Research into the secondary instability began with the work of Poll [83] who conducted an experiment in which a high-frequency disturbance was observed before transition. Poll used a swept cylinder in the experiment and observed a traveling crossflow wave at $1.1kHz$ at $Re_c = 0.9 \times 10^6$ and an intermittent signal at $17.5kHz$. When increasing chord based Reynolds number to $Re_c = 1.2 \times 10^6$ the frequency increased to $1.5kHz$, and at increased Reynolds number turbulent flow was measured. Poll concluded that the high-frequency disturbance only appeared in a narrow range before transition and attributed it to intermittent turbulence.

Kohama et al. [53] however argued that the fluctuations were evidence of a secondary instability and conducted an experiment using a 45° swept wing at $Re_c = 2.66 \times 10^6$. Kohama et al. [53] used hot-wire and flow visualisation to determine the location and behaviour of the secondary instability mode. The velocity fluctuation spectra results showed travelling crossflow wave activity at $350Hz$ and a broad high-frequency peak at $3kHz$. The experiment provided early evidence of a secondary instability, although a number of problems in the approach were identified by White & Saric [123]. They believe that the absence of full-field scans in the wall-normal and spanwise directions and poor interpretation of the velocity- fluctuation spectra meant that the results could not be used to support a general theory regarding secondary instability.

Kohoma et al. [52] and Kawakami et al. [50] provided further, more detailed experimental studies using a swept flat plate. They included velocity fluctuation maps that were filtered to give the secondary instability fluctuation levels. Kohoma found that a turbulent wedge would develop from the middle of the boundary layer upstream of the secondary instability. Kawakami refined these measurements using a speaker to force the instability. The natural secondary instability measured (without acoustic forcing) at $Re_c = 4.9 \times 10^6$ featured two separate high-frequency bands that became unstable. The first was located between 600 Hz and 2.5 kHz and destabilised

just downstream of $x/c = 0.35$, the second band located between 2.5 and 4.0 kHz destabilised just upstream of x/c = 0.50. Transition was observed around x/c = 0.70. For the forced instability the secondary instability frequency with the largest growth between x/c = 0.40 and x/c = 0.475 was observed to be 1.5 kHz.

More recently, Chernoray et al. [20] conducted an experiment to model the phenomenon under fully controlled conditions. They aimed to investigate the 'y' and 'z' high frequency instability modes of various packets of stationary crossflow vortices. Packets of crossflow vortices consist of multiple modes as apposed to forcing of a single mode. They used several methods to generate the primary instability: a $35mm$ span roughness element, circular disk and continuous suction. The secondary instability region was fully resolved using V-probe hot wire measurements. Chernoray et al. concluded that the behaviour of packets of crossflow vortices induced stronger distortions of the flow than single mode vortices and acted in a similar way to saturated single modes. They found that the 'z' type secondary instability mode, which develops in the extreme spanwise gradients of the streamwise velocity, grow faster than the 'y' type modes, observed further from the wall within the low-momentum area of the vortex.

White & Saric [123] conducted a benchmark study that aimed to provide an experimental database on the behaviour of the secondary instability. An experimental study was carried out that tracked the development of secondary instabilities on a 45° swept wing at various chord-based Reynolds numbers and initial disturbance configurations. They found that a number of distinct secondary modes can occur at different frequencies and locations. They found that the lowest frequency mode always had the highest amplitude and was always associated with the spanwise gradient of the stream wise velocity, 'z' mode instability. Higher frequency modes included harmonics of the 'z' mode and distinct 'y' modes that formed in the wall normal gradient near the top of the vortex. They also described how the breakdown procedure was highly localised, spectral data obtained at various points within the structure indicated that the first point to feature a broad, flat velocity fluctuation spectrum typical of turbulence, was very close to the wall in the region of highest shear. Other points in the structure remained laminar for a distance downstream.

This study from White & Saric [123] provided the most detailed experimental study to date on the secondary instability region and was initially conducted to enable assessment of the results obtained from numerical and theoretical approaches.

2.2.4.2 Theoretical Work

A theoretical approach based on the non-linear parabolised stability equations (NPSE) is a powerful tool for predicting amplitude growth rates of disturbances within a laminar boundary layer. Secondary instability theory coupled with the NPSE approach can also be used to track the high frequency instabilities and give an accurate prediction of the breakdown point. The NPSE approach is explained in more detail in section 2.4.2 of this chapter.

Malik et al. [61] used the secondary instability theory approach for their studies of crossflow instability. The NPSE approach is an improvement on linear stability methods as it captures the non-linear growth effects including amplitude saturation. Secondary instabilities were introduced in the Malik et al. work by the introduction of temporal instabilities on top of the crossflow disturbed base flow. Malik et al. [61] found that the peak mode amplitude of the secondary instability was on top of the stationary crossflow vortex structure. This corresponds to what Malik et al. [63] referred to as the 'y' mode.

Malik et al. [62] then performed a further comparison of the secondary instability theory method against the experimental setup of Poll [83]. Their approach predicted a $17.2kHz$ mode compared to Poll's high frequency signal which occurred at $17.5kHz$. Based on the shape of the disturbance, Malik et al. claimed that this was a 'y' mode. Malik et al. [63] applied the same approach to the swept-wing experiments by Reibert et al. [88] They applied a local, temporal stability analysis to the stationary crossflow vortices that were established by the primary instability. However, they found that better transition correlation can be obtained by following the growth of the secondary instability in an N-factor calculation (explained in Chapter 3.4). A method based on the primary instability alone cannot adequately predict the breakdown and transition location.

Malik et al. [63] found that the high frequency 'y' mode becomes unstable upstream of the 'z' mode. This contradicts what was observed in the experiment by White & Saric [123] where the 'z' mode always appeared upstream of the 'y' mode. The difference was attributed in [101] to the fact that freestream disturbance levels in the experiment were stronger at frequencies closer to the 'z' mode.

2.2.4.3 Numerical Work

In recent years Direct Numerical Simulation (DNS) has been playing an increasingly important role in the characterisation and understanding of the secondary instability.

Hogberg & Henningson [38] conducted a DNS study of the secondary instability of stationary crossflow vortices. They imposed an artificial randomly pulsed disturbance at the point where the stationary disturbance saturates. The artificial disturbances enhance the low and high frequency disturbances downstream. The high frequency impacts the upper part of the boundary layer and the low frequency part impacts the lower part.

Wassermann & Kloker [121; 122] conducted a benchmark DNS study on the nonlinear behaviour of stationary crossflow vortices and their secondary instability and breakdown regions. A first important conclusion from the work was that a packet of crossflow vortices of different wave numbers is more realistic than a single crossflow mode. A second important finding was that a wave-packet approach with unevenly spaced crossflow vortices may interact to bring an earlier onset of the secondary instabilities and breakdown than a single mode disturbance. Wassermann & Kloker also investigated secondary instabilities by forcing secondary disturbances in the computational domain. They found that various modes could be identified, which were located at different positions inside the most pronounced shear layer. Each secondary mode translated into a multi-frequency disturbance in physical space with a steady observer.

Another important observation from Wasermann & Kloker [121; 122] was that when the forcing that initiates the high-frequency secondary instability in their simulation was removed, the secondary instability disturbances are convected downstream, out of the computational domain. This indicates that the secondary instability is convective and that the explosiveness of the growth of the secondary instability is not associated with an absolute instability.

2.3 Flow Control

Control of laminar-turbulent transition is a key objective for future aircraft projects, its potential benefits from a systems perspective has been explained in detail in Chapter 2 of this thesis. From an aerodynamics engineer's perspective controlling the laminar-turbulent transition location on an aircraft wing requires manipulating the mechanisms that cause transition. In the 'Introduction' Chapter of this thesis the main transition mechanisms for a swept-wing aircraft that must be considered were explained and they are: 1) Attachment-Line Instability 2) Streamwise Instability and 3) Crossflow instability. A summary of the cause of the mechanisms 1) and 2) and their control strategy is explained below.

1. Attachment-Line Instability - The attachment line can be a mechanism for transition via two sources: contamination and instability. Turbulent contamination of the attachment line of the wing can arise when a swept body is attached to a solid wall (fuselage, wind tunnel wall). The attachment line can also undergo an instability in which extensive research has been conducted on control of and a clear control strategy has been established. By keeping the attachment line Reynolds number (see Arnal et al. [7] for a detailed explanation) below a certain value, by reducing the leading edge radius, stability can be achieved in the attachment line region.

2. Streamwise Instabilty - Tollmien-Schlichting (TS) waves begin to grow when a laminar boundary layer reaches a critical Reynolds number and becomes linearly unstable. The instability is via a subtle mechanism whereby viscosity destabilises the waves and they begin to grow exponentially, and lead to transition when critical flow parameters are reached. Extensive research has also been applied to the development of streamwise instabilities and a control strategy can be achieved by manipulating the pressure gradient on the aerofoil. The aerofoil can be designed to move the pressure minimum as far aft as possible, allowing a region of accelerating flow from the attachment line to the pressure minimum. This favourable pressure gradient energises the boundary layer and minimises the growth of TS waves.

Both control strategies for attachment line and streamwise instabilities are robust and have been applied in a number of wind tunnel and flight tests. However for aircraft with sweep, as explained in the previous section, the crossflow instabilities becomes

problematic and the leading mechanism for laminar-turbulent transition. Controlling CF disturbances is a much more difficult task, because the crossflow mean spanwise velocity profiles always exhibit at least one inflection point, which cannot be removed. Also, while a favourable pressure gradient stabilises streamwise instabilities it acts to destabilise crossflow.

For this reason flow control strategies within industry and academia are based on how the crossflow instability is manipulated to allow the control strategies for attachment line and streamwise instabilities to be effective.

Flow control can be placed into three main groups. 1) Natural Laminar Flow (NLF), 2) Laminar Flow Control (LFC) and 3) Distributed Roughness Elements (DRE). Each method takes a different approach to dealing with the crossflow instability problem and are at a different readiness level for implementation into civil aircraft design. The methods are described in detail in the next sub-sections.

2.3.1 Natural Laminar Flow (NLF)

Natural Laminar Flow (NLF) is a passive method for controlling laminar-turbulent transition. The strategy involves minimising the influence of the crossflow instability by reducing the sweep angle of the wing so that the development of the inviscid instability no longer arises. NLF employs a favourable pressure gradient to suppress streamwise instabilities. A general strategy for shaping of the aerofoil is given by Arnal et al. [8]. A typical pressure distribution strategy is illustrated in Figure 2.6(a).

The most recent European flight test was conducted between 1989-1992 called the ELFIN (European Laminar Flow Investigation) project [47]. It was initiated by the European Commission with the objective to improve the understanding of laminar flow and to develop the necessary research and experimental tools. Within this project two NLF flight tests were conducted using the ATTAS/VFW614 aircraft and the Fokker F100. A NLF glove was placed on the starboard wing that demonstrated a successful delay of transition. The change in pressure distributions are shown in Figure 2.7 for the original aircraft and the modified wing with the NLF glove.

A NLF trade study was conducted by Boeing [15] to assess the potential benefit of the design method for a single aisle aircraft carrying 196 passengers. They conducted an extensive design study at varying Mach numbers, lift coefficients and Reynolds numbers. One of the observations made was that for the crossflow instability to be eliminated the quarter chord sweep angle had to be reduced to 7°. Their

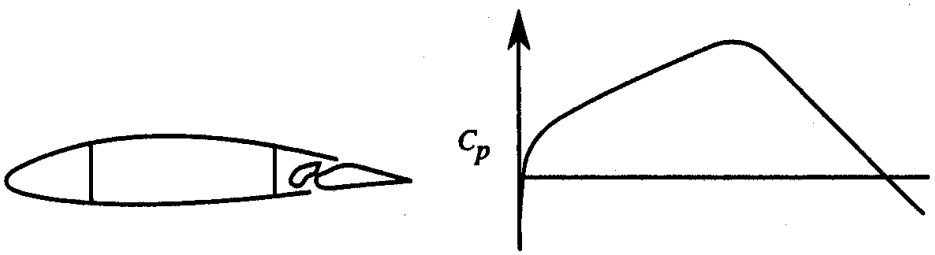

(a) Natural Laminar Flow (NLF)

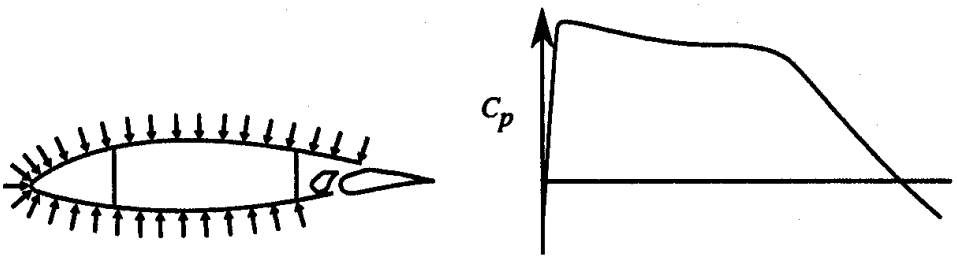

(b) Active Flow Control (AFC)

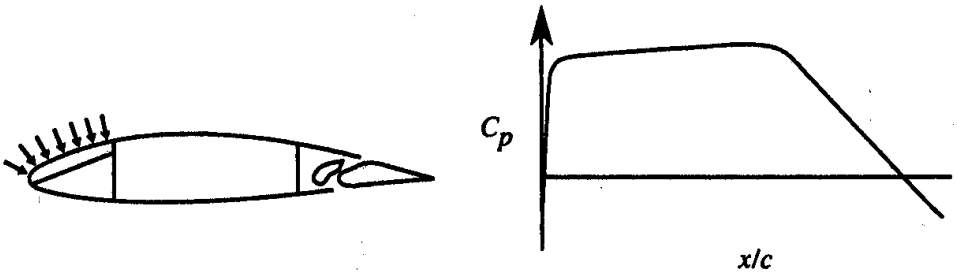

(c) Hybrid Laminar Flow Control (HLFC)

Figure 2.6: Flow control strategy and example pressure distributions (adapted from Joslin [47]

design methodology was to shape the pressure distributions such that transition occurs upstream of the shock location at around 50-60% chord. Their aircraft trade study concluded that an NLF airplane for this size aircraft was not competitive to a turbulent aircraft due to the additional weight and performance penalty associated with a larger wing area. Also the trade study commented on the ride comfort of an NLF aircraft being significantly worse than a turbulent aircraft.

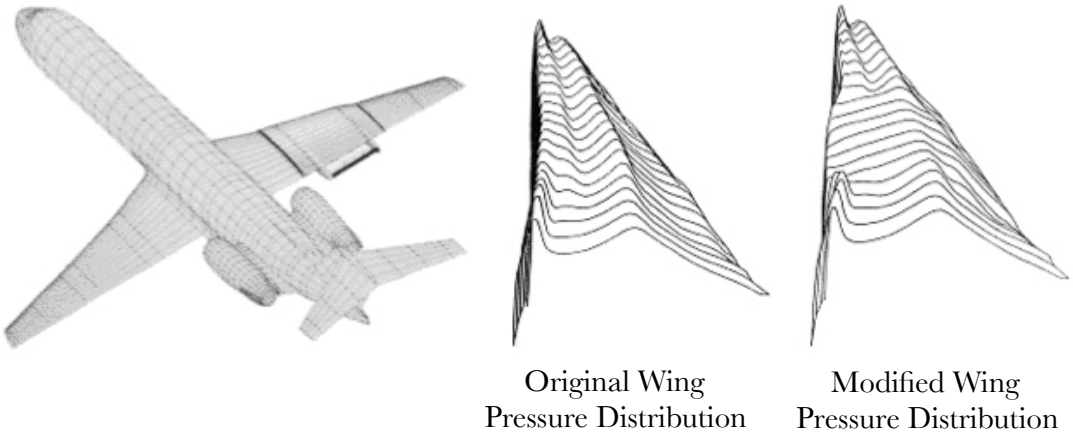

Figure 2.7: ELFIN Fokker 100 laminar glove flight test [107]

2.3.2 Laminar Flow Control (LFC)

Laminar Flow Control (LFC) is an active boundary-layer flow control technique employed to maintain the laminar state at chord Reynolds numbers beyond the capabilities of passive methods. LFC usually employs a suction surface over the entire wing surface to remove the inner regions of the boundary layer. The major drawback with LFC is the complexity of introducing suction across the entire wing area and its impact on other systems within the wing. Also the suction requirements are large which incur a penalty which could mitigate the positives of the reduced skin friction drag.

Another, more common technique for active flow control is using a Hybrid Laminar Flow Control (HLFC) system. HLFC integrates the concepts of LFC and NLF to reduce the suction requirements and reduce overall system complexity. On a swept aircraft wing, boundary layer suction is applied only around the leading edge, and then natural laminar flow is obtained over the wing box through a proper tailoring of the geometry. This concept avoids the undesirable characteristics of NLF, which is

sweep limited, and of full-chord LFC, which is very complex. Figure 2.6(b) shows the LFC concept while Figure 2.6(c) shows the HLFC concept and pressure distributions.

Several HLFC tests were also conducted in ELFIN programme using the ONERA-CERT T2 wind tunnel. Reneaux and Blanchard [90] discussed the design and testing of a HLFC airfoil model. An Airbus transport turbulent wing was modified to achieve the best compromise between transonic performance and the HLFC wing. For the wing swept to 27.5°, suction was applied from the leading edge to 20% chord and a favourable pressure gradient was maintained to 60% chord. For a Mach number 0.82 and chord Reynolds number of 42 million the computed transition location ranged from 25% chord at the wing root to 55% chord at the wing tip. The computed skin friction drag was 45% less than the turbulent wing and total drag was 10% less.

Another major milestone in the development of laminar flow technology was the Boeing 757 HLFC flight test during 1990-1991. The test programme aimed to demonstrate the effectiveness of the HLFC concept to a large subsonic commercial transport, evaluate real-world performance and reliability at flight Reynolds numbers (including off design) and to develop and validate integrated HLFC, anti ice and high lift systems [47; 60]. A 22ft span segment of the leading edge box on the port side wing was replaced with a HLFC leading edge box. The new leading edge section consisted of a perforated titanium outer skin, with suction flutes under the skin and collection ducts to allow suction control of the boundary layer CF and TS disturbance growth from leading edge to front spar. The leading edge included a Krueger shield integrated for high lift, insect protection and hot air de-icing systems.

The flight test demonstrated that the HLFC concept was extremely effective in delaying transition as far back as the rear spar around the design point. A sample test section shows that most of the hot films indicated laminar flow beyond 65% chord and the suction rates to achieve this were a third of those predicted during design [60]. Also wake-rake measurements indicated a local drag reduction of 29% with the HLFC system operational resulting in a projected 6% drag reduction of the aircraft. The flight test was a major success and demonstrated the capability of HLFC; however because only one third of the design suction was required to achieve laminar flow, there was significant uncertainty in the design tools.

While the HLFC method has proven to achieve a significant drag reduction it remains a complex systems engineering challenge to implement on a civil aircraft. Challenges remain across the disciplines such as materials for the suction surface, anti-icing, insect prevention and the impact of the additional weight of the systems.

2.3.3 Distributed Roughness Elements (DRE)

A third flow control method was proposed by Saric et al. [100] The strategy differs from NLF and HLFC which aim to remove crossflow development by reducing sweep or by applying suction. Here the crossflow vortices are manipulated to promote stable crossflow wavelengths and delay the growth of the unstable wavelengths that lead to early transition.

The method originated from the experimental work of Radeztsky et al. [86] and Reibert et al. [89] that used an array of cylindrical distributed roughness elements (DRE) close to the boundary layer neutral point at the leading edge of the wing. By spacing the roughness elements in the form of a DRE a narrow band of crossflow wavelengths can be forced. Reibert et al. [89] showed that by spacing the roughness elements at a wavelength λ apart excites integer division harmonic disturbances with spanwise wavelengths $\frac{\lambda}{2}$, $\frac{\lambda}{3}$, ... , $\frac{\lambda}{n-1}$, $\frac{\lambda}{n}$.

Literature has showed that stationary crossflow packets typical of natural roughness incur non-linear interactions that cause transition much earlier. By forcing a control wavelength, promoting only a narrow band of crossflow wavelengths and ensuring that the most unstable, critical crossflow wavelength is suppressed, a delay in laminar-turbulent transition can be achieved. The most unstable wavelength can be obtained from linear stability calculations. As described earlier forcing the control wavelength λ excites the control mode and integer divisions only of the control mode: no subharmonic disturbances are generated. For example, if λ is set at $18mm$, crossflow modes of wavelength $18, 9, 6, 4.5mm$... are excited. No modes greater than $18mm$ should occur. Therefore if the most critical crossflow wavelength was $18mm$, theoretically, a delay in the growth of the critical wavelength can be achieved with a spacing of $9mm$.

Saric et al. [100] conducted the benchmark experimental study that proposed this transition control method. They used an in-house aerofoil swept at 45° degrees; the aerofoil was designed such that streamwise instabilities were eliminated by a favourable pressure gradient, resulting in the crossflow instability dominating laminar-turbulent transition. The most unstable wavelength for their configuration was $12mm$. They conducted three cases, firstly with no DRE and only natural roughness, secondly with DRE spaced at the critical wavelength $12mm$, and thirdly with DRE at a control wavelength $8mm$. Their results showed a dramatic impact on the transition location. For the natural roughness case, transition occurs at 71% chord. Adding a DRE at $12mm$ (critical) the transition location moves transition forward

to 47% chord. However, at the control wavelength at $8mm$ transition was delayed beyond the pressure minimum and well beyond 80% chord (the actual location was out of the measurement domain).

Malik et al. [63] confirmed the stabilising effect of the controlled disturbances by using NPSE and the same laminar base flow as Saric et al. [100] Also using the same experiment Hunt & Saric [42] recently conducted a set of experimental receptivity tests to provide a database for numerical studies. They conducted tests at a critical and control wavelength at a number of micron sized roughness heights.

Recently, flight tests were conducted by Carpenter et al. [18] demonstrating the capability of the method at higher chord based Reynolds number and the transition location moved from 30% chord to 60% chord.

Various DNS work has also been conducted by a number of research groups. Wasserman & Kloker [121; 122] conducted a spatial DNS study on a swept flat plate, they observed at critical wavelengths that the streaky nature of the stationary crossflow disturbance caused a strong mean flow distortion while the control cases reduced non-linearly regions of deceleration within the steady mean flow. The strong deceleration favours the growth of secondary instabilities therefore Wasserman & Kloker [121; 122] also concluded that the control mode not only stabilised the primary crossflow modes but also reduced the growth of the secondary instabilities.

Tempelmann et al. [114] conducted a receptivity study using DNS and PSE and using results from an independent receptivity study with DRE's by Reibert et al. [88]. As the chord based Reynolds number for the experiment was > 2 million the DNS was applied to the boundary layer region up to 70% chord with an initial RANS solution providing boundary conditions. Modal amplitudes extracted from DNS were 40% of that measured in the experiment, however, nonlinear PSE calculations revealed that the linear spatial evolution of the steady crossflow mode from the DNS and experiment were in good agreement; the discrepancy was attributed to additional receptivity in the experiments. Following on from this study Hosseini et al. [39] used the same numerical method to perform a study using DRE's spaced at a control wavelength and a natural roughness case. They applied unsteady background disturbances using a weak randomly pulsed volume force and adjusted the amplitude until transition occurred at 45% chord for the natural roughness case. Using the same background disturbance transition was shown to move downstream using the control case.

The DRE control strategy has the ability to control transition passively by using roughness elements without the need for additional system complexity. The method

however remains a challenge and more research is required to fully understand the design of the DREs in different disturbance conditions. For the control strategy to be effective the roughness heights of the DRE are required to be micron sized. The complexity of manufacturing the roughness elements to the required tolerance may also require a further research effort. However, the DRE method has proven a subtle and effective control technique that incurs less impact on other aircraft systems as HLFC. Therefore it is a key research objective for the aircraft community.

2.4 Simulation of Crossflow Transition

Before laminar flow technology can become a reality for commercial aircraft appropriate design methods and tools must be developed. A major requirement for the design of laminar flow wings is a reliable and robust prediction process for the location of transition. As described in this chapter, the transition process is complex. Transition can occur through a number of mechanisms depending on the application and external environment. As a result, to this day, no overall complete model exists that can accurately predict the location of laminar-turbulent transition. This section will describe and give a critical analysis of the the transition simulation and prediction methods used in industry and academia. A Large Eddy Simulation (LES) method is used in this thesis for simulation of crossflow transition and a justification is given to using this method as opposed to others available.

2.4.1 Linear Stability Equations (LSE)

For a design engineer at an aircraft manufacturer, ideally, the transition prediction method should be instant, allowing many design iterations to be analysed quickly and efficiently. One of the more widely used methods for predicting transition is the e^N or N-Factor method. For predicting natural transition arising from streamwise instabilities on airfoils, this approach is considered the state of the art by the aircraft industry.

This method is based on local linear stability theory and the parallel flow assumption in order to calculate the growth of disturbance amplitudes from the boundary layer neutral point to the transition location. The physics of the e^N method is illustrated in Figure 2.8.

With the e^N method the N factor provides closure to the linear stability equations and N represents the amplification factor of the disturbance amplitude, A from an initial unknown amplitude, A_0, described below.

$$e^N = \frac{A}{A_0} \tag{2.2}$$

The initial amplitude of the disturbance in the boundary layer is related to the external disturbance environment through the generally unknown receptivity process, described in Chapter 2.1. For this reason the N factor at the onset of transition is not universal and must be determined by calibration to wind tunnel or flight tests. Hence the e^N approach is considered a semi-empirical method. For more details into

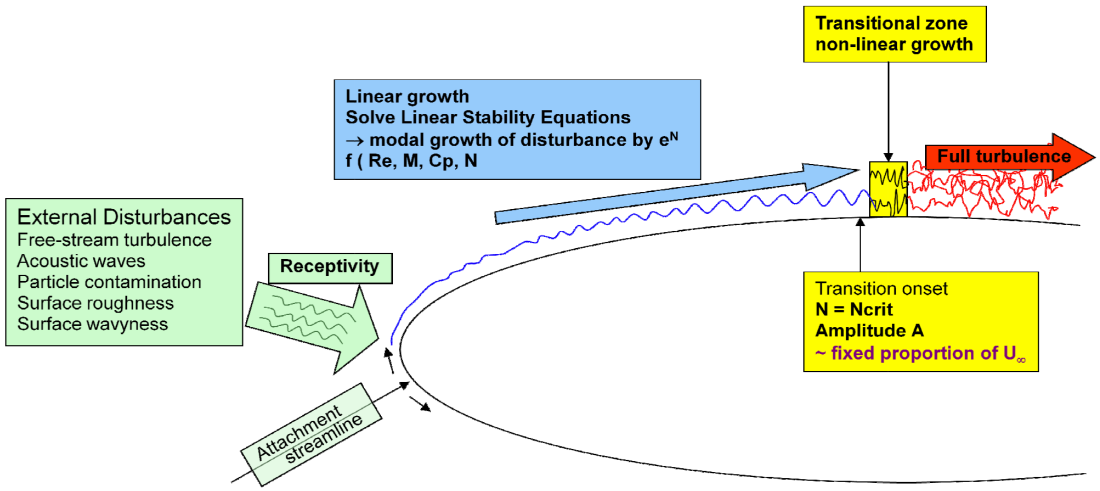

Figure 2.8: e^N method overview and physics, adapted from Benton [12]

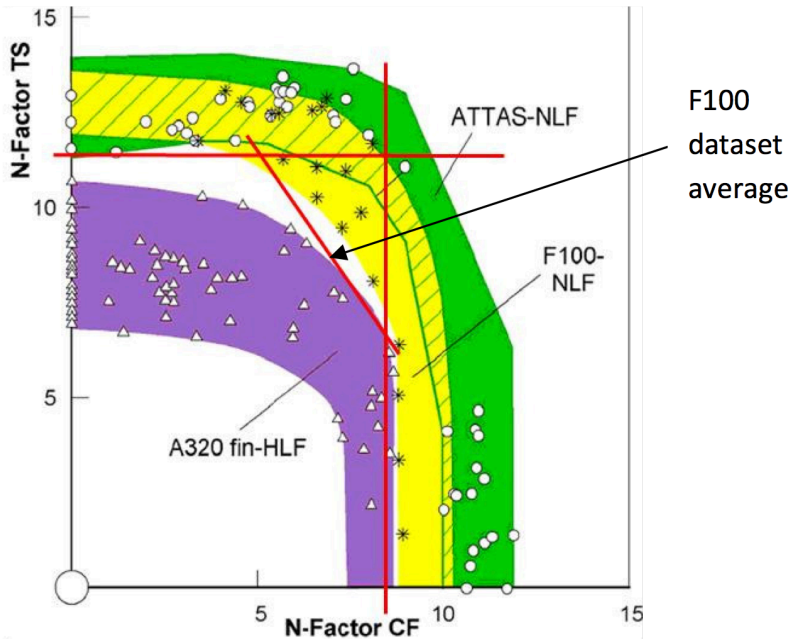

Figure 2.9: e^N method flight test and wind tunnel calibration for TS (Tollmien-Schlichting) and CF (Crossflow) N factors, adapted from Benton [12]

the equations and mathematics the reader is pointed to the overview by Saric [99].

Airbus have conducted several wind tunnel and in-flight tests to use the e^N method as a viable design tool. If the method is to be used for the design of aircraft then the critical N-factor values must be calibrated to in-flight conditions. Wind tunnel and flight tests have been conducted for the purpose of N-factor calibration and

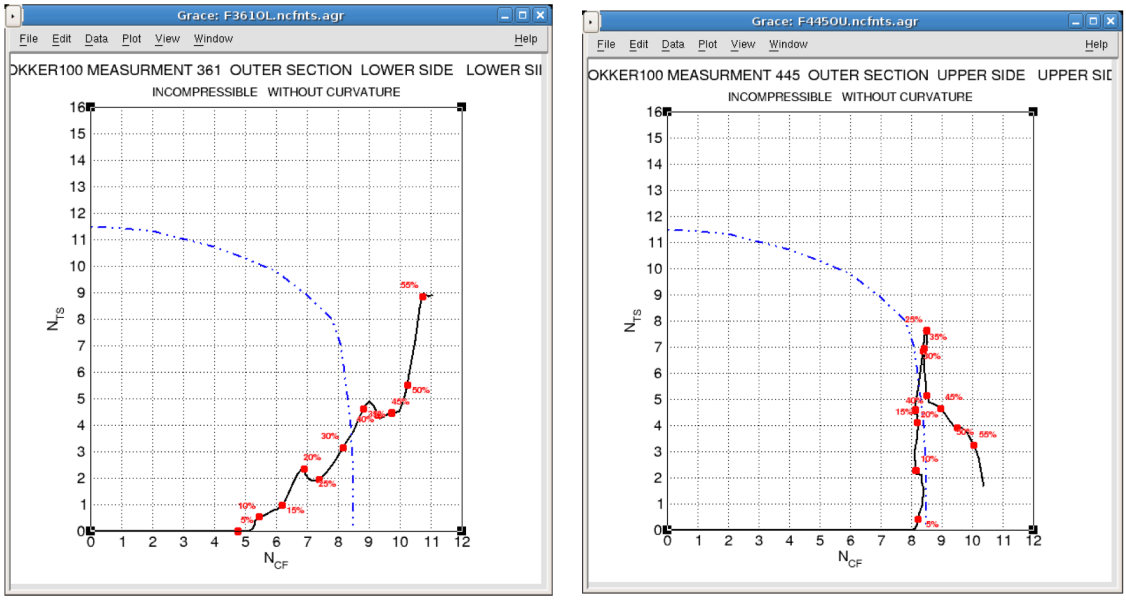

(a) Reliable prediction of crossflow dominated transition

(b) Unreliable prediction of crossflow dominated transition

Figure 2.10: Example outcomes of N_{CF} for crossflow dominated transition, adapted from Benton [12]

a summary of the results using a N_{TS} N_{CF} solving strategy is shown in Figure 2.9 from the ATTAS-NLF, Fokker 100 and A320 fin tests conducted as part of the ELFIN programme. N_{TS} is an N-Factor to track streamwise instabilities (Tollmien-Schlichting waves) and N_{CF} is an N-Factor to track crossflow instabilities.

Flight tests are conducted at a range of flight conditions to correctly characterise the external environment and both the C_p and transition locations are measured. From this the C_p data is solved in a laminar boundary layer solver/e^N analysis and the critical N-factor values for CF and TS waves are determined using the transition location. Using this data an N-factor locus is plotted and the data is averaged producing a curve shown in Figure 2.9. Figure 2.10(a) Figure 2.10(b) show possible outcomes using the Fokker100 flight test data. Figure 2.10(a) shows a reliable prediction of crossflow dominated transition, using this type of data a robust prediction method can be developed. However, Figure 2.10(b) shows an example of uncertain crossflow transition, where the correct N-Factors and hence transition location are difficult to determine. The problem is a combination of the onset of non-linear effects, low amplitude non-linear interactions and secondary instabilities that are not present in linear stability calculations. For this reason it is unlikely that linear stability can be used for robust transition prediction for detail design, typically design engineers

using the stability code will adjust their designs until their design produces N-Factor plots similar to that of Figure 2.10(a), usually be reducing the sweep angle.

Another limitation of the e^N method is that it cannot predict the transitional region, only the onset of transition. For this reason there is now growing interest in approaches that solve the non-linear Parabolised Stability Equations (PSE).

2.4.2 Parabolised Stability Equations (PSE)

In recent years the non-linear Parabolised Stability Equations (NPSE) have become a popular approach to stability analysis owing to their inclusion of non-parallel and non-linear effects with relatively small additional resource requirements as compared with Direct Numerical Simulation (DNS) [36; 87].

The NPSE approach has recently been validated for 3-D flows subjected to cross-flow disturbances by Haynes & Reed [35]. Their detailed comparison of linear PSE and non-linear PSE results with the experimental measurements of Reibert et al. [89] show excellent good agreement. The configuration used in the validation was for a 45° swept aerofoil model, in the experiment roughness elements were placed $12mm$ apart close to the boundary layer neutral point. The initial conditions for the NPSE calculation (with curvature) were obtained by solving the local linear stability equations at 5% chord location for the fundamental $12mm$ mode and adjusting its RMS amplitude such that the total disturbance amplitude matched that of the experiment at 10% chord. The NPSE was then marched from 5% chord to 45% chord. Transition occurred on the experimental model at 52% chord. Figure 2.11 shows a figure taken from the validation study that compares results from the PSE and NPSE calculations compared with the experiment. The NPSE results match the growth rate extremely well and manages to simulate the non-linear effects as well as the saturation amplitude.

To predict transition location secondary instabilities can be applied by the introduction of temporal instabilities on top of the crossflow disturbed base flow. This method has been successfully demonstrated in a number of studies by Malik et al. [61; 62; 63] (Described in Section 3.2)

Unfortunately, the disturbance inputs for flight conditions are not known, therefore the initial amplitude for the disturbances require further modelling. Schrauf et al. [107] however points out that transition information can be obtained by comparing results using initial conditions from standard environments to perform trade-off analyses. The NPSE has shown very encouraging results in validating against the

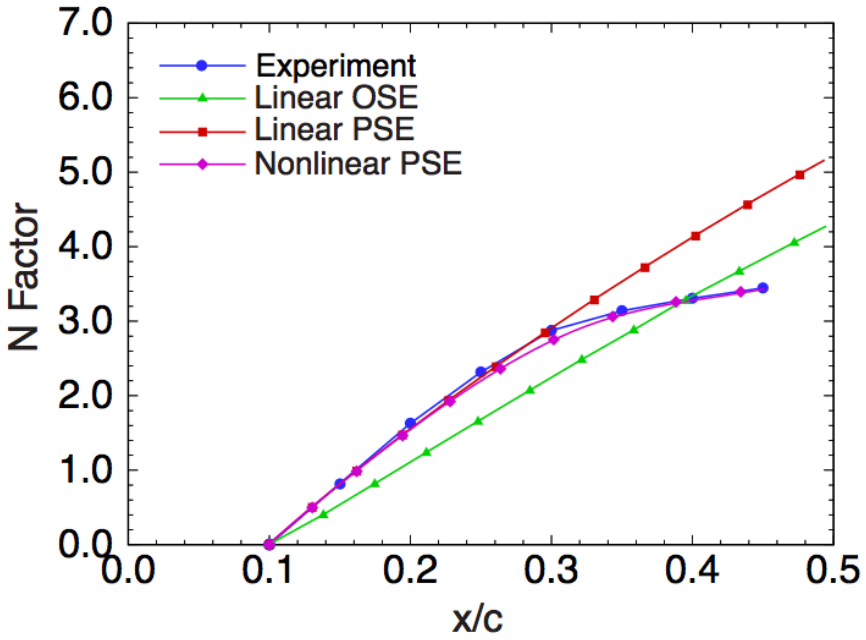

Figure 2.11: Comparison of stability methods (LSE, PSE, NPSE) conducted by Haynes & Reed [35] to experimental data conducted by Reibert et al. [89]

available experimental databases, but more work is still needed to simulate physical initial conditions. While the method can give a location for transition it does not model the breakdown region unlike numerical methods such as a DNS or LES.

2.4.3 Reynolds Averaged Navier-Stokes (RANS)

Until recently it had not been possible to model transitional flows using a Reynolds Averaged Navier Stokes (RANS) approach. The main reasons are that transition occurs through different mechanisms for different applications and RANS models average linear disturbance growth thus not lending itself to transitional flows. Integrating methods such as the e^N method are difficult as they involve numerous non-local operations e.g. tracking disturbance growth along streamlines. In practical terms, most of today's CFD methods use mixed elements and are domain decomposed on parallel computers resulting in boundary layers that can be split and computed on different processors, thus not easily compatible with non-local integral calculations. Successful e^N integration into RANS codes is normally coupled with a 2D laminar boundary layer solver to determine the transition location using several cuts along the 3D wing surface.

Langtry and Menter, [55] however, proposed a general purpose fully local RANS transition model. The central idea behind the model is to use a vorticity Reynolds number Re_v to provide a link between the momentum thickness Reynolds number Re_θ and the local boundary layer quantities using an empirical correlation, described below.

$$Re_\theta = \frac{\max(Re_v)}{2.193} \tag{2.3}$$

Since Re_v is based on wall distance and shear strain rate it can be computed at any grid point in an unstructured parallel code. The proposed formulation is based on Menter's $k-\omega$ turbulence model with an additional two transport equations. The first transport equation is for intermittency and used to trigger the transition process by controlling the production of turbulent kinetic energy in the boundary layer. In addition, a second transport equation formulated in terms of transition onset Reynolds number $Re_{\theta t}$ is developed in order to avoid the additional non-local operations introduced by the quantities used in the experimental correlations. These correlations are typically based on freestream values, such as the turbulence intensity and the pressure gradient at the boundary layer edge. A further correlation exists in the intermittency equation for the length of the transition region.

The transition model has proven successful for a range of transitional flows, from bypass transition in turbomachinery to natural transition for wind turbines For civil aircraft, however, the model does not at this moment have a reliable and robust correlation for crossflow transition. For this reason the model is not currently applicable to modelling of transition for civil aircraft, however it is expected with further research to play a key role in future RANS CFD capabilities.

2.4.4 Direct Numerical Simulation (DNS)

Direct Numerical Simulation (DNS) of the Navier-Stokes equations can be obtained by resolving the full energy cascade and capturing the kinetic energy dissipation, which occurs on the smallest scales. The size of the grid must not be larger than the viscous determined scale, known as the Kolmogorov scale, η. If L is a characteristic length for the flow e.g. the largest possible turbulent eddy, the number of points in each spatial direction should of order,

$$N \sim \left(\frac{L}{\eta}\right)^3 \sim \left(\frac{uL}{\nu}\right)^{\frac{9}{4}} = Re^{\frac{9}{4}} \tag{2.4}$$

For practical flows with high Reynolds numbers the number of grid points required becomes prohibitively too large. For example, to simulate a wing with $Re = 1 \times 10^6$, the estimated number of grid points required would be $N \approx 3 \times 10^{13}$. Due to this high computational cost, DNS is generally restricted to low Reynolds number flows. DNS also requires the use of high-order numerical methods which require simplified geometries and have additional restrictions on skewness and aspect ratio of mesh elements.

In recent years however, DNS is playing an increasingly important role in the investigation of crossflow transition thanks to the development of novel simulation techniques and the further advances in high performance computing. Various DNS work has been conducted by different groups using both a temporal only model and the computationally more demanding but physically more appropriate fully spatial and temporal model. Some recent work with spatial DNS by Wasserman & Kloker [121; 122] has successfully captured the secondary instability region using a swept flat plate with results comparing well to an independent experimental study conducted by White & Saric [123]. Kloker [51] has also confirmed the potential of methods for crossflow instability suppression using smart suction methods.

A novel technique was developed by Tempelmann et al. [114] using data from a precursor RANS simulation to feed boundary conditions in a DNS. This approach allowed the authors to simulate using DNS an infinite swept wing slice up to 70% chord for a case with a chord based Reynolds number of 2.4×10^6. Their simulations were based on the model of Reibert et al. [89] with an array of DRE's providing the initial disturbance source. Disturbance amplitude results showed a 40% discrepancy when compared with the experiment, however NPSE calculations revealed that the linear spatial evolution of the steady crossflow mode from the DNS and experiment were in good agreement, the discrepancy was attributed to additional receptivity in the experiments.

These simulations however remain a substantial computational challenge and the DNS methodology would be difficult to employ on more challenging geometries and flow conditions. For this reason, it is worthwhile to investigate the application of Large Eddy Simulation (LES) to the numerical study of crossflow transition.

2.4.5 Large Eddy Simulation (LES)

Large Eddy Simulation (LES) is a flow prediction method that shares similarities with both the fully resolved DNS method and the fully modelled RANS method. In LES

the large scale energy carrying eddies are resolved fully on a numerical grid while the small eddies are modelled using a sub-grid scale (SGS) model. As the small scales are generally considered homogeneous and isotropic they can be modelled relatively simply. By removing the need to resolve the small scales the grid spacing can be relaxed allowing a significant saving in computational cost when compared to a DNS.

Currently previous published work on LES of transitional flows is limited. LES is intrinsically advantageous for simulation of flows with large scales and separation zones and not inherently suitable for modelling of transitional flows. This is because transitional flows are substantially different from fully turbulent high Re flows. There is no fully developed energy cascade in the transitional region and the SGS model must be able to differentiate laminar, transitional and fully turbulent regions.

However, recent advancements in SGS modelling and an increase in available computational resources have made it a possible route to analysis and prediction of transition. Progress in LES transition modelling has been made in simulating natural transition in an incompressible channel flow by Schlatter [104]. Schlatter demonstrated the use of LES for modelling natural transition using the dynamic, structure-function and the high-pass filtered sub-grid models on relatively coarse grids. The results showed that LES can successfully capture the transitional region at a fraction of the computational cost of a DNS calculation.

Further calculations were conducted by Sayadi and Moin [103] who conducted studies on natural transition breakdown scenarios on a zero-pressure gradient boundary layer. They compared results of various SGS models to the the traditional Smagorinsky SGS model. The objective of the study was to assess the capability of SGS models to predict the location of transition and the skin friction throughout the transition process. The Smagorinsky model failed to detect transition, but the dynamic procedure allowed for a negligible turbulent viscosity in the early transition region. As a result, the laminar-turbulent transition location was estimated correctly. The authors noted however, that the skin friction in the turbulent region was over predicted after the laminar-turbulent region.

LES has also been used previously for modelling of crossflow vortices by Huai et al. [41] using a 45° swept wedge. Stationary and travelling crossflow vortices were generated using steady and random amplitude suction/blowing. The LES captured the essential features of the spatial evolution of the crossflow vortex packet and was in good agreement with DNS data.

These examples of recent literature has shown that LES is capable of simulating

the transitional behaviour correctly however they were all undertaken using simple geometries (swept flat plates, channel flow) and run at relatively unrealistic flow conditions (low Re_c). For this reason, the work in this thesis is investigating the use of LES for simulation of crossflow transition at more realistic flow conditions and complex geometries. The detailed aims and objectives of the work are explained in the next section.

2.5 Aim & Objectives

The literature survey described in this chapter has given a detailed understanding of the various stages of the transition process related to the crossflow instability mechanism. Literature in recent years has led to a wealth of knowledge in the field of the crossflow instability with the various stages of the process modelled using a variety of numerical techniques.

The Distributed Roughness Elements (DRE) control concept seeks to delay transition by forcing subdominant crossflow modes that cannot lead to transition on their own, but can keep the naturally unstable critical instability modes suppressed via non-linear modification of the base flow. This intrinsically non-linear control mechanism requires a high-fidelity prediction approach involving all of the relevant stages of the transition process explained in the first section of this chapter: receptivity, linear, and nonlinear growth of primary crossflow instabilities, secondary instability region and breakdown. The design of DRE's and further research into simulation of crossflow transition requires taking a 'holistic' approach to laminar-turbulent transition modelling: by involving accurate modelling of all parts of the transition process.

An LES approach has the ability to bridge the gap between the high fidelity, computationally expensive DNS method and the low fidelity stability analysis used for design. DNS is beginning to play a larger role in simulation of crossflow vortices and DRE's and recent literature has showed the use of novel techniques to reduce the computational expense and linking to RANS approaches. However, these approaches remain computationally expensive and requires large simplification of the test cases. LES has the potential to be able to simulate at a similar accuracy to DNS with a significantly smaller computational expense in the turbulent regions of the flow domain. This has been demonstrated on a number of simple test cases within recent literature, detailed in the previous section.

The test cases using an LES approach to laminar-turbulent transition have all been conducted for low fidelity cases with forced initial disturbance generation. The work in this thesis will aim to develop an LES method able to simulate the entire transition process, from receptivity of external disturbance sources to final breakdown to turbulence. The LES method will have to be able to handle the various stages of transition with appropriate SGS modelling and grid refinement. By choosing an SGS model that allows the sub-grid scale turbulent viscosity contribution to reduce to zero in a laminar region, the method can be considered an unsteady Navier-Stokes (UNS) for the laminar regions. The method should be robust, relatively quick and

be able to run on realistic geometries with validation against existing experimental data. Ideally, the method should be able to run and be used as a high fidelity design tool for engineers to gain invaluable data on the transitional flow regimes. It is worth noting that the proposed method will not couple two separate simulations for the laminar and turbulent regimes but will be a single simulation method.

The method will also be used to analyse the DRE control method with further validation to experimental data. The DRE control method requires a detailed understanding of the flow around the roughness elements aswell as the non-linear interaction of modes and final break down to turbulence. A demonstration of delay in transition from the LES results would be an ideal outcome.
Therefore formally, the aim of the work presented in this thesis is:

Develop a UNS/LES strategy to simulate the 'holistic' crossflow laminar-turbulent breakdown process and to apply the method to complex geometries, run at realistic flow conditions and to simulate crossflow control using distributed roughness elements (DRE).

The work is split into three main tasks, described below:

1. *Develop an UNS/LES methodology for modelling crossflow transition*

   (a) Investigate the required grid resolution for capturing transitional flow behaviour in the different stages of transition, in particular the flow around roughness elements used for DRE

   (b) Choose an appropriate sub-grid scale (SGS) model that can accurately handle the laminar, transitional and turbulent regions of the flow. The model must not be computationally too expensive.

   (c) Transition requires an external disturbance environment that can accurately simulate the correct transition mechanism and is physically appropriate. The receptivity and generation of the crossflow vortices must be investigated including the use of suction holes and roughness elements.

   (d) Investigate a method for generating realistic freestream turbulence levels. They should be able to be controlled easily without a great additional computational expense.

2. *Validate the UNS/LES method to existing experimental test data*

   (a) A first low fidelity experimental test case will be chosen to validate the LES method. The test case will have data on the physical behaviour of crossflow vortices for comparison.

   (b) A second test case will be chosen to demonstrate the method at more realistic flow conditions and to validate for the receptivity of distributed roughness elements.

3. *Use the UNS/LES method for simulation of flow control using DREs*

   (a) Simulate arrays in distributed roughness elements spaced at both unstable and control wavelengths.

   (b) Simulate the roughness elements at various micron-sized roughness heights and show its impact.

   (c) Apply realistic free stream turbulence to provide a simulate the breakdown to transition.

   (d) Demonstrate reliable transition simulation and prediction methodology for design.

Chapter 3

Methodology

3.1 Introduction

The following chapter describes the numerical simulation methodology used to deliver the objectives set out in Chapter 1. The literature review section outlined the fundamentals of crossflow transition and the various numerical and theoretical approaches to prediction. As described in the Aims and Objectives within Chapter 2, there is potential for the use of an unsteady Navier Stokes/ Large Eddy Simulation (UNS/LES) methodology for crossflow transition prediction. The aim of this chapter is to describe the methodology developed for simulation and prediction of crossflow transition.

The Chapter will begin by presenting the governing equations of fluid flow in section 3.2 and the strategy behind the approach to solving the equations in section 3.3. Section 3.3 will also described the filtering process used to obtain the LES equations and the sub-grid scale (SGS) modelling strategy used for modelling of laminar and turbulent regions. A literature review of current SGS modelling approaches is given before explaining the subsequent SGS model implemented: the Wall Adapting Local Eddy Viscosity (WALE) model.

The 'DELTA' CFD code was used for the calculations and an overview of the code including the technical aspects and simulation strategy is given in section 3.5. A synthetic inflow turbulence generation method called the 'Synthetic Eddy Method' (SEM) was implemented into DELTA . The mathematical details of the method along with a literature review and a results of a test case are described in section 3.7.

3.2 Governing Equations

The governing equations for fluid flows are the Navier-Stokes equations. The equations include the Continuity Equation (conservation of mass), Momentum Equations (Newton's 2nd Law) and the Energy Equation (1st law of thermodynamics). The Navier-Stokes equations may be obtained by using an infinitesimal or finite control volume approach and can be expressed in integral or differential form [6]. Incompressible isothermal (no energy equation required) forms of these equations are used and presented in this chapter as low speed, constant density ($M < 0.2$) cases were simulated. Equations 3.1 & 3.2 describe the conservative forms of the Navier-Stokes equations written in differential form in Cartesian tensor notation and for velocity components u_i $(i = 1, 2, 3)$, instantaneous pressure p and viscous stresses τ_{ij}. For a more detailed derivation of the governing equations the reader is referred to Anderson [6].

$$\frac{\partial u_i}{\partial x_i} = 0 \tag{3.1}$$

$$\frac{\partial u_i}{\partial t} + \frac{\partial}{\partial x_j}(u_i u_j) = \frac{1}{\rho}\frac{\partial p}{\partial x_i} + \frac{\partial \tau_{ij}}{\partial x_j} \tag{3.2}$$

For a constant density Newtonian viscous fluid, the viscous stress tensor τ_{ij} is given by Equation 3.3

$$\tau_{ij} = 2\nu S_{ij} \tag{3.3}$$

where ν is the fluid kinematic viscosity and S_{ij} is the strain-rate tensor described in Equation 3.4.

$$S_{ij} = \frac{1}{2}\left(\frac{\partial u_i}{\partial x_j} + \frac{\partial u_j}{\partial x_i}\right) \tag{3.4}$$

In terms of Equation 3.2, the momentum equations can be expressed as:

$$\frac{\partial u_i}{\partial t} + \frac{\partial}{\partial x_j}(u_i u_j) = \frac{1}{\rho}\frac{\partial p}{\partial x_i} + \frac{\partial}{\partial x_j}\left[\nu\left(\frac{\partial u_i}{\partial x_j} + \frac{\partial u_j}{\partial x_i}\right)\right] \tag{3.5}$$

3.3 Large Eddy Simulation

Except for a few simple laminar cases, no closed analytical solutions to these non-linear equations are known, therefore numerical simulation techniques are required in order to obtain an approximate solution to a given problem. Three main techniques are now in use for the computation of turbulent flows; Direct Numerical Simulation (DNS), Large Eddy Simulation (LES) and the Reynolds Averages Navier Stokes (RANS) equations. The advantages and disadvantages of each method related to crossflow transition are summarised in Chapter 2 resulting in a Large Eddy Simulation (LES) approach taken in the work in this thesis. In an LES, the turbulent eddies above a certain size are completely resolved on the numerical grid, whereas the effect of the smaller scales are modelled. The idea behind this scale-separation is that the large eddies are generally flow dependent and carry the majority of the fluctuating energy, whilst the smaller eddies are more homogenous and isotropic. Another benefit of the method is that the small scales are generally self-similar, leading to simpler and easier modelling. Whereas RANS methods perform temporal averaging, an LES performs a spatial filtering of the instantaneous velocity field [95]. There are four conceptual steps involved in LES [84]:

1. A filtering operation is required to decompose the instantaneous velocity $u_i(x,t)$ into the sum of a resolved component $\widetilde{u_i}(x,t)$ and a residual sub-grid component $u_i'(x,t)$. The filtered velocity field represents the motion of the large scales.

2. The equations for the evolution of the filtered velocity field are derived from the Navier-Stokes equations. The momentum equation contains the sub-grid scale (SGS) stress tensor for the residual motions

3. Closure of the equations is obtained by modelling the SGS stress tensor

4. The filtered equations are solved numerically for $\widetilde{u_i}(x,t)$ which provides an approximation to the large-scale motions

The use of LES to predict crossflow transition is appealing as it can provide accurate results at greatly reduced computational cost in comparison with a fully resolved DNS. However, LES is not inherently capable of modelling a complex flow such as a transitional flow. Transitional flows are substantially different from turbulent flows. Firstly, there is no fully developed energy case cascade in the transitional region and the SGS model must be able capable to discriminate a laminar and transitional region

from a fully turbulent one. Secondly, transition involves slow growth and subtle complex interactions between the base flow and the instability modes that can affect the physical changeover from laminar to turbulence, and must be resolved reliably and accurately [104]. A detailed literature survey was conducted to find an appropriate sub-grid scale model capable of handling transitional flows and careful consideration into the balance between resolution and modelling must be made independently for each test case.

Section 3.3.1 explains the filtering process of the governing equations to obtain the LES equations while section 4.3 gives a detailed literature review of SGS modelling for transitional flows and the SGS models used in this thesis.

3.3.1 LES Equations

In DNS, the velocity field $\widetilde{u}_i(x,t)$ has to be resolved on length scales down to the Kolmogorov scale η. In an LES, a low-pass filtering operation is performed so that the resulting filtered velocity field $\widetilde{u}_i(x,t)$ can be adequately resolved on a relatively coarser grid. In a similar manner to the Reynolds decomposition to obtain the RANS equations, we can use a filter function to decompose the velocity field into resolved and unresolved components, defined in Equation 3.6.

$$u_i(\overrightarrow{x},t) = \widetilde{u}_i(\overrightarrow{x},t) + u'_i(\overrightarrow{x},t) \tag{3.6}$$

The general form of the spatial filter, as presented by Pope [84] and introduced by Leonard [57], is described in Equation 3.7.

$$\widetilde{u}_i(\overrightarrow{x},t) = \int G(\overrightarrow{r},\overrightarrow{x})u_i(\overrightarrow{x}-\overrightarrow{r},t)d\overrightarrow{r} \tag{3.7}$$

$G(\overrightarrow{r},\overrightarrow{x})$ is the filter kernel. It is a local function and has a length scale filter width Δ associated with it. Eddies of size larger than Δ are kept within the numerically resolved flow, whilst those smaller than Δ are filtered out and require modelling. Clearly the filtering operation is the most important operation in the derivation of the LES Equations however it worth noting that for the work in this thesis the filtering operation is implicit i.e. it is entirely dependent on the grid generated.

There are a number of descriptions of the various filtering methods which are described in Sagaut [95]. In 2D for simplicity Sagaut mathematically describes the

'top hat' filtering for a finite volume code:

$$G(x) = \begin{cases} \frac{1}{\Delta}, & \text{if } |x| \leq \frac{\Delta}{2} \\ 0, & \text{otherwise} \end{cases} \tag{3.8}$$

The filtering operation yields the LES equations:

$$\frac{\partial \widetilde{u}_i}{\partial t} + \frac{\partial}{\partial x_j}(\widetilde{u}_i \widetilde{u}_j) = \frac{1}{\rho}\frac{\partial \widetilde{p}}{\partial x_i} + \frac{\partial}{\partial x_j}\left[\nu\left(\frac{\partial \widetilde{u}_i}{\partial x_j} + \frac{\partial \widetilde{u}_j}{\partial x_i}\right)\right] - \frac{\partial}{\partial x_j}(\widetilde{u_i u_j} - \widetilde{u}_i \widetilde{u}_j) \tag{3.9}$$

and the filtered continuity equation:

$$\frac{\partial \widetilde{u}_i}{\partial x_i} = 0 \tag{3.10}$$

The effect of the sub-grid small scales occurs through the term:

$$\tau_{ij} = \widetilde{u_i u_j} - \widetilde{u}_i \widetilde{u}_j \tag{3.11}$$

which is not closed since $\widetilde{u_i u_j}$ cannot be obtained from the filtered quantitates alone. Therefore Equation 3.11 must be modelled by an appropriate sub-grid model.

3.4 Sub-Grid (SGS) Modelling

3.4.1 Objectives

The success of LES for transitional flows is highly dependent on the quality of the underlying sub-grid scale (SGS) model used. Substantial research over the last 30 years has resulted in a number of 'universal' models for a wide range of applications. For transitional flows, a suitable SGS model must be chosen that can deal equally well with both the laminar and turbulent boundary regions as well as the various stages of transition. The model should leave the laminar base flow unaffected and only be effective once the non-linear interactions between the modes generates modes smaller than the mesh size. As the aim of the research is to allow high-fidelity modelling of crossflow transition at a lower computational expense, it is desirable that the model require minimal computationally expensive procedures.

The objectives for the sub-grid modelling for crossflow transition therefore can be summarised as follows:

1. For a laminar flow where no energy cascade exists, ensure the sub-grid scale dissipation is reduced to zero.

2. Accurately model dissipation in a turbulent boundary layer and with appropriate scaling towards the wall.

3. Handle complex geometries at a minimal computational expense, ideally to use a model without the requirement of averaging in a spatial direction (flow homogeneity) or a dynamic procedure.

3.4.2 Literature

The most widely used SGS models are functional models based on the eddy-viscosity assumption to model the sub-grid scale tensor. The τ_{ij} term can be represented by Equation 3.12.

$$\tau_{ij}^{r} = \tau_{ij}^{R} - \frac{1}{3}\tau_{ii}^{R}\delta_{ij} \tag{3.12}$$

Where R represents the actual sgs tensor and r represents the anisotropic part which can be modelled as:

$$\tau_{ij}^{r} = -2\nu_t S_{ij} \tag{3.13}$$

The isotropic part, τ_{ii}^R, is included with a modified filtered pressure[84]. Therefore τ_{ij} can be modelled using the eddy-viscosity assumption and ν_t is the sub grid-scale turbulent viscosity which requires modelling. $\widetilde{S_{ij}}$ is the rate of strain tensor for the resolved scale defined by:

$$\widetilde{S_{ij}} = \frac{1}{2}\left(\frac{\partial \widetilde{u_i}}{\partial x_j} + \frac{\partial \widetilde{u_j}}{\partial x_i}\right) \tag{3.14}$$

The first SGS model was suggested by Smagorinsky [109]. The Smagorinsky model for ν_t assumes that the sub-grid scale viscosity is proportional to a characteristic sub-grid length Δ and to a characteristic turbulent velocity, which is taken as the product of Δ and the local resolved strain rate $|\widetilde{S}|$ magnitude, described below.

$$\nu_t = (C_s\Delta)^2|\widetilde{S}|, \qquad |\widetilde{S}| = \sqrt{2\widetilde{S_{ij}}\widetilde{S_{ij}}} \tag{3.15}$$

From Lilly [58], the constant in this model, C_s may be obtained by assuming that the cut-off wave number $k_c = \pi/\Delta$ lies within a $k^{-5/3}$ Kolmogorov cascade for the energy spectrum $E(k) = C_K\epsilon^{2/3}k^{-5/3}$ and requiring that the ensemble-average sub grid dissipation is identical to ϵ. Therefore the constant is:

$$C_s = \frac{1}{\pi}\left(\frac{3C_K}{2}\right)^{-3/4} \tag{3.16}$$

For a Kolmogorov constant of $C_K = 1.4$ this gives $C_s = 0.18$ (isotropic turbulence).

The main problem with the Smagorinsky model is its behaviour near a wall. The Smagorinsky model generates a sub-grid scale viscosity wherever a velocity gradient exists; however, all turbulent fluctuations are damped near a wall, therefore ν_t should reduce to zero. A Van Driest [115] exponential damping function can be applied and used widely in early LES studies. The function is described in Equation 3.17.

$$C_s^{corr} = C_s(1 - e^{-y^+/A^+}) \tag{3.17}$$

This standard modification improved results compared with the original model and was easy to implement for simple geometries. However it is an ad-hoc modification based on y^+. It is difficult to implement for more complex geometries and requires reducing C_s to 0.1 to sustain turbulence in channel flow [72]. Also it is desirable to achieve a $\nu_t = O(y^3)$ scaling of the eddy viscosity from the wall within a turbulent boundary layer, the damping function produces $O(y^2)$, further reducing its applicability to wall resolved LES.

Germano et al. [29] proposed a dynamic Smagorinsky SGS model which adjusts the model coefficient to the local flow conditions. The computation of the model coefficient was subsequently changed by Lilly [58]. The dynamic procedure is based on the 'Germano identity', which relates the kinetic energy fluxes over a test filter level to the fluxes at the grid filter level. The model is non-local and requires averaging the model constant over a spatial direction; a localised model was subsequently proposed by Piomelli and Liu [80]. The model has been successfully applied for transitional flows in the work of Germano et al. [29] for transition in a channel flow and for incompressible boundary layers in the work of Huai et al. [40; 41] on a swept wedge to simulate crossflow vortices. A major problem with the model was the occurrence of singularities within the flow domain and usually required clipping of negative regions. Progress has been made in this area by Meneveau et al. [67] with a Lagrangian dynamic SGS model in which the evolution of the SGS stresses are tracked.

Whilst the dynamic model has showed promising results in the literature it is still limited; it is generally computationally expensive and can be difficult to implement for complex geometries and unstructured grids. Results from this model also have to be clipped and adjusted for each case to provide a proper y^{+3} near wall scaling for the eddy viscosity.

Another eddy-viscosity model that showed potential for transition is the filtered structure-function (FSF) model, introduced by Ducros et al. [26]. The original formulation suffered in similar ways to the Smagorinsky model and was too dissipative for transitional flows. However the temporal high-pass filter allowed the model to reduce influence in regions of the flow that are dominated by mean strain rate, i.e. a laminar region or close to a wall. Mixed-dynamic models introduced by Zang et al. [125] have shown good results for transitional flows. The approach takes the dynamic Smagorinsky model in conjunction with the mixed model of Bardina et al. [9] as the base model. Very accurate results were achieved for the case of a compressible transitional boundary layer at high Mach number [27] and for simulated bypass transition [75]. The simulation was able to simulate the growth of laminar streaks and turbulent spots. The approach however suffers from the same limitations as the Germano et al. [29] dynamic Smagorinsky model in that it is has a high computational expense and difficult to implement for complex geometries.

The approximate deconvolution model (ADM) has also been used recently for prediction of transition. With the approximate deconvolution model, an approximation of the unfiltered solution is obtained by repeated filtering, and, given a good

approximation of the unfiltered solution, the nonlinear terms of the Navier-Stokes equations are computed directly. The effect of scales not represented on the numerical grid is modelled by a relaxation regularisation involving a secondary filter operation. The model was introduced by Stolz and Adams [110] and adjusted for finite volume approaches by von Kaenel et al. [118; 119]. The ADM model was used for a study on transitional flows by Schlatter et al. [104] for a channel flow case. They performed LES of a transitional channel flow using several models including the ADM model, dynamic Smagorinsky model and a high-pass filtered Smagorinsky model. They concluded that the ADM model outperformed the other SGS models for predicting the breakdown of hairpin vortices. They also concluded that high pass filtered SGS models like the ADM model can provide excellent results in simulating transitional behaviour.

The high-pass filtered models and models with dynamic procedures discussed in this chapter have all shown promise and the ability to model the various stages of transition. They however, incur additional computational costs associated with the high pass filtering procedures and flow averaging and require tuning for each case. A more holistic SGS model that can handle laminar, turbulent and transitional boundary layers without explicit filtering or a dynamic procedure and based on local quantities would be ideal. Subsequently, Nicoud and Ducros [72] proposed the Wall-Adapting Local Eddy Viscosity (WALE) model discussed in the next section which is aimed at developing a SGS model similar to the structure of the Smagorinsky model that could better handle wall bounded flows and without the use of any computationally expensive procedures. The WALE model is explained in detail in the next section.

3.4.3 Wall Adapting Local Eddy Viscosity SGS Model

The WALE SGS model was developed by Nicoud and Ducros [72] to counter three main problems with the SGS models in the literature. Firstly, the ability to handle a near wall region: this requires the eddy viscosity in a laminar region to reduce to zero and to provide a $O(y^3)$ scaling of the eddy viscosity in the turbulent boundary layer. Secondly, it must be able to handle complex geometries without averaging in a flow direction and applicable to unstructured codes. Thirdly it must be able to run with minimal computational cost.

All of the eddy viscosity SGS models discussed may be written in a generic form, shown in Equation 3.18.

$$\nu_t = C_m \Delta^2 \widetilde{OP}(\overrightarrow{x}, t) \tag{3.18}$$

where C_m is a model constant associated with the SGS model, Δ is the characteristic turbulent length scale (usually the size of the grid cell) and $\widetilde{OP}$ is an operator of space and time and defined from the resolved fields. The WALE model provides a new representation for the operator $\widetilde{OP}$. $\widetilde{OP}$ must be based on the invariants of a tensor $\tau_{i,..j}$ and should be representative of the local turbulent activity. The velocity gradient tensor $\widetilde{g}_{ij} = \partial\widetilde{u}_i/\partial\widetilde{x}_j$ is the most obvious candidate to represent the velocity fluctuations at the characteristic turbulent length scale. Recall that the Smagorinsky model is based on the symmetric part of the strain rate tensor $\widetilde{S}_{ij}$. The main limitations for this approach were that it produced an eddy viscosity wherever a velocity gradient existed, producing a large eddy viscosity near the wall ($O(1)$).

The WALE model attempts to build a better operator by using the traceless symmetric part of the square of the velocity gradient tensor, described in Equation 3.19.

$$S^d_{ij} = \frac{1}{2}(\widetilde{g}^2_{ij} + \widetilde{g}^2_{ji}) - \frac{1}{3}\delta_{ij}\widetilde{g}^2_{kk}, \qquad \widetilde{g}^2_{ij} = \widetilde{g}_{ik}\widetilde{g}_{kj} \tag{3.19}$$

The WALE model is based on the relation $S^d_{ij}S^d_{ij}$ which has the ability to detect turbulent structures with either a large strain rate, a rotational quantity or both. For the case of pure shear, the term reduces to zero, which makes physical sense in that shear zones contribute to energy dissipation to a smaller extent than turbulent eddies. The benefit that this has for a wall-bounded transitional flow is that it produces an almost zero eddy viscosity in a laminar region within a boundary layer. As the term $S^d_{ij}S^d_{ij}$ scales from the wall with behaviour y^2 the term is naturally calibrated to achieve

a y^3 scaling. Subsequently the final model formulation is described in Equation 3.20.

$$\nu_t = (C_w \Delta)^2 \frac{(S^d_{ij} S^d_{ij})^{\frac{3}{2}}}{(\widetilde{S}_{ij} \widetilde{S}_{ij})^{\frac{5}{2}} + (S^d_{ij} S^d_{ij})^{\frac{5}{4}}} \tag{3.20}$$

where C_w is the WALE constant. The value of C_w was assessed in Nicoud and Ducros using several fields of homogenous isotropic turbulence. From their results the following relationship can be deduced between the Smagorinsky and WALE constants for isotropic turbulence.

$$C_w = \sqrt{C_s^2 \alpha} \tag{3.21}$$

where α is between $10.52 - 11.27$. For this range and a C_s of 0.1 the resulting C_w is between $0.32 - 0.34$.

The model has been validated in the original paper for isotropic turbulence and a channel flow in which transition occurred. The authors suggest that the model would be a suitable candidate for laminar-turbulent transition modelling. The model was also extensively tested by Temmerman and Leschziner [113] and compared to a highly resolved LES and several other SGS models. Their test was on a separated channel flow with a curved surface. They conclude that the WALE model was the most effective model in returning the closest result to the highly resolved case and managed to capture the correct y^3 scaling of turbulent viscosity.

The results in this thesis aim to quantify the model's ability and success in for transitional flows.

3.5 DELTA CFD Code

To perform the LES calculations and to achieve the objectives set out in Chapter 1 a CFD code was chosen. The main criterion for the choice of code was that it must have previous validation for aerodynamic flows and its performance and accuracy tested. As additional SGS models and features will be implemented it must have accessible source code. since some of the main objectives of this work were to work with complex and realistic geometries the code must be able to deal with an-isotropic grid cells and complex geometry.

An in-house code called DELTA was chosen that met the code requirements described above. The DELTA CFD code [73] has been continuously developed and applied in the Department of Aeronautical and Automotive Engineering at Loughborough University since 1994. The code was originally written as a structured Euler code but was extended for RANS calculations with the implementation of the high Re standard $k-\epsilon$ and low Re Launder-Sharma turbulence models. Further development occurred for LES calculations and to accommodate the increasing computational demands, the code was parallelised. The code utilities parallel processing through both shared memory (Open MP) and Message Passing Interface (MPI) approaches.

DELTA was written primarily for the computation of aerodynamic flow problems but has since been employed and validation for a wide range of flows. Previous work includes simulations of compressible [14; 120], incompressible [81; 96], external [74; 93], internal [96] and wall bounded [116].

3.5.1 Technical Overview

DELTA solves the governing equations (Section 3.2) using a cell-centred finite volume discretisation approach, on a multi-block structured grid with a curvilinear coordinate system. DELTA is a pressure-based code adopting the widely used SIMPLE (Semi-Implicit Method for Pressure Linked Equations) pressure correction algorithm, designed to handle both incompressible and compressible flow cases by switching on and off the energy equation.

The SIMPLE solution algorithm implemented in DELTA is as follows:

1. Guess the pressure field p.

2. Solve the x, y and z momentum equations using the pressure field p to obtain u, v and w at cell centroids.

3. Compute the face mass flow rates F via central-differencing of the cell centre values.

4. Solve the p' (pressure-correction) equation.

5. Correct the face flow rates.

6. Correct the cell-centred velocities u, v and w.

7. Correct the cell-centred pressure p.

8. Check for convergence. If converged, stop. Else go to 2.

The code uses a co-located flow variable arrangement, to suppress odd-even decoupling, the standard Rhie and Chow [92] approach is added to all convective velocities. For LES it is essential that the smoothing term should be kept small to avoid unphysical dissipation of the resolved eddies, therefore the Rhie and Chow smoothing term is scaled down by 0.1.

For RANS calculations DELTA employs a MUSCL (Monotone Upstream-Centred Scheme for Conservation Laws) spatial discretisation scheme of the flow variables. The 1st derivative convective fluxes are discretised using a flexible method which may be summarised as a family of schemes ranging from central differencing to upwind differencing selected via user set parameters. For time integration, DELTA can use either an explicit scheme or a 1st order Euler implicit scheme. A Gauss-Siedel line solver is used to solve the pressure correction equation.

For LES calculations various modifications and new spatial discretisation schemes were introduced combined into a single expression described in Equation 3.22 for a conserved scalar ϕ for the east e face of a cell P.

$$\phi_e = \phi_P + \frac{(1-\kappa)}{4}(\phi_P - \phi_W) + \frac{(1+\kappa)}{4}(\phi_E - \phi_P) \tag{3.22}$$

Where ϕ_W and ϕ_E are the cell centre values at the east neighbouring cell and west neighbouring cell. For the LES calculations in this thesis a second order upwind scheme, called QUICK (Quadratic Upwind Interpolation for Convective Kinetics) was selected for discretisation of convective fluxes by setting κ to be 0.5. A central-differencing scheme is employed for the diffusive fluxes.

Initially a central differencing scheme was employed for the convective fluxes however initial results showed large dispersion errors. The QUICK scheme provided a compromise between accuracy, robustness and acceptable numerical dispersion and

dissipation errors. Previous literature of LES calculations at realistic flow conditions and complex geometries have showed use of a similar scheme and previous use of DELTA have also showed that the 2nd order upwind scheme can provide an acceptable result [66]. For temporal discretisation an implicit 1st order backward Euler scheme was chosen. A 3rd order accurate low storage Runge-Kutta method [124] was also available however experience has showed that with the small time steps necessary for LES calculations, there was little difference between the alternatives.

The original implementation of DELTA contained the standard Smagorinsky model with the Van Driest damping function for LES SGS modelling. For the work in this thesis the Wall Adapting Local Eddy Viscosity (WALE) model was implemented to the code with the mathematical description of the model in Section 3.

3.5.2 Geometry Handling and Grid Generation

Complicated geometries are handled in DELTA by using a multi block approach. The flow domain is split into a number of structured blocks and linked together in an unstructured manner. The multi-block capability in DELTA requires the generation of two extra rows of cells, known as halo cells, along all block faces. Solution data is held within the halo which is a copy of solution data from internal cells in the adjacent block. This allows the computation of fluxes through the faces contributing to the internal cells of a block, without directly referring to solution data in the adjacent block. In addition, the halo also contains volume, face area, and face normal information to allow correct interpolation from cell centres to cell faces and to compute transformation metrics required for viscous fluxes.

DELTA does not incorporate grid generation or visualisation components, instead DELTA interfaces with 'foreign' grid files. A variety of grid file formats can be read into DELTA including PLOT3D files and multi-block outputs from ICEMCFD HEXA. For the grid generated in the present work, ICEMCFD HEXA 14.0 was used as it provided a powerful, interactive capability for generating multi-block meshes, particularly for complex geometries.

Grid generation starts with a 3D CAD representation of the flow geometry and its surrounding flow domain. Within ICEMCFD a single block is placed around the geometry. This encompassing block is then sub-divided into a number of blocks which fit the geometry in question. HEXA adopts a top-down approach whereby each time a block is modified all other connected blocks are also modified. Once the blocking strategy has been established, the blocks are then attached to the CAD geometry

through a process of association. Each node, line and face from each block is associated with the points, curves and surfaces of the CAD geometry. Once association is done the mesh can then be generated by assigning a node count and bunching ratio to each edge.

Once the blocking has been completed the mesh is output from ICEM HEXA into a neutral 'Multiblock Info' format. This multi block info format can then be read into DELTA and converted into the delta 'geom' format and a topology file is written that defines the linkages between each block at a face level. Most structured multi-block codes adopt an approach in which the linkages occur at the complete face of a block, shown in Figure 3.1(a). However DELTA, incorporates a more flexible definition of the linkages, where any sub-set of a single block face can be linked to any other block surface, shown in Figure 3.1(b). This enables more flexibility when developing the grid and a reduction in number of blocks required for a given CAD geometry.

The maximum number of cores that the simulation can run on depends on the number of blocks in the grid. This is because each block (or a selection of blocks to improve load balancing) is allocated to an individual processor on a multi-processor cluster. This is achieved using MPI, which is incorporated into the DELTA code. Therefore to increase the speed which the simulation takes, the grid is divided into a large quantity of blocks, some grids discussed in this thesis have over 300 blocks.

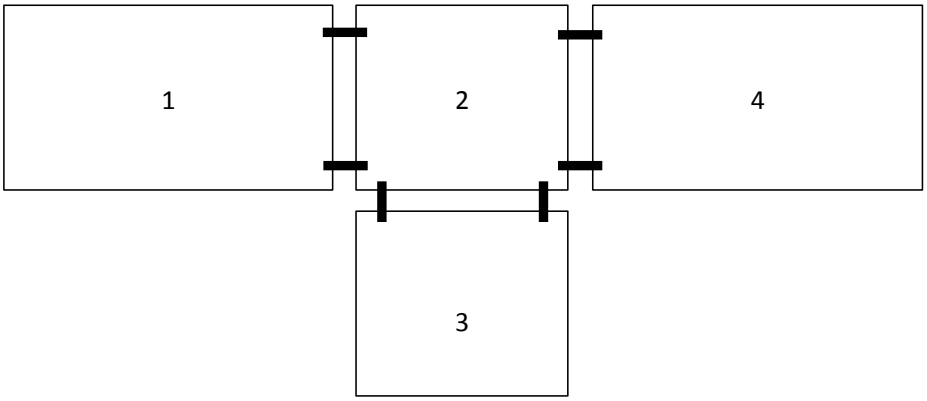

(a) Standard multi-block topology

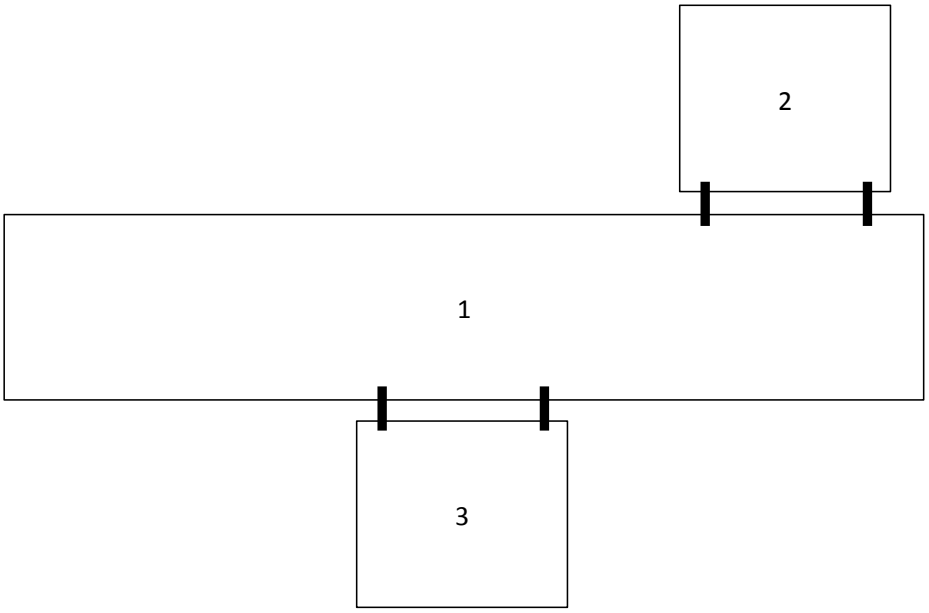

(b) DELTA complex multi-block topology

Figure 3.1: Multi-block topology

3.5.3 Boundary Conditions

A number of boundary conditions are available within DELTA. The boundary conditions that were used within this thesis are explained below. An additional boundary condition was implemented into DELTA called the 'Synthetic Eddy Method' to provide a better representation of external freestream turbulence. This is explained in detail, including a validation case in the next section.

1. **Fixed Velocity Inlet** - This boundary condition fixes a value of the velocity components at each grid node in the inlet plane. As the solutions conducted in this thesis were for freestream conditions, the fixed velocity condition was a

suitable inlet boundary condition (i.e. no wall boundary layers required interpolating onto the grid). As the fixed velocity boundary condition is a reflective boundary condition it is necessary to have the boundary a reasonable distance away from the area of interest.

2. **Outflow** - The LES outflow boundary condition used a convective outlet. The convective outlet is widely used in LES because it ensures the convection of the flow through the outlet plane, at a constant velocity defined by the bulk velocity at the outlet U_B, without the generation of disturbance wave reflection.

3. **No-Slip Wall (Viscous)** - This boundary condition applies the no-slip condition at the boundary. A zero-gradient extrapolation is used for pressure and total enthalpy at the wall, whilst the velocities at the wall are explicitly set to zero.

4. **Slip Wall (Euler)** - This boundary condition applies a zero shear (slip) condition at the boundary. Flow conditions at the wall are determined from the adjacent cell centre using a zero gradient extrapolation, the momentum component normal to the wall is then removed so that there is no flow through the wall.

5. **Cyclic** - To reduce the impact of the spanwise faces and to reduce the computational expense an infinite swept wing model was applied to the simulations described in this thesis. This was done by using a periodic or cyclic condition on the spanwise faces. This is achieved by linking the topology of each spanwise face from each block, allowing data to be passed from one side face back into the block on the opposite face.

6. **Numerical Trip** - A numerical transition trip can be applied to the flow at any prescribed location. The trip is applied by perturbing, at each computational time step, the flow solution in a row of computational cells near the wall. A random velocity perturbation with a Gaussian distribution and a given turbulence intensity is applied using a spatial stencil to give a weak spatial correlation to the disturbance.[81]

3.6 Calculation Methodology

LES simulations were run in a non-dimensional scheme based upon free stream velocity Q_0 and reference length, L. The time step for LES simulations was chosen such that the maximum CFL number was less than 1, resulting in a non-dimensional time step for the grids used in this thesis of $< 1.0 \times 10^{-05}$. The extremely small time steps were required for convergence and accuracy of the smallest resolved scales and resulted in long solution development times. 5 inner iterations were run within each time-step to allow the spatial results to converge within a time-step. The solver was typically run for 10 non-dimensional flow through times to allow the flow to develop. Once the flow had developed, statistical averages were gathered by sampling to generate a time-averaged solution. The time-averaged (mean) solution would be run until a statistically stationary solution was evident.

The strategy for running the LES calculations was to run using the stable Smagorinsky SGS model and at an order of magnitude larger time step as an initialisation. Then the WALE SGS model was used subsequently and the time step was reduced. For the Smagorinsky SGS model $C_s = 0.1$ was used and for the WALE SGS model C_w of 0.35 was used. A justification of this was given in the 'Sub-Grid Modelling' section of this chapter.

3.7 Synthetic Eddy Model (SEM)

For the accurate simulation of laminar-turbulent transition an important step is to accurately specify the freestream turbulence environment. As discussed in Chapter 2, the external environment plays a pivotal role in defining the transition mechanism and breakdown location. The use of inaccurate or unphysical correlated freestream perturbations can lead to all turbulent fluctuations decaying rapidly and any recovery to properly correlated turbulence can extend a long distance within the flow domain.

To provide free stream turbulence a new method was incorporated into the DELTA LES capability, called the 'Synthetic Eddy Method (SEM)'. The SEM model was initially developed and has been used in published literature to provide a inlet condition using synthetic turbulence; however, for this work it was modified to provide physically realistic perturbations at a location within the flow domain, similar to the numerical trip described in the previous section.

This section will give the strategy behind synthetic turbulence generation, a mathematical description of the method, and results for a test case used to validate the implementation of the method. First a brief literature study of inlet condition free stream turbulence is described with a justification behind using the SEM rather than other methods in the present work.

3.7.1 Literature

The specification of inlet conditions in LES has been investigated over the last three decades via a number of approaches. For more detailed reviews of inlet condition generation the reader is advised to read Lund et al. [59], Jarrin et al. [44] and Tabor and Baba-Ahmadi [112].

Generally inlet turbulence generation can be categorised into two main groups: (i) precursor approaches and (ii) synthetic methods.

The precursor methods use a separate LES simulation that generates a 'dataset' of turbulent data which can be applied as the inlet condition. This method is generally considered as the most accurate LES turbulence generation method and has the advantage that the perturbations are taken from genuine (within the constraints of LES) turbulence. The turbulence possesses most of the required characteristics of turbulence, including correlated temporal and spatial fluctuations and a correct energy spectrum (up to the cut-off wave number). The 'dataset' can be generated in a number of ways, for example using periodic or cyclic calculations. From this

'dataset' the velocity field in a plane normal to the streamwise direction is stored at each computational time step.

This approach however is limited and its drawbacks can be summarised into two points:

1. Precursor methods are restricted to very simple cases where the flow at the inlet plane can be regarded as a fully developed turbulent flow [49] or a spatially developing turbulent boundary layer [59]. Due to this it lacks the generality required for LES and would be difficult to employ for the present work where low-amplitude free stream perturbations are required.

2. The method incurs extra computational costs from an additional LES calculation and also adds to the storage capacities.

For these reasons precursor methods were not used for the present calculations and only synthetic turbulence generation methods were considered. This conclusion is also backed up by the weight of research effort in this field heading towards synthetic turbulence.

At the simplest level, synthetic turbulence generation involves introducing a white-noise random component to the inlet velocity, with the amplitude determined by a user-defined turbulent intensity level. It is well known that this method is insufficient, since a long development length is required before the flow reaches what might be considered a realistic turbulent state [82]. Also the data generated does not exhibit spatial or temporal correlations, the energy is uniformly spread over all wave numbers and due to a lack of energy in the low wave number range, the pseudo turbulence is quickly dissipated [43]. The inability of white-noise to generate turbulent inlet conditions has been demonstrated on several occasions [4; 112].

Another method to give spatial and temporal correlations to the turbulence is to create a time series of velocity fluctuations by performing an inverse Fourier transform for user-prescribed spectral densities [54; 56]. These methods have been applied with success for isotropic homogeneous turbulence and flow over a backward facing step in DNS calculations. However there are several limitations with this method, including that they are derived for periodic signals on uniform meshes. For more complex inlet meshes and for industrial applications, they become prohibitively expensive. Tabor et al. [111] also found that current Fourier synthesis methods were unable to predict higher order moments and its performance when compared against more robust methods were generally worse.

It is also possible to use statistical experimental data to generate synthetic turbulence. Proper orthogonal decomposition (POD) analysis has been applied as a way of analysing turbulence in general. POD takes as input an ensemble of instantaneous realisations or snapshots and extracts basis functions optimal for the representation of the data, decomposing the data into spatial and temporal eigenvectors. Druault et al. [24] applied this method with experimental data from hot-wire measurements for DNS and LES calculations. Using hot-wire measurements the temporal resolution of the data was good however the spatial resolution was a problem. Perret et al. [76] used the same approach using stereoscopic PIV measurements to provide inlet conditions for LES of a mixing layer. PIV however had the opposite problem to hot-wire; a good spatial resolution, under-resolved temporally.

A recent approach to inlet turbulence synthesis, which is used in the present work, is the synthetic eddy method (SEM). The method is based on the classical view of turbulence as a superposition of eddies. Eddies are based on a Lagrangian treatment, which generates coherent structures with a given vorticity distribution at the inlet which are then transported into the domain. The coherent structures generated are defined by a shape function that encompasses the structure's spatial and temporal characteristics. The development of the method is detailed in Jarrin et al. [44], which was based on an earlier PhD thesis by Sergent [108]. The method has been very successful and used in a range of test cases including pipe and channel flow, aerofoil flow and flow over a hill [64] and for indoor flows [2]. The method has also been implemented in commercial code STAR-CCM+ [64]. A recent comparison and extension to hybrid RANS/LES simulations by Jarrin et al. [45] showed that the method, when compared against a Fourier synthesis method [10] and Lund's method [59] it performed better needing a substantially shorter length of domain downstream of the inlet to develop realistic turbulence.

3.7.2 Method

The LES inflow plane on which synthetic velocity fluctuations are generated with SEM is a finite set of points $S = \{x_1, x_2, ..., x_s\}$.

The first step is to create a region surrounding S which will contain the synthetic eddies. Its minimum and maximum coordinates are defined by,

$$x_{i,min} = \min_{x \in S}(x_i - \sigma(x)) \quad \text{and} \quad x_{i,max} = \max_{x \in S}(x_i + \sigma(x)) \tag{3.23}$$

where σ is a user-defined characteristic length scale whose computation is discussed later. The number of eddies inside the box is defined by N. In the initial Jarrin et al. [44] formulation the number of eddies is given by:

$$N = \max(V_B/\sigma^3) \tag{3.24}$$

where V_B is the volume of the box of eddies. This value however is a maximum and it was found that lower values of N resulted in a better representation of the input Reynolds stresses.

The SEM decomposes a turbulent flow field into a finite sum of individual eddies. The velocity fluctuations generated by N eddies have the representation

$$u_{p,i} = u_{o,i} + \frac{1}{\sqrt{N}} \sum_{k=1}^{N} a_{ij} \epsilon_j^k f_{\sigma(x)}(x - x^k) \tag{3.25}$$

where $u_{o,i}$ is the original velocity on a plane within the the LES calculation and $u_{p,i}$ is the subsequent final perturbed velocity. In the first implementation of Jarrin et al. [44] (which was developed for an LES inlet condition) $u_{o,i}$ was defined as the bulk background velocity. In the present implementation $u_{o,i}$ is the velocity taken from a plane within the LES, allowing for free stream turbulence to be generated anywhere within the LES domain. The method has been implemented such that it can also be used in DELTA as in the original implementation as an inlet condition. The locations of the eddies are x^k, ϵ_j^k are their respective intensities and a_{ij} is the Cholesky decomposition of the Reynolds stress tensor, defined below.

$$a_{ij} = \begin{pmatrix} \sqrt{R_{11}} & 0 & 0 \\ R_{21}/a_{11} & \sqrt{R_{22} - a_{21}^2} & 0 \\ R_{31}/a_{11} & (R_{32} - a_{21}a_{31})/a_{22} & \sqrt{R_{33} - a_{31}^2 - a_{32}^2} \end{pmatrix} \tag{3.26}$$

The Reynolds stress tensor R_{ij} is defined by the user and can be retrieved from a precursor RANS simulation or experimental data. a_{ij} determines the magnitude of the velocity fluctuation as function of the Reynolds stress tensor.

The velocity distribution of an eddy located at x_k is $f_{\sigma(x)}(x - x^k)$. It provides spatial coherence to the fluctuations. Jarrin et al. [44] assumes that differences in the distributions between the eddies depend only on the length scale σ, thus f_σ can

be defined by:

$$\sqrt{V_B \sigma^{-3}} f\left(\frac{x - x^k}{\sigma}\right) f\left(\frac{y - y^k}{\sigma}\right) f\left(\frac{z - z^k}{\sigma}\right) \tag{3.27}$$

where f is a simple tent function,

$$f(x) = \begin{cases} \sqrt{\frac{3}{2}}(1 - |x|), & \text{if } x < 1 \\ 0, & \text{otherwise} \end{cases} \tag{3.28}$$

The position x^k and the intensity ϵ_j^k of each eddy are independent random variables. At the first iteration x^k is taken from a uniform distribution over the box of eddies B and $\epsilon_j^k = \pm 1$, with equal probability to take one value or the other. The eddies are convected through the box of eddies B with a constant velocity U_c characteristic of the flow, therefore giving temporal coherence to the fluctuations. For the calculations in this thesis U_c is determined during the CFD run as the bulk velocity at the plane where the SEM is defined. This is a modification to the original implementation and allows more flexibility. As the model was originally developed for inlet free stream turbulence in which the user specifies the bulk velocity, this modification allows the method to be applied a turbulence source (without specifying the velocity), at any plane within the computational domain.

At each new time-step of the LES, the new position of the eddy k is given by

$$x^k(t + dt) = x^k(t) + U_c dt \tag{3.29}$$

where dt is the time step of the simulation. If an eddy k is convected out of the box through a face F of box B, then it is immediately regenerated randomly (using a pseudo-random number generator) on the inlet face of B facing F with a new independent random intensity still taken from the same distribution.

The parameter σ controls the size of the structures. It is widely acknowledged that the specification of realistic length scales strongly affects the development of the turbulence downstream of the inlet. The value can be determined from a precursor RANS solution or estimated from the size of the maximum length scale of the simulation in question. The value is entirely dependant on the simulation being studied and its impact was investigated.

The method generates a stochastic signal with prescribed Reynolds stresses, length and time scale distributions. Although the SEM involves the summation of a large

number of eddies for each grid point on the defined plane, the CPU time (for Jarrin et al. [44]) required did not exceed 1% of the total CPU time per iteration of the LES. For the test cases and results in this work, the method added very little additional overhead.

3.7.3 Flat Plate Calibration

3.7.3.1 Introduction

To test the 'Synthetic Eddy Method (SEM)' described in the previous section a test case was chosen that was representative of the LES calculations described in Chapter 6 using the ASU-(67)-0315 aerofoil. Low-amplitude free stream turbulence is required that is representative of conditions in wind tunnels and at altitude. In the LES calculations shown in Chapter 6 a free stream turbulence plane was required for planes normal to the aerofoil surface. Therefore for the SEM calibration a flat plate geometry was chosen for ease of computational complexity which could replicate the laminar boundary layer of the ASU test case.

The aim of the test was to calibrate the SEM for generating turbulence at a high turbulence level and at a low turbulence level that would be used for further calculations. The rectangular solution domain for the flat plate is shown in Figure 3.2. Dimensions of $5mm$ in height and $24mm$ in width were the domain height and width for the first row of blocks in the ASU calculations. A length of $100mm$ was chosen that provided enough computational space for the laminar boundary layer to develop and enough space to analyse the SEM output. The plane in which the SEM was applied is also shown in the figure, the plane is taken at $50mm$ in the x-direction.

A no-slip wall boundary condition was applied to the lower surface and a symmetry boundary condition on the upper surface. For the side faces, a cyclic boundary condition was applied to ensure spanwise uniformity. This is achieved by linking the topology of each spanwise face from each block, allowing data to be passed from one side face back into the block on the opposite face. A uniform velocity inlet was applied with $U_0 = 22m/s$ and a standard outflow boundary condition was applied to the outlet face. The key boundary conditions are labelled and annotated in 3.2.

The grid applied to the domain consisted of 150 cells in the x-direction (labelled in Figure 3.2), 100 cells in the y-direction and 156 cells in the z-direction. The grid is refined near to the wall to resolve the boundary layer with a $\Delta y+$ of 0.5 at the wall. The grid is also refined near to the SEM plane location. Figure 3.3 shows the two

planes of the final grid, the SEM plane and a plane at $z = 0$. The figure shows the refined in the x-direction near the SEM Plane and the refinement near to the wall.

Figure 3.2 shows a mean SEM plane initial undisturbed laminar boundary layer at 0.5mm in height.

3.7.3.2 SEM Setup

The inputs for the SEM plane that are required are the target Reynold stresses, a length scale and the number of eddies applied. Two cases were run with different target Reynolds stresses for different free stream turbulence levels. The two cases are described below:

1. Case 1 (High Freestream Turbulence) - For the high turbulence level case a target turbulent intensity of u_{rms} was set at 10% of U_0 To achieve this the first term in the Reynolds stress tensor, $u'u'$ was set at 0.01 (non-dimensional).

2. Case 2 (Low Freestream Turbulence) - For the low turbulence level case a target turbulent intensity of u_{rms} was set at 0.3% of U_0 To achieve this the first term in the Reynolds stress tensor, $u'u'$ was set at 1×10^{-05} (non-dimensional).

The length scale was fixed at $0.45mm$ as an initial estimate based on 2% of the width of the domain size. In the original implementation the maximum number of eddies was given by the equation 3.24 based upon the length scale however upon initial testing it was shown that this value of N was far too large and severely over predicted the Reynold stresses. Using equation 3.24 gives an $N_{max} = 1500$, therefore for the tests an N of 250 was chosen.

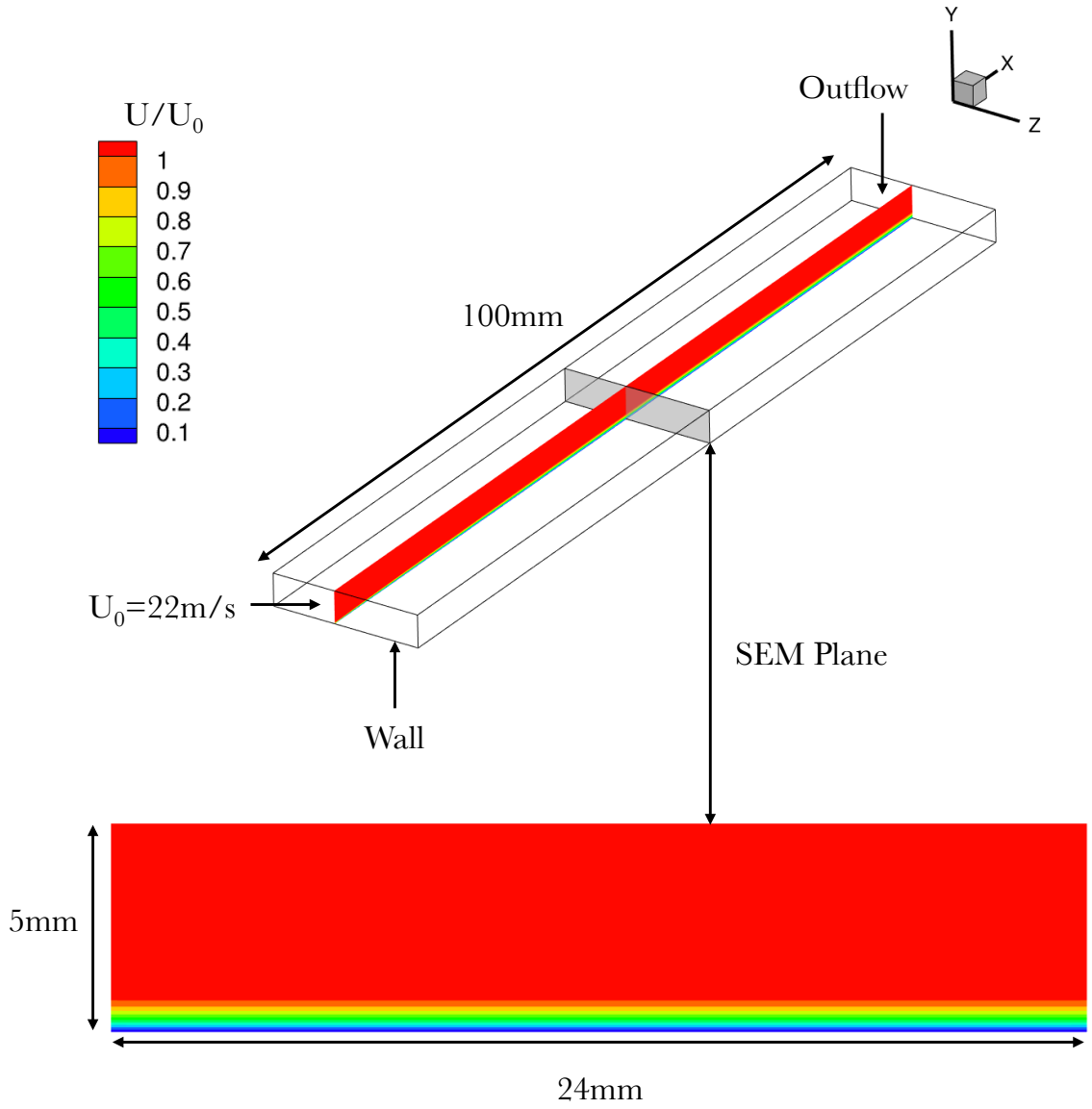

Figure 3.2: SEM flat plate test case and calibration - setup

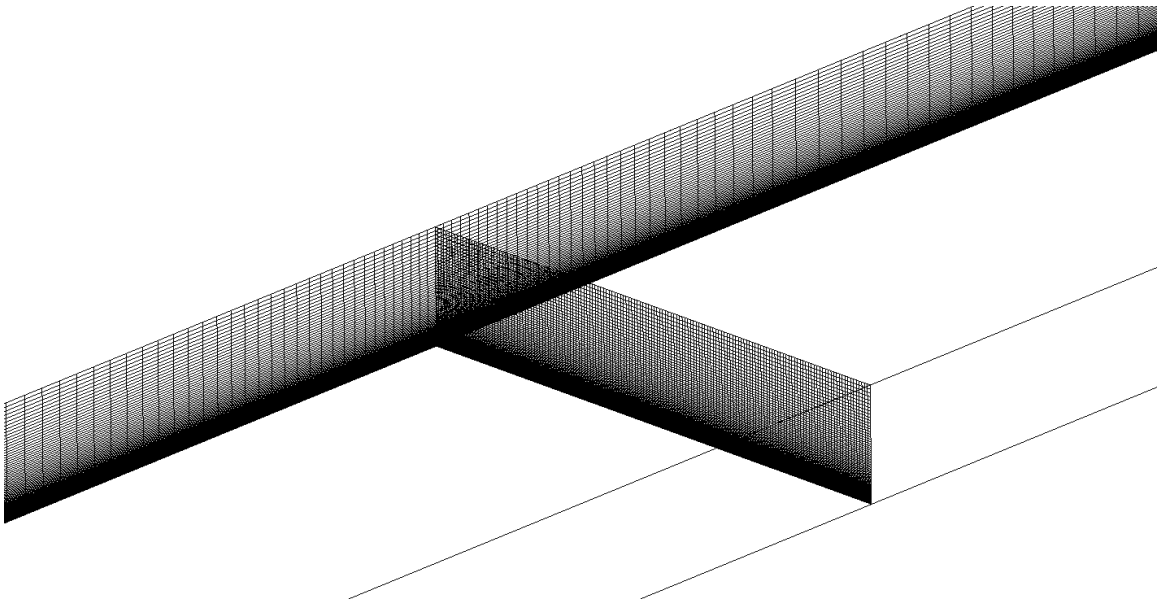

Figure 3.3: Grid for flat plate test case, SEM Plane and $z = 0$ Plane shown

3.7.3.3 Results

Figure 3.4 shows a contour plot of instantaneous U velocity $0.4mm$ away from the wall for Case 1. The view is looking in the negative y-direction onto the wall. The axis of the plot is labelled with 0 placed at the SEM plane. Figure 3.5 shows the same plane but with a contour of instantaneous vorticity magnitude, also for Case 1. Both plots show clearly where the perturbation plane is and where the synthetic eddies begin to be generated. The length scale of the eddies is small which is due to the SEM input of a small length scale at $0.45mm$. After a streamwise distance of $0.01m$ the eddy length scale begins to reduce and long streamwise streaks begin to form. These streamwise velocity streaks are more clearly apparent in Figure 3.5. Streaks of streamwise velocity are commonly associated with turbulent boundary layers and can be shown to form at a very short distance along the flow domain.

The instantaneous data was sampled into a mean data file of the velocity components and Reynolds stress terms. Figure 3.6 shows for Case 1 the time-averaged $\overline{u'u}'$ Reynolds stress term plotted at the SEM plane. The input $u'u'$ for the SEM initialisation was a value of 0.01 to achieve a turbulent intensity of 10%. The figure shows peak fluctuations in the upper regions of the boundary layer. The peak $\overline{u'u'}$ can be shown in the colour map at 0.01. Therefore the SEM successfully initialised the synthetic turbulence at the user-defined value. The number of eddies used to achieve this was 17% of N_{max}, using a large number of eddies causes the stresses to increase

significantly. This is due to the fact that the total perturbation at a certain grid point is calculated by taking a perturbation from each eddy close to it. Therefore if too may eddies are initialised there is more chance of overlapping eddies, causing the over prediction of the Reynolds stress terms. Figure 3.7 shows a plot of the peak $\overline{u'u'}$ against distance from the SEM plane. For a short distance the impact of the SEM plane causes the peak stress to rise as the superimposed eddies begin to interact.

Figure 3.8 shows a contour plot of instantaneous vorticity magnitude $0.4mm$ away from the wall for Case 2. The plot view is the same as that of Figure 3.4 and 3.5. It is quite clear for this low freestream turbulence setup the amplitude of the perturbations is much lower. The eddies result in streaks of velocity with a much lower vorticity range than Case 1. Figure 3.9 shows the time-averaged $u'u'$ at the SEM initialisation plane. The figure shows the low amplitude average fluctuations. The fluctuations are close to the target $u'u'$ of 1×10^{-05}.

Overall the test case has showed that the SEM perturbation method could be a viable method of generating realistic low amplitude freestream turbulence. The method is simple and easy to use with minimal computational cost. For the simulations conducted in this test case, the addition of the SEM into the calculations only increased the computational cost by 5%. Subsequently the SEM was used in calculations described in Chapter 6.

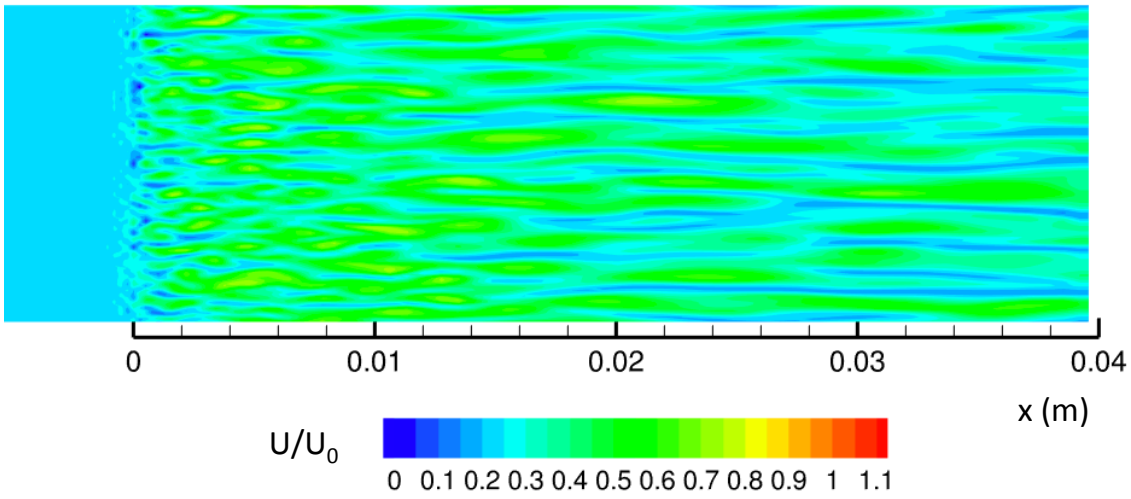

Figure 3.4: Case 1 - Contour of Instantaneous U Velocity at $0.4mm$ from wall surface

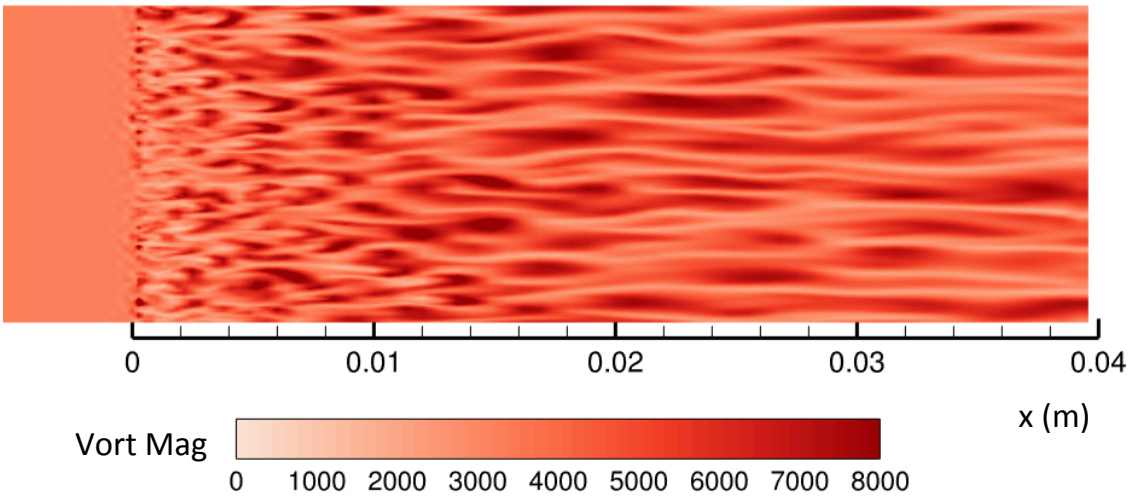

Figure 3.5: Case 1 - Contour of Instantaneous Vorticity Magnitude at $0.4mm$ from wall surface

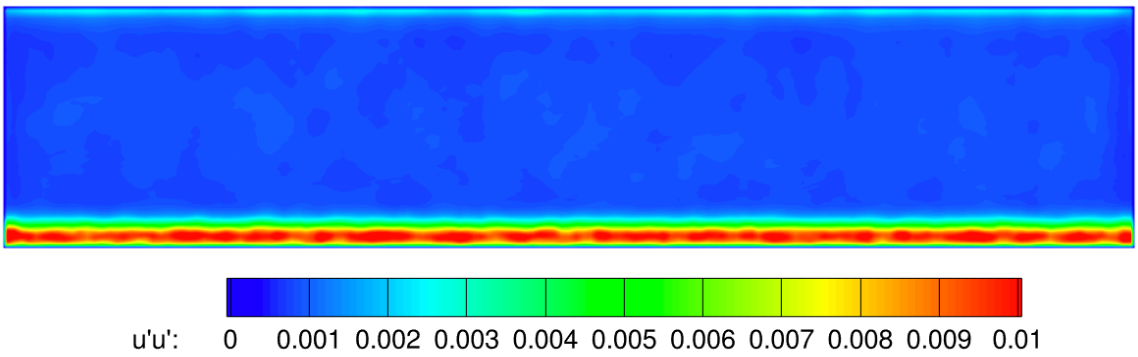

Figure 3.6: Case 1 - Contour of Mean $u'u'$ at the SEM initialisation plane

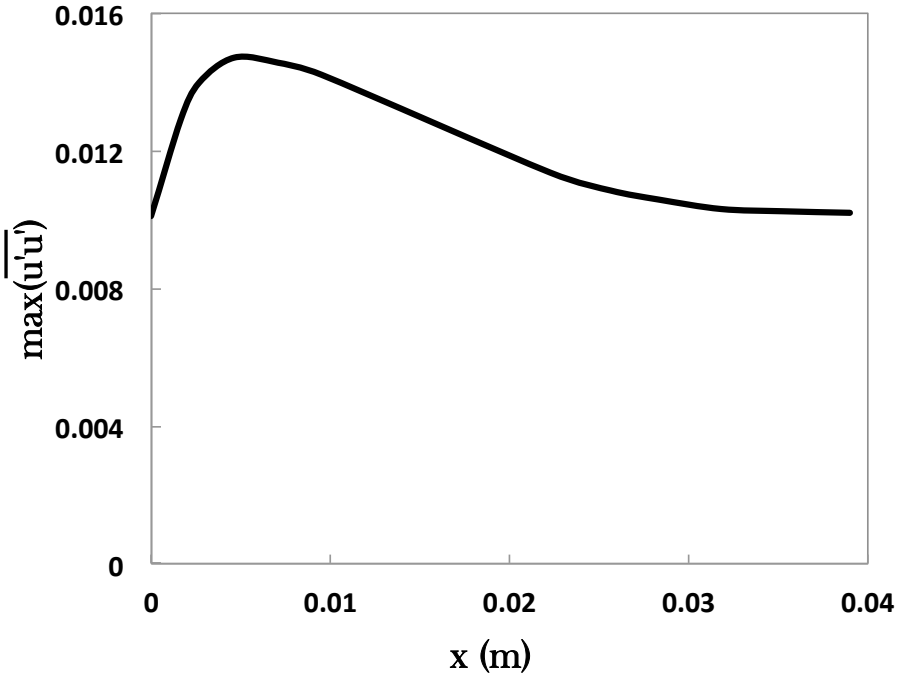

Figure 3.7: Plot of maximum time-averaged $u'u'$ against distance from SEM Plane

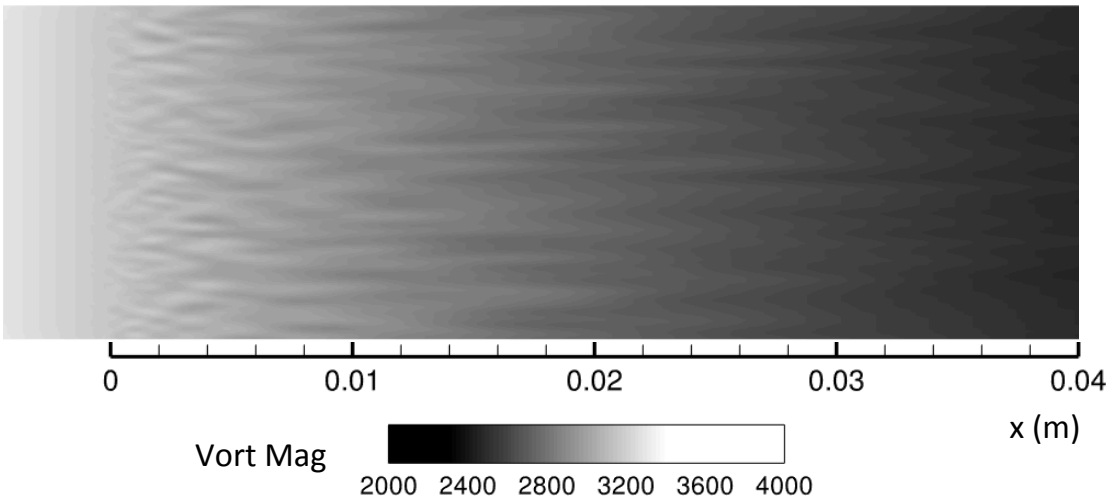

Figure 3.8: Case 1 - Contour of Instantaneous Vorticity Magnitude at $0.4mm$ from wall surface

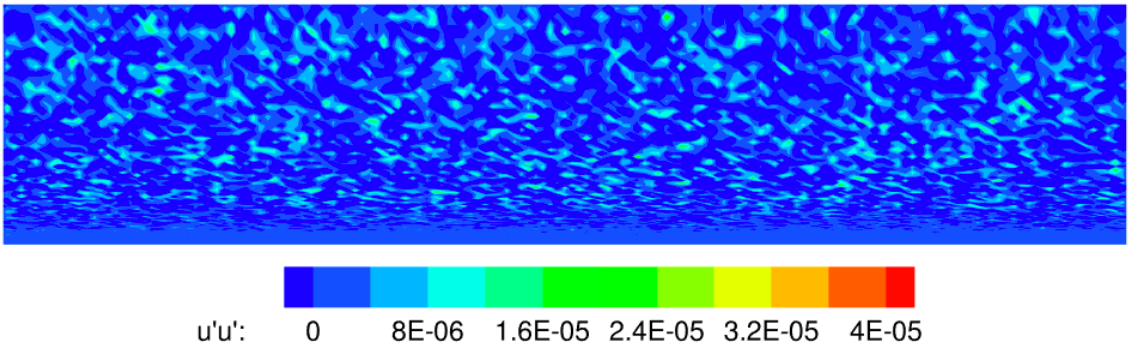

Figure 3.9: Case 2 - Contour of Mean $u'u'$ at the SEM initialisation plane

3.8 Closure

This chapter has detailed the numerical methodology used to obtain results for the aims and objectives set out in Chapter 2. The main aim of the work is to show the capability of an unsteady Navier-Stokes/Large Eddy Simulation (UNS/LES) to model the crossflow transition mechanism on swept wing aircraft. The required numerical methodology has to handle the complex transition process within a laminar boundary layer. This Chapter has explained how UNS/LES may be a suitable route to transition simulation with carefully selected parameters of the LES. In an LES the large scales are fully resolved on the numerical grid while the smaller small scales are modelled. The chapter began by explaining the strategy behind an UNS/LES calculation and the problems it has with modelling the wall and transition. The governing equations were introduced along with the filtering process used to derive the LES equations. For closure of the equations a sub-grid scale (SGS) model is required to model dissipation. SGS modelling is complex for transition as no full energy cascade exists in laminar and transitional regions to model dissipation.

The DELTA CFD code was used for this work and the technical details of the code were explained. The Wall Adapting Local Eddy Viscosity (WALE) was implemented into the DELTA CFD code as it has key properties required for transitional flows. It allows the sub-grid viscosity to reduce to zero in a laminar region and predicts the correct scaling of sub-grid viscosity in a turbulent boundary layer. A new boundary condition using the 'Synthetic Eddy Method (SEM)' was also implemented into the DELTA CFD code. This method will be used for generating free stream turbulence at a plane within the simulation. The method is a recent innovation in LES boundary conditions and literature has showed it to perform better than other alternatives.

Chapter 4

Simulation of Crossflow Vortices on a C16 Swept Wing

4.1 Introduction

The literature survey conducted in Chapter 3 concluded that simulation of transition using a Large Eddy Simulation (LES) approach has been limited. The reasons for this lack of previous work are mainly due to the computational expense required for wall-resolved disturbance tracking numerical simulations and the perceived limitations of sub-grid modelling of wall regions. The literature survey has also detailed how Direct Numerical Simulation (DNS) is playing a large role in developing an understanding of the flow physics associated with the breakdown of crossflow vortices. DNS however, is restricted to simulations at low Re_c using simple geometries due to the heavy computational cost in the transitional and turbulent regions, for example the recent studies by Wasserman & Kloker [121; 122] were run at Re_c = 100,000.

This chapter will use an alternative numerical approach that fully resolves the laminar and disturbance growth regions of the boundary layer while being able to convert smoothly to an LES approach in the turbulent regions. The hope with this methodology is to provide accurate results, comparable with a DNS solution, while running at a lower computational cost. Currently, LES is still used mainly as a research tool with a number of research papers conducting simulations at low Re_c. With increasing computational power, LES may in the near future, be a viable method for simulating much more complex geometries and flow conditions including laminar-turbulent transition on full wing geometries. Therefore this chapter aims to demonstrate this capability using existing experimental data.

The methodology chapter has explained how in LES the governing equations are low-pass filtered and only the relatively large scales (eddies of size larger than the grid cell size) are resolved while the smaller scales are modelled. The impact that this has on a transitional flow that incurs many complex stages was also considered. The main considerations can be summarised into two key points, described below:

1. In a laminar region there is no energy cascade for the SGS model to simulate dissipation of the small scales. The sub-grid scale model must be capable of discriminating a laminar region from a turbulent region and to reduce its contribution to zero in a laminar region so that only the fluid molecular viscosity is responsible for any damping of the stability growth.

2. The receptivity region, where external disturbances are filtered by the laminar boundary layer must be fully resolved to capture the initial amplitude of the disturbance. Therefore in the early phases of transition (receptivity and primary growth), particular consideration to grid refinement will be required. Once non-linear interactions begin to occur the grid spacing can be relaxed to allow a reduction in computational expense and the benefit of using a LES methodology can be quantified. This approach will be investigated in this chapter.

The Wall-Adapting Local Eddy Viscosity (WALE) sub-grid scale (SGS) model, described in detail in Chapter 4, was identified as a potential solution to the first key point to provide a more realistic sub-grid representation of the laminar/turbulent boundary layer regions. The model is based on the square of the velocity gradient tensor and has proven ability to reduce to zero in a laminar region. The potential for using LES with a WALE SGS model for crossflow transition has thus far not been researched and a validation study is required to demonstrate its capability. For this reason, an initial experimental test case was chosen that could investigate the resolution requirements and to quantify the capability of the WALE SGS model.

Results from an experiment carried out by Chernoray et al. *"Experiments on secondary instability of streamwise vortices in a swept wing boundary-layer"* [20] were chosen as the initial test case. The experiment lends itself to an LES approach as it was run at a relatively low $Re_c = 390,000$ while still large enough to be computationally difficult for a DNS simulation. The experimental results provide hot wire measurements for both stationary crossflow vortices and the initial laminar boundary layer, making it ideal for a numerical comparison.

The objectives for this numerical study were summarised into three main areas:

1. **Receptivity and Primary Instability** - The initial disturbance for the primary instability is varied to show crossflow vortices at different saturated amplitudes and growth rates. The results are compared to the experimental data. Disturbance generation methods are investigated (suction and roughness element) to show the ability of the method to model an initial amplitude associated with different disturbance types.

2. **Growth of secondary instability** - Natural secondary instabilities will be analysed for high initial disturbances to model the final stages of laminar-turbulent transition.

3. **Impact of varying the grid spacing** - The grid used to analyse the initial laminar base flow will be used as a coarse grid and a new, finer grid will be developed. From here the suitability and dependancy of the grids will be analysed.

This chapter is organised as follows:
Section 4.2 describes the experimental test case chosen to meet the objectives. The setup of the experiment and its initial purpose is described along with the measurement techniques used to obtain the experimental data.
Section 4.3 describes results of a preliminary study which aimed to assess the computational resources required and to assess the general flow behaviour in the chosen test case. From here techniques will be described that aimed to reduce the computational expense of the further simulations.
Section 4.4 describes the results from the undisturbed laminar base flow compared to the experiment.
Section 4.5 explains the disturbance devices used to generate the initial amplitude of the stationary crossflow vortices. Two different devices were used: a $1mm$ continuous suction hole and a $35mm$ span isolated roughness element.
Section 4.6 describes the results obtained from the continuous suction hole device and a comparison of the results against experimental data. Section 4.7 describes the results from the isolated roughness element device and a further comparison to the experiment. The sections will also explain the flow field in detail and the various stages of transition.
Section 4.7 will end the chapter with final conclusions and lessons learned for further study.

4.2 Experiment

The general setup of the experiment is shown in Figure 4.1. The aim of the experiment was to investigate the breakdown of crossflow vortices within a laminar boundary layer. They focused on obtaining results for the 'y' and 'z' high frequency secondary instability modes for various packets of stationary crossflow vortex modes. An explanation of high frequency secondary breakdown mechanisms was given in the Literature Review (Chapter 2).

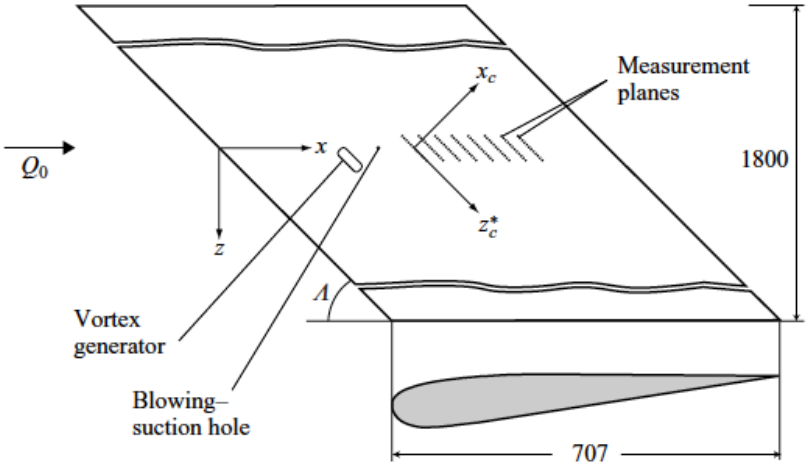

Figure 4.1: Chernoray et al. [20] C16 aerofoil & Experiment setup

All experimental runs were performed using a wind turbine aerofoil named C-16. The aerofoil was positioned at a sweep angle $\angle$ of 45° and with an onset velocity of $Q_0 = 8.2m/s$ giving a Re_c of $390,000$. The chord length 'c' of the configuration was $0.707m$ with a chord measured perpendicular to the wing leading edge of $0.5m$. The upper surface of the wing (aft of $0.4x/c$) is a flat surface allowing study of the flow without the presence of wall curvature effects. The wing was angled at 2° positive incidence relative to the upper flat surface and a sandpaper trip was placed close to the leading edge on the lower aerofoil surface to stabilise large-scale separation and to avoid associated global unsteadiness of the flow. Note that the incidence is not in reference to the mean chord line but the angle of the upper flat surface of the aerofoil, this was the angle given in the original paper.

Initially the experiment was run without external disturbance generation and a full three-dimensional laminar boundary layer was achieved. Following this stationary crossflow vortices were generated in the laminar boundary layer by roughness elements and by localized continuous suction. The perturbation of the boundary

layer was performed at 0.3 of the wing chord. Single and V-probe hot wire measurements were taken streamwise stations along the chord. These were measured from $0.4c$ to $0.75c$ in $0.05c$ intervals. Details on the experimental procedure as well as on the measurement equipment used can be found in Chernoray et al. [19], a summary of the tests conducted are detailed in Table . Note that the difference between A and B is strength of the forced secondary instabilities. The paper suggests an error of less than 0.5% for all points in the calibration range. The growth of the disturbances were captured in contour plots of mean streamwise velocity and the disturbance of the streamwise velocity to the laminar base flow at a station downstream of the initial disturbance for both disturbance generation methods. From here the experiment conducted natural secondary instabilities studies using an artificial disturbance generated using a suction/blowing hole to monitor the final stages of transition and breakdown to turbulence.

The aim of the present numerical study is to simulate the laminar boundary layer and the primary and secondary instability of the stationary crossflow vortices detailed in the experiment. The WALE model and standard Smagorinsky SGS models were used and the results of each compared. The following section details results from a preliminary study used to reduce the computational cost of the simulation.

Table 4.1: Experimental Test Summary

Case	Vortex Generator	Roughness Element
A	Left-hand side of roughness element	35 x 8 x 0.39
An	Left-hand side of roughness element	35 x 8 x 0.39
B	Right-hand side of roughness element	35 x 8 x 0.39
Ar	Circular roughness element	8 x 0.39
As	Suction	

4.3 Preliminary Study

The aim of the preliminary study is to study and analyse the flow over the full chord representing the setup used for the wind tunnel model described in the experiment. The results would then be used to assess the flow around the aerofoil and the influence of the lower surface on the upper surface flow where the measurements are taken. The wing is angled at negative incidence to the mean chord line, making it likely that separation could occur on the lower surface. This preliminary study will attempt to develop a method for reducing the size of the solution domain and reducing the impact of the lower surface, without impacting on the accuracy of the solution.

4.3.1 Initial Solution Domain

The initial solution domain for the computational model is shown in Figure 4.2.

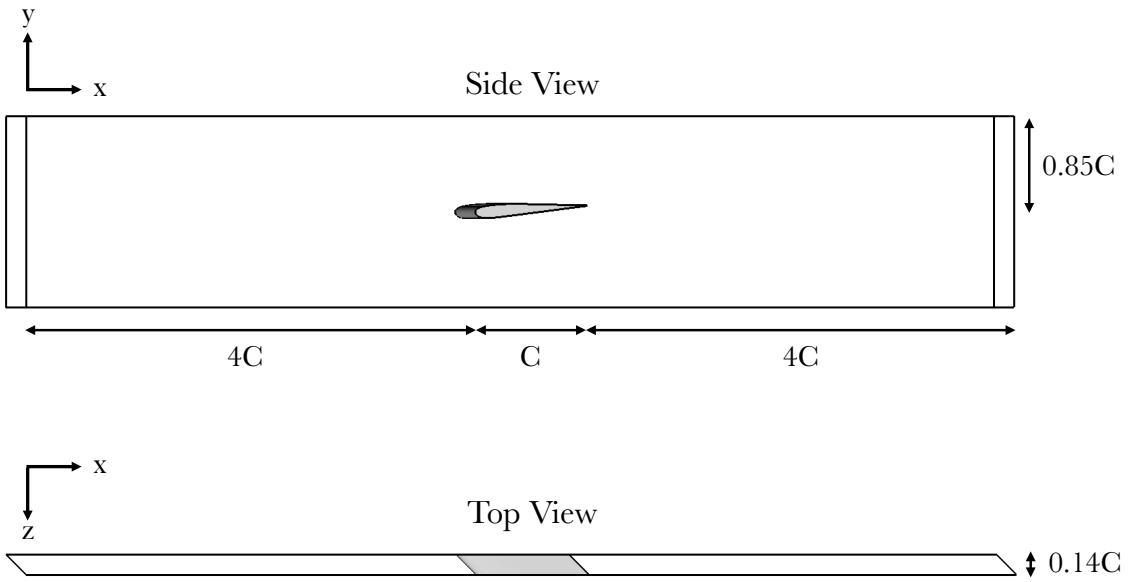

Figure 4.2: Initial Solution Domain

The x and y dimensions of the domain were kept the same as the wind tunnel used in the experiment at $9x/c$ in the streamwise direction and $1.7y/c$ in the transverse direction. The spanwise dimension is an important quantity for the simulation; a large enough segment is required so that the crossflow vortices and turbulent eddies within turbulent regions are not constrained. However a too large segment requires a much greater computational expense. To reduce the impact of the spanwise faces an infinite swept wing model was applied using a cyclic boundary condition on the

spanwise faces. This is achieved by linking the topology of each spanwise face from each block, allowing data to be passed from one side face back into the block on the opposite face.

The spanwise wavelength of the crossflow vortices measured in the experiment was $20mm$. A spanwise segment in the Z coordinate of $100mm$ $(0.14c)$, with the addition of 45° sweep gives a leading edge distance of $141mm$ allowing for greater than 7 wavelengths of the crossflow vortices within the spanwise domain. The impact of the spanwise dimension was investigated and increasing the span showed no further change to the results presented. The angle of attack was adjusted so that no laminar separation occurred on the upper surface, as was the process in the experiment. The final angle of the upper surface was $-1.8°$.

A slip wall boundary condition was used for the upper and lower bounds of the domain and simulations were initialised with an inlet velocity of $Q_0 = 8.2m/s$. A sandpaper trip was used near the leading edge of the lower surface in the experiment as it was expected to separate. Therefore a numerical trip was applied near the leading edge on the lower surface in the simulation to trip the boundary layer from laminar to turbulent and reduce the likelihood of separation and any associated global unsteadiness of the flow.

4.3.2 Initial Grid

The initial structured grid was developed using the blocking package within ICEM-CFD 14.0. The strategy used for the grid development was to employ a C grid around the aerofoil with slices in the C to refine the grid near to the wall. The C Grid was then extended towards the inlet. The final grid consisted of 160 blocks within the solution domain shown in Figure 4.2. Piomelli & Balaras [79] advise on the necessary grid requirements for resolving the wall in LES. They suggest grid spacing at the wall of $\Delta x+ < 100$, $\Delta y+ < 1$and $\Delta z+ < 20$ and the initial grid is close to meeting this metric. The grid consists of 700 nodes on each of the upper and lower surface of the aerofoil with 160 nodes in the wall normal direction. 140 nodes extend towards the outlet and the span contains 320 nodes. For the x-coordinate the leading edge $\Delta x+$=30 which is reduced to 20 at $x/c = 0.3$ where the suction hole was placed; the mesh is expanded at a rate of 1.05 to $\Delta x+ = 60$ towards the trailing edge. $\Delta y+ = 1.5$ at the wall with a slow wall normal expansion rate of 1.06, the z-spacing was kept uniform with a $\Delta z+ = 22$. The resulting grid consists of 76 million cells, the refinement near the wall can be visualised in Figure 4.3 and the block structure is shown

in Figure 4.4.

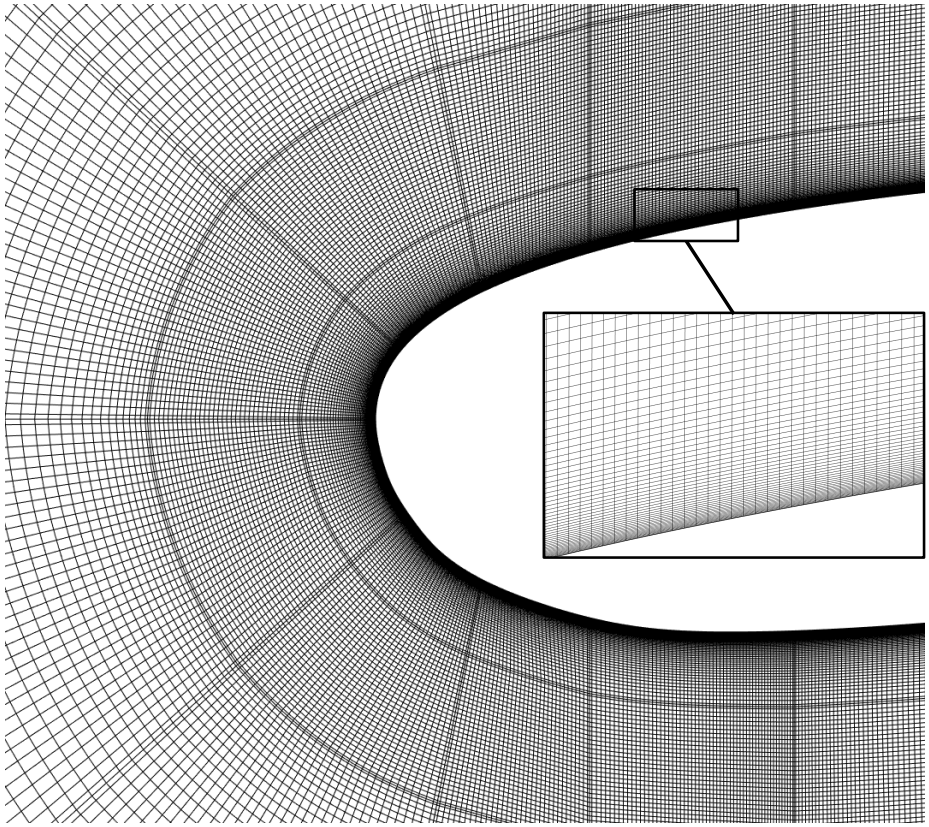

Figure 4.3: Initial Grid

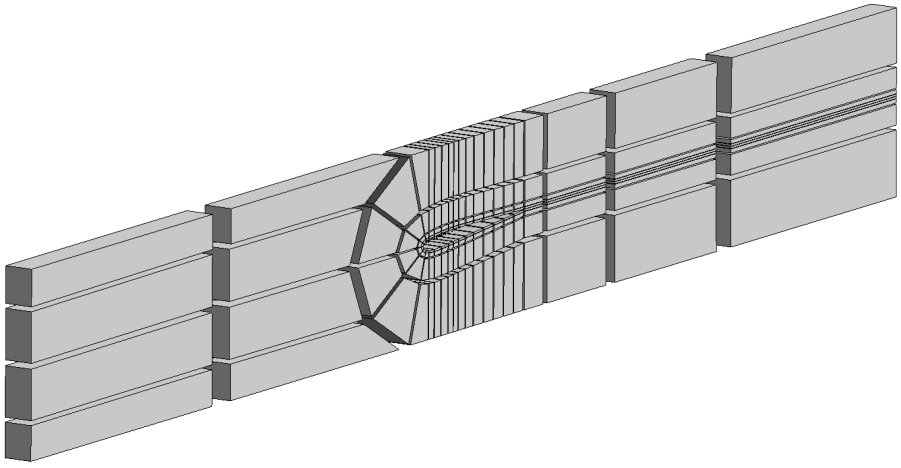

Figure 4.4: Initial Block Structure

4.3.3 Initial Results

The initial grid was run using a standard Smagorinsky sub-grid model with a Van Driest [115] exponential damping function. The Smagorinsky constant C_s was set at 0.1 as suggested by Deardoff (1970) [22] for wall-bounded flows. The flow times were non-dimensionalised using a 'flow through time' determined using the chord length c and free stream velocity Q_0. This resulted in a physical flow through time of $0.0862s$. The solver was run until 10 non-dimensional flow through times had elapsed to allow the flow to develop; subsequently statistical averages were gathered by sampling to generate a time-averaged solution of 5 flow through times. The non-dimensional time step was chosen as 1.0×10^{-03} for the initial grid with 5 inner time step iterations.

Figure 4.5 shows mean streamwise velocity at mid-span and Figure 4.6 shows an instantaneous plot of vorticity magnitude. The aerofoil upper surface shows clearly a thin laminar boundary layer extending across the full length of the chord. The location of the numerical trip on the leading edge of the lower surface is identified in Figure 4.6. The trip triggers early breakdown to turbulence and the development of a fully turbulent boundary layer.

Figure 4.7 shows mean pressure coefficient around the wing at mid-span. The experiment assumes that the sandpaper trip applied would reduce the global unsteadiness of the flow and reduce the impact on the upper surface. For the simulation it is not ideal to fully resolve the lower surface turbulence boundary layer as the experimental measurements were taken only in the laminar boundary of the upper surface. Resolving the lower surface will increase the computational expense of the calculation and requires a numerical trip to ensure the flow does not separate and impact the results of the upper surface.

For this reason a method of removing the need to resolve the lower surface was developed by extracting the upper surface and streamlines dividing the upper and lower surfaces, this method is described in the next sub section.

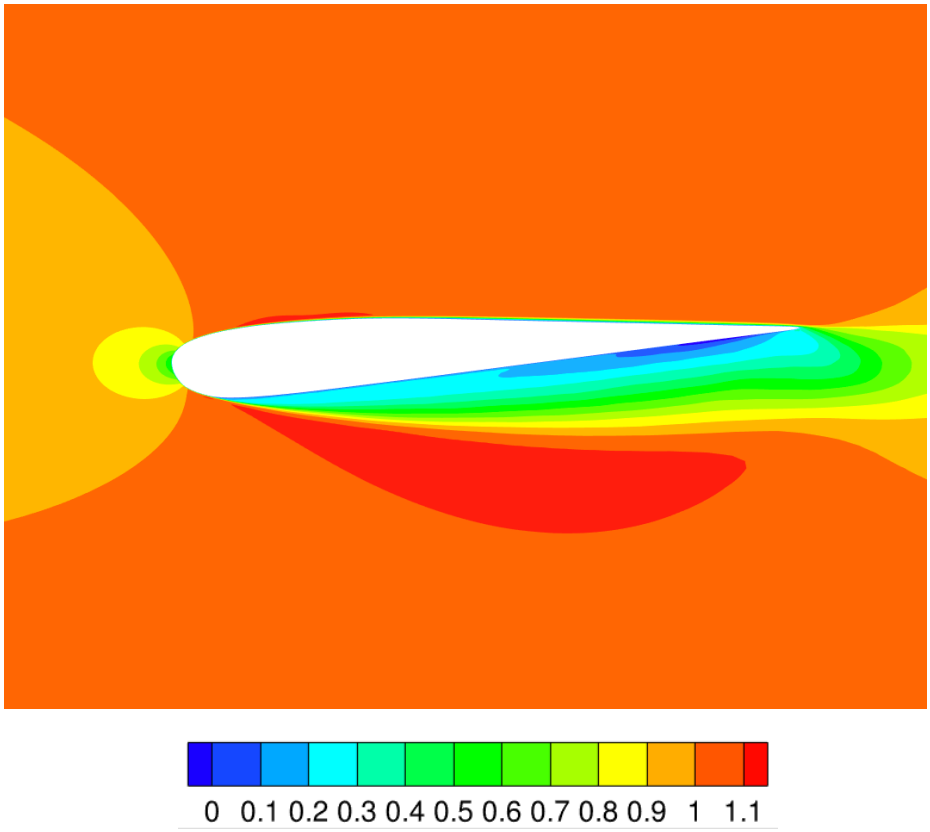

Figure 4.5: Mean U/Q_o at 50% Span

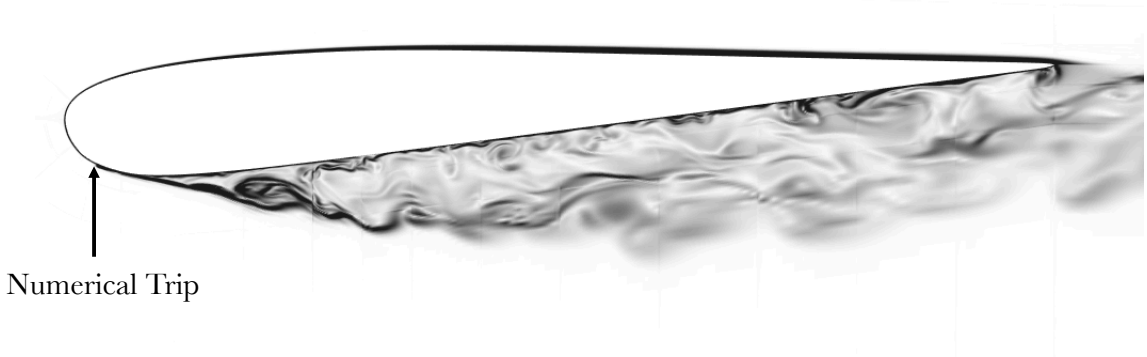

Figure 4.6: Instantaneous Vorticity Magnitude at 50% Span, Scale: White - 0 Black - 100 s^{-1} (Note: Discontinuous lines at block boundaries are due to a post processing artefact)

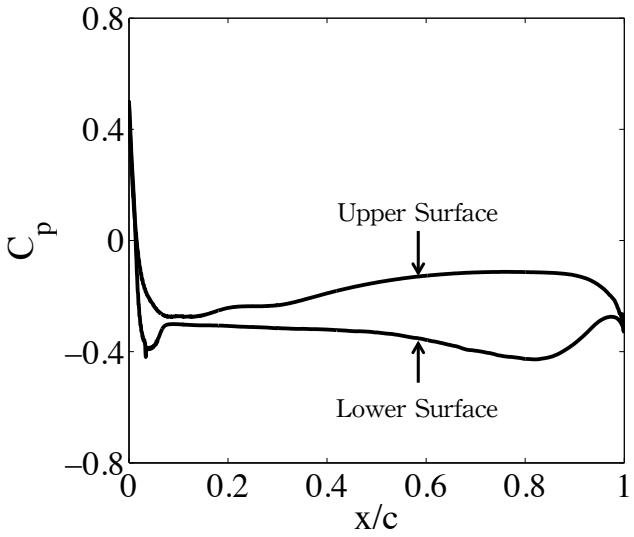

Figure 4.7: Initial Grid Simulation Pressure Coefficient

4.3.4 Streamline Extraction

To reduce the overall computational expense of the simulations a method was devised only to simulate the upper surface laminar boundary layer. To achieve this a streamline extraction process was developed that involved exporting from the steady, time-averaged solution the stagnation streamline upstream of the leading edge and aft of the trailing edge. These were averaged across the span and converted (together with the geometry of the upper aerofoil surface) into a plane which defined the inner boundary of a new solution domain. The upper, inlet and downstream boundaries remained the same as the initial (full C-16) solution domain. Figure 4.8 shows the extracted streamlines from the initial grid and the conversion into the final streamline solution domain. Note, it can reasonably be expected that the onset flow stagnation streamline will not fluctuate in time. However, downstream of the trailing edge the flow will almost certainly be unsteady, and this effect is absent in the streamline solution domain since the mean streamline is used. However this is expected to only affect the simulation near the rear of the upper surface and the behaviour of the crossflow vortex packet will not be unduly influenced.

The upper half of the initial grid was placed upon the streamline solution domain, reducing the overall cell count by a half. The streamline geometry grid subsequently consisted of 80 blocks with 38million cells. The streamline geometry was then run with a slip wall boundary condition placed on the streamline surfaces. To examine whether the streamline geometry results were equal to those from the full geometry, results of pressure coefficient, laminar boundary layer profiles and wall shear stress are compared, shown in Figure 4.9.

The comparison shows that the upper surface velocity profiles for the streamline extracted domain lie nearly exactly upon the full grid solution in the profiles shown, which is the area of interest. The pressures aft of $0.8x/c$ differ in the streamline geometry from the initial geometry case due to the impact of the lower surface and the absence of a trailing edge. A small variation can also be shown for the skin friction coefficient figure. It was decided that the discrepancy between the initial geometry and the streamline geometry is small enough to use the streamline grid for further analysis, especially as the results are nearly identical in the region of interest $0.3 - 0.7x/c$. The benefit of simplification of the geometry and overall reduction in computational cost outweigh the small discrepancies in accuracy. Also the saving in computational expense can be used to increase the resolution of the laminar-turbulent transition region.

(a) Span averaged extracted Initial Grid Streamlines

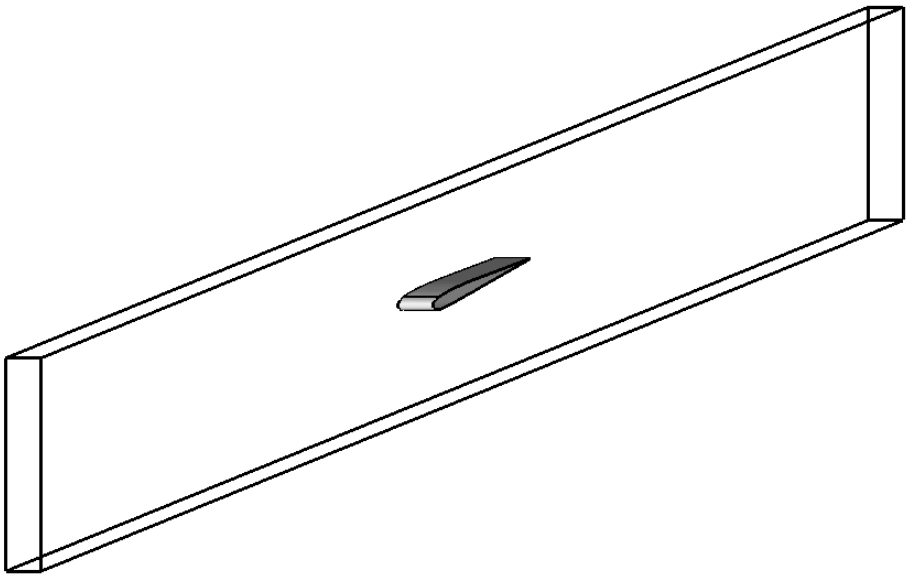

(b) Initial Solution Domain

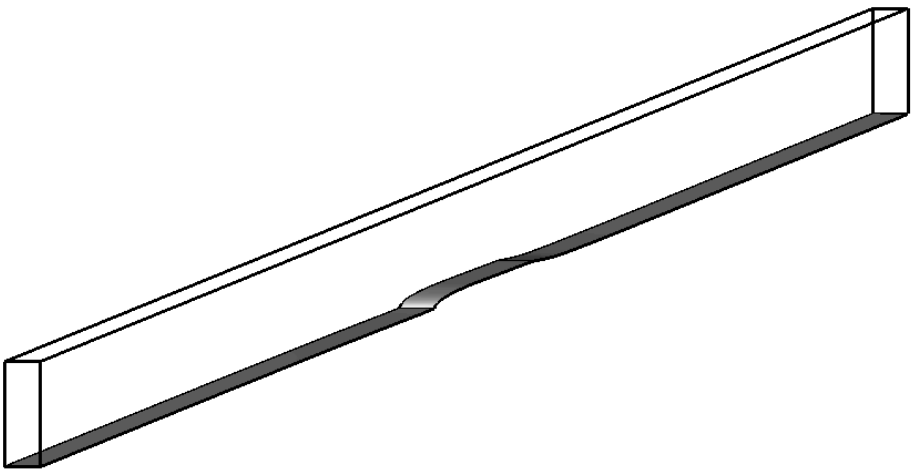

(c) Streamline Solution Domain

Figure 4.8: Streamline Extraction

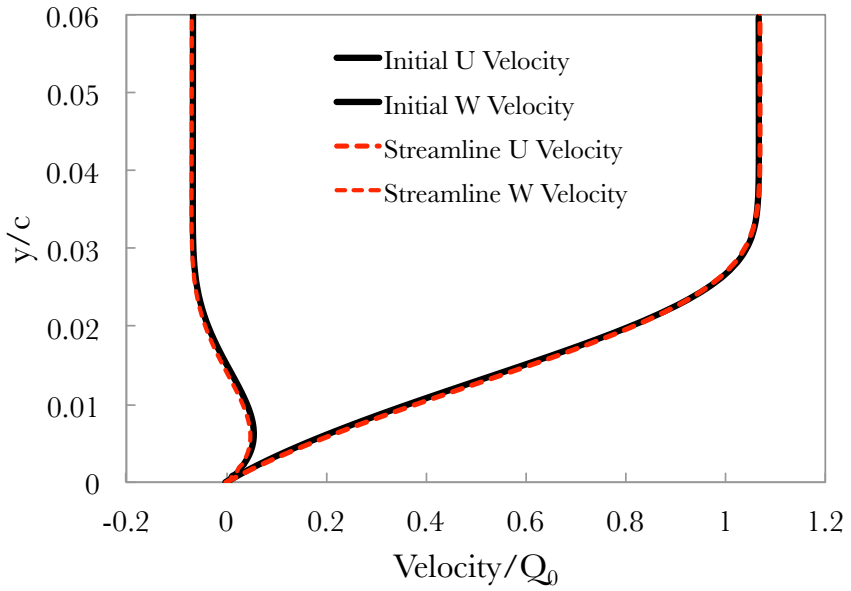

(a) Velocity profiles for Initial & Streamline solution domain at $0.5x/c$ (Red dashed =

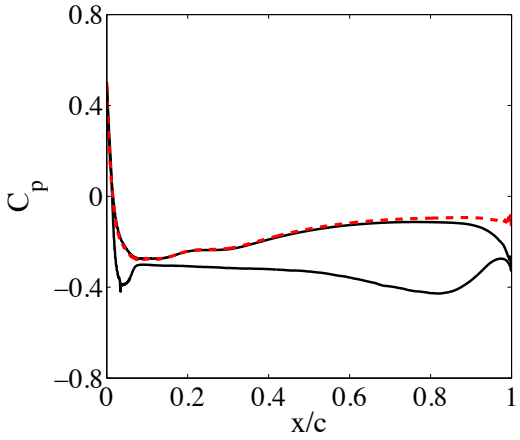

(b) Pressure Coefficent

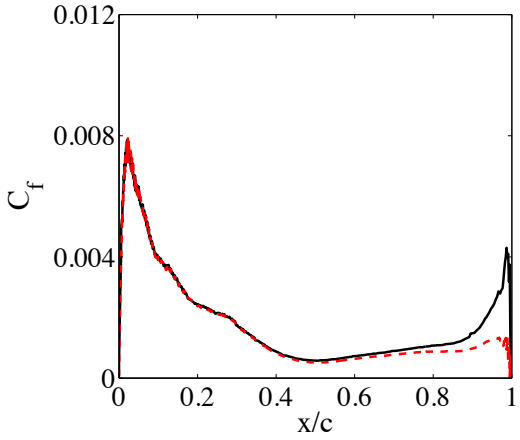

(c) Skin Friction Coefficent

Figure 4.9: Comparison of Initial & Streamline Geometry, Red - Streamline, Black - Initial

4.4 Laminar Base Flow

With the solution domain reduced by half due to the streamline extraction process the computational resources were be focused only upon the upper surface and in the region where the crossflow vortices are generated. This sub-section details the laminar boundary layer on the upper surface and comparisons are made with results taken from the experimental data. Simulation results are obtained for the laminar velocity profiles using the initial streamline extracted grid and both SGS models: a) Standard Smagorinksy and b) WALE model. The impact of the sub-grid scale model is key to successfully capture of the correct velocity profiles in the laminar boundary layer. As a laminar boundary layer requires no sub-grid scale viscosity the expectation is that the models should to effectively turn themselves off.

The simulation laminar boundary layer profiles in the streamwise (u) and spanwise (w) (eye of streamline) direction using the WALE SGS model are shown in Figure 4.10. With no artificial disturbance excited a 3-dimensional laminar boundary layer is formed with an initial accelerated region followed by an area of deceleration. The boundary layer profiles are shown at a series of downstream stations and the spanwise velocity component becomes s-shaped between $0.3 - 0.4x/c$. Aft of $0.4x/c$ the profiles can be shown to be self similar. Chernoray et al.[20] reported measured velocity profiles at $0.3x/c$.

Figure 4.11 shows comparison of the simulated laminar boundary layer results to the experimental results. Figure 4.11(a) shows the experimental profile at $x/c = 0.3$ and compared to the simulation. The figure shows simulated velocity profiles using the standard Smagorinsky model and WALE model. The results show that the Smagorinsky model over-predicts the boundary layer thickness by 15% while the WALE model produces a profile nearly identical to the experimental points. An explanation for this can be obtained by looking at Figure 4.12 which shows the ratio of molecular viscosity to SGS viscosity against distance to the wall at $0.3x/c$ for the standard Smagorinsky and WALE model. The Smagorinsky model produces a large amount of SGS viscosity near the wall, reducing the effective local Reynolds number which in turn increases the boundary layer thickness. The WALE model however produces a near zero eddy viscosity near to the wall, essentially becoming a real laminar flow. The standard Smagorinsky model consistently over-predicts the boundary layer thickness across the chord due to the model formulation producing an eddy viscosity at velocity gradients. For this reason the WALE model is used for all further calculations and for the crossflow vortex cases.

Figure 4.11(b) compares experimental streamwise & spanwise velocities (line of flight: aligned with the global x and y coordinate system) at a line $0.014x/c$ above the aerofoil with the WALE SGS model results. The results show a good agreement to the the experimental data which implies the pressure gradient distribution over the aerofoil is correct. Figure 4.11(c) shows a comparison of the momentum thickness (θ) from the experimental results with the simulation. The results of the simulation using the WALE model lie very close to the experimental points. From these comparisons the laminar boundary layer simulated are extremely well matched to the experimental data.

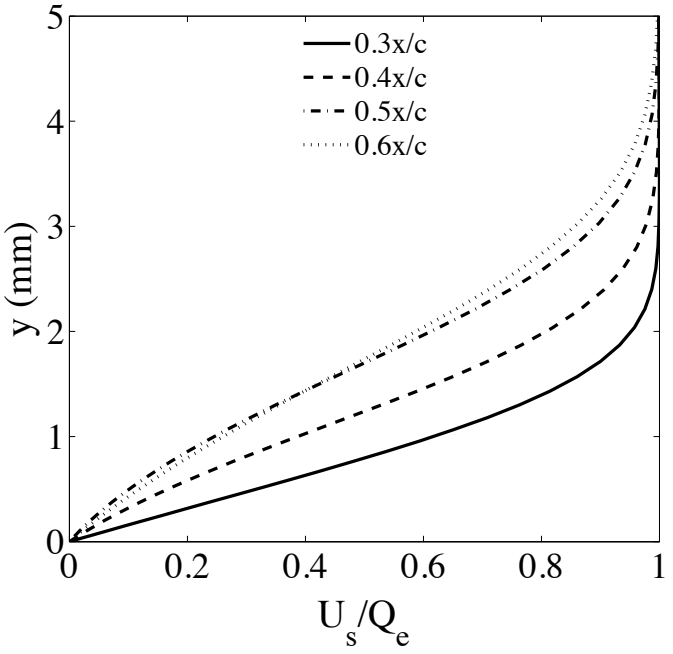

(a) U (Streamwise) Velocity

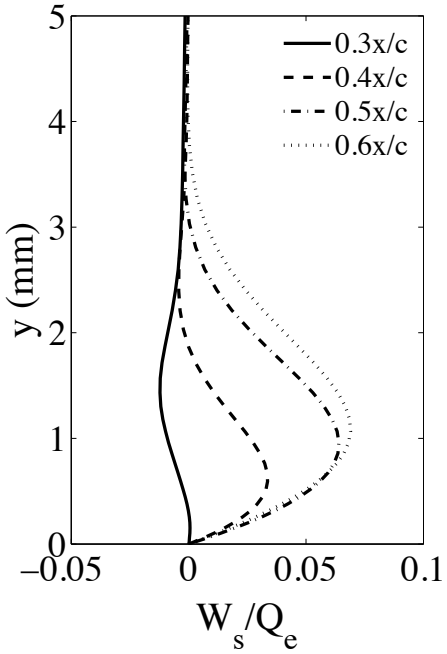

(b) W (Spanwise) Velocity

Figure 4.10: Boundary Layer Velocity Profiles at $0.1, 0.2, 0.4, 0.6 x/c$

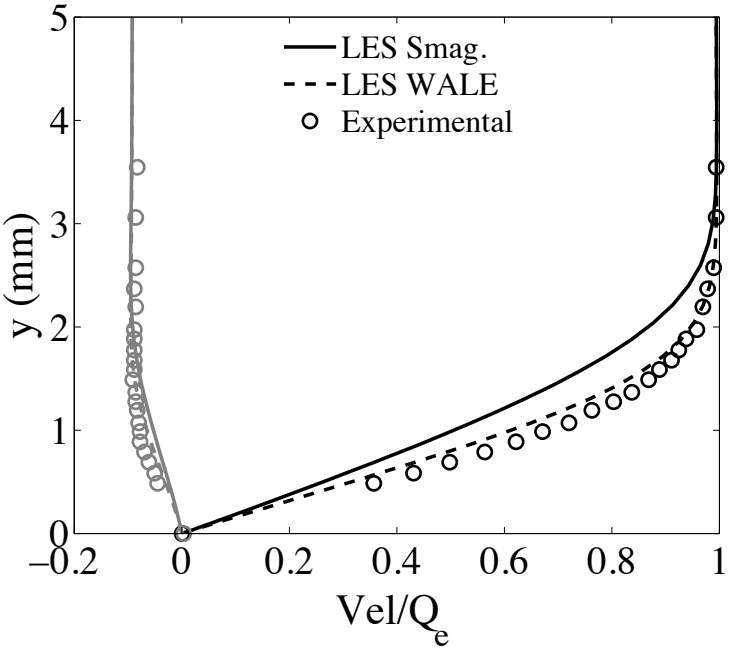

(a) Laminar boundary layer profile at $0.3x/c$ (U and W Velocity are line of flight)

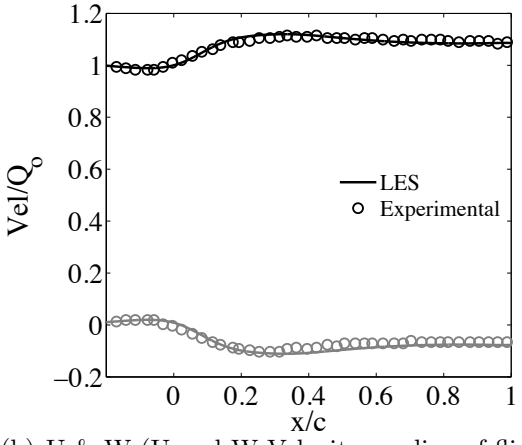

(b) U & W (U and W Velocity are line of flight) Velocity at 1cm above aerofoil

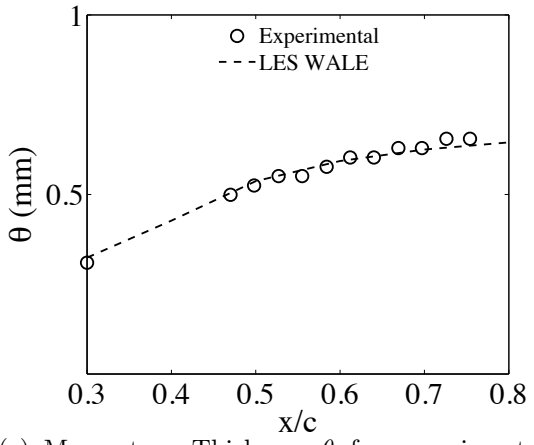

(c) Momentum Thickness θ for experiment & UNS/LES

Figure 4.11: Analysis of laminar base flow & comparison to experimental data

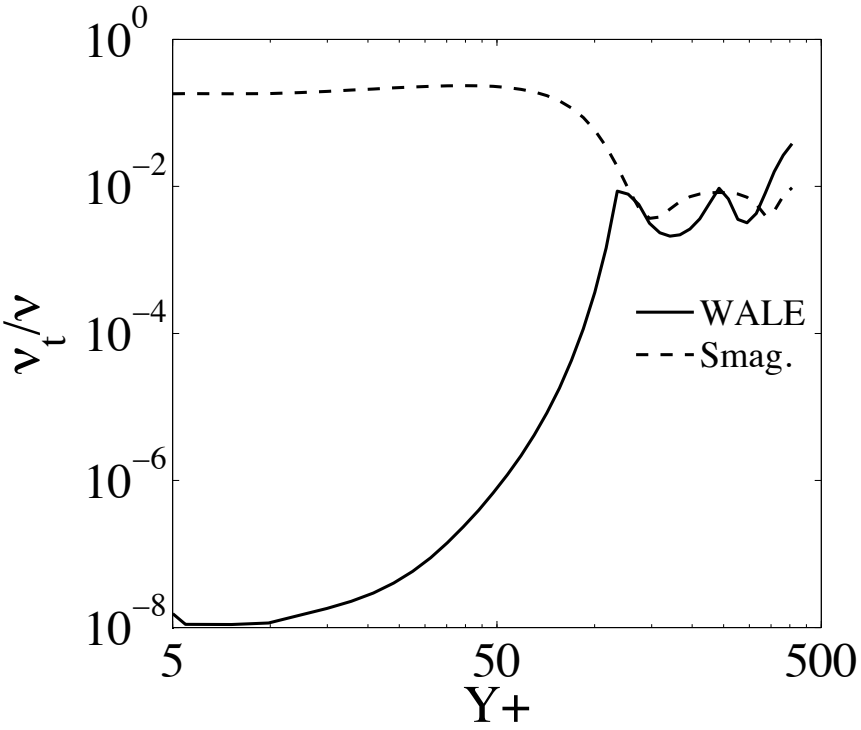

Figure 4.12: Ratio of eddy-viscosity ν_t to molecular viscosity ν against wall distance $(y+)$ at $0.3x/c$

4.5 Generation of Crossflow Vortices

The primary instability for crossflow vortices on swept-wing boundary layers can be controlled and generated from a variety of devices including isolated roughness elements, roughness arrays and suction holes. The following section details the results for two receptivity methods: continuous suction hole and a roughness element.

4.5.1 Grids

Two grids were used for this numerical study: the streamline grid used for the analysis of the laminar base flow was used as the baseline grid and a finer grid developed to capture the disturbances. Figure 4.13 shows the streamline solution domain that was used for this section for both grids.

Table 4.2 summarises the grid spacing for both the baseline and fine grid. The finer grid has an increased cell count in all 3 coordinate directions. The number of cells in the wall normal direction within the boundary layer was increased from 50 to 70. The spanwise node count was also increased from 320 to 500 cells allowing a

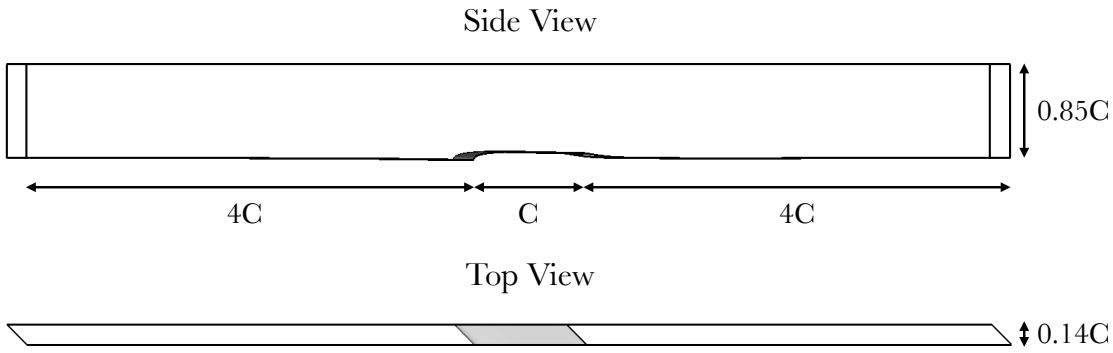

Figure 4.13: Streamline extracted geometry

$\Delta z+$=10 for the fine grid. The streamwise spacing was also increased with particular refinement at $x/c = 0.3$. The initial disturbances are generated at this location and it was crucial to capture the initial amplitude of the disturbance. Figure 4.14 shows the grid spacing at the spanwise station $z = 0$, the figure shows the added refinement at the $x/c = 0.3$ location.

Results from the continuous suction hole disturbance are used to compare predictions from both grids and an assessment was made as to the grid resolution requirement required to capture both the initial disturbance and tracking of its amplitude growth.

Table 4.2: Grid Diagnostics

	Initial Grid	Fine Grid
Block Count	76	170
Aerofoil Nodes	700	1100
Wall Normal Boundary Layer Nodes	50	70
Spanwise Nodes	320	500
Leading Edge, $\Delta x+$	30	20
$0.3x/c, \Delta x+$	20	10
Trailing Edge, $\Delta x+$	60	35
$\Delta y+$	1.5	1.0
$\Delta z+$	20	12
Total Mesh Size	38mil	125 mil

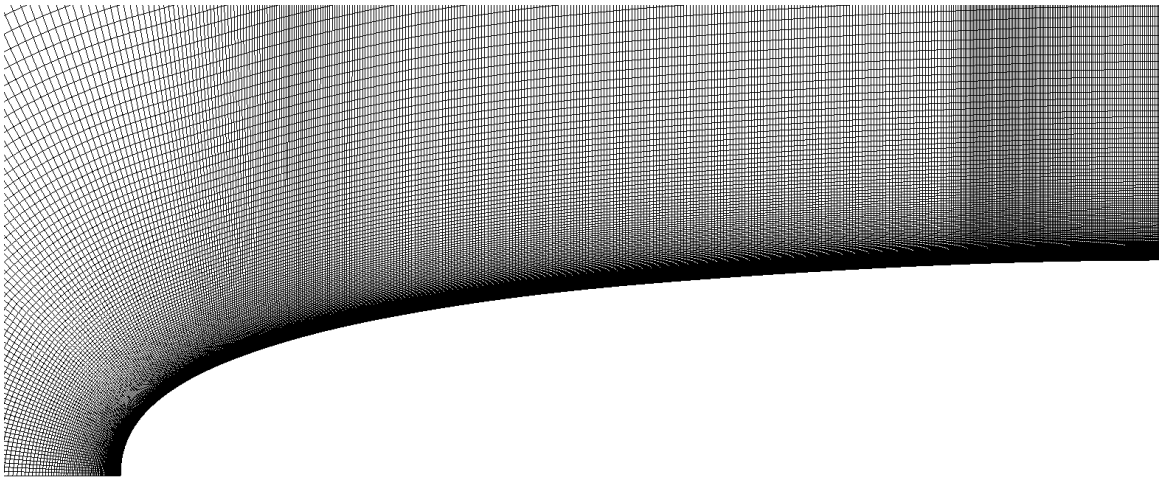

Figure 4.14: Fine Grid, cross section across 50% of span

4.5.2 Disturbance Generation

Chernoray et al. [20] generated the primary instability of the crossflow vortex modes using two methods: a continuous suction hole and a roughness element. Both disturbance generation methods were placed at $0.3x/c$, upstream of the location of pressure gradient changeover from favourable to adverse.

For the continuous suction case the suction hole diameter was $0.00141x/c$ $(1mm)$ with a variable suction rate. The shape of the suction hole was not identified in the experimental procedure. A square 1x1mm suction hole was used for this study to allow simplification of mesh generation. The suction hole boundary condition was a fixed and uniform velocity, and results were obtained using several suction rates. The suction rate was quantified in terms of C_q, see Equation 4.1.

$$C_q = \frac{Q_s}{Q_0} \tag{4.1}$$

Where Q_s is the suction hole velocity in m/s and Q_0 is the freestream velocity. For this study the values of C_q used were: $0.1, 0.15, 0.25, 0.5, 1$.

The roughness element used in the experiment had dimensions of $35mm$ span, $8mm$ width and $0.39mm$ in height. The simulation results use the same dimensions for the roughness element as is shown in Figure 4.15. In terms of Reynolds number the roughness element has Reynolds number based on k=roughness height and free stream velocity of $Re_k = 305$.

The results presented in this chapter are described in a transformed local axis (x^*, y^*, z^*). The origin $(0, 0, 0)$ of the transformed axis for the continuous suction

case is at the point of the suction hole and for the roughness element is placed at centre of the roughness element. The (x^*, y^*, z^*) axis remains aligned with the global (x, y, z) axis.

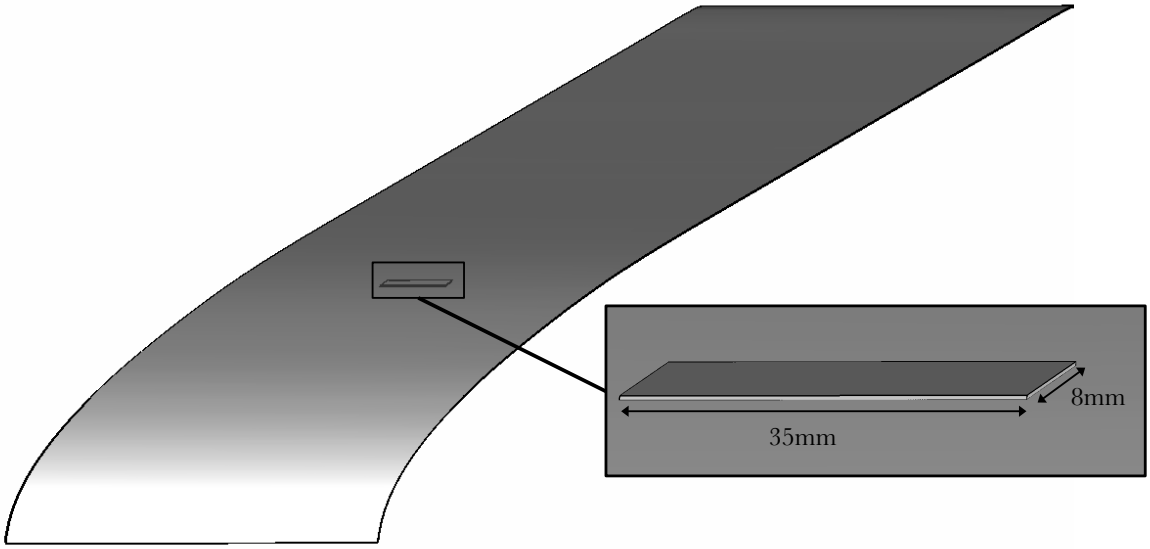

Figure 4.15: Geometry of roughness element

4.6 Continuous Suction Disturbance Results

4.6.1 Flow Field - Primary Growth

The simulation results aimed to replicate the experimental procedure and achieve similar results, the suction rate was adjusted until the crossflow vortices were of similar amplitude to that of the experiment. This section describes results using a suction rate $C_q = 0.1, 0.15, 0.25, 0.5, 1$.

The impact that the suction hole has on the flow in the boundary layer is much like a roughness element, causing a strong spanwise (w) velocity component leading to vortices of opposite rotation either side of the suction hole. An example of this is shown in Figure 4.16 with streaklines showing the generation of the crossflow disturbance either side of the suction hole. The figure also shows the development of the primary instability of the crossflow vortices with strong positive and negative W velocity either side of the suction hole. This disturbance amplifies downstream aft of the boundary layer neutral point and Figure 4.17 shows contours of mean streamwise (U) velocity with superimposed crossflow velocity vectors at $x^*/c = 0.28$ for the same suction rate. The velocity vectors show the formation of the crossflow vortices, the disturbance for this case grew to a substantial level at $x^*/c = 0.28$ due to the high initial disturbance amplitude. The vectors show the core of the vortex at $15mm$ left of the suction hole. The vectors clearly show the upwash and downwash effect of the crossflow vortex packet. At $z = -12mm$ the vectors show an upwash of the low-momentum fluid, rising further away from the wall. At $z = -5mm$ the figure shows the velocity vectors pushed downwards and the high-momentum fluid moving lower in the boundary layer.

Figures 4.18 and 4.19 show slices of mean streamwise (U) velocity at $0.1, 0.2, 0.3$ and 0.4 x^*/c. Figure 4.18 shows the slices for $C_q = 0.1$ and Figures 4.19 shows the slices for $C_q = 0.5$. The figures show how the disturbance develops downstream of the suction hole and the disturbance grows to a much larger amplitude for the larger suction rate. The suction hole disturbs the streamwise velocity and a packet (a number of crossflow vortices with different wavelengths) of crossflow vortices can be shown to develop. The crossflow mode that develops on the left hand side of the suction hole amplifies greater than that of the right hand side. The cause of the disparity between the left and right modes can be related to the rotation of the mode. The rotation of the crossflow mode on the left hand side of the suction hole is positive (clockwise for a positive base crossflow) while the mode on the right is

negative (anti-clockwise for a positive base crossflow). The positive rotation amplifies the disturbance and was shown in Chernoray et al. [20] to develop a secondary breakdown mechanism much earlier than the right hand side.

The initial suction rate can be related to the disturbance amplitude by analysing the U velocity (streamwise) contour above the suction hole. Figure 4.20 shows contours of U velocity above the centre of the suction hole for $C_q = 0.10, 0.15, 0.25$ and 0.50. The strong primary instability can be shown in the figures to be deep within the low momentum fluid in the boundary layer, below $0.5mm$. To calculate the initial amplitude a $10mm$ wide segment is used that captures the region that is disturbed by the suction hole, the segment used is highlighted in the figures. Individual velocity profiles are taken within this region and the disturbance profiles are calculated by taking away the initial undisturbed laminar base flow velocity profile. The disturbance velocity profiles are shown in Figure 4.28 for $C_q = 0.10, 0.15, 0.25$ and 0.50. The profiles show S-shaped disturbed profiles with the $C_q = 0.5$ case showing extremely large disturbance amplitudes in the profiles nearest to the suction hole. These profiles can then be assessed to give a stationary mode shape by taking the root mean square as detailed in Equation 4.2.

$$A = rms[(U - U_{lam})/U_e] \tag{4.2}$$

Where U is the streamwise velocity for the disturbed case, U_{lam} is the stream wise velocity for the undisturbed case and U_e is the boundary layer edge streamwise velocity. The disturbance rms for each suction rate is shown in Figure 4.22. The plot shows a spike in the disturbance between $0-0.1mm$ above the wing surface due to the suction at the wall. The suction imparts a disturbance up until 2.5mm above the wing surface until the edge of the boundary layer. The maximum amplitude of the rms is plotted against the suction rate C_q in Figure 4.23. The figure shows that at suction rates lower than $C_q = 0.5$ the amplitude increases with the suction rate. For suction rates $C_q = 0.5$ & 1.0 the initial amplitude becomes greater than 0.1 and the disturbance amplitude increases less with increasing suction rate. Also the $C_q = 0.5$ & 1.0 cases are the only cases that breakdown to turbulence due to their extremely high initial amplitude. The next section identifies the breakdown region in more detail.

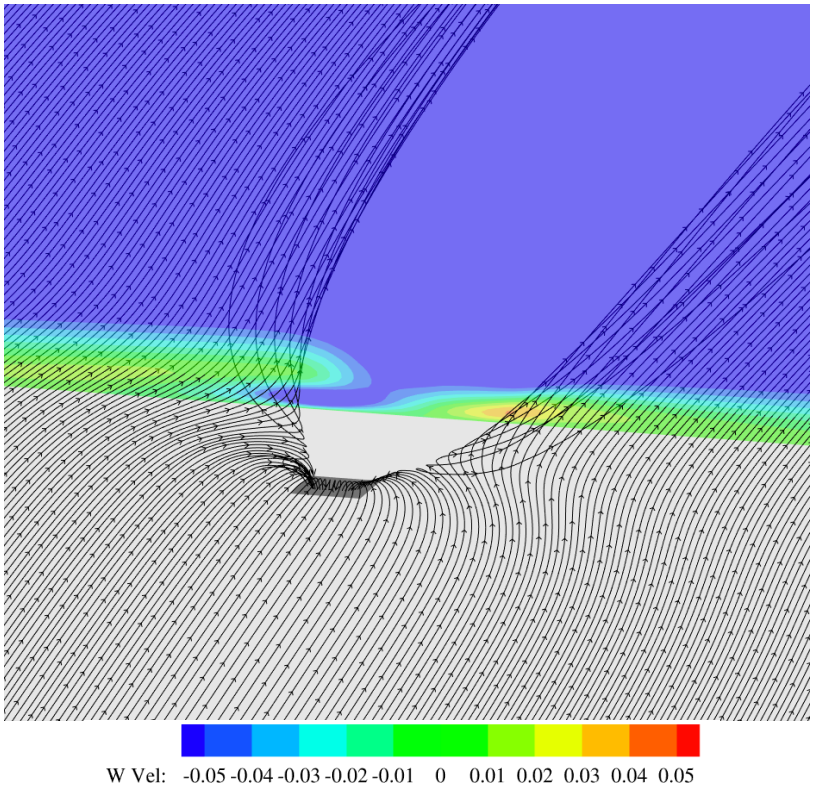

Figure 4.16: Streamlines over continuous suction hole and contour of W (Spanwise) Velocity $0.004x/c$ downstream of continuous suction hole with $C_q = 0.5$ (Fine Grid)

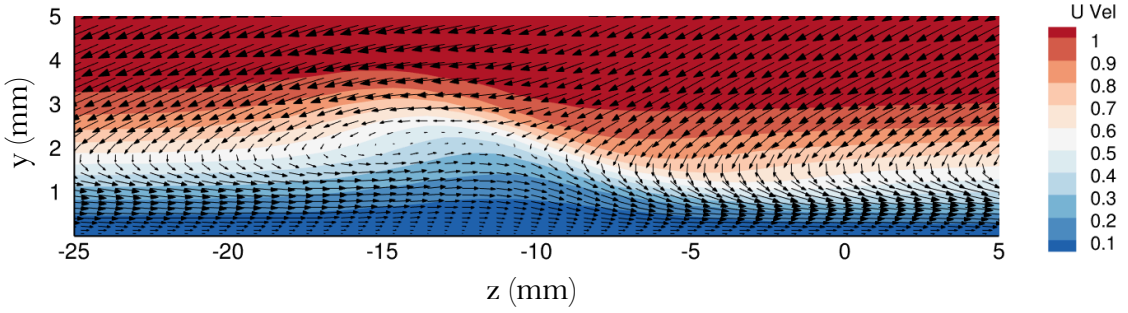

Figure 4.17: Crossflow velocity vectors and contour of U (streamwise) Velocity at $x^*/c = 0.28$, $C_q = 0.5$ (Fine Grid)

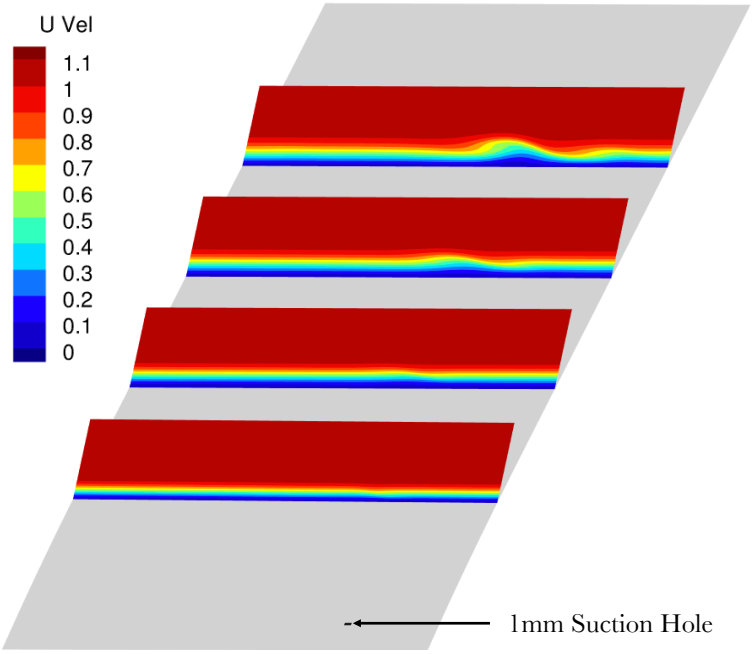

Figure 4.18: Mean contours of U (streamwise) Velocity aft of continuous suction hole, $C_q = 0.1$, Stations $x^*/c = 0.1, 0.2, 0.3, 0.4$ (Fine Grid)

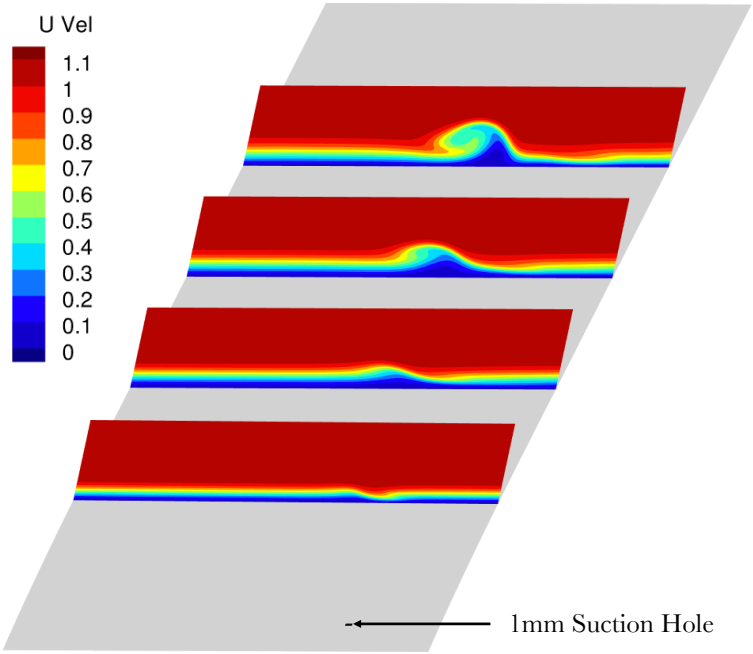

Figure 4.19: Mean contours of U (streamwise) Velocity aft of continuous suction hole, $C_q = 0.5$, Stations $x^*/c = 0.1, 0.2, 0.3, 0.4$ (Fine Grid)

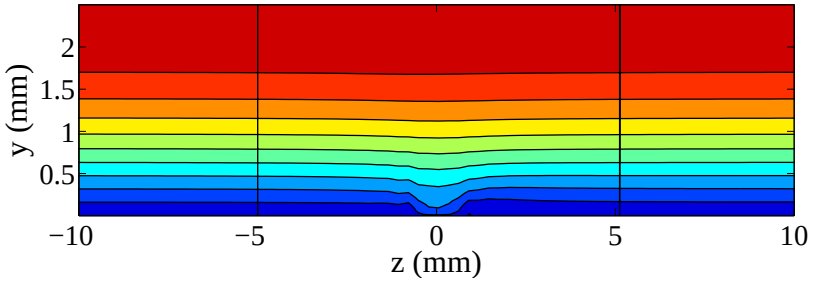

(a) $C_q = 0.10$

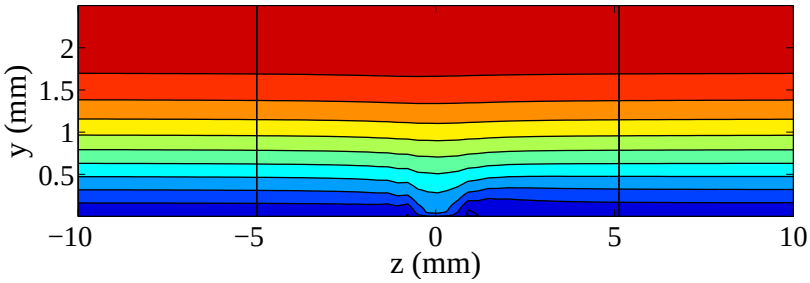

(b) C_q - 0.15

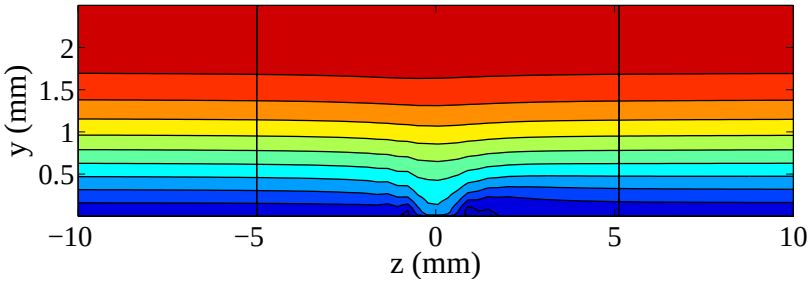

(c) C_q - 0.25

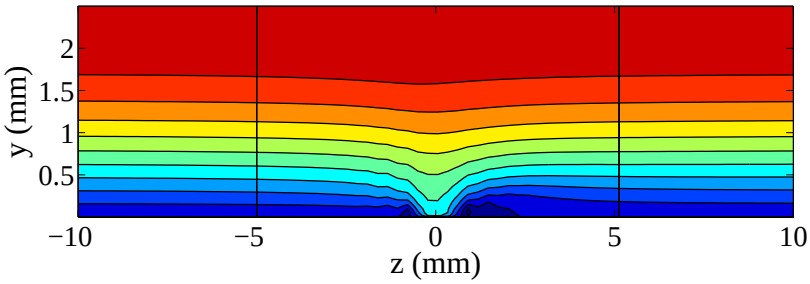

(d) C_q - 0.50

Figure 4.20: Contours of streamwise velocity U over continuous suction hole with C_q = 0.10, 0.15, 0.25 and 0.50 (Contour lines from 0.1,0.2,...,0.9 Q_e) (Fine Grid)

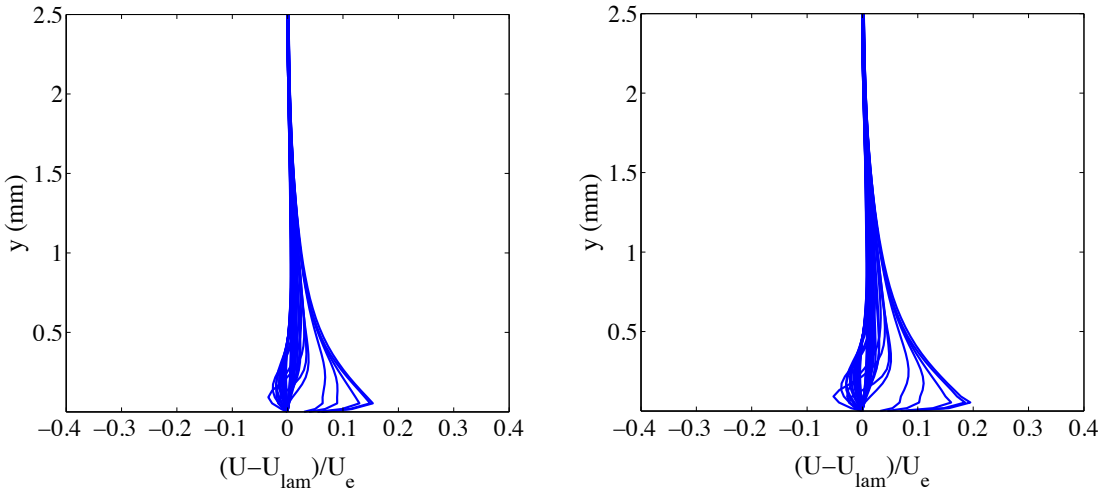

(a) $C_q = 0.10$ (b) C_q - 0.15

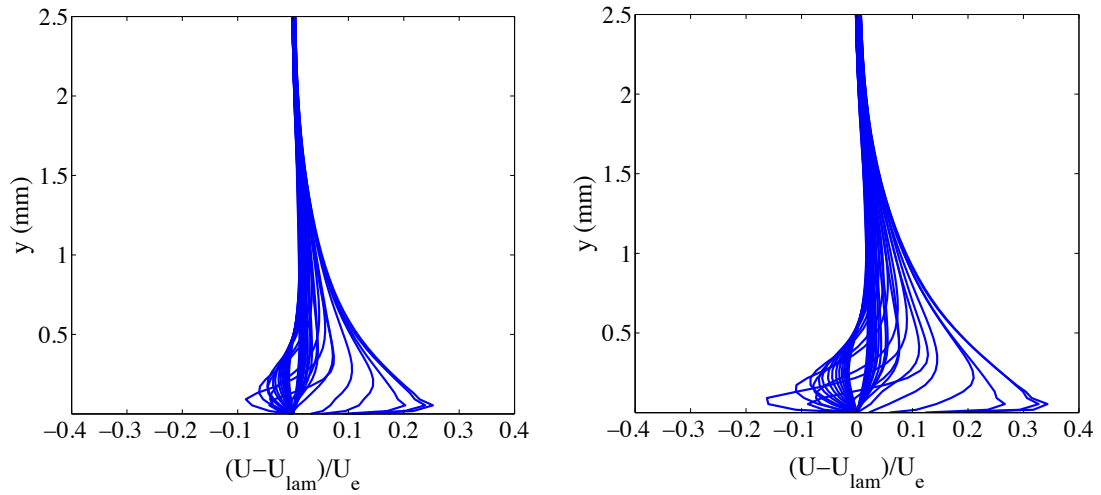

(c) C_q - 0.25 (d) C_q - 0.50

Figure 4.21: Disturbance velocity profiles for $C_q = 0.10, 0.15, 0.25$ and 0.50

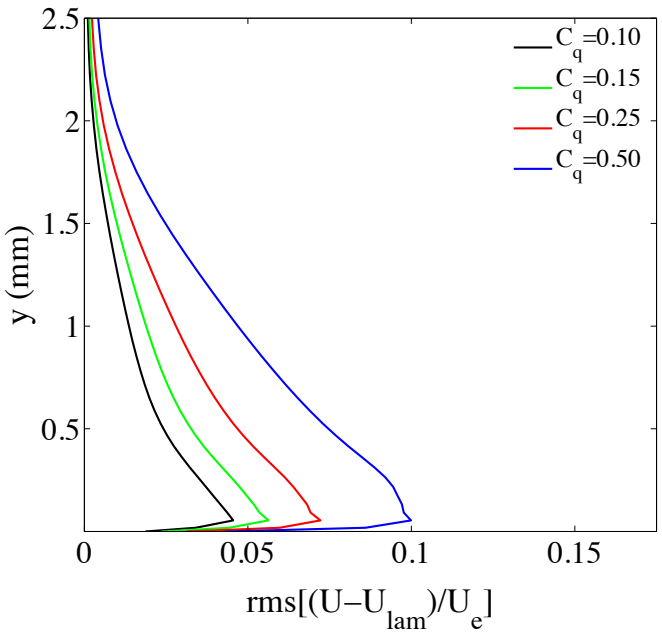

Figure 4.22: RMS of Disturbance velocity profiles for $C_q = 0.10, 0.15, 0.25$ and 0.50

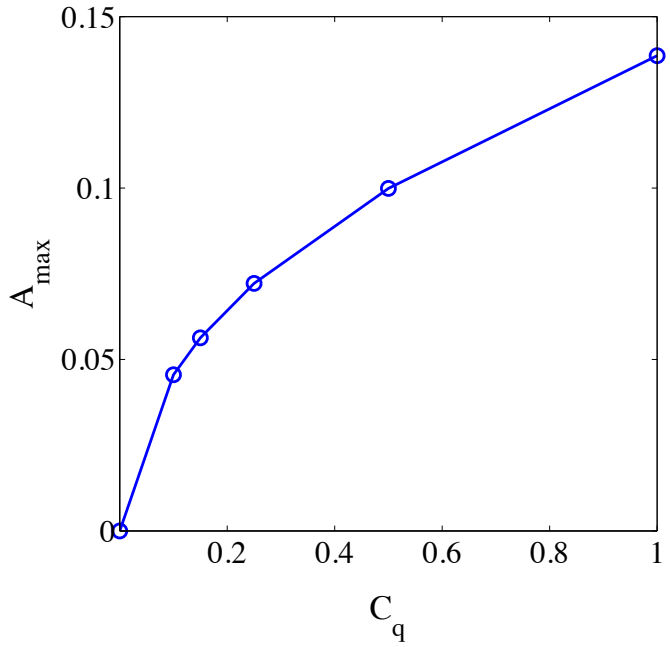

Figure 4.23: Initial amplitude (maximum of disturbance rms) for various C_q

4.6.2 Secondary Disturbance and Transition

For stationary crossflow vortices, recent literature (explained in Chapter 2) confirms that a high frequency secondary instability occurs prior to an explosive rapid local breakdown.

Figure 4.24 shows a contour of instantaneous vorticity magnitude at a wall normal slice $2mm$ away from the wing surface. The contour is shown for 3 suction rates: $C_q = 0.25, 0.5$ & 1.0. For all of the cases shown an initial primary disturbance to the velocity gradients occurs which amplifies downstream. Breakdown occurs at different locations for each of the different cases.

The contour shows a breakdown region between $x^*/c = 0.25-0.35$ for the $C_q = 1.0$ case. The figure shows also the formation of a wedge shaped turbulent region with turbulent streaks. For the $C_q = 0.5$ case the transition location is further downstream at $x^*/c = 0.45 - 0.55$ and for the $C_q = 0.25$ case transition begins to appear at $x^*/c = 0.55$. The wedge shaped turbulent region is typical of the breakdown region for crossflow transition and the $C_q = 1.0$ case captures such a region successfully.

Visualisation of the vortices and breakdown is demonstrated by iso-surfaces of λ_2 in Figures 4.25 for case $C_q = 1.0$. The λ_2-definition is used to define vortical structures and was developed and described by Jeong & Hussain[46]. λ_2 is a real eigenvalue of the tensor $S^2+\Omega^2$ where S and Ω are the symmetric and antisymmetric parts respectively of the velocity gradient tensor $\overline{g}$. As $S^2+\Omega^2$ is real and symmetric, it has only real eigenvalues. With λ_1, λ_2 and λ_3 as the eigenvalues such that $\lambda_1 \geq \lambda_2 \geq \lambda_3$, a vortex core is defined as a region of having a negative value of λ_2. This definition captures the pressure minimum in a plane perpendicular to the vortex axis.

The growth of the vortex core for the crossflow vortex and the initial primary growth is seen between $x^*/c = 0.1-0.3$. A secondary instability develops at $x^*/c = 0.3$ with velocity fluctuations near the top of the vortex. The fluctuations grow rapidly and the wedge formation is evident with a fully turbulent region. The memory of the secondary instability however remains for a substantial distance within the turbulent wedge region. The fluctuations on the top of the vortex are clearly visible up until $x^*/c = 0.42$. Downstream of $x^*/c = 0.42$ a fully turbulent region can be shown and the development of a full energy cascade.

Figure 4.26 shows a plot of average velocity perturbation (u_{rms}) for the $C_q = 0.5$ case. The slice is taken at $x^*/c = 0.28$ before breakdown occurs. The slice shows the region where the secondary perturbations occur at the side of the vortex. This region corresponds to the upwash region of the vortex where the low momentum fluid

is pushed towards the high momentum region of the boundary layer. The naming convention of the secondary instability modes was defined by Malik et al. [63] and the secondary instability shown in this figure represents the high frequency 'z' mode, induced by the spanwise shear component. This secondary instability mode grows in Figure 4.25 and as described in the previous paragraph, maintains until a considerable distance in the turbulent wedge region. This secondary instability 'memory' has also been confirmed by recent DNS work by Duan et al. [25]

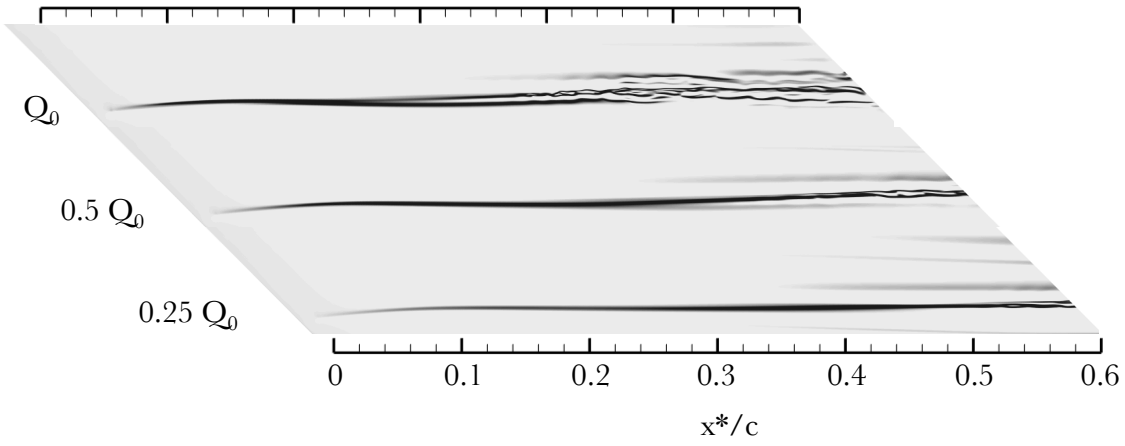

Figure 4.24: Instantaneous contours of Vorticity Magnitude at 2mm above aerofoil for continuous suction hole, $C_q = 0.25, 0.5, 1.0$

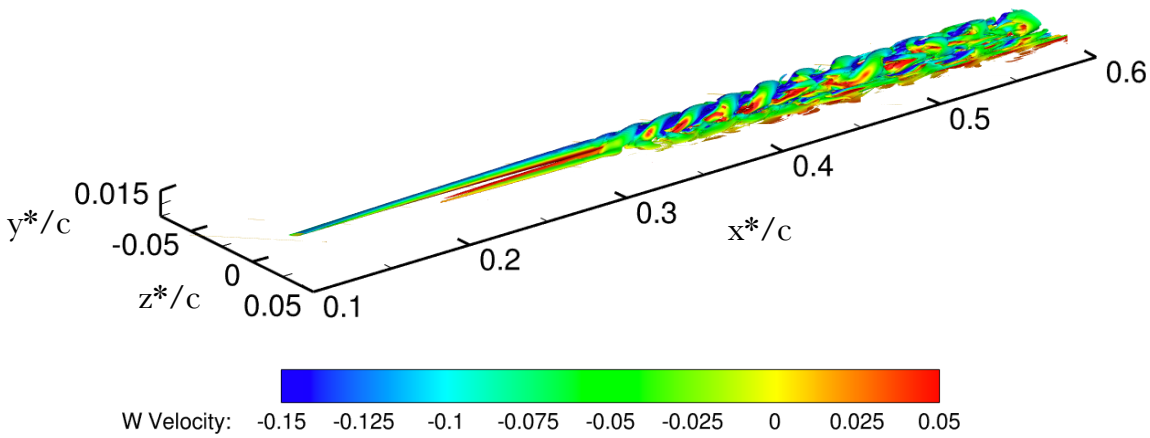

(a) Full view

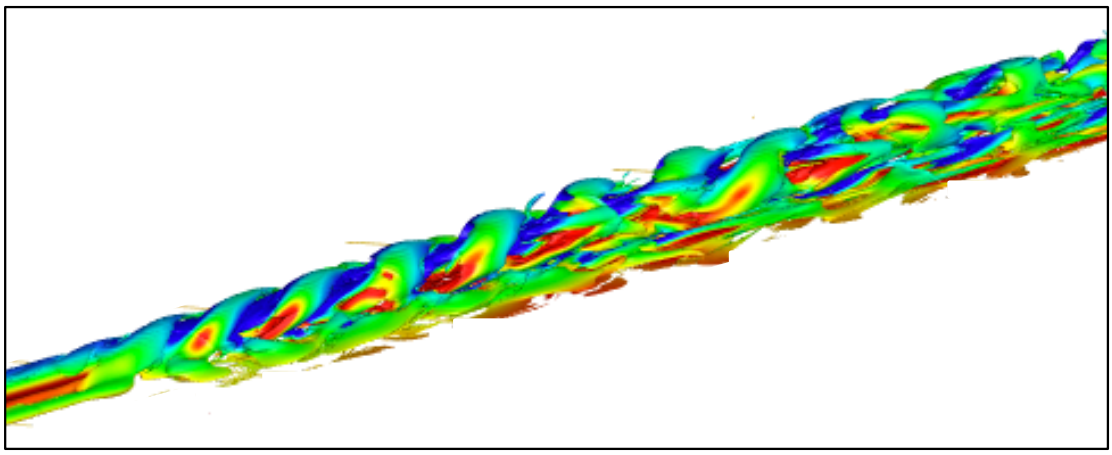

(b) Zoomed view

Figure 4.25: λ_2 Iso-Surface for $C_q = 1.0$, coloured by W Velocity

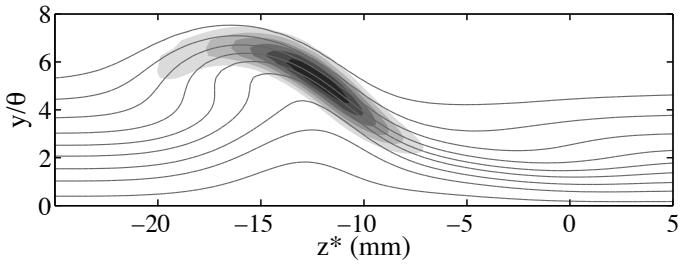

Figure 4.26: u_{rms} at $x^*/c = 0.28$ for $C_q = 0.5$

4.6.3 Comparison to Experiment

Comparisons are made with the experimental data from Chernoray et al. [20] The experimental data were only available in the form of contour plots measured using hot wires. The original data were not available and only the contour plots were used for comparison. The contour plots illustrate the mean streamwise U velocity and the disturbance of streamwise velocity U' at $x^*/c = 0.28$. The disturbance of streamwise velocity u' is calculated by removing the mean streamwise velocity of the laminar base flow from the mean streamwise velocity from the suction-disturbed flow. Figure 4.27 shows the experimental contour plot of u' velocity on the left and u velocity on the right at 0.28 x^*/c. The disturbance velocity plot (left) shows two areas of negative (dashed lines) and positive disturbance (solid lines). This corresponds to the mean velocity plot (right) with the disturbance clearly visible.

The simulation results at the equivalent chordwise location can be shown in Figure 4.28. Figure 4.28(a) shows the results for suction rate $C_q = 0.10$, Figure 4.28(b) for $C_q = 0.15$ and Figure 4.28(c) for $C_q = 0.25$. The contour levels remain the same for the simulation and experimental results. For all initial disturbances the shape and size of the disturbance regions correspond well with the experimental data and in particular the $C_q = 0.10$ case matches very well the experimental contours. The peak disturbance amplitudes occur at $y/\theta = 3.5$ for both experimental and simulation results at this amplitude. The mean contour lines in the right hand side plots also match well with the experimental data. The position of the disturbance within the boundary layer contour lines can be clear shown. The larger initial suction cases show a larger growth of the disturbance at this chordwise location due to the larger initial disturbance.

Overall the simulations agree well with the experimental data and the key flow physics resolved.

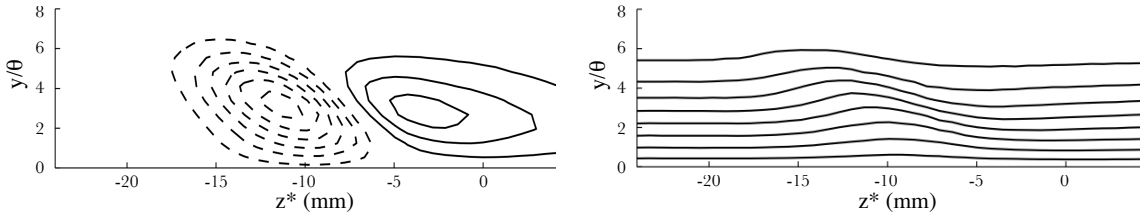

Figure 4.27: Experimental contours at station $0.28x^*/c$ behind continuous suction hole from Chernoray et al. [20] **Left:** Mean streamwise velocity disturbance U' (Contour levels in steps of $0.05Q_0$, dashed lines negative) **Right:** Mean Streamwise Velocity (Contour levels $0.1138, 0.2276, ..., 0.9103$ of Q_e)

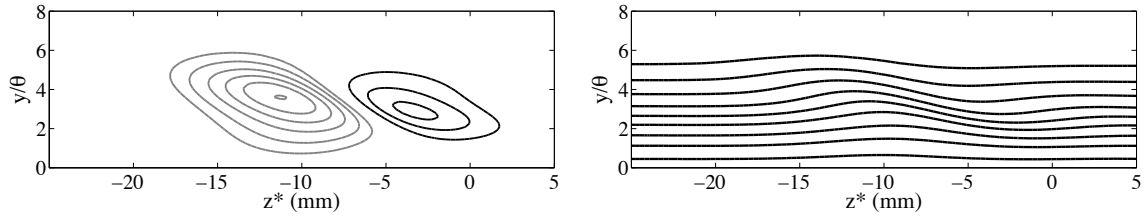

(a) $C_q = 0.10$

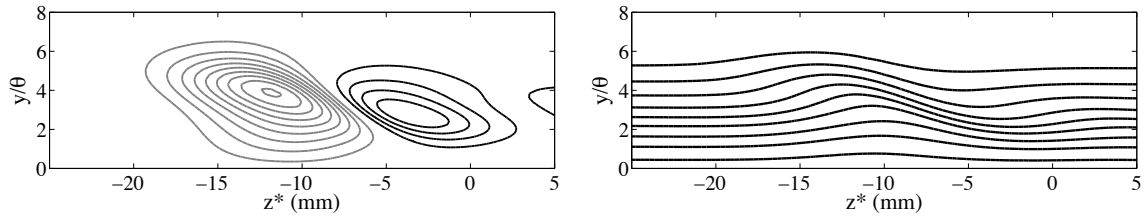

(b) C_q - 0.15

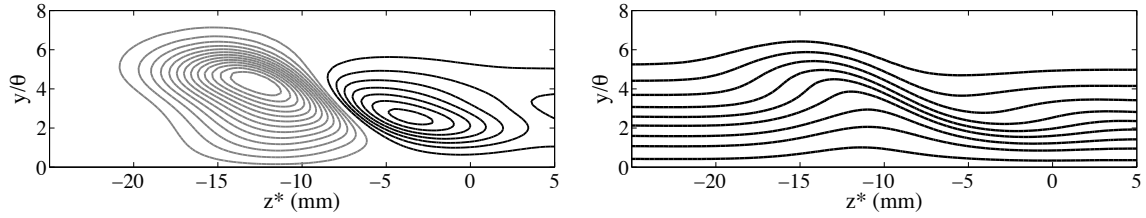

(c) C_q - 0.25

Figure 4.28: Simulation contours at station $0.28x^*/c$ behind continuous suction hole with $C_q = 0.10, 0.15$ and 0.25 **Left:** Mean streamwise velocity disturbance U' (Contour levels in steps of $0.05Q_0$, grey lines negative) **Right:** Mean streamwise velocity U Contour lines from 0.1,0.2,...,0.9 Q_e

4.6.4 Comparison of Baseline and Finer Grid

One of the key objectives from for this validation case was to analyse the grid resolution requirements for capturing the initial amplitude and growth of the crossflow vortices. Two grids were run for this study, a baseline coarse grid and a finer grid, detailed in Table 5.2. The baseline grid has a streamwise grid resolution of $\Delta x+ = 40 - 60$ in the primary growth phase while the fine grid has a resolution of $\Delta x+ = 20 - 35$. Around the suction hole the finer grid captures the $1mm$ suction hole with 8 cells while the baseline grid contains 4 cells for the suction hole. The finer grid consists of three times the cell count of the baseline grid and hence can be used to assess the necessary computational requirements and trade-off accuracy. Figure 4.29 shows a comparison of the baseline and finer grid at chordwise station $x^*/c = 0.28$ and for the case $C_q = 0.15$. The finer grid results are the same as that of Figure 4.28(b) with the mean streamwise velocity disturbance on the left and the mean streamwise velocity figures on the right. The baseline grid simulates the disturbance extremely well in comparison to the fine grid. The shape and location of the disturbance regions are also very well matched.

To compare the disturbance amplitudes across the chord of the wing an N-factor plot is produced for four different suction cases. The plot is shown in Figure 4.30. The N-Factor is defined in Equation 4.3 where A_0 is the initial disturbance amplitude and A is the disturbance amplitude a location downstream from A_0. The calculation of the amplitudes is given by Equation 4.2. The N factor in this plot represents the average growth rate of the total disturbance of all crossflow modes.

$$N = ln(A/A_0) \tag{4.3}$$

For Figure 4.30, A_0 is taken at $x^* = 0.35$ close to the boundary layer neutral point. The figure shows curves for suction cases $C_q = 0.1, 0.15, 0.25, 0.5$. The finer grid is represented by solid curves and the baseline grid with dashed curves. All four different suction cases show an initial disturbance growth region followed by amplitude saturation. For the larger initial amplitude case ($C_q = 0.5$), amplitude saturation occurs at $0.55x^*/c$. The baseline grid results closely match that of the finer grid and amplitude saturation occurs at the same chordwise location. In the saturation region the amplitudes differ, possible due to the unsteadiness arising from breakdown to turbulence for this case at $0.6x^*/c$. For the lower initial amplitude cases ($C_q = 0.1, 0.15, 0.25$) the baseline and finer grids are well matched. The baseline grid underpredicts the growth rate for the $C_q = 0.1$ case by 5% however it follows the finer

grid curve very well.

Overall the coarser grid spacing has provided a good agreement with the finer grid at a fraction of the computational cost. Therefore it can be concluded that this coarse grid spacing can provide a good estimation of the primary growth phase which will be crucial for cases at higher Re_c.

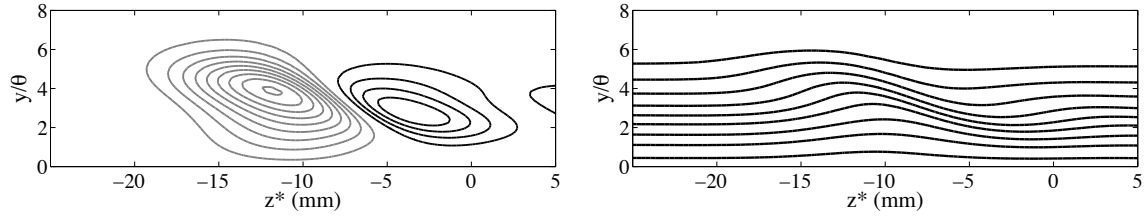

(a) Baseline Grid

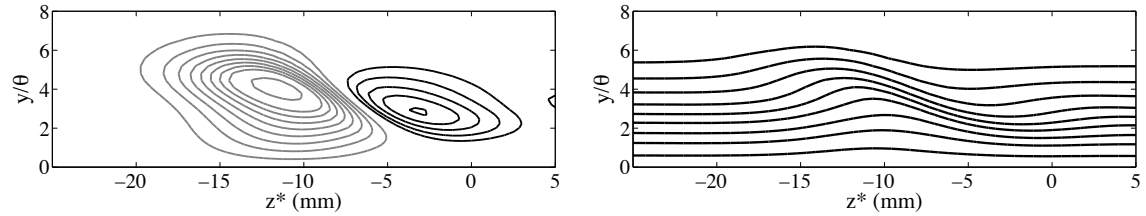

(b) Finer Grid

Figure 4.29: Simulation baseline and finer grid contours at station $0.28x^*/c$ behind continuous suction hole for $C_q = 0.15$ **Left:** Mean streamwise velocity disturbance U' (Contour levels in steps of $0.05Q_0$, grey lines negative) **Right:** Mean streamwise velocity U Contour lines from 0.1,0.2,...,0.9 Q_e

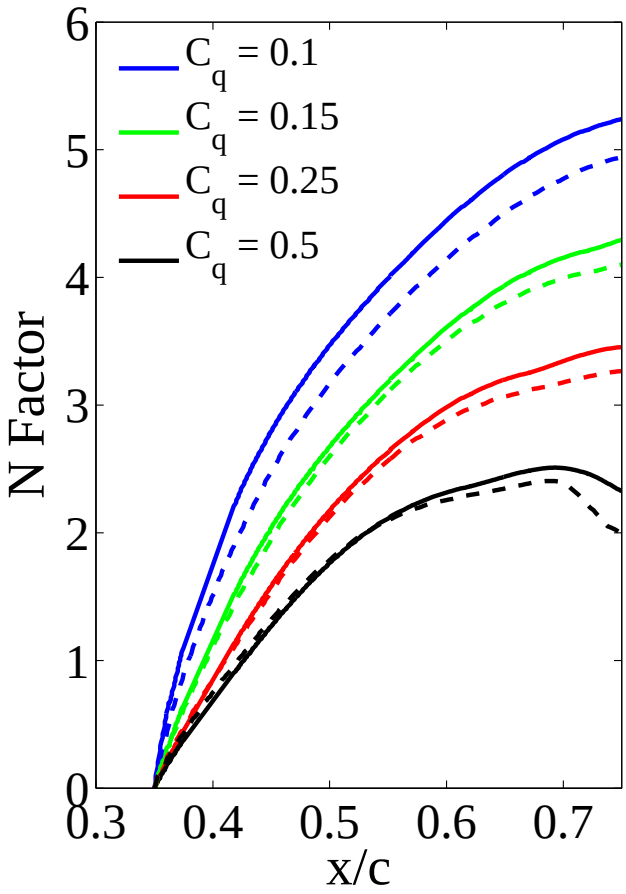

Figure 4.30: N factor growth for $C_q = 0.1, 0.15, 0.25, 0.5$, Solid lines - Fine Grid, Dashed lines - Coarse Grid

4.7 Roughness Element Disturbance Results

4.7.1 Flowfield

The second disturbance generation method was the use of an isolated roughness element. Section 4.5.2 describes the shape and size of the roughness element used in the experiment and replicated for the simulations. The roughness element has dimensions of $35mm$ span, $8mm$ width and a $0.39mm$ height. The roughness element height in terms of roughness height Reynolds number is: $Re_k = 305$.

The experimental goal for the isolated roughness element was to generate crossflow vortices of spanwise wavelength $20mm$. In experiments by Boiko et al. [16] at the same conditions it was observed that a vortex packet with primarily this mode can be generated using an isolated roughness element with $35mm$ width. It was shown that a pair of independently developing vortices of opposite rotation is generated either side of the roughness element. Simulation results can be seen in Figure 4.31 via contours of mean streamwise velocity and in Figure 4.32 via contours of mean vorticity magnitude.

Figure 4.31 shows the development of the stationary crossflow vortex packet either side of the roughness element. The contours are taken at $0.1x^*/c$ intervals up until $x^*/c = 0.6$. It is clear from the figures that the disturbance amplitude growth rate of the left hand side (LHS) vortex is significantly greater then that of the right hand side (RHS) vortex. The vortices are counter rotating with an upward motion dominating on the LHS vortex and a downwash motion dominating on the RHS vortex. The effect of this is low-momentum fluid being pushed upwards on the LHS and the high momentum fluid pushed downwards on the RHS, similar to the continuous suction vortex packets described in the previous results section.

The impact that the roughness element has on the velocity gradients can be visualised in the vorticity magnitude contours in Figure 4.32. As the disturbance amplitude grows on the LHS vortex packet the gradients around the vortex increase. A large velocity gradient forms on top of the vortex and on the side of the vortex in the upwash region. These velocity gradient regions are key contributors to the secondary instability mechanism and the final breakdown to turbulence. For the continuous suction disturbance results the secondary perturbations begin to grow at the side upwash region of the crossflow vortex which corresponds to the 'z' mode secondary instability. No breakdown to turbulence is shown for the roughness element cases as the initial amplitude is small enough such that the crossflow vortices maintain until the trailing

edge. However from Figure 4.32 the gradients in the ‘z’ mode region (side of the vortex)and ‘y‘ mode region (top of the vortex) can be shown to grow significantly.

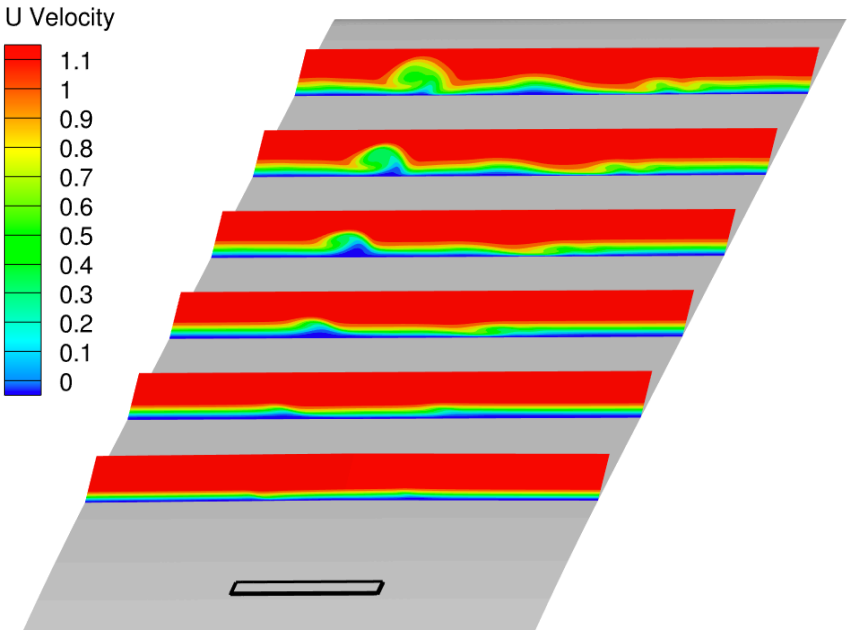

Figure 4.31: Mean contours of U (streamwise) Velocity aft of $35mm$ roughness element, Stations $x^*/c = 0.1, 0.2, 0.3, 0.4, 0.5, 0.6$

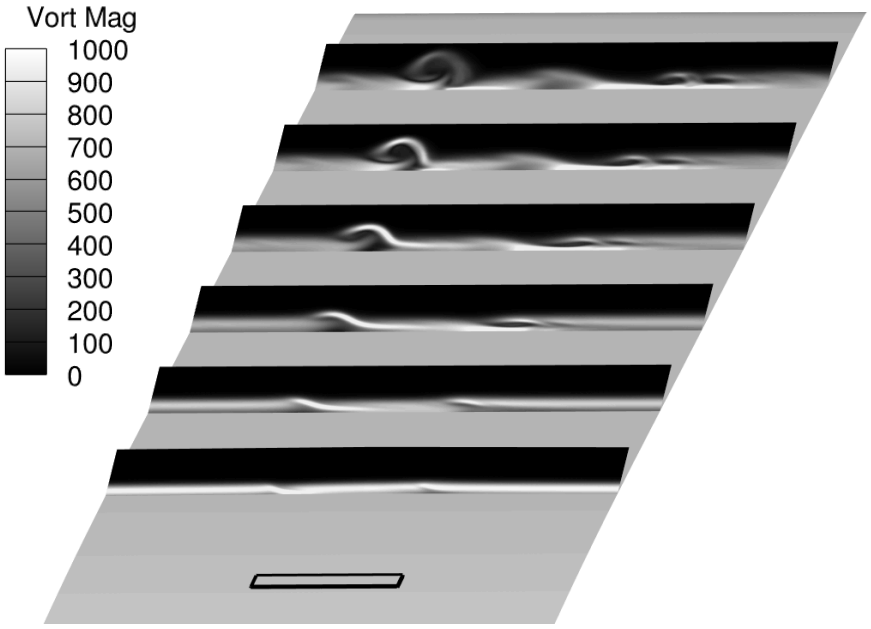

Figure 4.32: Mean contours of Vorticity Magnitude aft of $35mm$ roughness element, Stations $x^*/c = 0.1, 0.2, 0.3, 0.4, 0.5, 0.6$

4.7.2 Comparison to Experiment

The simulation results are compared to the Chernoray et al. [20] experimental data in a similar manner to the continuous suction results. The experimental data featured three plots for comparison: a) streamwise velocity contour at $x^*/c = 0.24$, b) streamwise velocity disturbance contour at $x^*/c = 0.24$ and c) iso-surface of streamwise velocity disturbance between $x/c = 0.5 - 0.85$.

Figure 4.33 shows a contour plot taken from the Chernoray paper of mean streamwise velocity disturbance at $0.24x^*/c$ aft of the roughness element. Figure 4.34 shows the equivalent plot for the simulation results. Both figures show three distinct disturbance regions. Either side of the roughness element a negative disturbance is generated represented by the dashed lines in the experimental contour and grey lines in the simulated contour. In between these disturbance regions is a positive disturbance that impacts roughly a $30mm$ region. The positive disturbance region is well matched between the experiment and simulation results. However, the negative disturbance regions show clearly a much higher amplitude of disturbance. To show this clearer a comparison of the mean streamwise velocity is shown, detailed in the next paragraph.

Figure 4.35 shows a contour plot of mean streamwise velocity at $0.24x^*/c$ aft of the roughness element, extracted from the experiment. Figure 4.36 shows the equivalent plot for the simulation results. The negative disturbance shown in Figures 4.33 and 4.34 can be visualised with the peaks at $-5mm$ and at $30mm$. The peaks are clearly larger for the simulation than the experiment and a possible cause for this can be related to the receptivity of the roughness element. It is possible that the simulation may have captured the initial amplitude of the roughness element disturbance incorrectly leading to a larger growth of the disturbance at this chord wise location. However, this is unlikely as the roughness element is extremely well resolved with 20 cells covering the roughness height and a resolution equivalent to a DNS solution. Another potential cause of the mis-match is that there are discrepancies in the shape of the roughness element between the simulation and the experiment. The experiment gave dimensions of the roughness element however did not include details of the exact shape and cambering of the corners. The sharp corner in the simulation have incurred an additional receptivity disturbance leading to the larger amplitude shown in the figures.

It remains clear that the while the amplitudes are mismatched the capture of the flow physics and structures of the disturbances are well predicted. This can be shown

clearer in Figures 4.37 and 4.38. The figures show iso-surfaces of the streamwise velocity disturbance between $x/c = 0.55$ and 0.85 ($x^*/c = 0.25 - 0.55$). Figure 4.37 shows an iso surface for the experiment while 4.38 shows the iso-surface for the simulation. For both figures the iso-surface levels are at a disturbance level $\pm 6\%$ of Q_0.

Both figures show three distinct streaks behind the roughness element and deep within the boundary layer. Firstly an area of velocity acceleration right behind the roughness element and two areas of velocity reduction. The iso-surfaces for the simulation match very well with the experimental plots with the growth of the LHS disturbance matching well with the experiment as well as the velocity acceleration directly behind the experiment. The RHS iso-surface shows an elongated distortion and no clear vortex formation which is also matched to the experiment.

Overall the roughness element contours for the simulations give good agreement to the experiment in terms of disturbance size and structure and the relevant flow physics are well resolved. The disturbance amplitudes are higher for the simulation however it may be attributed to the difficulty and uncertainty in matching the exact initial roughness element and the initial amplitude in the simulations to the experiment.

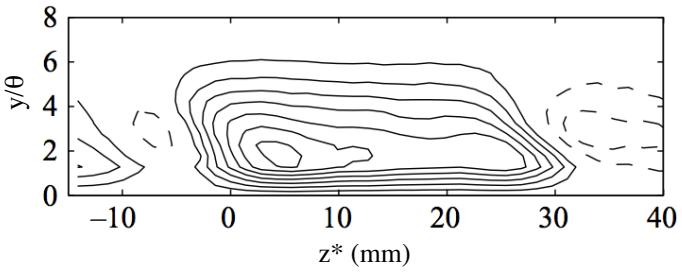

Figure 4.33: Experimental mean streamwise velocity disturbance U' contour at station $0.24x^*/c$ aft of $35mm$ roughness element from Chernoray et al. [20] (Contour levels in steps of $0.05Q_0$, dashed lines negative)

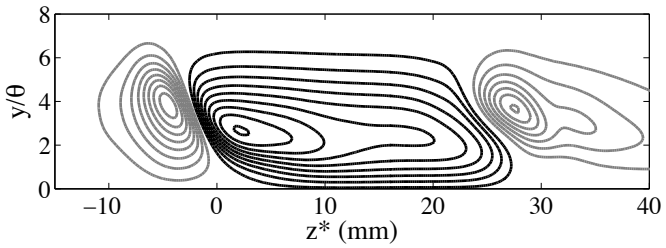

Figure 4.34: Simulation mean streamwise velocity disturbance U' contour at station $0.24x^*/c$ aft of $35mm$ roughness element (Contour levels in steps of $0.05Q_0$, grey lines negative)

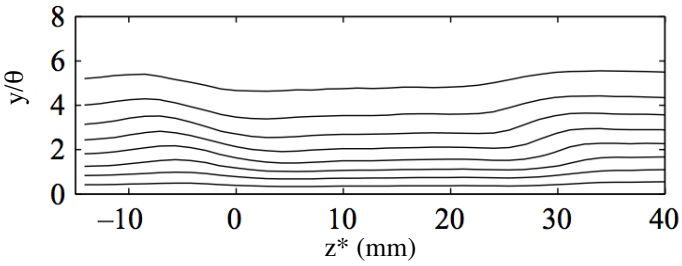

Figure 4.35: Experimental mean streamwise velocity U contour at station $0.24x^*/c$ aft of $35mm$ roughness element from Chernoray et al. [20] (Contour levels $0.1138, 0.2276, ..., 0.9103$ of Q_e)

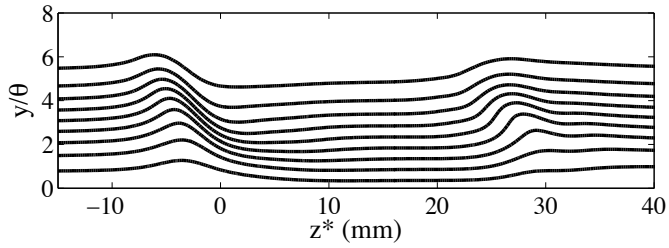

Figure 4.36: Simulation mean streamwise velocity U contour at station $0.24x^*/c$ aft of $35mm$ roughness element (Contour lines from 0.1,0.2,...,0.9 Q_e)

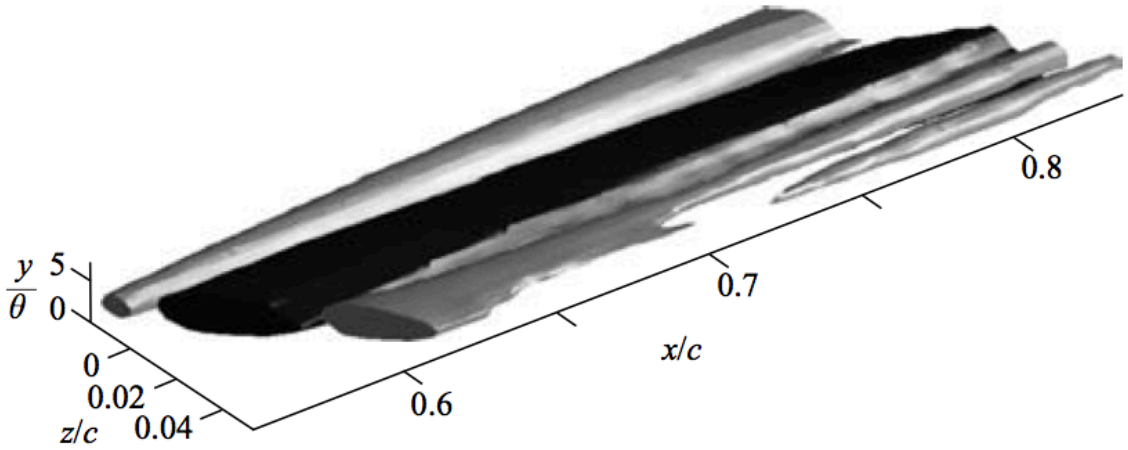

Figure 4.37: Experimental Iso-Surface of the stationary disturbance of streamwise velocity, U', due to the $35mm$ long roughness element (light: -6%, dark +6% of Q_0)

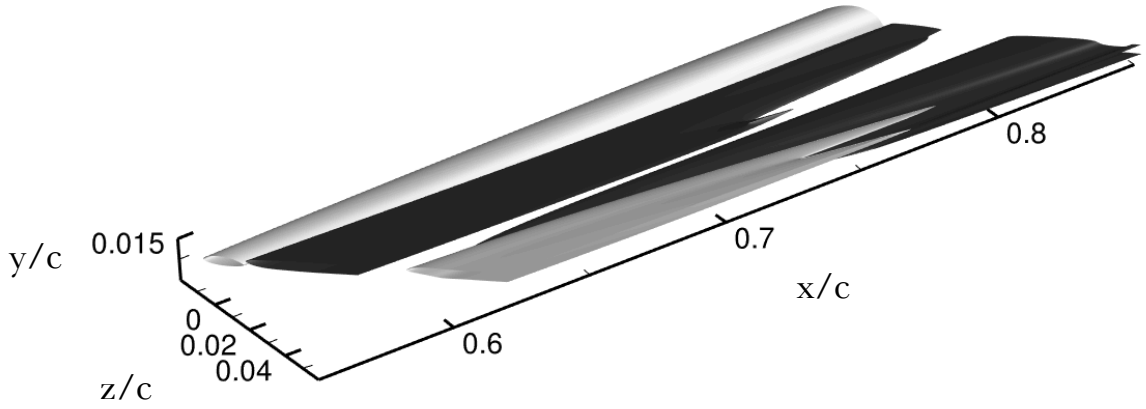

Figure 4.38: Simulation Iso-Surface of the stationary disturbance of streamwise velocity, U', due to the $35mm$ long roughness element (light: -6%, dark +6% of Q_0)

4.8 Closure

Results from an experimental test case conducted by Chernoray et al. using a 45° swept C16 aerofoil were chosen as an initial validation case for the UNS/LES simulation methodology. The experiment was chosen as it lends itself to an UNS/LES approach as it was run at a relatively low Reynolds number of $390,000$ while still large enough to be computationally difficult for a DNS simulation. The experiment also provided results of the laminar base flow as well as contours of the mean streamwise velocity and disturbance of the crossflow vortices.

A preliminary UNS/LES study was conducted using the C16 aerofoil with the solution domain replicating the experimental setup. The preliminary study showed a large turbulent boundary layer on the lower surface with some separation, as the results from the lower surface are not required for the validation study a method was devised to remove the need to resolve the lower surface. This involved extracting the time-averaged, span wise averaged stagnation and trailing edge streamlines and using them to define the lower bound of a new solution domain. The results from the reduced streamline model showed good correlation to the full model and was subsequently used for further analysis. As this process reduced the computational cost by a half, further refinement of the upper surface could be achieved.

The laminar base from the experiment was compared against the experimental data using the standard Smagorinsky and WALE SGS models. As predicted the WALE model provided a better result due to the models inherent ability to distinguish a laminar boundary layer from a turbulence one. The laminar base flow using the WALE model provides a suitable representation of the experimental base flow and was used for further analysis of the stationary crossflow vortices and transition.

Two receptivity devices were used to generate the stationary crossflow vortices: a $1mm$ continuous suction hole and a $35mm$ isolated roughness element. The continuous suction hole was run at a sweep of suction velocities and the initial amplitudes were captured. A non-linear relationship between suction velocities and disturbance amplitude is shown. For the large suction velocity, breakdown to turbulence was shown via a secondary instability. The turbulent region was characterised by an initial secondary perturbation followed by explosive breakdown to turbulence and the formation of a turbulent wedge. Such breakdown phenomena have been verified and validated in a number of recent studies. The suction cases were also compared against the experimental data and the disturbance growth was captured well by the simulations.

The roughness element disturbance generation showed the development of three stationary disturbance regions behind the element. Two areas of flow deceleration at each edge of the roughness element characterised with an upwash of low momentum fluid to the upper parts of the boundary layer. Also one region of flow deceleration directly behind the roughness element characterised by a downwash of high momentum fluid to the lower part of the boundary layer. The results were measured against the experimental data, the size and shape of each disturbance regions were in good agreement suggesting that the method was capable of simulating the stationary crossflow vortices. However, the amplitudes of the disturbances were over-predicted. The cause of this mis match was attributed to errors in the capturing of the initial disturbance, a mostly like cause of this is that the roughness element shapes were not exactly matched.

Overall the key outcomes of this study can be summarised into the following points:

1. The methodology of using an unsteady Navier-Stokes simulation for the laminar region and a wall-resolved LES approach for the turbulent region proved capable of resolving the stages of the complex transition process. The full transition process was simulated from initial disturbance capture to final breakdown to turbulence.

2. The flow field described by the simulations matched well with experimental results and captured phenomena reported in recent literature. In particular the secondary instability region was captured as well as its breakdown to turbulence. It was clear from the results that the memory of the secondary instability remained deep into the turbulent region, which was also been reported recently by DNS results from Duan et al. [25].

3. The computational expense of the simulation can be reduced by relaxing the grid spacing in the primary growth and early stages of disturbance growth, where the flow is entirely laminar. This chapter also described a streamline extraction approach which reduced the computational cost by a half.

Chapter 5

Simulation and Control of Crossflow Vortices by Distributed Roughness Elements (DRE)

5.1 Introduction

A method for control of the crossflow instability was proposed by Saric et al. [100] using distributed roughness elements (DRE) as detailed in the Chapter 2. The strategy of the control method is to eliminate streamwise (TS) instabilities by moving the pressure minimum as far aft as possible and to employ a favourable pressure gradient; this in turn promotes crossflow instabilities at large sweep angles. By allowing crossflow instabilities to dominate laminar turbulent transition, the wavelengths can be manipulated to suppress the most harmful unstable wavelengths to attain a delay in transition.

This can be achieved by employing a spanwise row of DRE close to the leading edge. Using artificial surface roughness in the form of the DRE's, a single mode is forced resulting in a smaller set of harmonic modes (integer divisions of the single mode) to measure and identify e.g. if an $18mm$ spacing is employed, crossflow modes of $18mm, 9mm, 6mm, 4.5mm$ etc. will be forced.

Saric et al. [100] demonstrated a delay in transition to turbulence using a DRE with micron-sized roughness elements and a wavelength spacing less than the most unstable wavelength (critical wavelength). The smaller wavelength (control wavelength) modifies the basic state such that the most unstable wavelength can no longer grow. The control wavelength then decays before amplitudes large enough to cause

transition can occur.

The following chapter describes results of the simulation method employed in Chapter 4 to simulate DRE control at different wavelengths and roughness heights. The base flow for the simulations was based upon the experiments run in the PHD Thesis *"Boundary-Layer Receptivity to Three-Dimensional Roughness Arrays on a Swept Wing"* by Lauren Hunt [42]. The experiment uses an ASU(67)-0315 aerofoil with a 45° sweep angle and a chord based Reynolds number of 2.4 million. This flow configuration has been tested extensively by Saric and co-workers at Texas A&M University and numerical work recently by the Henningson group at KTH Mechanics.

The aim of the simulations was to investigate the capability of modelling distributed roughness using the Unsteady Navier-Stokes/ Large Eddy Simulation (UNS/ LES) approach. The experimental test setup is replicated and the simulations model two different spanwise wavelengths of DRE's at varying roughness heights. The results for the receptivity phase of transition are measured against the experimental data. The objectives of the study can be divided into four areas:

1. **Grid requirements** - The distributed roughness elements are cylindrical and of micron size and pose a challenge for a structured grid suitable for UNS. Capturing the flow around these regions was crucial for capturing the initial disturbance amplitude. As the flow around the cylinder is laminar and deep within the low momentum fluid of the boundary layer careful refinement is required to capture the disturbance. The grid was modified to ensure capture of the flow around the cylindrical roughness elements as well as the grid spacing downstream of the cylinders, capturing the growth of the crossflow vortices.

2. **Flow around DRE** - The flow around the cylinders was investigated to show their impact on the laminar base flow.

3. **Validation of Receptivity to DRE** - The receptivity of the flow to DRE's was measured against the experimental data. Initially no freestream perturbations were generated allowing the growth of the primary crossflow modes to be captured and analysed.

4. **Breakdown and transition** - The transitional region was investigated for the smallest roughness height case using both the control and critical wavelength. A synthetic eddy method (SEM) is employed to add low freestream perturbations upstream of the DRE's.

5.2 Experimental Test Case

The base flow for the simulations was determined by the experiments of Hunt [42]. The experimental test case used an ASU(67)-0315 aerofoil, originally designed at Texas A&M by Mark Reibert and is the same model used for the crossflow breakdown studies by White & Saric [123]. The design philosophy behind the ASU(67)-0315 is that it minimises the presence of attachment-line, T-S or Görtler instabilities allowing crossflow disturbances to dominate boundary layer transition. The aerofoil was swept at an angle of 45° and mounted vertically within the test section with an onset velocity $Q_0 = 22.5m/s$ giving a Re_c of 2.4 million. The chord length c of the configuration was $1.83m$, the wing was angled at $-2.9°$ incidence and had a pressure minimum at 71% x/c. Figure 5.1 shows a CAD drawing of the experimental model and wind tunnel. Wall liners were designed for the test section to ensure spanwise uniformity and reduce contouring towards the test walls.

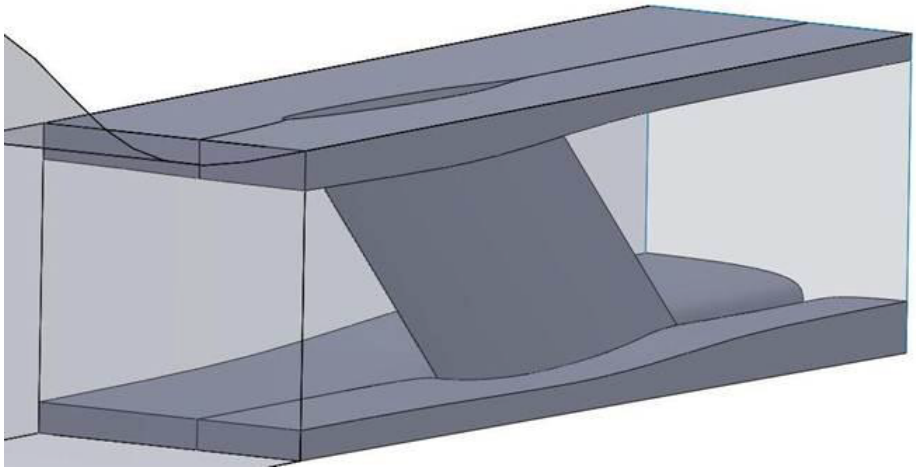

Figure 5.1: Hunt and Saric [42] Test section CAD

The experiments used cylindrical shaped roughness elements of diameter $3mm$ for their DRE studies placed at 2.9% x/c near the crossflow neutral point to ensure uniform disturbances. Several configurations of the roughness arrays were used and designated with the notation [k,λ], where k is the amplitude of the roughness in microns and λ is the spanwise wavelength in millimetres. The wavelength is measured from the centre of each roughness element. Hunt and Saric [42] used two λ spacings. The first was termed the critical wavelength $\lambda = 12mm$ and the second was the control wavelength $\lambda = 6mm$. The experiments were conducted at several roughness heights, the cases that were run in this thesis are detailed in Table 5.1. Hot-wire

Table 5.1: Experimental cases [42]

	Height k (μm)	Spanwise Wavelength λ (mm)
Case 1a	14	6
Case 1b	27	6
Case 1c	42	6
Case 1d	56	6
Case 2a	12	12
Case 2b	24	12
Case 2c	36	12
Case 2d	47	12

measurements were taken at 10%, 15% and 20%x/c to measure the receptivity and growth rate of the disturbances.

5.3 Computational Domains

5.3.1 Solution Domain and Boundary Conditions

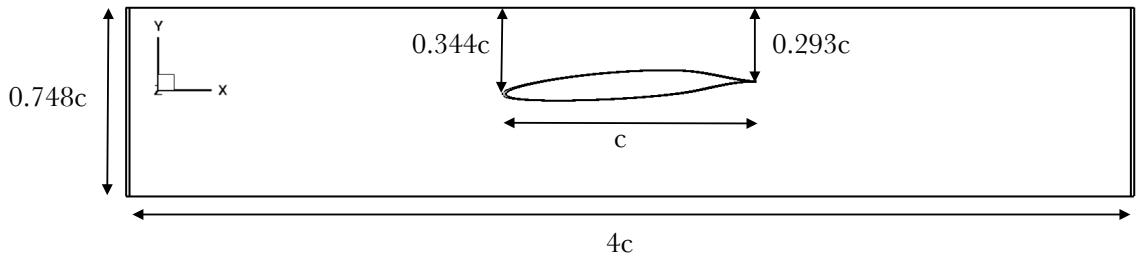

Figure 5.2: Full Solution Domain

The initial solution domain for the computational model is shown in Figure 5.2. The (x-y) plane dimensions of the domain were kept similar to that of the experimental wind tunnel at $0.748c$ in the transverse direction, and a length of $4c$ in the streamwise direction. To reduce the impact of the spanwise faces an infinite swept wing model was applied using a periodic or cyclic condition on the spanwise faces. This is achieved by linking the topology of each spanwise face from each block, allowing data to be passed from one side face back into the block on the opposite face. DNS studies [114] showed that using two roughness elements was adequate for modelling a spanwise cyclic roughness array. A spanwise segment (parallel to the leading edge) of $24mm$, which allows for 2 roughness elements spaced at the critical wavelength was used for all cases. The upper bound of the solution domain was modelled as a symmetry boundary condition.

To reduce the computational expense of the simulations only the flow over the upper surface of the wing was simulated. This was achieved by exporting the stagnation streamline upstream of the leading edge and the streamline aft of the trailing edge from the steady, time averaged mean solution of an initial coarse UNS/LES of the full domain. This process was used and validated in Chapter 4 and helped reduce the computational expense by a half. The streamlines were averaged across the span and converted (together with the geometry of the upper airfoil surface) into a plane which defined the inner boundary of a new solution domain. The initial coarse UNS/LES contained 50million elements and was initialised with velocity inlet of $22m/s$. Figure 5.3 shows a contour of mean U (streamwise) velocity, cut through the centre of the span. A red line shows the streamlines that were extracted from the solution. Figure 5.4 shows the subsequent streamline extracted domain.

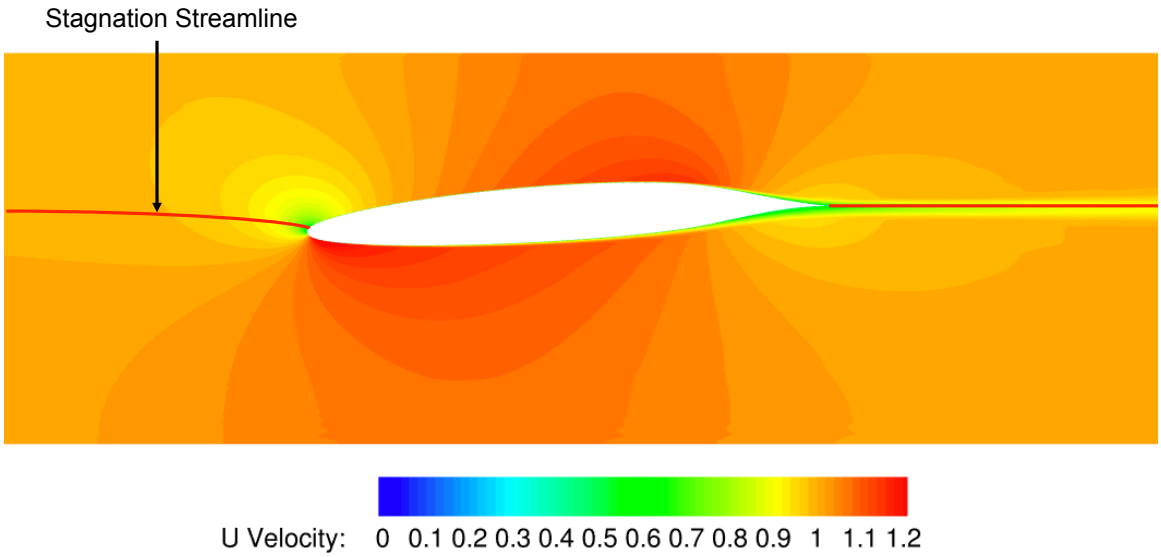

Figure 5.3: Mean U (streamwise) Velocity Contour (Red lines show stagnation streamlines)

Pressure and velocity results taken from the streamline extracted domain showed good agreement with the full domain and the experimental data as explained in the Laminar Base Flow sub-section (5.6) in Figure 5.10.

The cylinders were added to the solution domain and new grids were generated for simulating the distributed roughness arrays. The methodology for the grid generation and description of the grids is detailed in the next section.

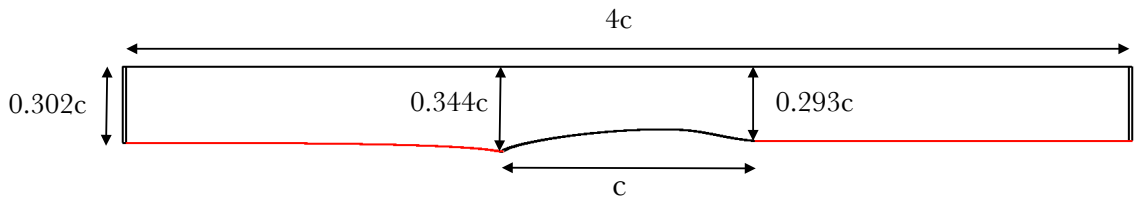

Figure 5.4: Streamline Extracted Domain

5.4 Initial and Modified Grid

5.4.1 Grid Generation Strategy

Careful consideration was given to the generation of a grid for this case. As explained in Chapter 1 transition to turbulence contains a number of stages that must be captured carefully. The initial receptivity phase requires capturing the disturbance from the distributed roughness elements. The flow around the cylinder is laminar and immersed within the low momentum fluid of the boundary layer. No turbulence is generated from the roughness element and the flow accelerates around the sides of the cylinder and over the top of the cylinder. This acceleration and disturbance to the streamwise velocity must be captured. As the size of the cylinder is small compared to the boundary layer height a fine resolution is required around the cylinder to capture the disturbance.

Downstream of the roughness element the initial growth of the disturbance is linear before non-linearity occurs. This primary growth also requires heavy refinement, once amplitude saturation occurs around the mid-chord region the grid spacing is relaxed. For the results where the freestream perturbations are introduced the benefit of using the sub-grid model in occur for the breakdown regions.

The first grid used in this study was developed to be relatively coarse and was used to define the subsequent grid resolution requirements for capturing the cylinder flow and primary growth. This grid was termed the 'initial grid'. From the results of this initial grid a modified grid was developed to improve the results. The remainder of this section gives an overview of the grid generation and grid diagnostics for both grids, the next section compares the results from the initial and modified grids.

5.4.2 Grid details

The grids were generated using the blocking tool within ICEMCFD 14.0. For both grids a C-grid was place around the aerofoil to ensure good quality cells in the boundary layer region. Blocks were then extended towards the inlet and outlet from the C-grid. To mesh the circular cylinders on the wing surface an O-grid was placed above each cylinder. The O-grid allowed for better quality cells over the cylinder. Figure 5.5 shows images of the C-grid blocking set-up with blocks extending from the C to the upstream boundary. The second image shows the blocking around the cylinders.

The grid diagnostics for each grid are listed in Table 5.2. The initial grid consists of 2137 nodes in the streamwise direction and a $\Delta x+ = 15$ near the cylinder. 70

nodes in the wall normal direction capture the boundary layer with a $\Delta y+ = 0.5$ at the wall. In the spanwise direction 100 nodes are placed (parallel to the leading edge) with a $\Delta z+ = 16$. Figure 5.7(a) shows the mesh resolution around the cylinder for the initial grid. No extra refinement is placed around the cylinder.

The modified grid contained additional refinement placed around the cylinder to capture the disturbance near the wall. The grid spacing was decreased in all directions, 2550 nodes in the streamwise direction ($\Delta x+ = 8$ near the cylinder), 100 nodes in the wall normal boundary layer region ($\Delta y+ = 0.25$ at the wall) and 156 nodes in the spanwise direction ($\Delta z+ = 11$).

Figure 5.6 shows two figures of the modified grid. The first figure shows the fine grid spacing around the leading edge of the aerofoil and a close-up of the number of layers in the boundary layer. The second image shows the O-grid mesh above the cylinders. Figure 5.7 shows a comparison of the initial and modified grid around the cylinders, the view is looking in the negative y-direction (above aerofoil). This shows clearly the finer grid spacing around the cylinders in the modified grid and the coarse spacing for the initial grid.

Table 5.2: Grid Diagnostics

	Initial Grid	Modified Grid
Block Count	142	190
Airfoil Nodes	2137	2550
BL Wall Normal Nodes	70	100
Spanwise Nodes	100	156
Leading Edge, $\Delta x+$	40	30
Cylinder,$\Delta x+$	15	8
Trailing Edge, $\Delta x+$	60	60
$\Delta y+$	0.5	0.25
$\Delta z+$	16	11
Total Mesh Size	60mil	95 mil
CPUs	142	190
Average CPU Hours	12,000	18,240

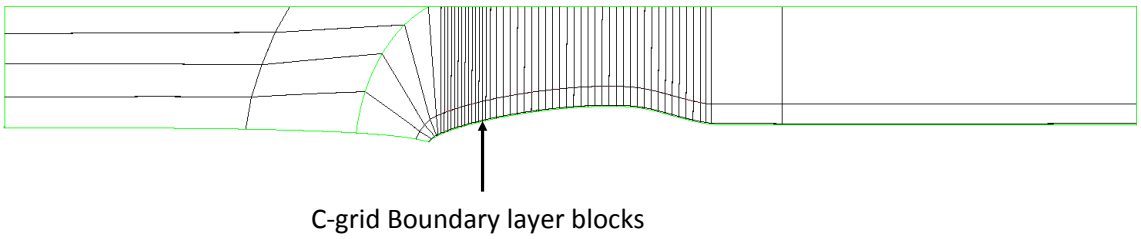

(a) Overall blocking structure for initial and modified grid

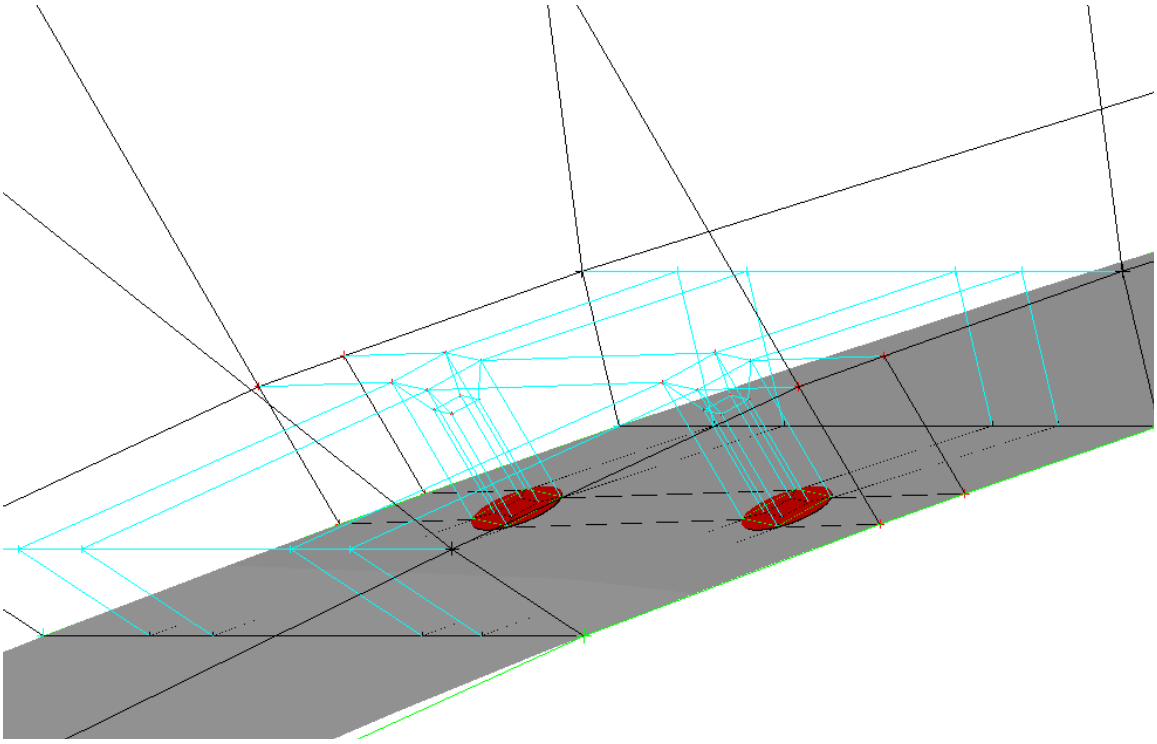

(b) Blocking structure over cylinders

Figure 5.5: Blocking Setup

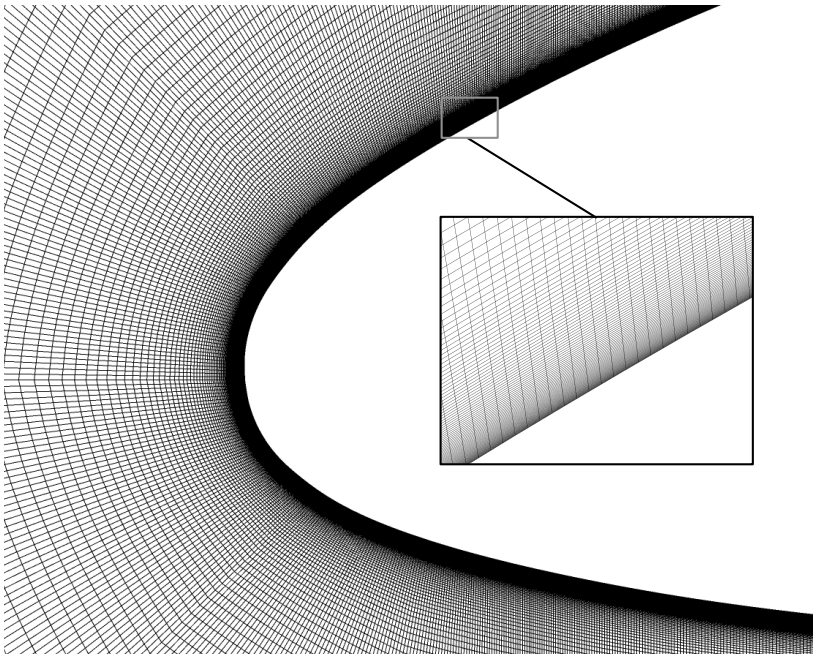

(a) Grid around aerofoil (Modified Grid)

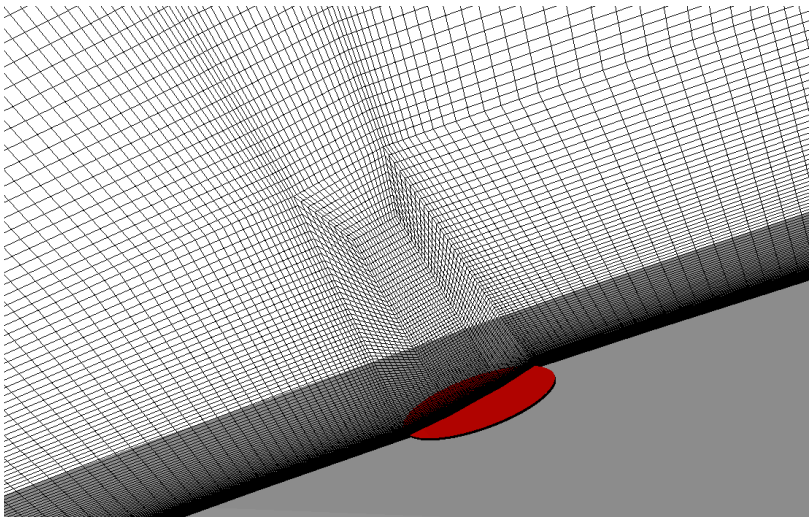

(b) Slice of grid over cylinder (Modified Grid)

Figure 5.6: Modified Grid

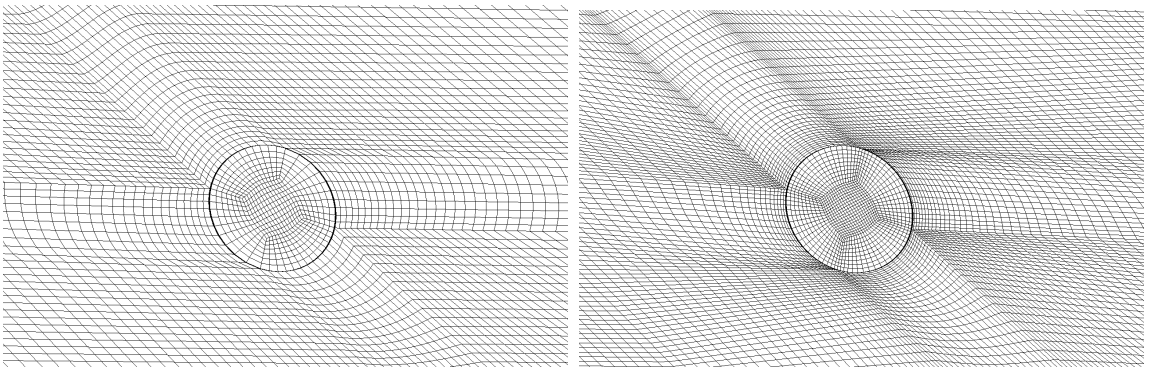

(a) Initial Grid (b) Modified Grid

Figure 5.7: Grids

5.5 Impact of Grid Spacing

The velocity results described in this thesis are aligned with the global cartesian coordinate system shown in Figure 5.2. Note: The w velocity component is not parallel to the leading edge of the wing, but parallel to the unswept z-coordinate.

Both grids were run on a single case to demonstrate the impact of grid spacing on the results. Figure 5.8 shows contours of spanwise velocity around the cylinder for both initial and modified grid. The slice is taken at the upper edge of the cylinder with the flow from left to right. The contours shows acceleration of the spanwise velocity component on each side of the cylinder. The area of acceleration can be shown to extend 1/5 of the cylinder diameter away from the cylinder. For the initial grid only 3-5 cells capture this acceleration around the cylinder, resulting in the simulation poorly capturing the initial disturbance amplitude. The modified grid was developed to capture this region better with 8-10 cells capturing the acceleration of flow around the cylinder. The impact of the poor resolution of the cylinder in the initial grid can be seen in Figure 5.9. The figure shows a stationary mode shape for Case 2b ($\lambda = 12mm$, k = 24 μm) at 15% chord. The calculation of the mode shape is explained in Section V. The initial grid underpredicts the amplitude while the modified grid matches very well with the experiment. This suggests that the emphasis must be placed on the cells nearest to the cylinder and to capture fully the initial amplitude. Subsequently, the modified grid was used for all remaining simulations and the results presented in the following sections are from the modified grid.

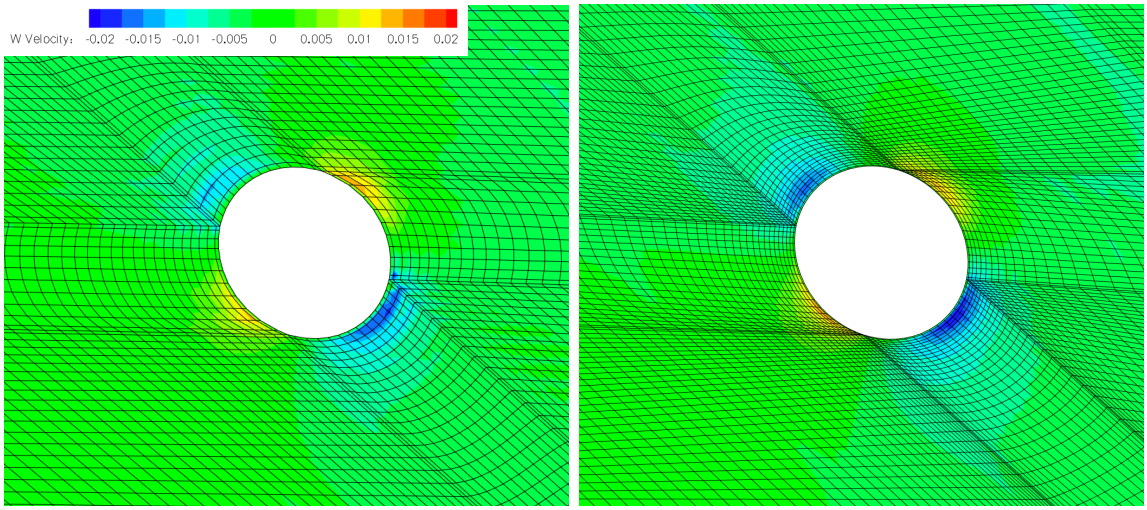

(a) Initial Grid (b) Modified Grid

Figure 5.8: $k = 24\mu m$, $\lambda = 12mm$ Contours of spanwise velocity at cylinder height (w/Q_0), top view at cylinder edge, Flow: Left to Right

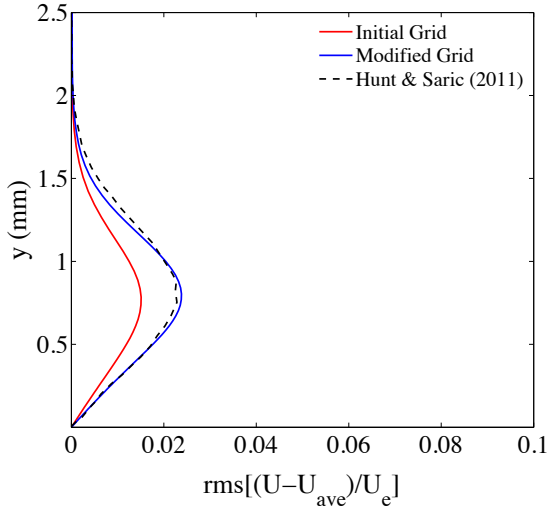

Figure 5.9: $k = 24\mu m$, $\lambda = 12mm$, Stationary mode shape for initial grid, modified grid and experimental results at $15\%x/c$

5.6 Laminar Base Flow

The base flow from the UNS/LES results was validated against the experimental results available from Hunt and Saric[42]. The pressure coefficients extracted from the UNS/LES are compared to the experimental results in Figure 5.10(a). The figure shows a curve for the full domain and the streamline extracted domain shown in Figure 4.2. The streamline extracted domain pressures match very well with the full domain demonstrating the success of the approach. The experimental pressure coefficient results are presented at two locations, the wing was mounted vertically in the wind tunnel and pressure measurements were taken on the upper and lower part of the span to ensure spanwise uniformity. The results from the UNS/LES show very good agreement with the experimental pressure measurements. The actual pressure is slightly higher than the experimental results in the favourable pressure gradient region leading to the pressure minimum, however, the pressure gradient is well matched. As the pressure gradient is the feature that effects boundary layer transition and stability the UNS/LES is considered to be suitably matched to the experiment.

Figure 5.10(b) shows a boundary layer profile for the streamwise (u) velocity component at 10% x/c for both the UNS/LES and the experimental results. The graph shows an excellent agreement between the simulation and experimental profiles.

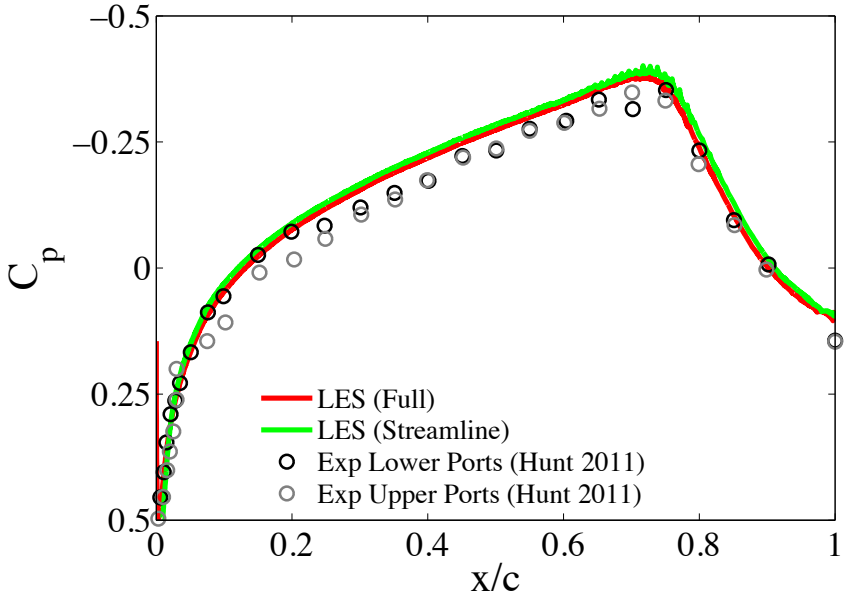

(a) Pressure Coefficient

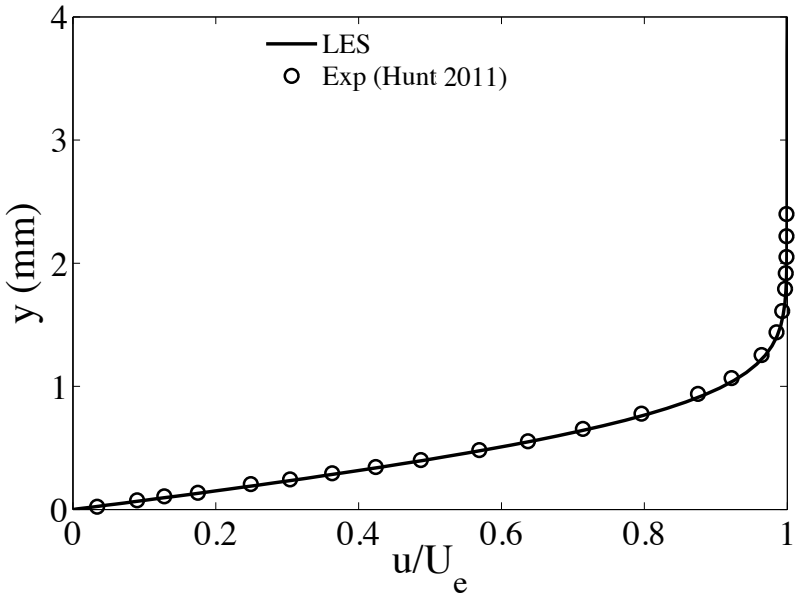

(b) Streamwise (u) boundary layer profile at 10% x/c

Figure 5.10: Comparison of Laminar Base Flow from UNS/LES to Experimental

5.7 Flow Around Cylinder

Simulation of the array of micron-sized cylinders was carried out once the laminar base flow was validated. The cylinders disturb the laminar base flow by accelerating the flow around the cylinders, illustrated in Figure 5.8 by contours of spanwise velocity (w/Q_0). The figure shows a disturbance velocity of 0.02 w/Q_0 of opposite sign each side of the cylinder. This disturbance can be visualised in Figure 5.11 in the form of streamlines. Figure 5.11(a) shows streamlines close up to the cylinder with the streamlines following the shape of the cylinder. Figure 5.11(b) shows the disturbance generated for the roughness array and beginning to develop downstream of the roughness element array.

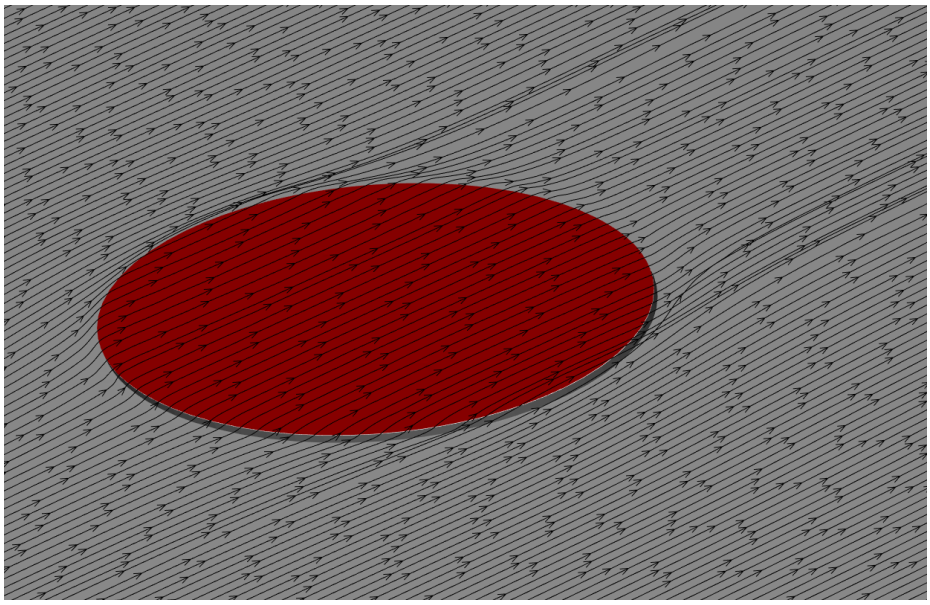

(a) Streamlines at cylinder height edge, $k = 36\mu m$, $\lambda = 12mm$ (Isometric view)

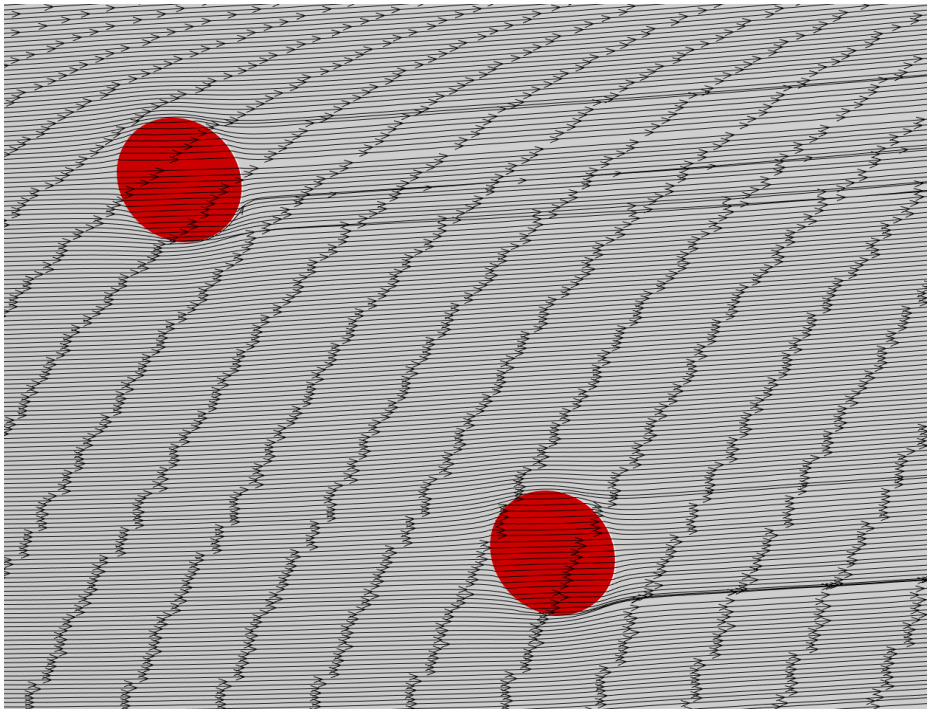

(b) Streamlines at cylinder height edge, $k = 36\mu m$, $\lambda = 12mm$ (Top view)

Figure 5.11: Streamlines around cylindrical roughness element

5.8 Receptivity Results

5.8.1 Receptivity of DRE Array at Critical Wavelength

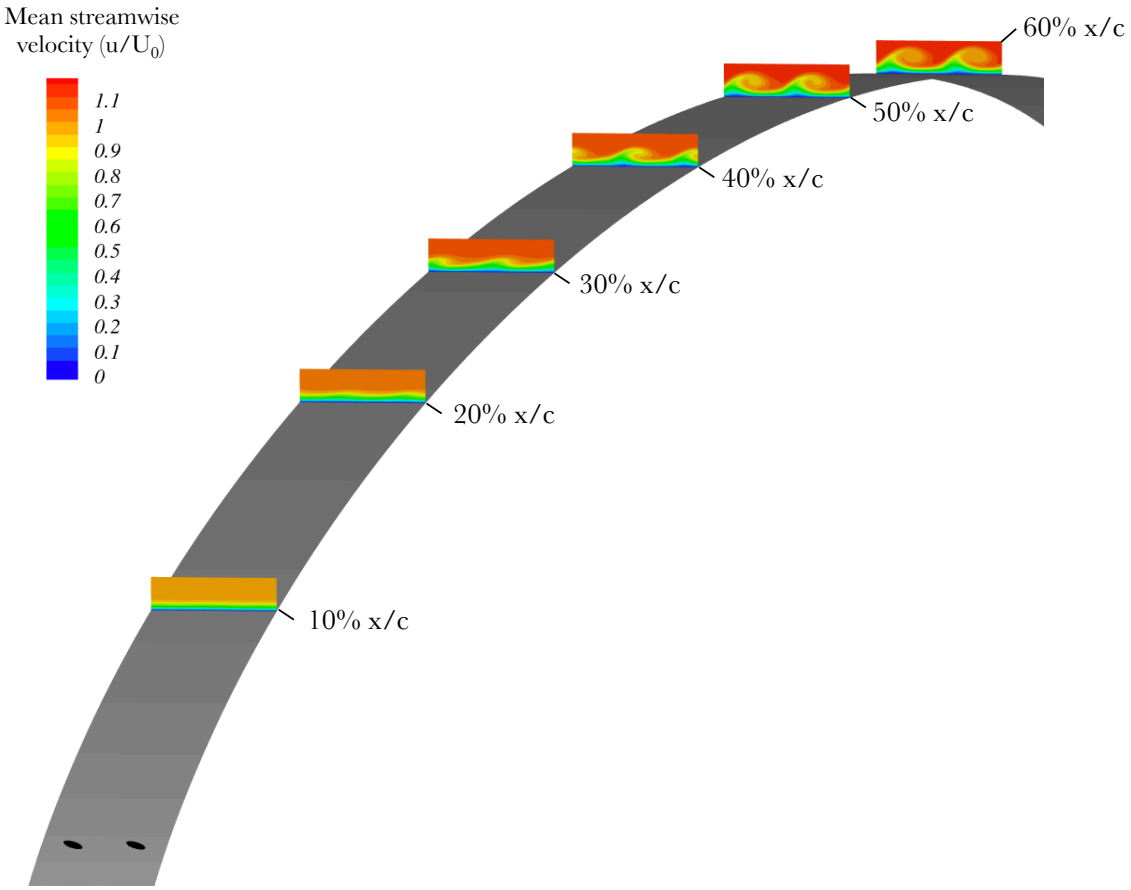

Figure 5.12: Contours of mean streamwise velocity u/U_0, $k = 36\mu m$, $\lambda = 12mm$, Contours taken at $x/c = 10\%, 20\%, 30\%, 40\%, 50\%, 60\%$

Simulations were run initially for the critical ($\lambda = 12mm$) wavelength for the cylindrical roughness heights described in Table 5.1. An overview of the flowfield is shown in Figure 5.12 for the the $k = 36\mu m$ case. The figure shows contours of streamwise velocity and the spatial development of the crossflow vortices. The disturbance and spanwise variation of the flow field becomes apparent from 20% x/c with the disturbance growing rapidly and the formation of two distinct crossflow vortex formations at 40% x/c. Also evident from the contours at 40% x/c is the rollover effect, the low momentum fluid overlapping the high momentum fluid. The overall development, shape and size of the crossflow vortex conforms with descriptions and images from previous literature using the same base flow [42; 88; 114].

The experimental test case measured the receptivity of the roughness element arrays by applying hot-wire measurement scans at 15% and 20% x/c. The process to determine the amplitude and stationary mode shape for each roughness element is replicated for the UNS/LES to measure the accuracy of the method.

Figure 5.13 shows contours of mean flow streamwise velocity (u/U_e) at 15% x/c for the three roughness element heights. The figures on the left show the experimental hot-wire scans while the figures on the right show the simulation results. The hot-wire scans were taken with a 1mm spacing resulting in 65 locations across the span. The simulation however contains 156 spanwise locations across 24mm and the additional detail can be seen in the contours. The contours show a clear 12mm periodicity in the results for both the experiments and simulations. The increase in disturbance amplitude for the three roughness heights can also be clearly visualised for both the experiments and simulations.

Figure 5.14 shows mean flow streamwise velocity profiles taken from the contours shown in Figure 5.13. The mean boundary layer profile is displayed in the figure and coloured red. The mean velocity profile does not represent the base flow in absence of roughness element, but rather the disturbed flow downstream of the roughness array. The range of velocity profiles for the simulations match well with the experimental profiles.

Figure 5.15 shows the disturbance velocity profiles. These figures are obtained by calculating a mean of the individual velocity profiles (shown in red in Figure 5.14) and subtracting from each individual velocity profile in the span. The disturbance profiles make it much easier to show how the roughness height increases the disturbance and deviation away from the mean velocity profile. The simulation figures shown on the right display a good resemblance to the experimental data. The main deviation from the experimental results are in the positive disturbance, the simulation results show a stronger positive disturbance compared to the experiment, particularly for the 12 μm case. The increased positive disturbance is balanced from the UNS/LES by less negative disturbance. A possible reason for this imbalance is that more individual profiles are taken to calculate the mean profile, resulting in more symmetrical disturbance profiles.

The stationary mode shape can be calculated by taking the root-mean-square of the disturbance profiles, this shows the total disturbance amplitude of all modes at the streamwise location. Figure 5.16(a) shows stationary mode shapes for each roughness element at 15% x/c and Figure 5.17(a) at 20% x/c.

At 15% x/c the stationary mode shapes show a single lobe with a maximum amplitude at approximately $0.75mm$ from the wall. The stationary modes show a linear growth between each roughness height. The simulations for the larger roughness height show excellent agreement with the experimental profile. For the $k = 36\mu m$ and $k = 24\mu m$ cases the profiles lie very close to the experimental curve. However at $k = 12\mu m$ the amplitude of the disturbance for the simulation is approximately 25% greater than that of the experiment. The cause of the additional receptivity in the simulations is unclear but as the $k = 12\mu m$ is the smallest roughness height used the resolution of the grid may be insufficient. Also at this roughness height the experimental geometry showed a substantial standard deviation ($\sim 2\mu m$) in the roughness height which may also impact the receptivity.

The stationary mode shape is a representation of the total disturbance signal which may contain multiple modes. Using the boundary layer height at which the disturbance is at its maximum the mode shape can be spatially decomposed into its modal amplitudes by taking a Fast Fourier Transform (FFT) of the signal. Figure 5.16(b) shows a plot of amplitude against wave number for a spanwise signal at maximum amplitude ($0.75mm$) at 15% x/c. The figure shows predominant modal amplitudes at $12mm$ and $6mm$ at 15% x/c.

At 20% x/c the stationary mode shapes remain with a single disturbance lobe and a greater distance between amplitudes for each roughness height. The $k = 12\mu m$ and $k = 24\mu m$ cases match extremely well with the experiment, however, the $k = 36\mu m$ case underpredicts the maximum amplitude of the disturbance compared to the experiment. The difference in amplitude is approximately 15%. Figure 5.17(b) shows an amplitude spectral plot for a spanwise signal at maximum amplitude ($0.9mm$) at $20\%x/c$. The fundamental $12mm$ mode is the predominant wave number while the $6mm$ mode remains stable.

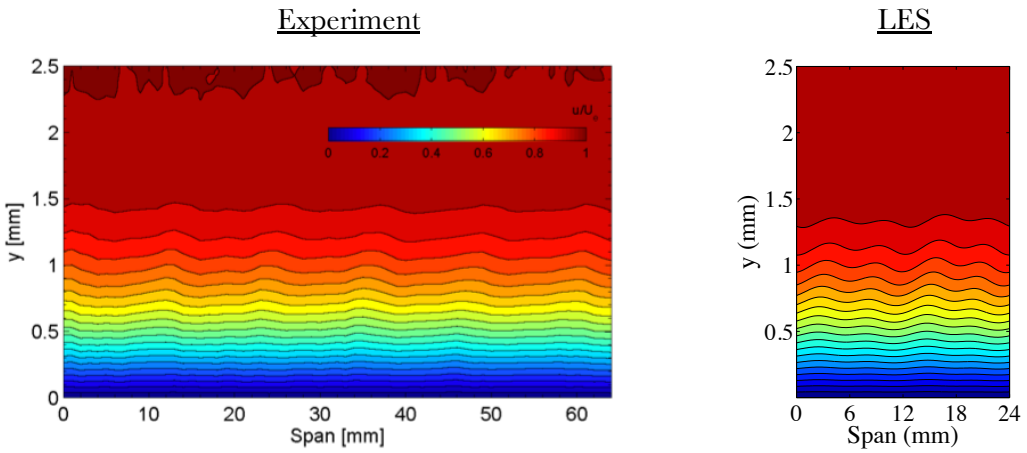

(a) $k = 12\mu m$, $\lambda = 12mm$

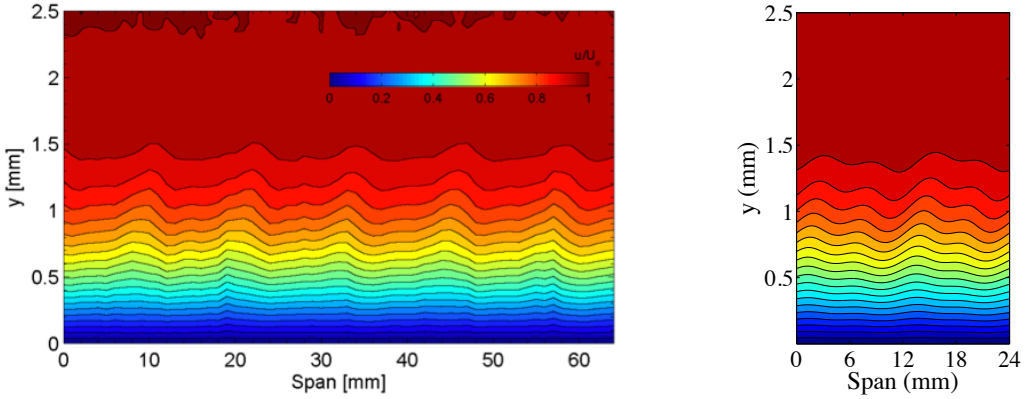

(b) $k = 24\mu m$, $\lambda = 12mm$

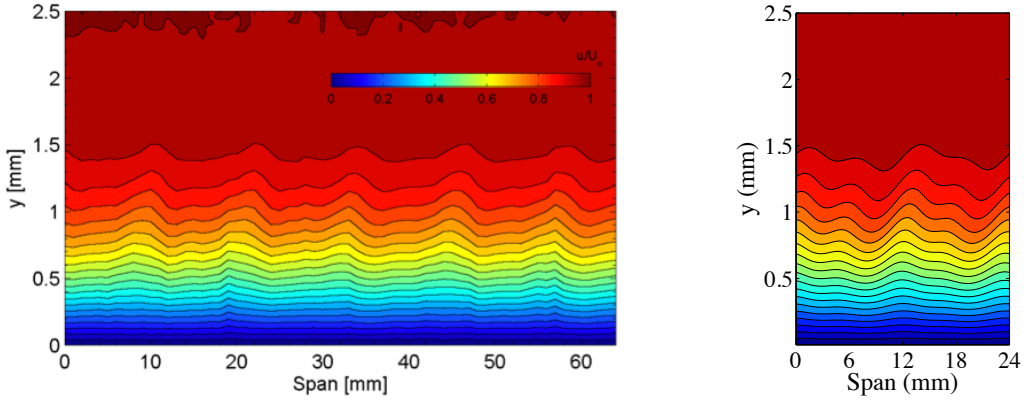

(c) $k = 36\mu m$, $\lambda = 12mm$

Figure 5.13: Contours of streamwise velocity (u/U_e) at 15% x/c Left: Experimental (Hunt [42]) Right: UNS/LES

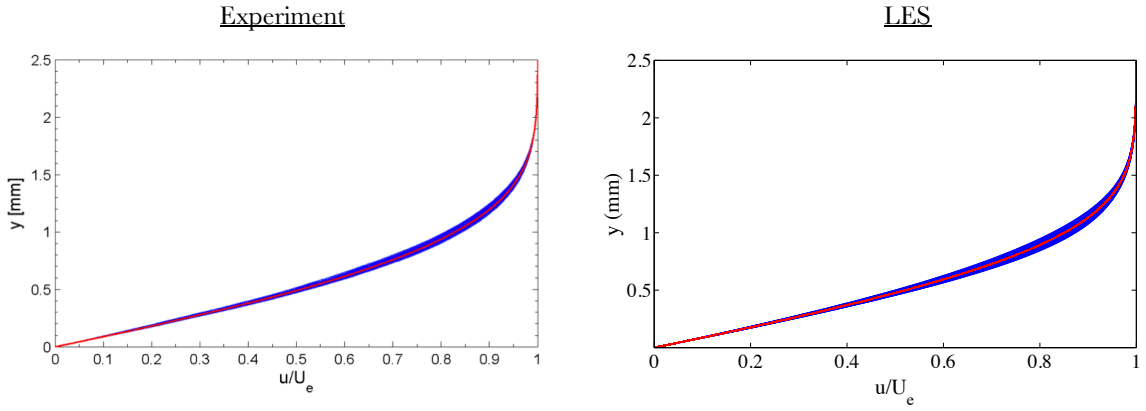

(a) $k = 12\mu m$, $\lambda = 12mm$

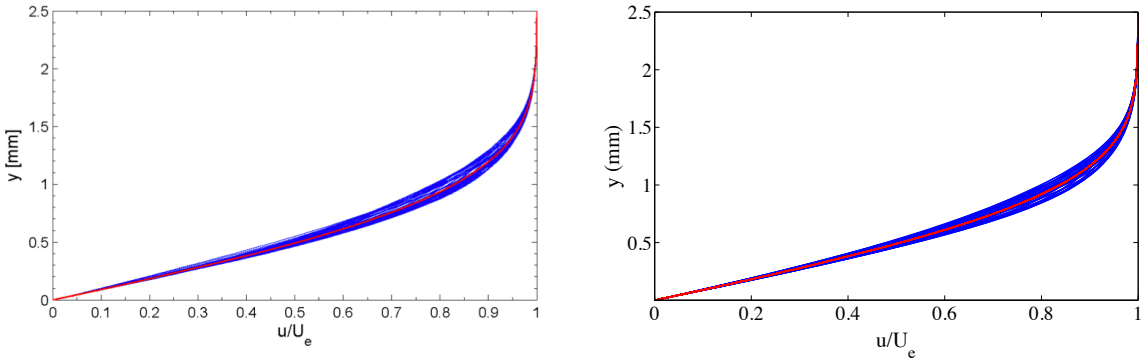

(b) $k = 24\mu m$, $\lambda = 12mm$

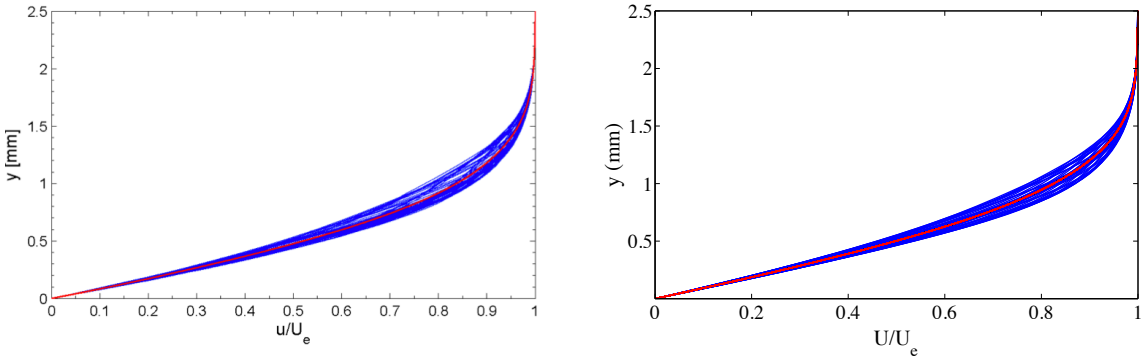

(c) $k = 36\mu m$, $\lambda = 12mm$

Figure 5.14: Spanwise array of mean-flow boundary-layer profiles across span at 15% x/c, The mean of the profiles is displayed in red, Left: Experimental (65mm span) (Hunt [42]) Right: UNS/LES (24mm span)

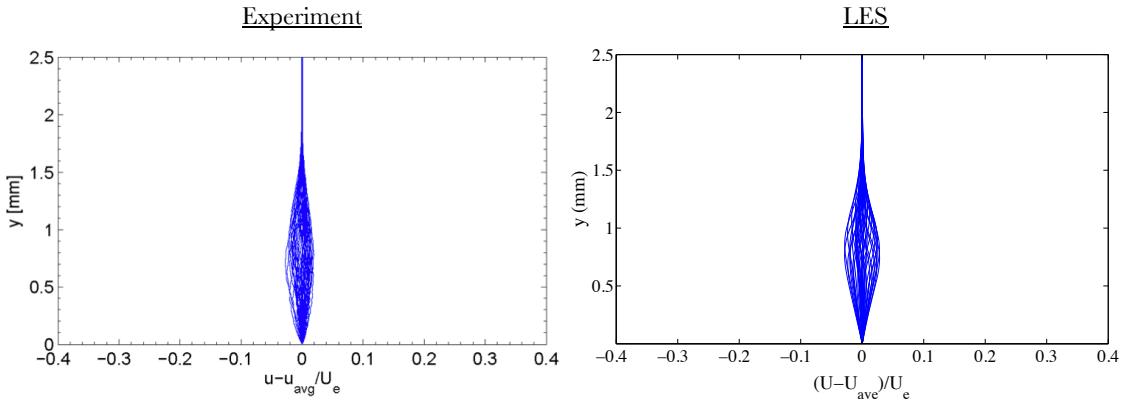

(a) $k = 12\mu m$, $\lambda = 12mm$

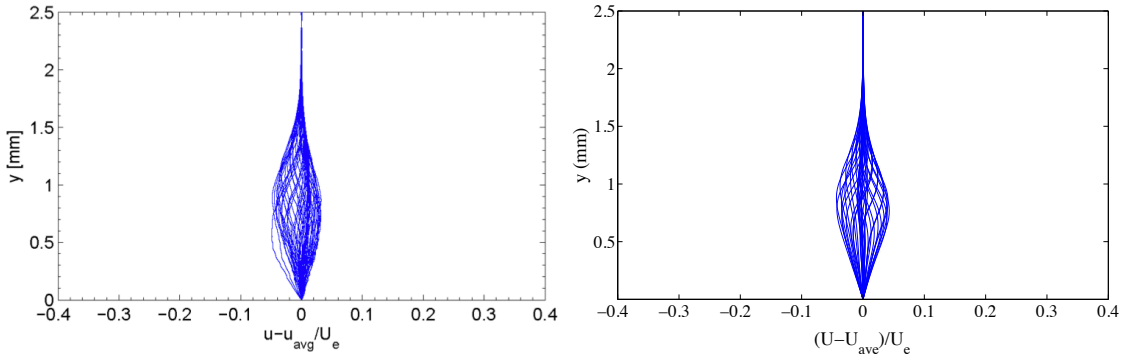

(b) $k = 24\mu m$, $\lambda = 12mm$

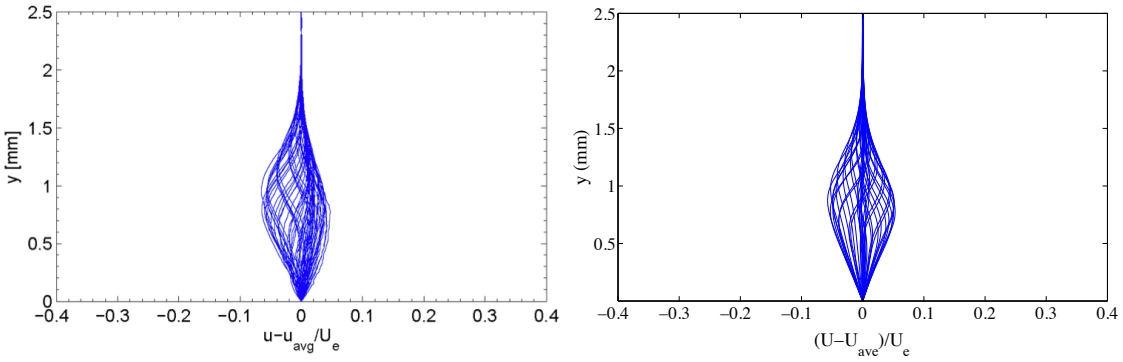

(c) $k = 36\mu m$, $\lambda = 12mm$

Figure 5.15: Spanwise array of disturbance velocity profiles across span at 15% x/c Left: Experimental (65mm span) (Hunt [42]) Right: UNS/LES (24mm span)

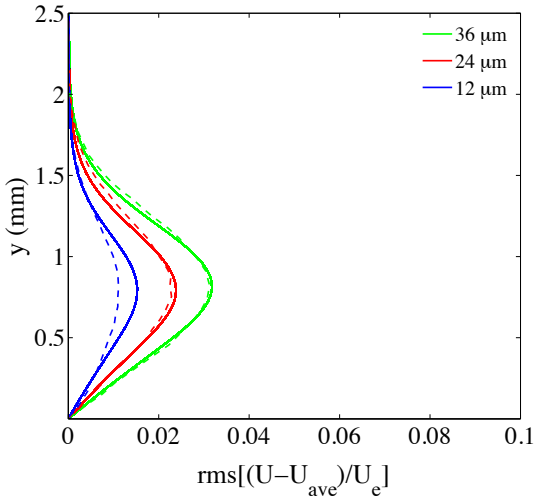

(a) Stationary crossflow mode shape

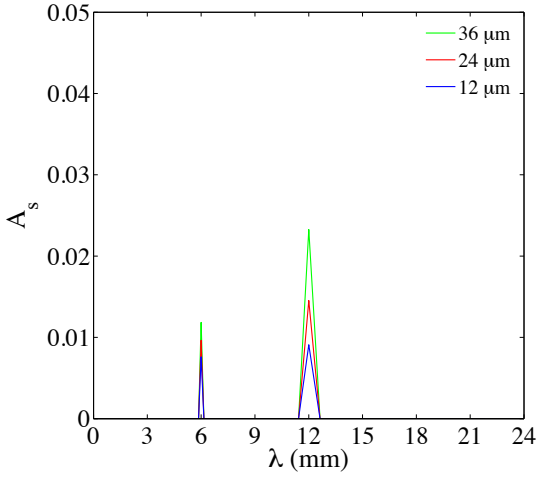

(b) Amplitude vs wave number for spanwise signal at maximum amplitude

Figure 5.16: Stationary mode shape and amplitude spectra at 15% x/c, $\lambda = 12mm$ (Roughness height, k, indicated on graph)

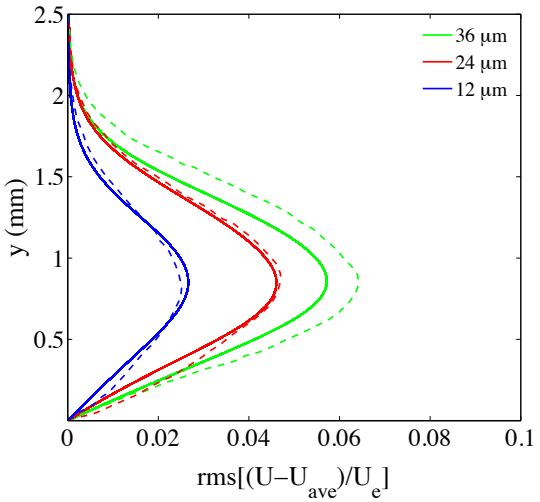

(a) Stationary crossflow mode shape

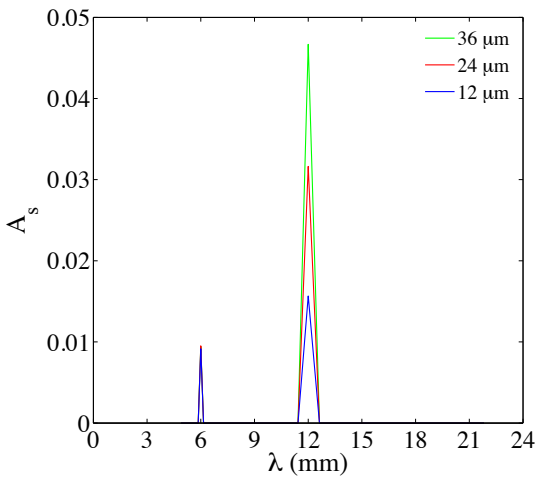

(b) Amplitude vs wave number for spanwise signal at maximum amplitude

Figure 5.17: Stationary mode shape and amplitude spectra at 20% x/c, $\lambda = 12mm$ (Roughness height, k, indicated on graph)

5.8.2 Receptivity of DRE Array at Control Wavelength

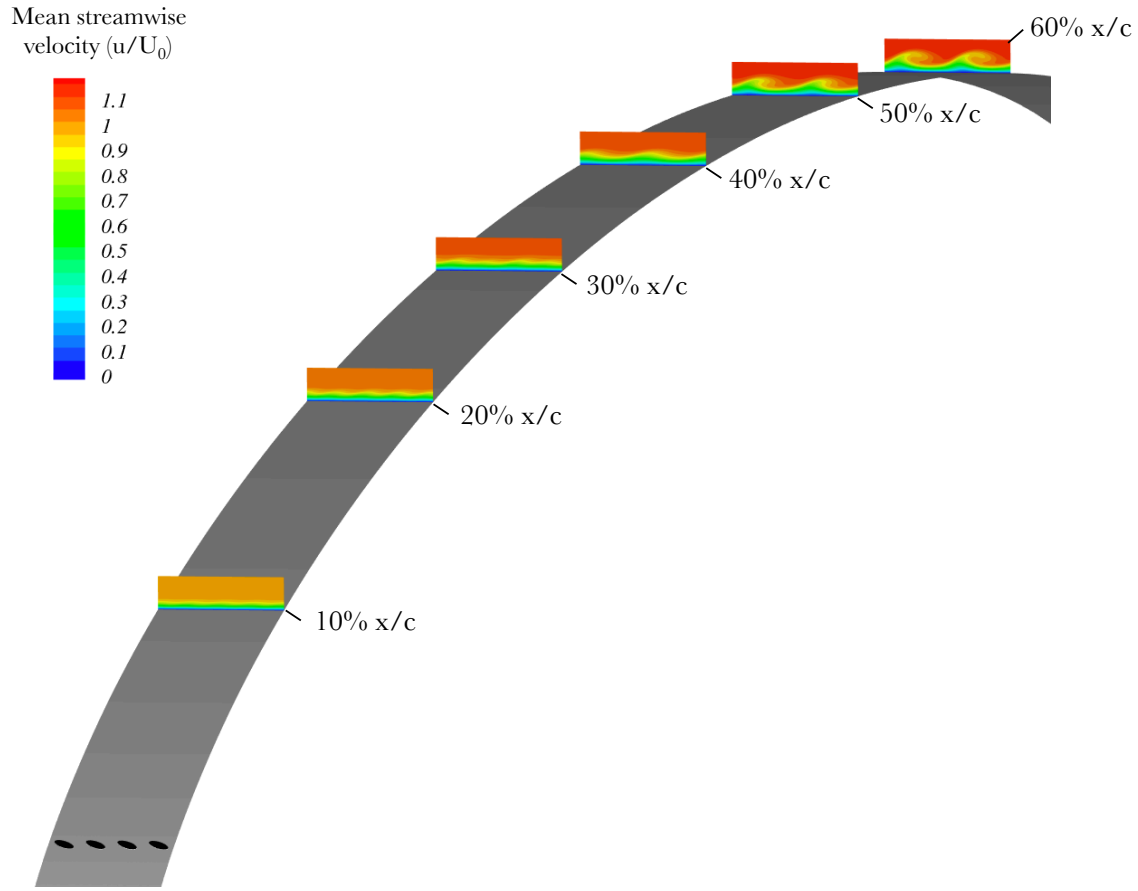

Figure 5.18: Contours of mean streamwise velocity u/U_0, $k = 42\mu m$, $\lambda = 6mm$, Contours taken at $x/c = 10\%, 20\%, 30\%, 40\%, 50\%, 60\%$

Simulation results were obtained for modelling of roughness arrays at the control wavelength $6mm$. Figure 5.18 shows an overview of the flowfield for the $6mm$ wavelength roughness array and $k = 42\mu m$. At 20 x/c the disturbance can be clearly visualised and a spanwise periodicity with a clear $6mm$ wavelength. At 30 x/c however a $12mm$ mode appears dominant resulting in 2 clear crossflow vortex formations by 50% x/c. The experiment by Hunt [42] used a naphthalene flow visualisation method to visualise the transition locations. They report that the transition location does not move downstream at the control wavelength but in fact moved upstream. A cause for this can be perhaps attributed to the size of the roughness elements being too large and the $12mm$ mode is not suppressed, clearly shown in Figure 5.18.

For the control wavelength the experimental test case measured the receptivity of the roughness element arrays by applying hot-wire measurement scans at 15% x/c.

Figure 5.19 shows contours of mean flow streamwise velocity (u/U_e) at 15% x/c for the three roughness element heights. The figures on the left show the experimental hot-wire scans while the figures on the right show the simulation results. As with the critical wavelength results the hot-wire scans were taken with a 1mm spacing resulting in 65 locations across the span. The simulation however contains 156 spanwise locations across a span of $24mm$. The larger roughness element sizes ($k = 27\mu m$ and $k = 42\mu m$) show a spanwise periodic signal with a clear $6mm$ wavelength and a good resemblance to the experimental data. The $k = 14\mu m$ case however features variations in amplitude for each disturbance across the span, suggesting that the initial amplitude was not captured accurately and that the grid may be too coarse near the cylinder for the smallest roughness height to capture the exact initial amplitude.

Figure 5.20 shows mean flow streamwise velocity profiles taken from the contours shown in Figure 5.19. The mean boundary layer profile is displayed in the figure and coloured red. Figure 5.21 shows the subsequent disturbance velocity profiles obtained by removing the mean of the individual profiles away from each individual profiles. For both figures the experimental plots are displayed on the left while the simulation results are displayed on the right. The simulation results show a good agreement with the experimental plots; the size and shape of the disturbance is accurately modelled along with the pattern of s-shaped profiles.

The stationary mode shape for the $6mm$ wavelength at $15\%x/c$ is shown in Figure 5.22(a) and the maximum modal decomposition amplitude plot in Figure 5.22(b). The stationary mode shape for the experiment shows a primary lobe centred at $0.9mm$ and a smaller secondary lobe at $0.2mm$. The simulations capture the primary lobe and the amplitude with very good accuracy for the $k = 27\mu m$ and $k = 42\mu m$ cases. However the $k = 14\mu m$ case over-predicts the amplitude by 33%, similar over prediction to the results of the smallest roughness height obtained for the critical wavelength. The secondary lobe in the lower part of the boundary layer however is not captured by the simulations, the secondary lobe may have been a remnant of the coarse resolution of the hot wire measurements. The amplitude plot in Figure 5.22(a) shows a predominant $6mm$ mode at this location with amplitude close to the overall disturbance amplitude.

Overall the results from both the critical and control spanwise wavelengths show good agreement to the experiment using the modified grid and the UNS/LES captures the flow features well.

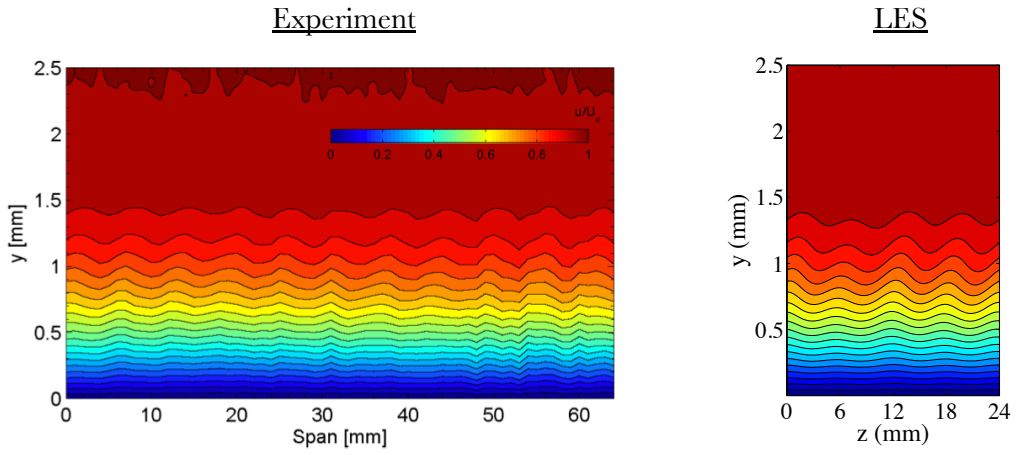

(a) $k = 14\mu m$, $\lambda = 6mm$

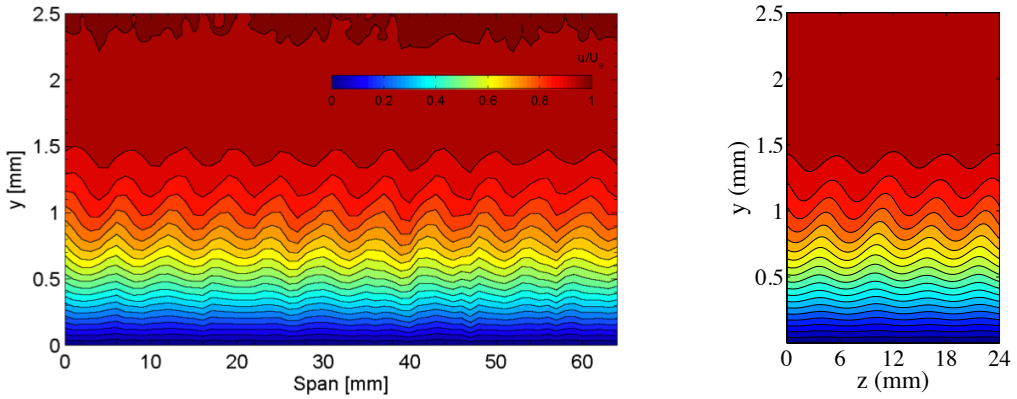

(b) $k = 27\mu m$, $\lambda = 6mm$

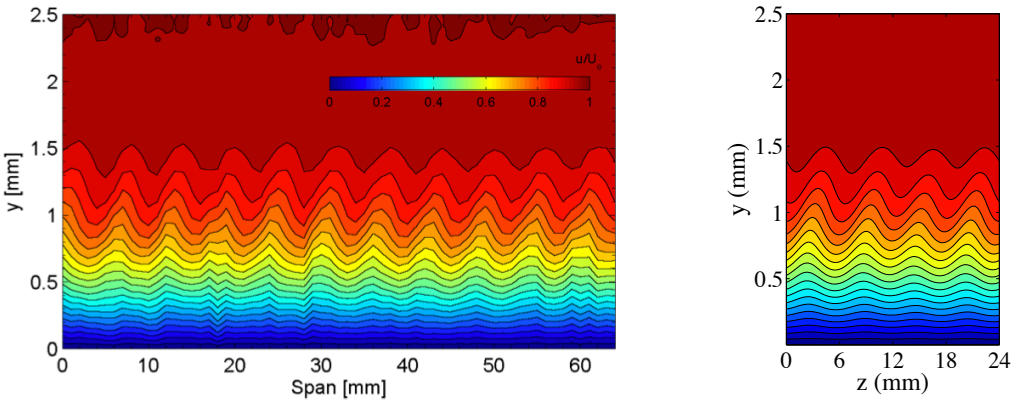

(c) $k = 42\mu m$, $\lambda = 6mm$

Figure 5.19: Contours of streamwise velocity (u/U_e) at 15% x/c Left: Experimental (Hunt [42]) Right: UNS/LES

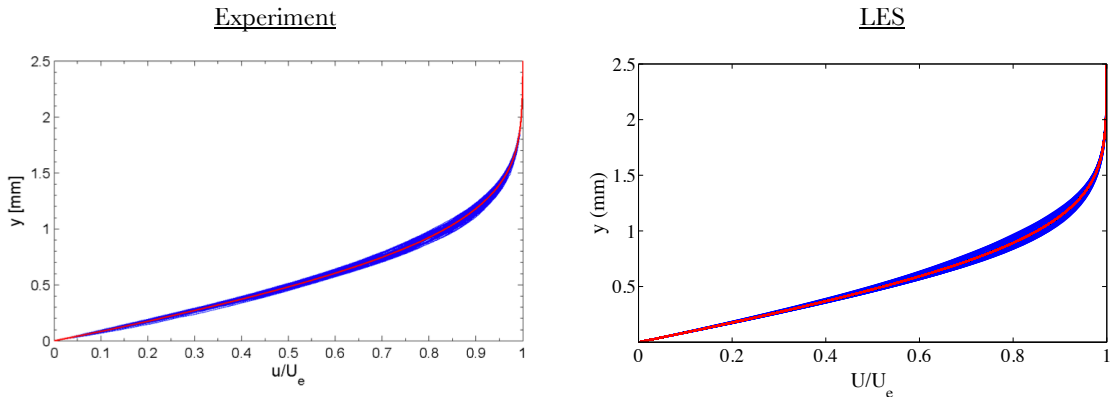

(a) $k = 14\mu m$, $\lambda = 6mm$

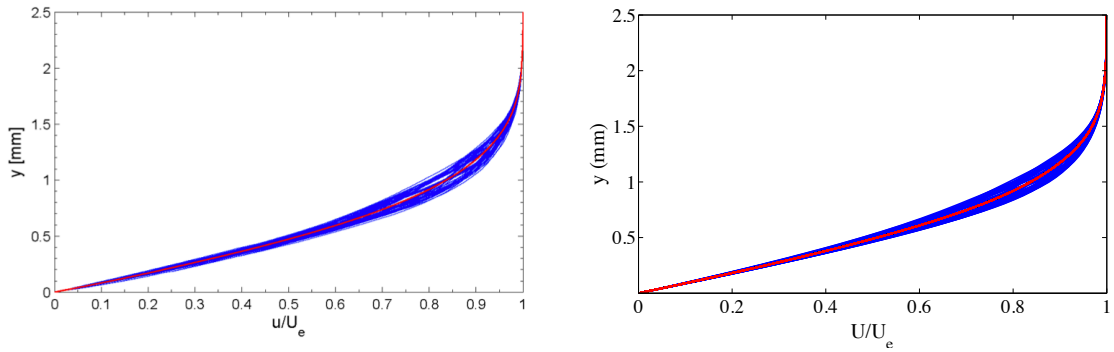

(b) $k = 27\mu m$, $\lambda = 6mm$

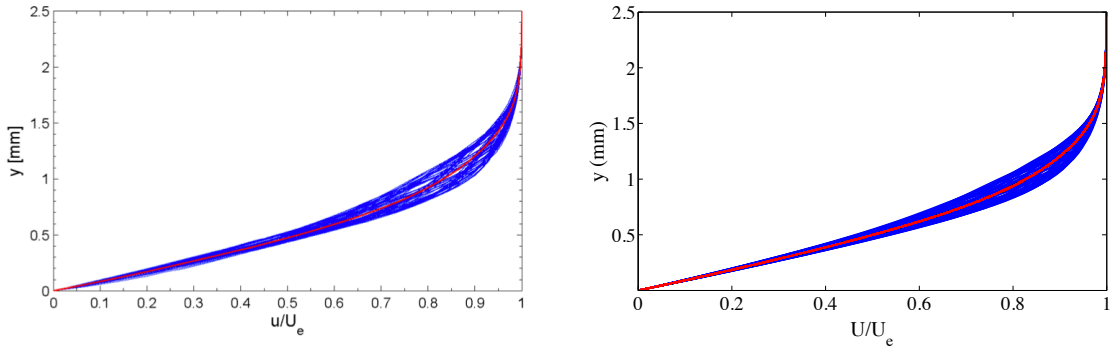

(c) $k = 42\mu m$, $\lambda = 6mm$

Figure 5.20: Spanwise array of mean-flow boundary-layer profiles across span at $15\%x/c$, The mean of the profiles is displayed in red, Left: Experimental (65mm span) (Hunt [42]) Right: UNS/LES (24mm span)

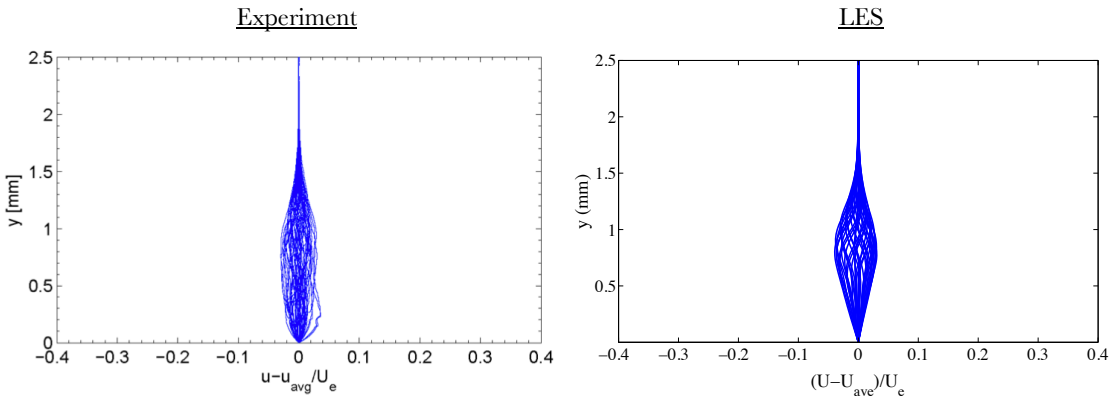

(a) $k = 14\mu m$, $\lambda = 6mm$

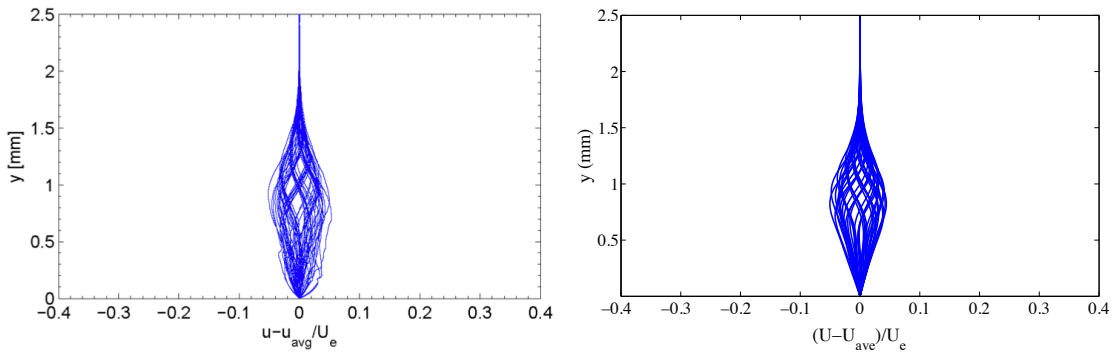

(b) $k = 27\mu m$, $\lambda = 6mm$

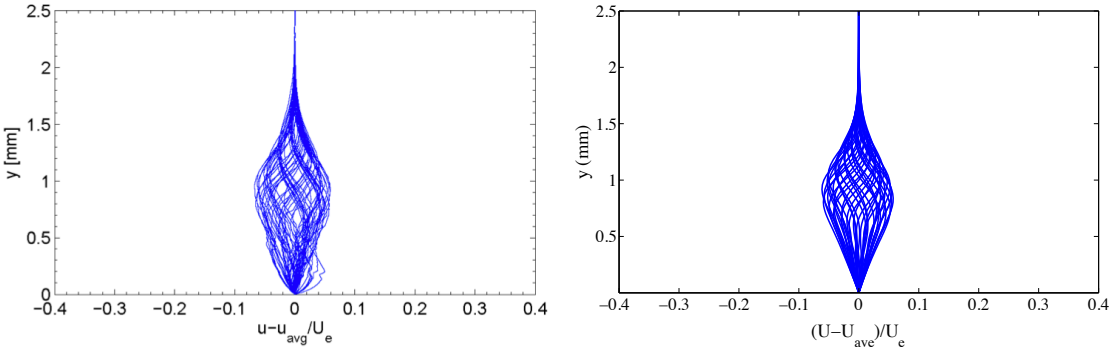

(c) $k = 42\mu m$, $\lambda = 6mm$

Figure 5.21: Spanwise array of disturbance velocity profiles across span at 15% x/c Left: Experimental (65mm span) (Hunt [42]) Right: UNS/LES (24mm span)

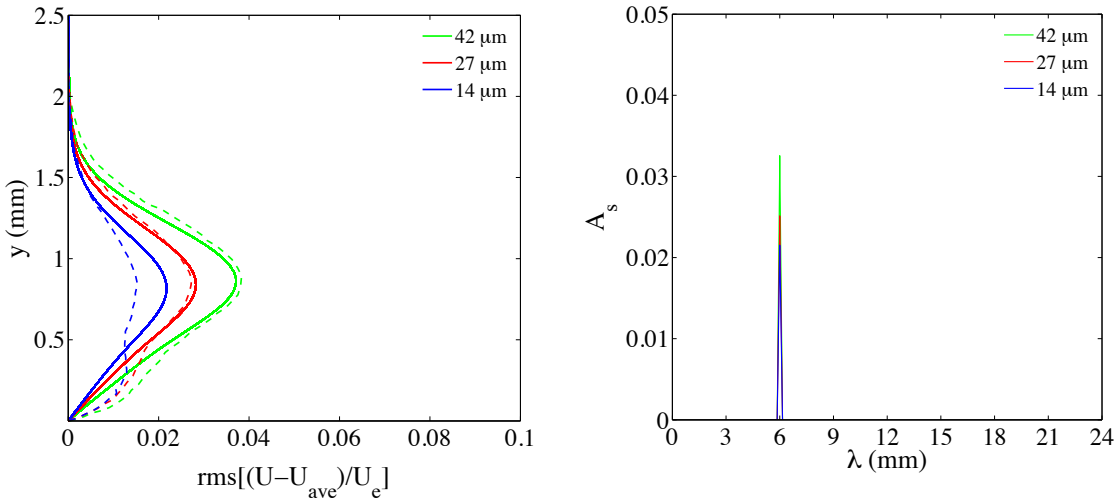

(a) Stationary crossflow mode shape

(b) Amplitude vs wave number for spanwise signal at maximum amplitude

Figure 5.22: Stationary mode shape and amplitude spectra at 15% x/c, $\lambda = 6mm$ (Roughness height, k, indicated on graph)

5.9 Transition to Turbulence

5.9.1 Introduction

The experimental results in Hunt [42] also provided results and images of the final location of transition to turbulence obtained using a Naphthalene flow visualisation (NFV) technique. Naphthalene when at near room temperature sublimes at a rate proportional to shear stress. Regions of higher shear stress, such as a turbulent wedge, will cause the crystals to sublime faster, providing a well-defined image of laminar and turbulent regions. Using this technique the experiments showed that without any artificial disturbance the baseline boundary layer flow was laminar aft of the pressure minimum at 70% chord. With the addition of artificial roughness in the form of the DRE's the transition location was shown to move upstream with the location varying between $50 - 80\%$ chord. This was to be expected especially for the critical wavelength cases which force the most unstable crossflow modes. A further, unexpected observation from the experiment was that transition location was shown to move upstream with increasing roughness height, they report that this has not been observed in previous transition experiments in the same facility. In previous experiments the transition line was shown to be fairly constant with increasing roughness heights.

The experimental results could not determine a single transition location as a percentage of the chord as they found that the transition locations were not spanwise uniform. The cause for this is related to the variation in roughness height of the distributed elements. Crossflow vortices breakdown locally, with the formation of a turbulent wedge and transition is observed in a saw-tooth pattern. This phenomenon was visualised in the experimental results however at a number of points in the span, the turbulent wedges were shown much further upstream of other locations. An explanation for this can be related to the roughness heights of the cylinders, the experiment reported mean heights, with a root mean square of $2 - 3\mu m$. In addition the thesis reports that a $1 - 2\mu m$ variation was possible when comparing roughness heights applied by different users setting up the experiment. Due to this uncertainty it was very difficult to get a uniform spanwise transition line. Transition is expected to be much more uniform across the span in flight conditions as the operating conditions are at an order of magnitude higher Reynolds number. With the larger Reynolds number, the initial disturbance amplitude is greater, therefore the the receptivity process would be less sensitive to local variations in roughness height.

The experiment compared transition images for DRE's spaced at both the critical and the control wavelength. The NFV results suggested that transition moved upstream for the control wavelength cases related to the critical wavelength cases. They suggest that as there is a large extent of laminar flow present in the baseline case (no roughness) the disturbance amplitudes are too large for flow control purposes. As the experiment already adhered to, the experiments were setup to measure initial amplitudes and growth rates at different roughness heights and wavelengths on an aerofoil with extensive laminar flow. The control method has been validated and proven in a number of other experimental studies described in the literature review in Chapter 3. Therefore it is not necessary to repeat the exercise in this study.

The main aim of this study was to demonstrate that simulation of the final breakdown to turbulence can be achieved using the current methodology and that it captures the correct physics and mechanisms. The benefit of the methodology used in this thesis is that the full transition process can be simulated, from initial receptivity of the disturbance to the final breakdown to turbulence.

The next subsection will detail the results obtained when assessing the final stages of transition for selected cases from the receptivity study.

5.9.2 Freestream Turbulence

The literature review reported how the secondary instability of crossflow vortices is sensitive to the level of freestream turbulence. The results so far in this thesis have been run in a 'quiet' environment, i.e. no artificial freestream turbulence (however there may have been numerical noise due to round-off error etc. To simulate the breakdown region in realistic conditions such as wind tunnels or atmospheric flight, a turbulence source was required in the freestream.

Freestream turbulence was introduced into the calculation using the synthetic eddy method (SEM) (described in Section 3.7). This method is capable of generating coherent turbulent structures with a given Reynolds stress tensor which are transported into the domain via convection through an arbitrary plane within the simulation. The method was originally written as a method for generating turbulence at inlet boundaries for LES calculations however the method presented in this thesis has modified the implementation to allow turbulent fluctuations to be introduced as a source, anywhere in the computational domain.

The perturbation plane was chosen at a position downstream of the roughness elements to ensure that the disturbances would not influence the primary instability and initial growth stages and not require a scaled disturbance level to account for dissipation. The perturbations were placed at a position in which secondary instabilities are likely to occur, which is downstream of the linear growth stage and in the region in which non-linear interactions occur. Figure 5.23 shows an image of the plane in which the free stream turbulence source was placed. The plane was placed at 40% of the chord for all cases discussed in this section. A simulation was run with an SEM plane upstream of the roughness elements however this showed no difference to the original results without SEM. This is likely as the initial amplitude of the disturbance is small and the fluctuations dissipated before they could make an impact.

The level of free stream turbulence was chosen to replicate the conditions in the wind tunnel test. This data was available in the experimental data provided by Hunt [42] and is listed in Table 5.3. The data is shown in the form of average velocity fluctuations (u'_{rms}) which were then converted into Reynolds stresses and chosen as the initial strength of the disturbances used for the SEM.

The laminar-turbulent transition region is discussed for three cases in this section:

1. $k = 12\mu m$, $\lambda = 12mm$, No freestream turbulence
2. $k = 12\mu m$, $\lambda = 12mm$, SEM freestream turbulence

3. $k = 14\mu m$, $\lambda = 6mm$, SEM freestream turbulence

A single case was chosen for both the critical and control wavelength cases and the transitional region is assessed for the critical case without any SEM freestream turbulence to judge the impact of the freestream turbulence on the results. The results of the region aft of the SEM plane are discussed in the next subsection.

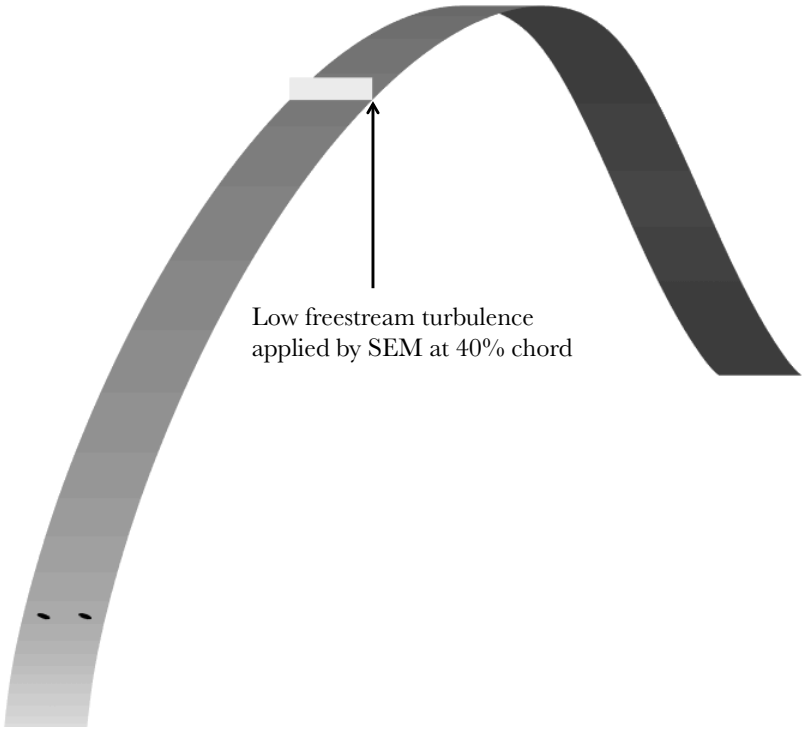

Figure 5.23: Freestream turbulence source applied at 40% of chord

Table 5.3: Experimental free stream turbulence root mean square velocity fluctuations [42]

$u'_{rms}/U_0 =$	0.138%
$v'_{rms}/U_0 =$	0.04%
$w'_{rms}/U_0 =$	0.021%

5.9.3 Results

Figure 5.24 shows an image of an instantaneous λ_2 iso-surface at level -10 and coloured in spanwise (w) velocity for the case $k = 12\mu m$, $\lambda = 12mm$ (critical wavelength) without SEM freestream turbulence. A negative value iso-surface of λ_2 shows the location of eddy vortex cores and is a useful quantity for visualising turbulence and vortical structures. The direction of the farfield inlet velocity is shown on the image for clarity. The figure shows the development of the saturated stationary crossflow vortices from 40% chord to the trailing edge of the wing with a 'wave' formation. It shows the transitional region at roughly 80% chord and clear turbulence with a range of scales in the turbulent region. While the image is useful for demonstrating laminar-turbulent transition, there is little evidence of the mechanism for final breakdown to turbulence. The transitional region at, 80% however coincides with the location of pressure gradient changeover, from favourable to adverse. This pressure gradient changeover region can be shown to be at 70% in the pressure coefficient plot of Figure 5.10(a). To further investigate and identify the mechanism of breakdown to turbulence for this case without generated freestream turbulence a closer image of instantaneous λ_2 from a side view is shown in Figure 5.25.

The figure identifies two locations of interest in the transitional region. The first is annotated 'A' in the figure and here the destabilisation of the upper part of the vortex core with structures are beginning to become visible. The second is annotated 'B' in the figure and is a significant streamwise distance prior to transition of high spanwise (w) velocity, very close to the wall. This area of high spanwise velocity ($> 0.15U_0$) occurs just aft of the pressure minimum and pressure gradient changeover, which may provide evidence to the mechanism for transition.

To investigate the transitional region further, Figure 5.26 shows a contour of instantaneous streamwise velocity at mid-span, with the y-axis scaled by 5 for clarity of the boundary layer. The figure shows a region of zero velocity in the lower part of the boundary layer between $75\% - 80\%$. This potential cause of this may be that the the boundary layer is separating, causing the bubble of zero streamwise velocity in the inner part of the boundary layer.

Figure 5.27 shows skin friction coefficient on the surface of the wing for all cases discussed in this section. The upper figure shows the plot for the critical case with no freestream turbulence. The skin friction coefficient contour is useful is showing the state of the boundary layer. The figure shows prior to turbulence, a region of near zero skin friction occurs. This region occurs within a streamwise distance of 5% chord

and is where the boundary layer separates due to the adverse pressure gradient and reattaches as a turbulent boundary layer. This turbulent attachment can be shown at 76% chord which is at a significantly higher skin friction value than before the separation occurred.

The figures have shown conclusive evidence for a laminar separation bubble mechanism for the critical wavelength case without freestream turbulence. Figure 5.28 shows a figure of λ_2 iso-surface for the critical wavelength case with the introduction of SEM perturbations. The figure is orientated identically to Figure 5.24 and shows a similar full picture of laminar-turbulent transition. The 'waves' can be seen from 40% to 70% chord. Aft of this region, laminar-turbulent transition can be seen with unsteadiness in the upper stationary vortex cores and a subsequent turbulent region. The mechanism for transition again is not clear from this figure alone but it does gives an overall view of the breakdown. Figure 5.29 shows a side view of the same image, zoomed in to the transitional region. Annotation 'A' highlights where the upper part of the vortex cores shows signs of unsteadiness and a 'ripple' effect. This occurs before breakdown to turbulence and is evidence of a secondary instability which is more in line with the breakdown of crossflow vortices shown in the literature. Downstream of the ripples on the vortex cores, transition to turbulence occurs rapidly, and clear turbulence with a range of length and velocity scales can be shown.

Figure 5.30 shows two sets of figures to further understand the breakdown region. The left hand side shows contours of time-averaged streamwise velocity fluctuation (u'_{rms}/U_0) at while the right hand side shows contours time-averaged streamwise velocity both at 10% chord intervals between 50% - 80% which is identified as the breakdown region from Figure 5.29. At 50% chord the time-averaged fluctuations can be seen, with the green regions of the contour, to be focused within the core of the stationary crossflow vortices. The amplitude of the averaged fluctuations is less than 5% of U_0. Further fluctuations can be seen on the side of the vortex (left of the vortex core) however they are at a much lower amplitude. These two regions of time-averaged fluctuations are in separate regions however at 60% chord they begin to coincide and smear and the amplitude of the fluctuations grows larger than 5% U_0. At 70% chord the fluctuations and unsteadiness are smeared across the lower part of the boundary layer and a full turbulent boundary layer can be seen at 80% chord with $> 10\%$ averaged streamwise fluctuations and the increased boundary layer height in the mean velocity contour. An interesting point is that in the turbulent region at 80% chord the stencil of the original stationary crossflow vortices mean flow remains

clearly visible.

The middle contour of Figure 5.27 shows skin friction coefficient on the surface of the wing for the critical wavelength case with SEM freestream turbulence. The contour shows clearly the location of laminar-turbulent transition compared to the critical wavelength case without SEM turbulence (upper contour). The transition location is roughly 75% chord without SEM turbulence and transition can be shown to move downstream at 80% chord with SEM turbulence. This was not an expected result of the simulation as it seems counter intuitive for the introduction of unsteadiness to result in laminar-turbulent transition moving downstream. A possible explanation into the delay in laminar-turbulent transition could be due to a change in mechanism of breakdown. Without freestream turbulence transition occurs due to laminar separation in the adverse pressure gradient region. However with the addition of artificial turbulence, the unsteadiness may have acted to prevent the laminar boundary layer from separating. Looking at Figure 5.27 there is a significant reduction in blue (zero skin friction) upstream of the turbulent red region. This reduction in separation is likely the cause of the delay in transition. Also when assessing Figure 5.30 there is substantial unsteadiness in the laminar boundary layer at 70% which could have acted to prevent the separation of the laminar boundary layer.

The critical wavelength case has shown interesting results for the laminar-turbulent transition region and demonstrated the capability of the UNS/LES simulation method. A final test case using a control wavelength was used to test the method with SEM freestream turbulence. This test case used the smallest height at $k = 14\mu m$, as it is more representative of control roughness heights.

Figure 5.28 shows a full view iso-surface of λ_2 for the control wavelength case and Figure 5.32 shows the same image zoomed in from a side view. The figure shows that transition occurs slightly earlier for the control case than the critical. A 'wave' formation in the iso-surface can be shown similar to the critical cases for the stationary crossflow vortices. Aft of 60% chord, however, fluctuations begin to occur and turbulence can be seen clearly in Figure 5.32 by 80% chord.

Figure 5.33 shows contours of time-averaged streamwise velocity fluctuation on the left and time-averaged streamwise velocity on the right as in Figure 5.30. Contours are shown for $60, 70$ and 80% chord. At 60% chord, strong time-averaged fluctuations can be seen to occur at the core of the vortex. A region of fluctuations also occurs at the top of the vortex, however, lesser in amplitude. At 70% chord the fluctuations have grown to a considerable amplitude ($> 10\%U_0$) and have smeared into multiple

modes. By 80% chord a full turbulent boundary layer can be shown. The mechanism for transition is similar to that of the critical wavelength however transition occurs further upstream.

Figure 5.27 shows clearly the move in transition location in the control wavelength case. The lower contour in Figure 5.27 shows skin friction coefficient on the surface of the wing. Transition can be seen to occur at approximately 72% chord, while transition occurs at 80% chord for the critical wavelength case with artificial turbulence. The control wavelength case shows that one of the crossflow vortices is much more unstable than the other and triggers the breakdown to turbulence. At 70% chord it is clear that one vortex triggers the breakdown locally and the start of a turbulent wedge forms, typical of crossflow transition. The cause for transition to move upstream using the control wavelength is unclear but likely due to the larger unsteadiness in one of the stationary crossflow vortices. This asymmetry may have occurred in the non-linear modification of the mean flow in the decay of the control wavelength modes and the growth of the critical modes. This modification of the mean flow may have resulted in larger amplitude unsteadiness in the laminar boundary layer and an earlier onset of the secondary instability.

The main aim of this exercise was to ensure that the simulation method is capable of simulating crossflow transition with physical results. This has been shown for three test cases and the effect of imparting artificial freestream turbulence has been shown. It is the recommendation of the author that a more detailed analysis is required for the secondary instability region using the UNS/LES method and a separate validation study must be developed. Subsequently a study varying the level of freestream turbulence and the impact on transition would be a insightful exercise to further validate this simulation method.

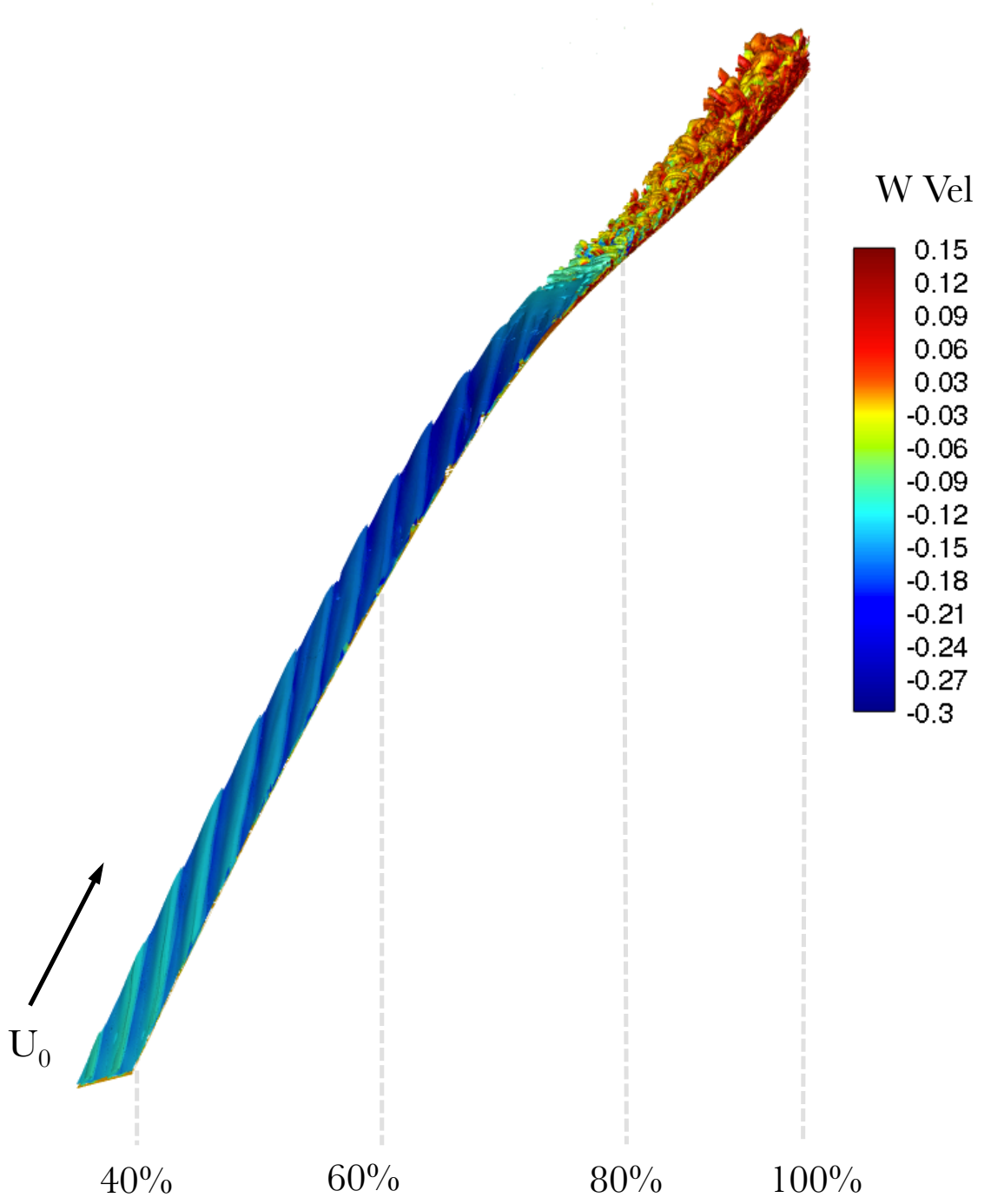

Figure 5.24: λ_2 Iso-surface (Level = -10) Iso-surface coloured in w (spanwise) velocity (Iso-metric view), Case: $k = 12\mu m$, $\lambda = 12mm$, No freestream turbulence

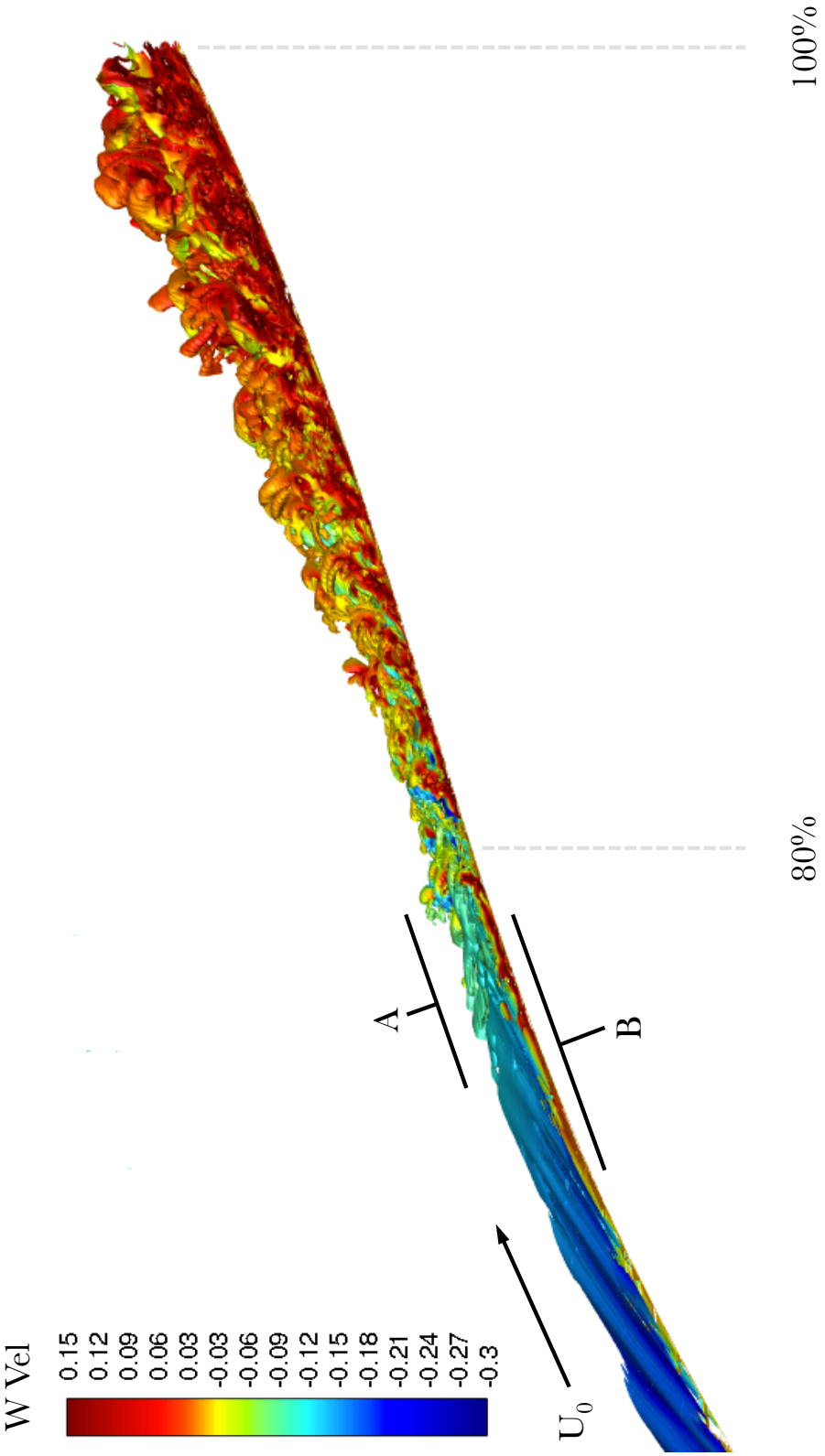

Figure 5.25: λ_2 Iso-surface (Level = -10) Iso-surface coloured in w (spanwise) velocity (Side view), Case: $k = 12\mu m$, $\lambda = 12mm$, No freestream turbulence

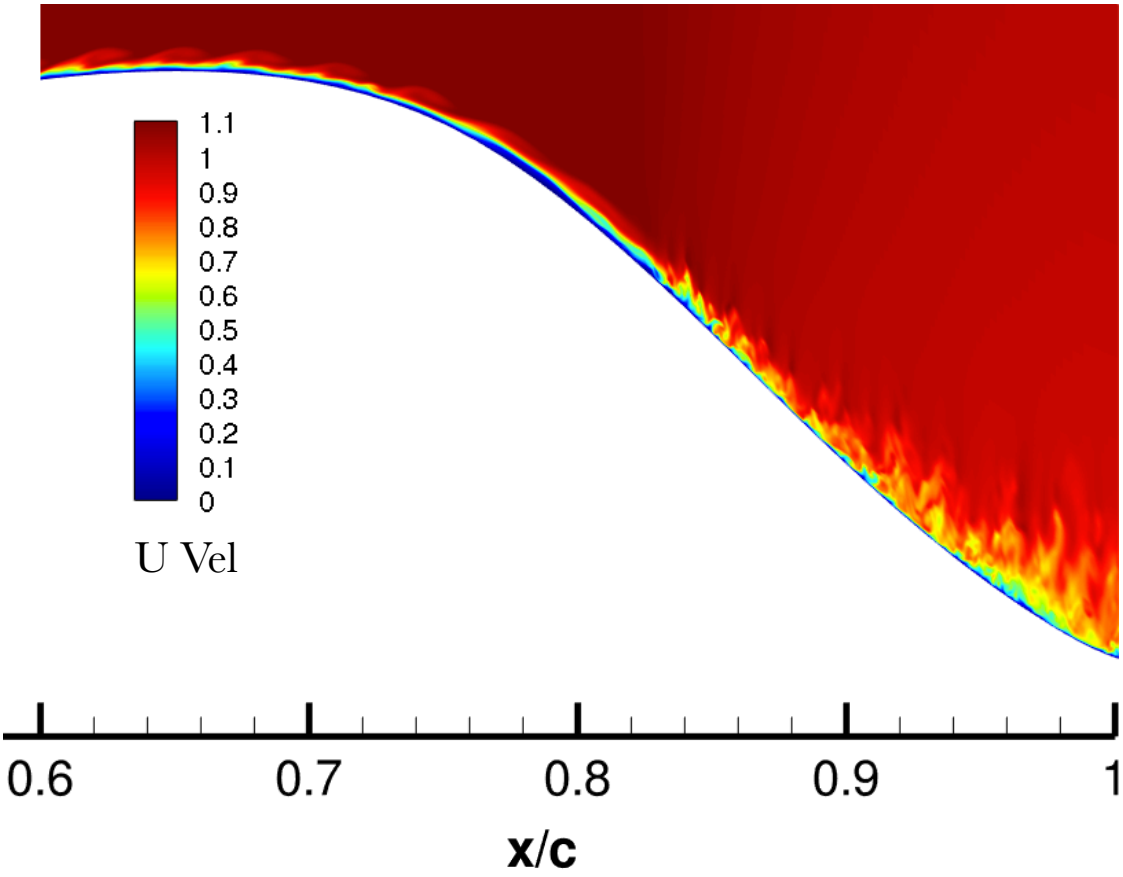

Figure 5.26: Contour of u (streamwise) velocity at mid-span, image scaled 5x in the y-direction for clarity of the boundary layer, Case: $k = 12\mu m$, $\lambda = 12mm$, No freestream turbulence

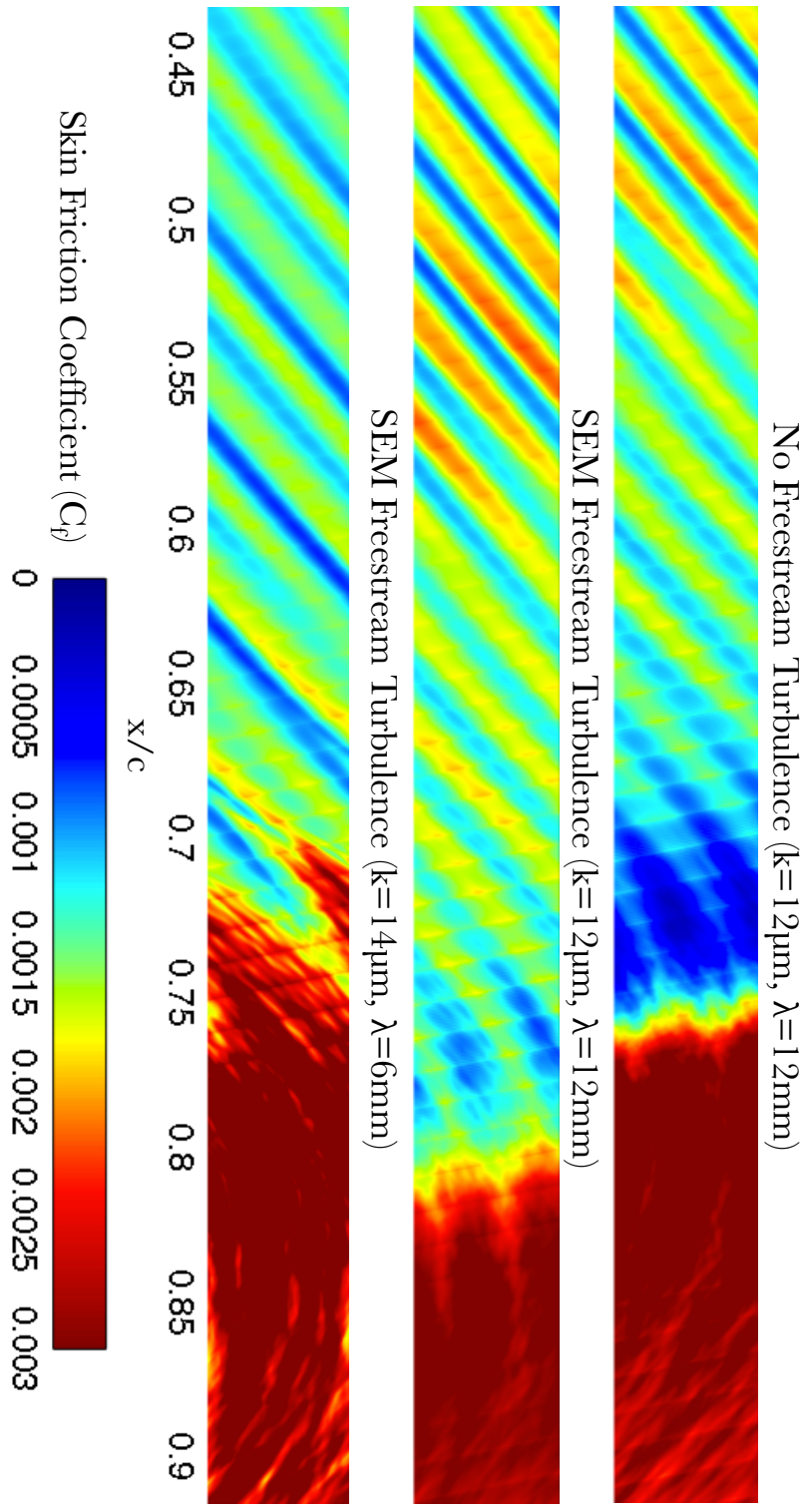

Figure 5.27: Contours of skin friction coefficient (C_f) for all three test cases (Upper: Critical Wavelength No Freestream Turbulence, Middle: Critical Wavelength SEM turbulence, Lower: Control Wavelength, SEM turbulence)

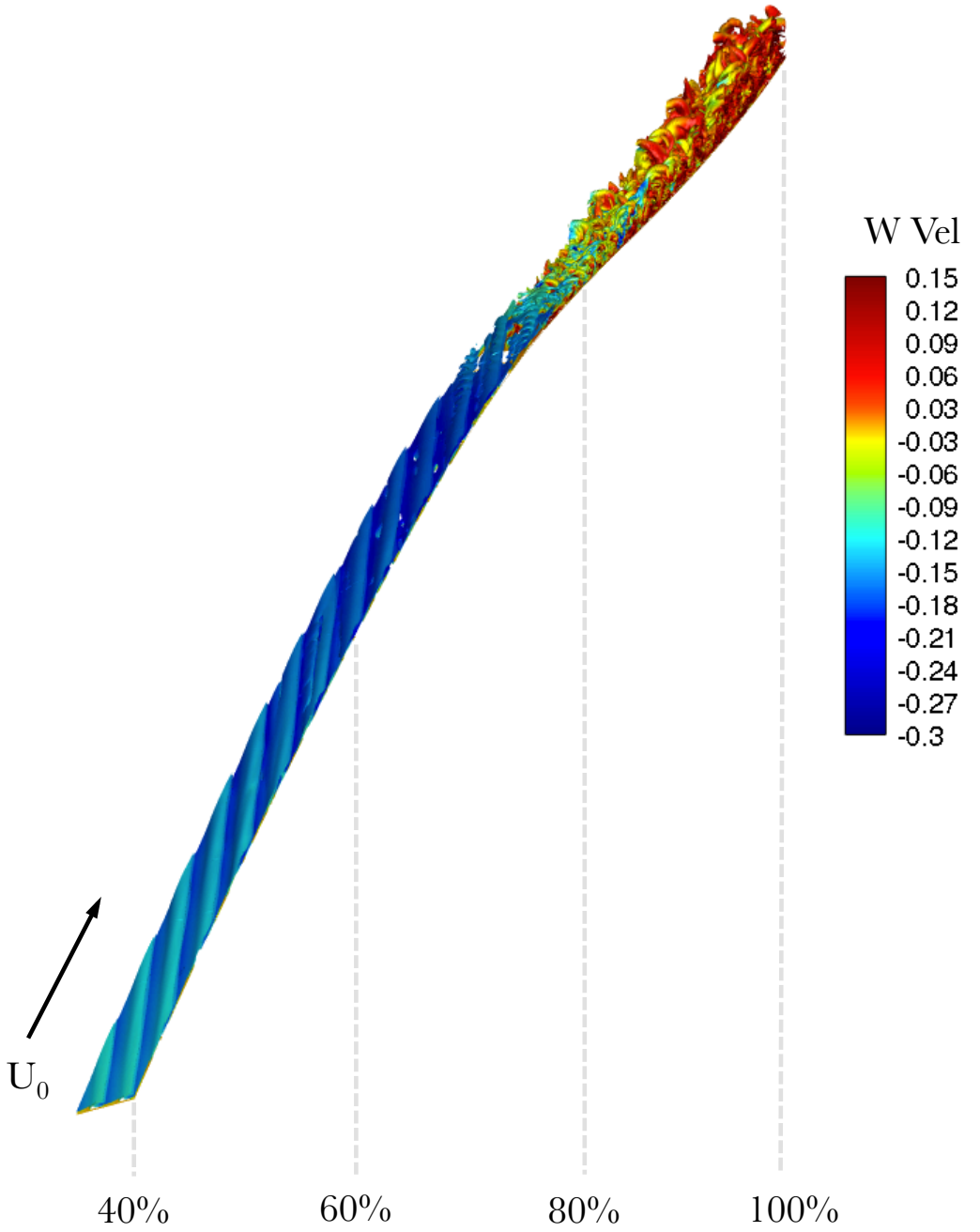

Figure 5.28: λ_2 Iso-surface (Level = -10) Iso-surface coloured in w (spanwise) velocity (Iso-metric view), Case: $k = 12\mu m$, $\lambda = 12mm$, SEM freestream turbulence

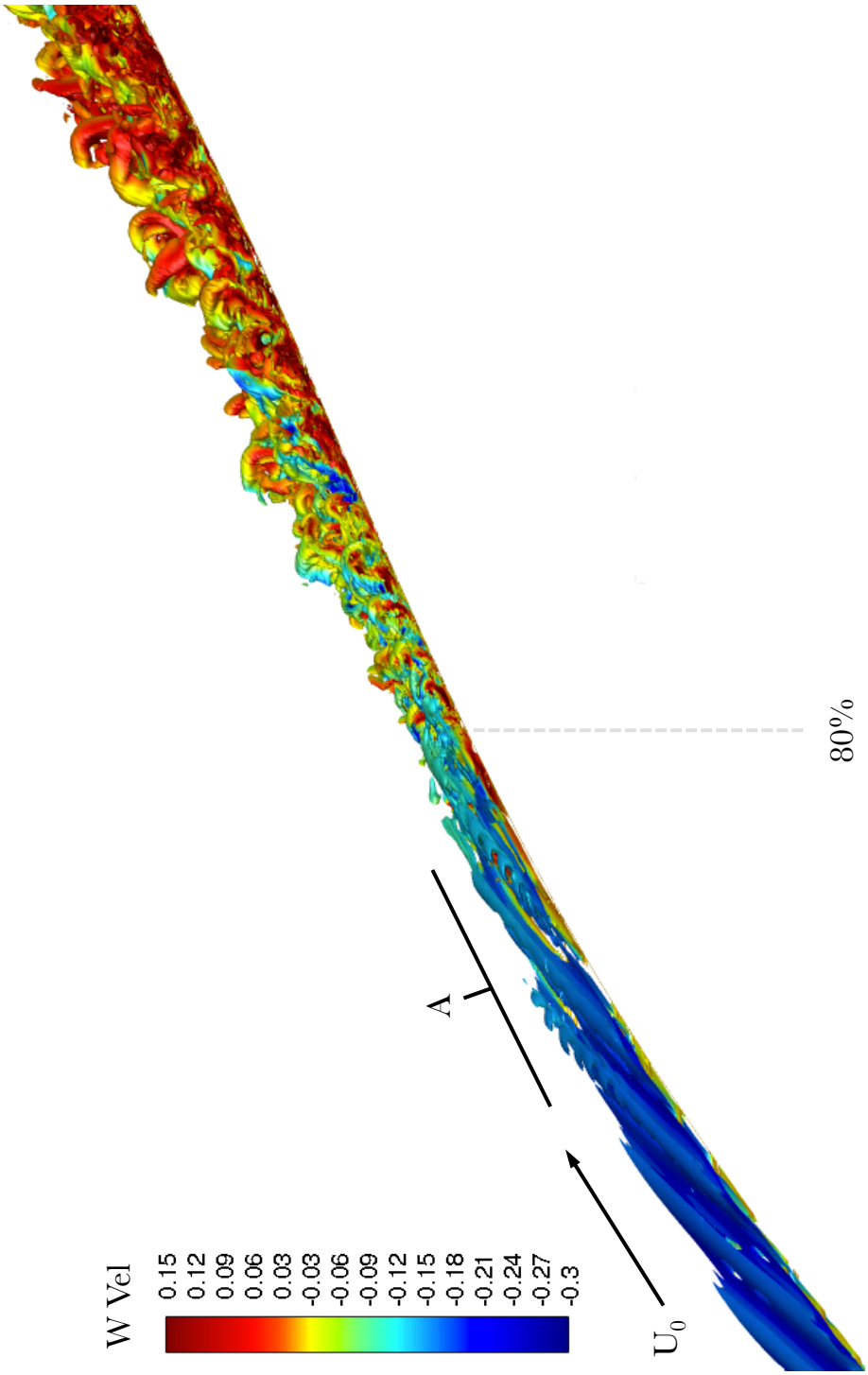

Figure 5.29: λ_2 Iso-surface (Level = -10) Iso-surface coloured in w (spanwise) velocity (Side view), Case: $k = 12\mu m$, $\lambda = 12mm$, SEM freestream turbulence

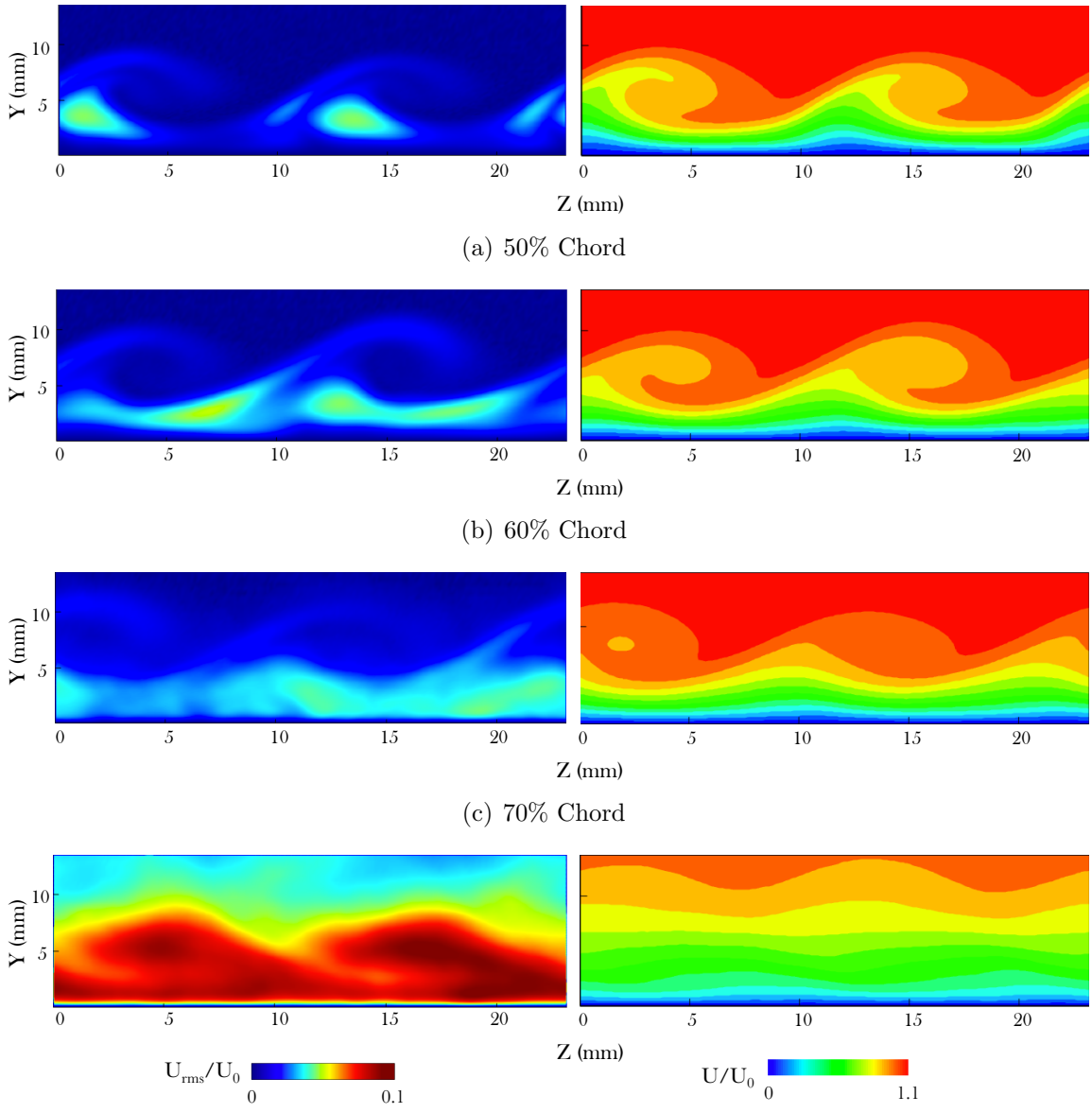

(a) 50% Chord

(b) 60% Chord

(c) 70% Chord

(d) 80% Chord

Figure 5.30: Left: Mean velocity fluctuation U_{rms}/U_0 Right: Mean velocity U/U_0, Case: $k = 12\mu m$, $\lambda = 12mm$, SEM freestream turbulence

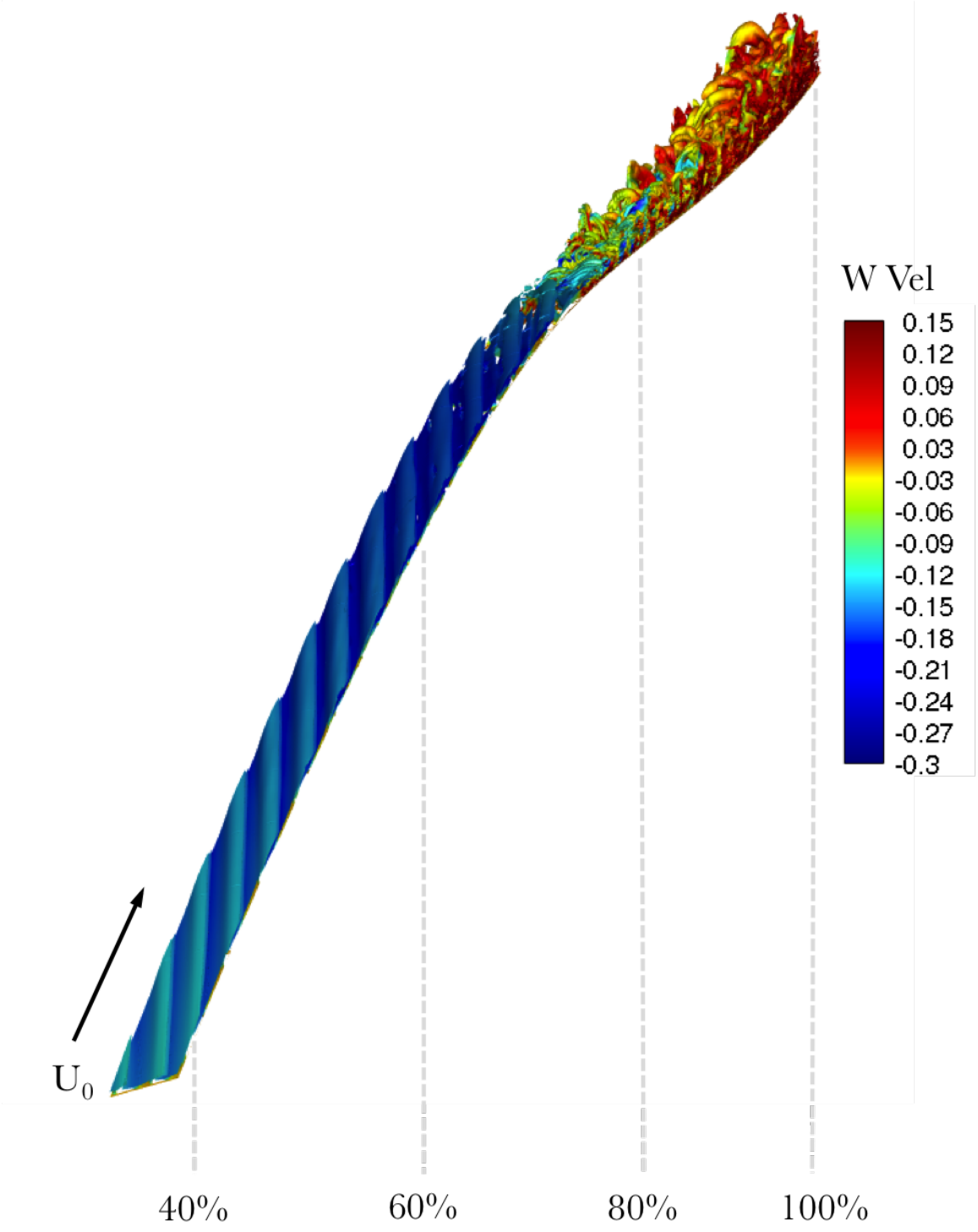

Figure 5.31: λ_2 Iso-surface (Level = -10) Iso-surface coloured in w (spanwise) velocity (Iso-metric view), Case: $k = 14\mu m$, $\lambda = 6mm$, SEM freestream turbulence

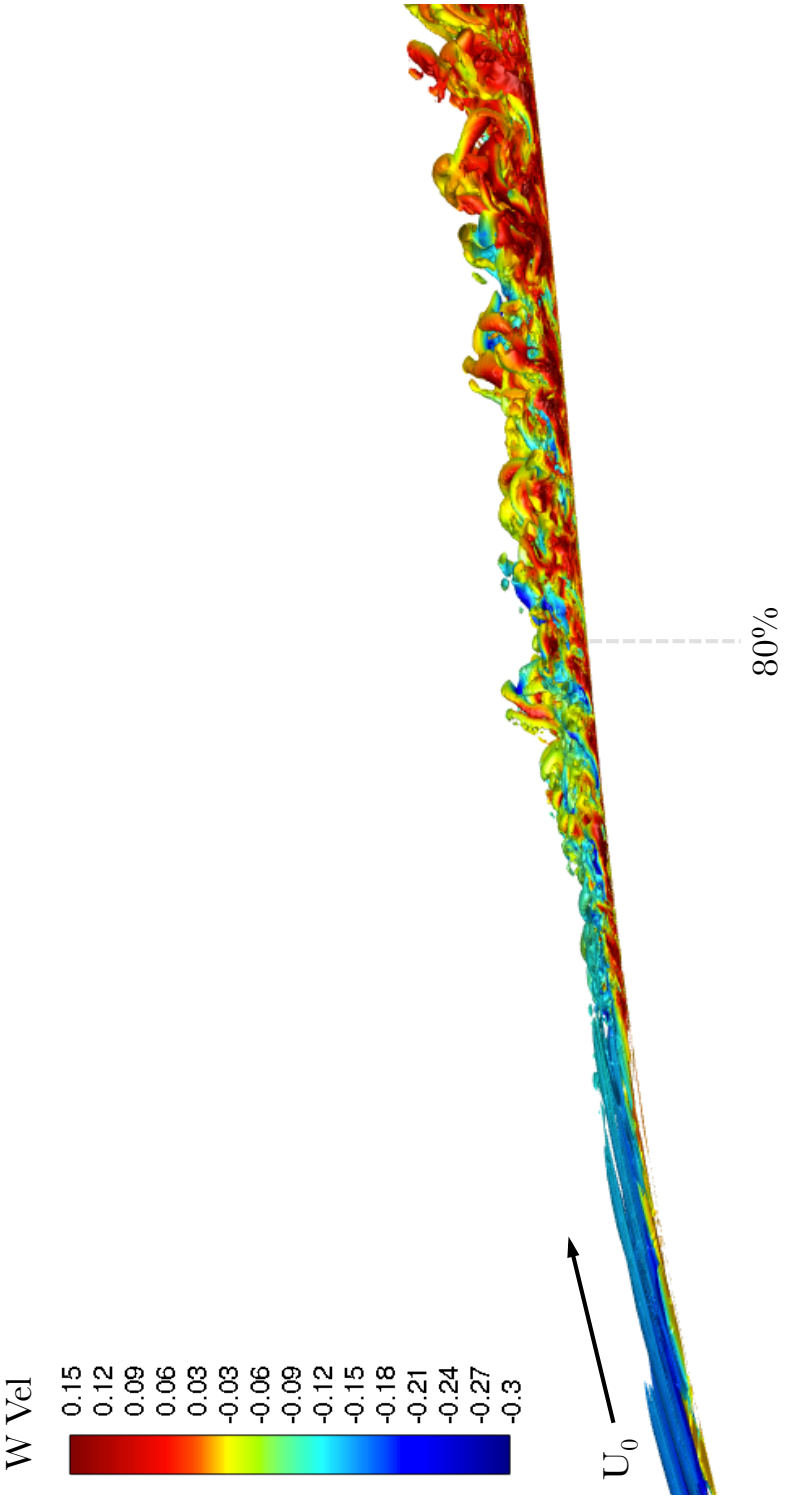

Figure 5.32: λ_2 Iso-surface (Level = -10) Iso-surface coloured in w (spanwise) velocity (Side view), Case: $k = 14\mu m$, $\lambda = 6mm$, SEM freestream turbulence

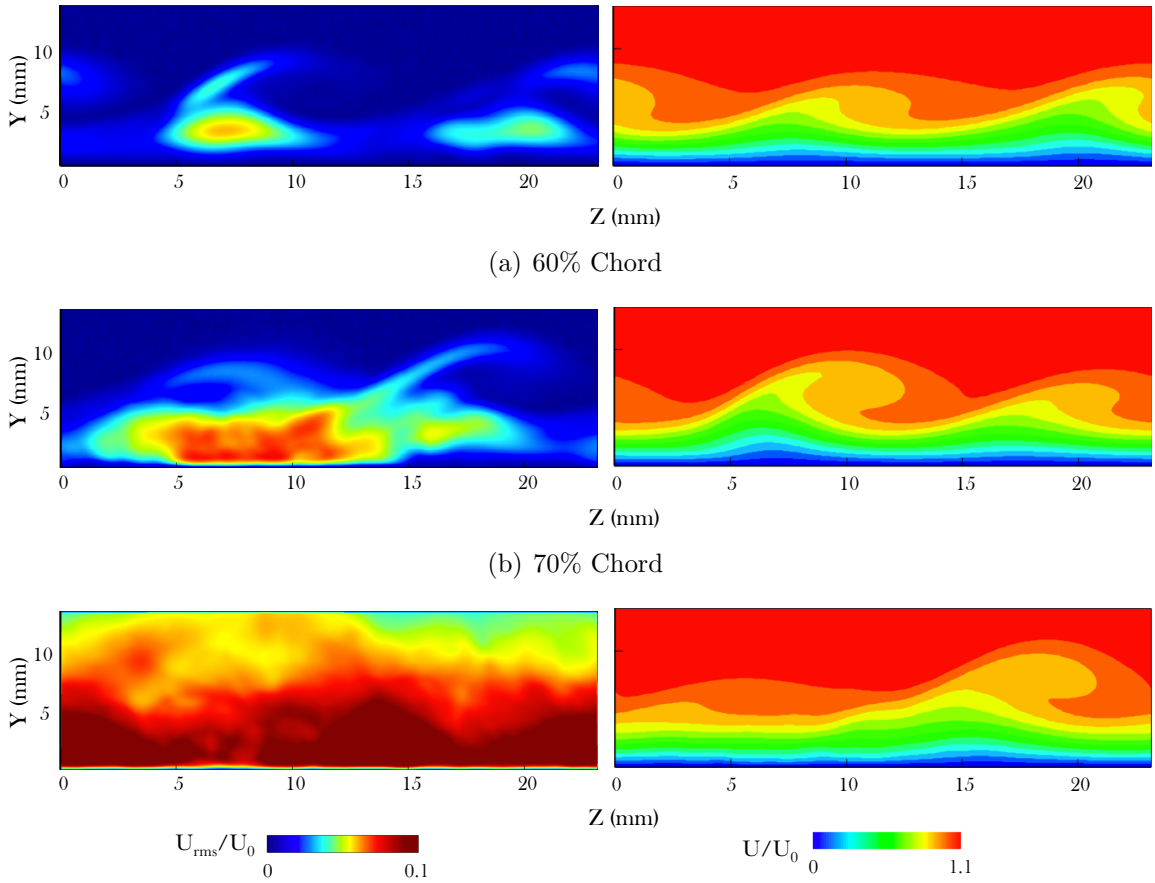

(a) 60% Chord

(b) 70% Chord

(c) 80% Chord

Figure 5.33: Left: Mean velocity fluctuation U_{rms}/U_0 Right: Mean velocity U/U_0 Case: $k = 14\mu m$, $\lambda = 6mm$, SEM freestream turbulence

5.10 Closure

This chapter aimed to develop the UNS/LES approach to modelling of crossflow transition using a more challenging test case. The chosen test case was based upon the experiments run in the Doctoral Thesis of Lauren Hunt [42] from Texas A&M. The experiment uses a ASU(67)-0315 aerofoil with a 45° sweep angle and a chord based Reynolds number of 2.4 million. An Re_c of 2.4 million presents a significant challenge for a wall-resolved numerical approach. The experiment conducted a number of tests on distributed roughness elements spaced at a critical and control wavelength and for a number of roughness heights. The aim of the work presented in this Chapter were to investigate the simulation capability of explicitly modelling distributed roughness elements and compare results to the experiments.

An initial and modified grid were developed to study the effect of grid spacing in capturing the disturbance around each roughness element. The initial grid contained a coarse grid spacing around the roughness element which led to a refined modified grid. The initial grid failed to capture the disturbance accurately and further grid refinement was required in the immediate vicinity around the cylinder. The cylinders disturbed the flow up to 1/5 of the cylinder diameter ($0.6mm$) away from the cylinder and this region must be resolved carefully. For the modified grid in this paper the region was capturing using 10 computational grid cells. Streamlines around the cylinder showed how the flow deflects around the roughness element with a disturbance in the spanwise velocity of up to $0.02Q_0$.

For the critical wavelength case ($\lambda = 12mm$) results were obtained at roughness heights $k = 12, 24$, and $36\mu m$. The simulations were compared to experimental results at $15\%x/c$ and $20\%x/c$. The simulations compared well with the experimental data, the stationary mode shapes showed excellent agreement in terms of size, shape and amplitude of the disturbance. Decomposition of the spanwise signal showed a predominant $12mm$ mode with shorter peaks at $6mm$. The overall view of the flow field showed the $12mm$ mode dominate to form saturated crossflow vortices.

For the control wavelength case ($\lambda = 6mm$) results were obtained at roughness height $k = 14, 27$, and $42\mu m$. The simulations were compared to experimental results at $15\%x/c$. Much like the critical wavelength case the simulations successfully captured the disturbance to a good agreement with the experimental data. The $6mm$ mode dominates the spanwise signal and a clear spanwise uniformity is shown. The amplitudes match well with the experimental data however the smallest roughness height ($k = 14\mu m$ over predicts the amplitude by 33%. The cause of this could be

that for this roughness height the grid may require addition cells, or can be attributed to variations in roughness element shape and size in the experiments. The overall flow field showed the $6mm$ mode decay by $30\%x/c$ and the critical wavelength begin to grow.

Finally, the final stages of transition were discussed. To simulate a similar external free stream environment to the experiment, a synthetic turbulence generation method, called the Synthetic Eddy Method (SEM) was employed. An SEM plane was placed at 40% chord aft of the linear growth stage. This plane was placed for three cases: a critical wavelength case at $12\mu m$ with and without artificial freestream turbulence using SEM and a control wavelength case at $14\mu m$ with SEM. The results showed the full process of laminar-turbulent transition for all three cases. Without SEM artificial turbulence the critical wavelength case showed transition at 75% chord due to separation of the laminar boundary layer at 70% chord. With the addition of SEM artificial turbulence transition was shown to move downstream (80% chord) due to the stabilising effect on the laminar boundary layer of the unsteadiness.

The conclusions made were that the method could be successfully employed using the UNS/LES approach and excellent agreement was made in the receptivity and primary growth stage from distributed roughness elements. Simulation of the secondary instability and transitional region requires additional validation and further studies on the impact of the artificial freestream turbulence.

Chapter 6

Conclusions

The key conclusions and contributions from the work outlined in this thesis is outlined in bullets below:

- A methodology for laminar-turbulent transition has been suggested that can bridge the gap between very high-fidelity DNS and low-fidelity theoretical methods such as LSE. The method uses a LES approach with a low-computational cost sub-grid scale model that has inherent ability to reduce its turbulent viscosity to zero in laminar regions. With careful grid spacing the laminar regions can be explicitly modelled as an unsteady Navier-Stokes. The methodology has been labelled as an unsteady Navier-Stokes/Large Eddy Simulation (UNS/LES) approach.

- The Synthetic Eddy Method (SEM) and WALE SGS model have been written into the 'DELTA' CFD code. The SEM has been modified for the DELTA to allow it to be used in a more flexible manner. Originally the implementation was concerned with turbulence generation for inlet boundary conditions. The method has been implemented such that it provides superimposed coherent turbulent eddies on a plane anywhere in the domain. By implementing the method in this way, a source of turbulence can be applied anywhere in the domain.

- The computational expense of the simulations were reduced by using a streamline extraction approach. This approach exported from the steady, time averaged mean solution the stagnation streamline upstream of the leading edge and the streamline aft of the trailing edge. These were averaged across the span and converted (together with the geometry of the upper aerofoil surface) into a plane which defined the inner boundary of a new solution domain. This approach was

validated against the full geometry case and results of pressure, velocity and skin friction overlapped up to 80% of the chord. This unique approach allowed the simulations to be run at roughly half the cost of the full simulation.

- The UNS/LES approach is capable of modelling the full transitional process. Typically low-fidelity methods require a number of segregated models for each stage of transition (receptivity, primary growth and secondary instabilities). Also a high-fidelity approach require a simplification of the geometry or a recent approach has been to embed the DNS into a RANS calculation. The UNS/LES approach explicitly models each stage of the laminar-turbulent transition process, employing the UNS for the receptivity and primary growth stages. As secondary instabilities begin to occur the sub-grid scale viscosity will increase and will effectively switch to an LES approach for the final stages of laminar turbulent transition.

- An initial first test case was developed to demonstrate the ability of the method using two disturbance generation methods and compared to existing experimental data. Firstly a continuous suction hole and an isolated roughness element. The results matched well with the available experimental data.

- An interesting observation from the first test case flow field results in the secondary instability region was the effect of the memory of secondary instability remained deep into the turbulent region which was also reported recently by DNS results from Duan et al. [25].

- A second test case was chosen to test the approach at more demanding flow conditions (higher Re_c) and to use the approach for modelling of Distributed Roughness Elements (DRE). The DRE control approach has potential to provide a delay in laminar-turbulent transition by forcing stable wavelengths of crossflow vortices using an array of roughness elements. A mesh sensitivity study was conducted to capture the initial amplitude disturbance around the roughness elements. It was clear from the results that to properly resolve the flow around the cylinders at least 10 cells were required in the distance 20% of the cylinder diameter away from the cylinder. If not correctly captured the growth rate and development of the crossflow vortices are unduly affected.

- Results were then obtained for the critical wavelength, $\lambda = 12mm$ at roughness heights $k = 12, 24$, and $36\mu m$. The simulations were compared to experimental

results at 15%x/c and 20%x/c. The simulations compared well with the experimental data, the stationary mode shapes showed excellent agreement in terms of size, shape and amplitude of the disturbance. Decomposition of the spanwise signal showed a predominant $12mm$ mode with shorter peaks at $6mm$. The overall view of the flow field showed the $12mm$ mode dominate to form saturated crossflow vortices.

- For the control wavelength case ($\lambda = 6mm$) results were obtained at roughness height $k = 14, 27$, and $42\mu m$. The simulations were compared to experimental results at 15%x/c. Much like the critical wavelength case the simulations successfully captured the disturbance to a good agreement with the experimental data. The $6mm$ mode dominates the spanwise signal and a clear spanwise uniformity is shown. The amplitudes match well with the experimental data however the smallest roughness height ($k = 14\mu m$ over predicts the amplitude by 33%. This cause of this could be that for this roughness height the grid may require addition cells, or could be attributed to variations in roughness element shape and size in the experiments. The overall flow field showed the $6mm$ mode decay by 30%x/c and the critical wavelength begin to grow.

- Transition was studied for three cases: a critical wavelength case at $12\mu m$ with and without artificial freestream turbulence using SEM and a control wavelength case at $14\mu m$ with SEM. The results showed the full process of laminar-turbulent transition for all three cases. Transition was observed at for all three case close to the pressure minimum of the wing. For the critical wavelength case without freestream turbulence, transition was observed at 74% chord, with SEM freestream turbulence transition was observed at 80% chord. For the control wavelength case with SEM freestream turbulence transition was observed at 72% chord. The mechanism of transition changed with the addition of the freestream turbulence for the critical case, without freestream turbulence transition occurred via laminar separation and turbulent reattachment while transition occurred via a secondary instability with the addition of freestream turbulence.

- The control wavelength case showed a unexpected result in moving transition further upstream from 80% using the critical wavelength case to 72% for the control wavelength case. This shows that for this test case the control wavelength of half the critical wavelength is ineffective in delaying transition. This

was also demonstrated in the experiment of Hunt [42]. Results have shown that control wavelength is more susceptible to a secondary instability than the critical wavelength, this may be due to the additional non-linear modification of the base flow causing higher levels of shear. A conclusion made from this is that applying a control method from just the growth of the primary instability may not be enough but consideration must be made on the development of the secondary instability. Also choosing a control wavelength half of the critical wavelength may not be suitable for control.

The author makes the following recommendations for further work leading on from this thesis:

- Further testing of the secondary instability and final breakdown region - The method described in this thesis has showed promising results and the primary growth and disturbance amplitudes have matched well with experimental results. The secondary instability region however requires further detailed analysis and validation. Results have shown promise and the addition of the SEM method will allow further research to be able to vary the levels of turbulence and the impact it has on the secondary instability region. A more detailed analysis involving full spectral analysis of the growth of individual modes would be required for validation.

- Further development of DRE control method - The simulation method described has proved to be a powerful tool for simulating DRE's. The work from this thesis could be extended further for simulation of a range of roughness heights and spanwise wavelengths to optimise the method.

References

[1] Abbot, I. H., and Von Doenhoff, A. E. *Theory of Wing Sections*. Dover Publications, Inc. New York, 1959. 5

[2] Abdilghanie, A. M., Collins, L. R., and Caughey, D. A. Comparison of turbulence modeling strategies for indoor flows. *Journal of Fluids Engineering 131* (2009). 71

[3] ACARE. European Aeronautics: A vision for 2020, July 2001. 1

[4] Aider, J.-L., and Danet, A. Large-eddy simulation study of upstream boundary conditions influence upon a backward-facing step flow. *Comptes Rendus Mécanique 334*, 7 (2006), 447 – 453. 70

[5] Airbus. Airbus Global Market Survey 2011-2030, Sept. 2011. 1

[6] Anderson, J. D. *Fundamentals of Aerodynamics, Third Edition*. Mcgraw-Hill, 2001. 52

[7] Arnal, D. Boundary layer transition: prediction, application to drag reduction. *Special Course on Skin Friction Drag Reduction, AGARD Report 786* (1992). 8, 31

[8] Arnal, D., and Archambaud, J. Laminar-turbulent transition control: Nlf, lfc, hlfc. Tech. Rep. RTO-EN-AVT-151, Von Karmen Institute, 2008. 32

[9] Bardina, J., Ferziger, J. H., and Reynolds, W. C. *Improved turbulence models based on large eddy simulation of homogeneous, incompressible, turbulent flows*. PhD thesis, Stanford University, 1983. 58

[10] Batten, P., Goldberg, U., and Chakravarthy, S. Interfacing statistical turbulence closures with large-eddy simulation. *AIAA Journal 42*, 3 (2001), 485–492. 71

[11] Becker, K., and Abbas-Bayoumi, A. Airbus Aerodynamics R&T Strategy Internal Report. 3

[12] Benton, J. Presentation on boundary layer methods: Cast2 review. Tech. rep., Airbus, 2008. ix, 40, 41

[13] Bippes, H. Environmental conditions and transition prediction in 3-D boundary layers. *AIAA 97-1906* (1997). 9

[14] Birkby, P., and Page, G. J. Numerical predictions of turbulent underexpanded sonic jets using a pressure-based methodology. *IMESH 215* (2001), Part G: 165–173. 62

[15] Boeing. Natural Laminar Flow Airfoil Analysis and Trade Studies, June 2008. 32

[16] Boiko, A. V., Kozlov, V. V., Sova, V. A., and Scherbakov, V. A. Generation of streamwise structures in a boundary layer of a swept wing and their secondary instability. *Thermophysics and Aeromechanics 7(1)* (2000). 120

[17] Carpenter, A., Saric, W., and Reed, H. Laminar flow control on a swept wing with distributed roughness. *AIAA Paper*, 2008-7335 (2008). 22

[18] Carpenter, A., Saric, W. S., and Reed, H. L. Laminar flow control on a swept wing with distributed roughness. *AIAA Pap. No. 2008-7335* (2008). 11, 37

[19] Chernoray, V., Kozlov, V., Pratt, P., and Löfdahl, L. Hot wire visualizations of breakdown to turbulence in complex flows. In *Proc. EUCASS Conf. Moscos, Russia* (2005), pp. 2.11–2.12. 87

[20] Chernoray, V. G., Doval, A. V., Kozlov, V. V., and Löfdahl, L. Experiments on secondary instability of streamwise vortices in a swept-wing boundary layer. *Journal of Fluid Mechanics 534* (June 2005), 295–325. x, xi, xii, 15, 28, 84, 86, 97, 103, 106, 115, 116, 123, 124, 125

[21] Dagenhart, J. R., and Saric, W. S. Crossflow stability and transition experiments in swept-wing flow. *NASA TP 1999-209344* (1999). 9, 10, 26

[22] Deardoff, J. W. A numerical study of three-dimensional turbulent channel flow at large Reynolds numbers. *Journal of Fluid Mechanics 41* (1970), 453–480. 91

[23] Deyhle, H., and Bippes, H. Disturbance growth in an unstable three-dimensional boundary layer and its dependence on initial conditions. *Journal of Fluid Mechanics 316* (1996), 73–113. 9, 20, 21

[24] Druault, P., Lardeau, S., Bonnet, J.-P., Coiffet, F., Delville, J., Lamballais, E., Largeau, J.-F., and Perret, L. Generation of three-dimensional turbulent inlet conditions for large-eddy simulation. *AIAA Journal 42*, 3 (2004), 447–456. 71

[25] Duan, L., Choudhari, M. M., Li, F., and Wu, M. 43rd Fluid Dynamics Conference, San Diego. In *Direct Numerical Simulation of Transition in a Swept Wing Boundary layer* (2013). 113, 128, 179

[26] Ducros, F., Comte, P., and Lesieur, M. Large-eddy simulation of transition to turbulence in a boundary layer developing spatially over a flat plate. *Journal of Fluid Mechanics 326* (1996), 1–36. 58

[27] El-Hadi, N. M., and Zang, T. A. Large Eddy Simulation of non linear evolution and breakdown to turbulence in high-speed boundary layers. *Theoret. Comput. Fluid Dynamics 7* (1995), 217–240. 58

[28] Ergin, F., and White, E. Unsteady and transitional flows behind roughness elements. *AIAA Journal 44 (11)* (2006), 2504–2514. 22

[29] Germano, M., Nicoud, F., U. Moin, P., and Cabot, W. H. A dynamic subgrid-scale eddy-viscosity model. *Physics of Fluids A: Fluid Dynamics 3*, 1760 (1991). 58

[30] Goldstein, M. E. The evolution of tollmien schlichting waves near a leading edge. *Journal of Fluid Mechanics 127* (1983), 59–81. 19

[31] Gray, W. E. The effect of wing sweep on laminar flow. *Tech. Rep Aero 255 RAE* (1952). 17

[32] Green, J. E. Greener by Design: The Technology Challenge. *The Aeronautical Journal 106* (2002), 57–113. ix, 2, 3

[33] Gregory, N., Stuart, J. T., and Walker, W. S. On the stability of three-dimensional boundary layers with applications to the flow due to a rotating disk. *Phil. Trans. R. Soc. London Ser. A 248:155-99* (1955). 17

[34] Gregory, N., and Walker, W. The effect on transition of isolated surface excrescences in the boundary layer. *ARC CM 2779, Part 1* (1955). 21

[35] Haynes, T. S., and Reed, H. L. Simulation of Swept-Wing Vortices using Nonlinear Parabolized Stability Equations. *Journal of Fluid Mechanics 305* (2000), 325–349. ix, 42, 43

[36] Herbert, T. Parabolized Stability Equations. *Annual Review of Fluid Mechanics 29* (1997), 245–283. 42

[37] High level group on aviation research. Flightpath 2050: Europe's vision for Aviation, July 2011. 1

[38] Hogberg, M., and Henningson, D. S. Secondary instability of crossflow vortices in falkner–skan–cooke boundary layers. *Journal of Fluid Mechanics 368* (1998), 339–57. 30

[39] Hosseini, S. M., Tempelmann, D., Hanifi, A., and Henningson, D. S. Stabilization of a swept-wing boundary layer by distributed roughness elements. *Journal of Fluid Mechanics Rapids 718* (2013), R1. 37

[40] Huai, X., Joslin, R., and Piomelli, U. Large-eddy simulation of transition to turbulence in boundary layers. *Theoretical Computational Fluid Dynamics 9* (1997), 149–163. 58

[41] Huai, X., Joslin, R., and Piomelli, U. Large-eddy simulation of boundary-layer transition on a swept wedge. *Journal of Fluid Mechanics 381* (1999), 357–380. 13, 46, 58

[42] Hunt, L. *Boundary-Layer Receptivity to Three-Dimensional Roughness Arrays on a Swept-Wing*. PhD thesis, Texas A&M University, Dec. 2011. xii, xiii, 15, 37, 130, 131, 132, 141, 145, 148, 149, 150, 152, 154, 155, 156, 158, 160, 161, 176, 181

[43] Jarrin, N., Benhamadouche, S., Addad, Y., and Laurence, D. Synthetic turbulent inflow conditions for large eddy simulation. In *Proceedings,*

4th International Turbulence, Heat and Mass Transfer Conference (Antalya, Turkey, 2003). 70

[44] Jarrin, N., Benhamadouche, S., Laurence, D., and Prosser, R. A synthetic-eddy-method for generating inflow conditions for large-eddy simulations. *International Journal of Heat and Fluid Flow 27*, 4 (2006), 585 – 593. 69, 71, 72, 74

[45] Jarrin, N., Prosser, R., Uribe, J.-C., Benhamadouche, S., and Laurence, D. Reconstruction of turbulent fluctuations for hybrid rans/les simulations using a synthetic-eddy method. *International Journal of Heat and Fluid Flow 30*, 3 (2009), 435 – 442. 71

[46] Jeong, E. and Hussain, F. On the identification of a vortex. *Journal of Fluid Mechanics 285* (1995), 69–94. 112

[47] Joslin, R. D. *Overview of laminar flow control (SuDoc NAS 1.60:208705).* National Aeronautics and Space Administration, Langley Research Center National Technical Information Service, distributor, 1998. ix, 9, 10, 32, 33, 35

[48] Juillen, J. C., and Arnal, D. Etude expérimentale du dé clenchement de la transition par rugosités et par rainer sur de bord d'attaque d'une aile en flèche en éncoulement incompressible. *Rapport Final CERT/ONERA No. 51/5018.35.* (1990). 21, 23

[49] Kaltenbach, H.-J., Fatica, M., Mittal, R., Lund, T. S., and Moin, P. Study of flow in a planar asymmetric diffuser using large-eddy simulation. *Journal of Fluid Mechanics 390* (7 1999), 151–185. 70

[50] Kawakami, M., Kohoma, Y., and Okutsu, M. Stability characteristics of stionary crossflow vortices in three-dimensional boundary layer. *AIAA Paper 99-0811* (1999). 27

[51] Kloker, M. Advanced laminar flow control on a swept wing - useful crossflow vortices and suction. In *38th Fluid Dynamics Conference and Exhibit, 23-26 June* (Seattle, Washington, 2008). 45

[52] Kohama, Y., Onodera, T., and Egami, Y. Design and control of crossflow instability field. In *In Duck P, Hall P (eds) IUTAM Symp. on Nonlinear*

Instability and Transition in Three-Dimensional Boundary Layers. ed. P. Duck and P. Hall (Manchester, UK, 1996), pp. 147–156. 27

[53] Kohama, Y., Saric, W. S., and Hoos, J. A. A high-frequency, secondary instability of crossflow vortices that leads to transition. In *In Proc. Royal Aero. Soc. Conf. on Boundary-Layer Transition and Control* (1991). 27

[54] Kondo, K., Murakami, S., and Mochida, A. Generation of velocity fluctuations for inflow boundary conditions of les. *Journal of Wind Engineering and Industrial Aerodynamics 67:68* (1997), 51–64. 70

[55] Langtry, R. B. *A Correlation-Based Transition model using Local Variables for Unstructured Parallelized CFD Codes*. PhD thesis, University of Stuttgart, Aug. 2006. 44

[56] Lee, S., Lele, S., and Moin, P. Simulation of spatially evolving compressible turbulence and the application of taylors hypothesis. *Physics of Fluids* (1992), 1521–1530. 70

[57] Leonard, A. Energy Cascade in Large Eddy Simulation of turbulent fluid flow. *Adv. Geophys. 18A* (1986), 237–248. 54

[58] Lilly, D. K. A proposed modification of the Germano subgrid-scale closure method. *Physics of Fluids A: Fluid Dynamics 4*, 3 (1992), 633. 57, 58

[59] Lund, T., Wu, X., and Squires, K. Generation of turbulent inflow data for spatially-developing boundary layer simulations. *Journal of Computational Physics 140*, 2 (1998), 233–258. cited By (since 1996)461. 69, 70, 71

[60] Maddalon, D. Boeing 757 hybrid laminar-flow contol flight tests. Tech. Rep. TM-104090, NASA, Langley Aerospace Test Highlight, 1990. 35

[61] Malik, M. R., Li, F., and Chang, C. L. Crossflow disturbances in three-dimensional boundary layers: Nonlinear development, wave interaction and secondary instability. *Journal of Fluid Mechanics 268* (1994), 1–36. 29, 42

[62] Malik, M. R., Li, F., and Chang, C. L. Nonlinear crossflow disturbances and secondary instabilities in swept-wing boundary layers. *IUTAM Symposium on Nonlinear Instability and Transition in Three Dimensional Boundary Layers* (1996). 29, 42

[63] Malik, M. R., Li, F., Choudhari, M. M., and Chang, C.-L. Secondary instability of crossflow vortices and swept-wing boundary-layer transition. *Journal of Fluid Mechanics 399* (1999), 85–115. 26, 29, 37, 42, 113

[64] Mathey, F., Cokljat, D., Bertoglio, J., and Sergent, E. Assessment of the vortex method for large eddy simulation inlet conditions. *Progress in Computational Fluid Dynamics 6*, 1-3 (2006), 58–67. 71

[65] McCollum, D., Gould, G., and Greene, D. Greenhouse gas emissions from aviation and marine transportation: Mitgation potential and policies. Tech. rep., Pew Center on Global Climate Change, 2009. 4

[66] Meinke, M., Schröder, W., Krause, E., and Rister, T. A comparison of second- and sixth-order methods for large-eddy simulations. *Computers Fluids 31*, 4–7 (2002), 695 – 718. 64

[67] Meneveau, C., Lund, T. S., and Cabot, W. H. A Lagrangian dynamic subgrid-scale model of turbulence. *Journal of Fluid Mechanics 319* (1996), 353–385. 58

[68] Morkovin, M. V. Critical evaluation of transition from laminar to turbulent shear layer with emphasis on hypersonically travelling bodies. *Technical Report AFFDL-TR-68-149* (1969). 19

[69] Morkovin, M.V. On the many faces of transition. *Viscous Drag Reduction* (1969), 1–31. 7, 18

[70] Morkovin, M.V. and Reshotko, E. and Herbert, T. Transition in open flow systems - a reassessment. *Bull. APS 39(9) 1882* (1994). ix, 18, 19

[71] Müller, B., and Bippes, H. Experimental study of instability modes in a three-dimensional boundary layer. *Fluid Dynamics of Three-Dimensional Turbulent Shear Flows and Transition. AGARD CP 438* (1990), 13–15. 21

[72] Nicoud, F., and Ducros, F. Subgrid-Scale Stress Modelling Based on the Square of the Velocity Gradient Tensor. *Flow, Turbulence and Combustion 62* (1999), 183–200. 57, 59, 60

[73] Page, G. J. Loughborough University, Department of Aeronautical and Automotive Engineering, Loughborough. *Delta User's Guide release 2.1 edition* (May 1999). 62

[74] Page, G. J., Li, Q., and McGuirk, J. J. LES of Impinging Jet Flows Relevant to Vertical Landing Aircraft. In *The 23rd Applied Aerodynamics Conference* (Toronto, Canada, 2005). 62

[75] Péneau, F., Boisson, H. C., Kondjoyan, A., and Djilali, N. Structure of a flat plate boundary layer subjected to free-stream turbulence. *Int. J. Comput. Fluid Dynamics 18 (2)* (2004), 175–188. 58

[76] Perret, L., Delville, J., Manceau, R., and Bonnet, J.-P. Generation of turbulent inflow conditions for large eddy simulation from stereoscopic piv measurements. *International Journal of Heat and Fluid Flow 27*, 4 (2006), 576 – 584. 71

[77] Pfenniger, W., and Lachman, G. V. *Boundary Layer and Flow Control.* Pergamon, 1961. 6

[78] Pfenninger, W. Some observations of the transition process on the windward face of a long yawed cylinder. *Recent Developments in Boundary Layer Research AGARDograf 97* (1965). 8

[79] Piomelli, U., and Balaras, E. Wall-layer models for large-eddy simulations. *Annual Review Of Fluid Mechanics 34* (2002), 349–374. 89

[80] Piomelli, U., and Liu, J. Large-eddy simulation of rotating channel flows using a localized dynamic model. *Physics of Fluids 7*, 4 (1995), 839. 58

[81] Pokora, C. D., McMullan, W., Page, G. J., and McGuirk, J. J. Influence of a numerical boundary layer trips within LES of a subsonic jet on spatio-temporal correlations. In *17th AIAA/CEAS Aeroacoustics Conference* (Portland, Oregon, 2011). 62, 67

[82] Poletto, R., Craft, T., and Revell, A. A new divergence free synthetic eddy method for the reproduction of inlet flow conditions for les. *Flow, Turbulence and Combustion* (2013), 1–21. 70

[83] Poll, D. I. A. Some Observations of the Transition Process on the Windward Face of a Long Yawed Cylinder. *Journal of Fluid Mechanics 150* (1985), 329–356. 8, 27, 29

[84] Pope, S. B. *Turbulent Flows.* Cambridge University Press, 2000. 53, 54, 57

[85] Prandtl, L. In *Proc. Third Intern. Math. Congress* (Heidelberg, 1904), pp. 484–491. 5

[86] Radeztsky, R. H. J., Reibert, M. S., and Saric, W. S. Effect of isolated micron-sized roughness on transition in swept-wing flows. *AIAA Journal 37(11):1371-7* (1999). 21, 22, 23, 36

[87] Reed, H. L., and Saric, W. S. A Validation of the Parabolized Stability Equations for Three- Dimensional Boundary Layers. *Asme Paper No. FEDSM2000-11345, June* (2000). 42

[88] Reibert, M. S., Saric, W. S., Carrillo, R. B., and Chapman, K. L. Experiments in nonlinear saturation of stationary crossflow vortices in a swept-wing boundary layer. *AIAA Pap. No. 96-0184* (1996). ix, 22, 26, 29, 37, 145

[89] Reibert, M. S., Saric, W. S., Carrillo, R. B., and Chapman, K. L. xperiments in Nonlinear Saturation of Stationary Crossflow Vortices. *AIAA Paper 96-0184* (1996). ix, 36, 42, 43, 45

[90] Reneaux, J., and Blanchard, A. The design and testing of an airfoil with hybrid laminar flow control. *First European Forum on Laminar Flow Technology Vol. DGLR-Bericht 92-06* (1992), 164–174. 35

[91] Reynolds, O. An experimental investigation of the circumstances which determine whether the motion of water shall be direct or sinous. *Phil Trans Roy Soy London 174* (1883), 935–982. 6

[92] Rhie, C. M., and Chow, W. L. Numerical study of the turbulent flow past an aerosol with trailing edge separation. *AIAA Journal 21* (1983), 1525–1535. 63

[93] Rife, R. E., and Page, G. J. Large Eddy Simulation of high Reynolds number jets with microject injection. In *17th AIAA/CEAS Aeroacoustics Conference* (Portland, Oregon, 2011). 62

[94] Ruban, A. I. On the generation of tollmien schlichting waves by sound. *Fluid Dynamics 19, 709-716.* (1985). 19

[95] Saguat, P. *Large Eddy Simulation for Incompressible Flows: An Introduction.* Springer Berlin Heidelburg, 1998. 53, 54

[96] Salman, H., Jiang, D., McGuirk, J. J., and Page, G. J. Linear and non-linear turbulence model predictions of vortical flows in lobed mixers. *Aeronautical Journal*, 108 (2004), 65–73. 62

[97] Saric, W. S. Görtler Vortices. *Annual Review of Fluid Mechanics 26* (1994), 379–409. 8

[98] Saric, W. S. Experiments in 3-d boundary layers: Stability and receptivity. Tech. Rep. RTO-EN-AVT-151, Von Karmen Institute, 2008. 24

[99] Saric, W. S. Introduction to linear stability. Tech. Rep. RTO-EN-AVT-151, Von Karmen Institute, 2008. 40

[100] Saric, W. S., Carrillo, R. B., and Reibert, M. S. Leading-edge roughness as a transition control mechanism. *AIAA Pap. No. 98-0781* (1998). 11, 36, 37, 129

[101] Saric, W. S., Reed, H. L., and White, E. B. Stability and Transition of Three-Dimensional Boundary Layers. *Annual Review of Fluid Mechanics 35*, 1 (Jan. 2003), 413–440. 9, 24, 29

[102] Saric, W. S. and Reed, H. L. and Kerschen, E. J. Boundary-layer receptivity to free stream disturbances. *Annual Review of Fluid Mechanics 34* (2002), 291–319. 6, 7, 19

[103] Sayadi, T., and Moin, P. Large eddy simulation of controlled transition to turbulence. *Physics of Fluids 24* (2012). 46

[104] Schlatter, P. *Large Eddy Simulation of Transition and Turbulence in Wall Bounded Shear Flow*. PhD thesis, Swiss Federal Institute of Technology Zurich, Apr. 2005. 13, 46, 54, 59

[105] Schlichting, H. *Boundary-Layer Theory, Sixth Edition*. Mcgraw-Hill, 1968. 5

[106] Schrauf, G. Status and perspectives of laminar flow. *Aeronautical Journal 109*, 1102 (2005), 639–644. ix, 2, 5, 7

[107] Schrauf, G., Herbert, T., and Stuckert, G. K. Evaluation of Transition in Flight Tests Using Nonlinear PSE Analysis. *AIAA Paper 95-1801* (1995). ix, 34, 42

[108] Sergent, M. E. *Vers une méthodologie de couplage entre la simulation des grandes echelles et les modèles statistiques.* PhD thesis, Ecole Central de Lyon, 2002. 71

[109] Smagorinsky, J. General circulation experiments with the primitive equations I. The basic experiment. *Monthly Weather Review 91* (1963), 99–164. 57

[110] Stolz, S., and Adams, H. A. An approximate deconvolution procedure for large-eddy simulation. *Phys. Fluids A 11 (7)* (2003), 1699–1701. 59

[111] Tabor, G., Bab-Ahmadi, M. H., de Villers, E., and Weller, H. G. Construction of inlet conditions for les of turbulent channel flow. In *Proceedings of the ECCOMAS congress, Finland* (2004). 70

[112] Tabor, G., and Baba-Ahmadi, M. Inlet conditions for large eddy simulation: A review. *Computers Fluids 39*, 4 (2010), 553 – 567. 69, 70

[113] Temmerman, L., and Leschziner, M. A. Large eddy simulation of separated flow in a streamwise periodic channel construction. In *Int. Symp. on Turbulence and Shear Flow Phenomena* (2001). 61

[114] Tempelmann, D., Schrader, L. U., Hanifi, A., Brandt, L., and Henningson, D. S. Swept wing boundary-layer receptivity to localised surface roughness. *Journal of Fluid Mechanics 711* (2011), 516–544. 37, 45, 133, 145

[115] Van Driest, E. R. On turbulent flow near a wall. *Journal of the Aeronautical Sciences 23* (1956), 1007–1011. 57, 91

[116] Veloudis, I. *A study of Subgrid Scale Modelling and Inflow Boundary Conditions for Large Eddy Simulation of Wall-bounded Flows.* PhD thesis, Loughborough University, 2006. 62

[117] Von Doenhoff, A. E., and Braslow, A. L. The effect of distributed roughness on laminar flow. *Boundary-Layer Control (ed. Lachmann) 2* (1961), 657–81. 22

[118] von Kaenel, R., Adams, H. A., Kleiser, L., and Vos, J. B. The approximate deconvolution model for large-eddy simulations of compressible flows with finite volume schemes. *J. Fluid Engng 124* (2002), 829–835. 59

[119] von Kaenel, R., Adams, H. A., Kleiser, L., and Vos, J. B. The approximate deconvolution model for large-eddy simulations of compressible flows with finite volume schemes. *J. Fluid Engng 125* (2003), 375–381. 59

[120] Wang, P. C., and McGuirk, J. J. Large eddy simulation of supersonic jet plumes from rectangular con-du nozzles. *International Journal of Heat and Fluid Flow* (2013). 62

[121] Wasserman, P. and Kloker, M. Transition mechanisms induced by travelling crossflow vortices in a three-dimensional boundary layer. *Journal of Fluid Mechanics 483* (2003), 67–89. 30, 37, 45, 83

[122] Wasserman, P. and Kloker, M. Transition mechanism in a 3D boundary layer with pressure gradient changeover. *Journal of Fluid Mechanics 530* (2005), 265. 9, 26, 30, 37, 45, 83

[123] White, E. B., and Saric, W. S. Secondary instability of crossflow vortices. *Journal of Fluid Mechanics 525* (2005), 275–308. ix, 9, 10, 18, 27, 28, 29, 45, 131

[124] Williamson, J. H. Low-storage Runge-Kutta schemes. *Journal of Computational Physics 35* (1980), 48–56. 64

[125] Zang, Y., Street, R. L., and Koseff, J. R. A dynamic mixed subgrid-scale model and its application to turbulent recirculating flows. *Phys. Fluids A 5 (12)* (1990), 3186–3196. 58